

**New Approaches to Simultaneous
Multislice Magnetic Resonance Imaging:
Sequence Optimization and Deep
Learning based Image Reconstruction**

Dissertation

submitted to the Faculty of Physics and Electrical Engineering

University of Bremen, Germany

for the degree of

Doctor of Natural Sciences (Dr. rer. nat.)

Klaus Eickel

Referees:

Prof. Dr. Matthias Günther

Prof. Dr. Tony Stöcker

Bremen, 2019

You can actually suffer a little bit more going slowly than when you're going really fast. A faster marathon might even be easier than a slow one, in terms of what it takes out of you mentally.

Frank Shorter

Contents

Abstract and Outline	v
I Introduction and Basic Concepts	1
1 MRI in Medicine	3
1.1 Radiology: From X-Ray to Modern Imaging	3
1.2 Anatomy and Physiology	4
1.2.1 Blood	4
1.2.2 The Vascular System and Perfusion	5
1.2.3 Angiogenesis	5
1.3 MRI in Radiation Oncology	6
1.4 Accessing Physiological Parameters	7
1.4.1 Contrast-Enhanced Perfusion MRI in Oncology	8
1.4.2 BOLD Imaging in fMRI	10
2 Basics of MRI	11
2.1 Nuclear Magnetic Resonance	11
2.1.1 Nuclear Spin	11
2.1.2 Magnetic Moment and Magnetization	12
2.2 RRF and RF Excitation	13
2.3 Relaxation Processes and Image Contrast	15
2.4 Gradients and Spatial Encoding	16
2.4.1 Slice Selective RF Excitation	17
2.4.2 In-plane Spatial Encoding	17
2.5 Image Contrast	21
3 Acceleration Techniques	23
3.1 Echo Planar Imaging	23
3.1.1 Theory of echo-planar imaging (EPI)	23
3.1.2 Multi-Shot EPI	25
3.2 MRI with Multiple Receiver Coils	26
3.2.1 Elimination of Noise Correlation in Coils	28
3.2.2 Parallel Imaging and GRAPPA	29
3.2.3 Signal-to-Noise and g-Factor	34
3.3 Simultaneous Multi-Slice Imaging	36
3.3.1 Multiband Excitation	37

3.3.2	SMS Reconstruction	37
3.3.3	CAIPIRINHA Shifting	39
II	SMS for Dynamic Imaging	43
4	Materials and Methods: Dynamic Imaging	45
4.1	Combined DCE and DSC	45
4.2	Segmented EPI for multi-contrast SMS	46
4.2.1	Slice Profiles in SMS	47
4.3	In-vivo Perfusion Experiments	49
4.3.1	Subjects and Experimental Setup	49
4.3.2	Imaging Parameters and Protocol	50
4.3.3	Postprocessing	52
4.3.4	Image Reconstruction and Quality Assessment	52
4.4	Dependency of slice-GRAPPA on Image Contrast Variations	54
4.5	Slice Profiles and MB RF Pulse Imperfections	55
4.5.1	Slice Profiles: Experiments	55
4.5.2	Effects of Excitation Imperfections	56
5	Results: Dynamic Imaging	59
5.1	In-vivo Perfusion Experiments	59
5.1.1	Signal Separation and Dynamic Imaging	59
5.1.2	Reconstruction Performance and Image Quality	61
5.2	Dependency of slice-GRAPPA on Image Contrast Variations	64
5.3	Slice Profiles in SMS and RF Pulse Imperfections	70
III	Deep Learning in MRI	79
6	Neural Networks and Deep Learning	81
6.1	Deep Learning	81
6.1.1	Terminology and Network Structures	82
6.2	Training of a Neural Network	85
6.2.1	Backpropagation	85
6.2.2	Overfitting and Regularization	88
6.2.3	Generalization by Randomness	92
7	Materials and Methods: SMSnet	95
7.1	Software and Architecture	96
7.2	Architecture of SMSnet	98

7.3	Data for Training and Testing	101
7.4	Training of SMSnet	103
7.5	Evaluation of Reconstructions with SMSnet	104
7.6	Higher Acceleration Factors	108
7.7	Layer Activations	108
7.8	Manipulation of Input Data	109
8	Results: SMSnet	111
8.1	Image Quality	111
8.1.1	Comparison with Established Reconstruction Strategies	113
8.1.2	Reconstruction of Phantom Data	116
8.1.3	Noise Propagation and Signal Sensitivity	121
8.1.4	Severe Changes in the Coil Sensitivities	124
8.1.5	Robustness to Object Motion	127
8.1.6	Synthesized and Acquired SMS Data	128
8.1.7	Cross-System Transferability	131
8.2	Higher Acceleration Factors	132
8.3	Layer Activations	135
8.4	Manipulation of Input Data	139
IV	Discussion & Conclusions	141
9	Discussion and Outlook	143
9.1	SMS for Dynamic Imaging	143
9.1.1	Slice Profiles and MB RF Imperfections	149
9.2	Deep Learning in SMS	150
10	Conclusions	157
V	Appendix	159
Appendix A	Appendix	161
A.1	Signal-Dynamics in In-vivo Perfusion Experiments: Further Subjects	161
A.2	SMS Reconstruction for In-vivo Perfusion Experiments - Further Subjects	163
A.3	Bias-Variance Dilemma	166
A.4	SMSnet: MR Protocol for Data Acquisition	167
A.5	SMSnet: Additional Figures and Tables	168
A.5.1	Phantom Data	168

A.5.2	Robustness to Object Motion	171
A.5.3	Severe Changes in the Coil Sensitivities	171
A.5.4	Cross-System Transferability	172
A.5.5	Higher Acceleration Factors	173
A.5.6	Manipulation of Input Data	174
A.6	SMSnet: Summary of Trainings	175

Bibliography		187
---------------------	--	------------

Abstract and Outline

Magnetic resonance imaging (MRI) is a versatile imaging modality in clinical diagnostics. Despite the impressive range of application, a main drawback of MRI is its inherently low acquisition speed. However, scan time is crucial for many applications and also for an efficient utilization of MRI in clinical routine. Two developments have influenced MRI recently: Simultaneous multislice imaging (SMS) and deep learning (DL).

Simultaneous multislice imaging is a paradigm shift in MRI which has re-emerged in the early 2010'. It yields improved image quality compared to in-plane parallel imaging, because it benefits from increased signal-to-noise ratio and robustness for higher accelerations. SMS sequences accelerate data acquisition by undersampling along the slice dimension and specific algorithms allow reconstruction of these under-sampled data.

In the first part, SMS was extended to measure multiple image contrasts in contrast-enhanced dynamic MRI. Therefore, a bespoke MRI sequence was developed to accelerate segmented echo-planar imaging of three echoes. Dynamic in-vivo data with sufficient spatial coverage were acquired in an animal model. Data acquisition were fast enough to sample the arterial input function which is essential for pharmacokinetic modeling. Imperfections in the excitation of multiple slice and their relevance for reconstruction algorithms were closely investigated and evaluated for processing of multi-contrast data.

This work connects SMS and deep learning. Today, the application of deep learning in medicine assists decision making in medical diagnosis, analysis of radiologic data or personalized medicine in genomics [Fou16]. In magnetic resonance imaging (MRI) however, deep learning has just entered the stage. With two abstracts matching the search term 'deep learning' at the ISMRM 2016, the number of abstracts rose to 42 in 2017 and to 139 in 2018 [Mag17a; Mag17b; Mag18]. Most of the early contributions to DL in MRI concern image processing and data evaluation. Image reconstruction itself is mostly conducted in standard fashioned way. Common algorithmic approaches applying deep neural networks for (some) processing steps have shown impressive results and can often be generalized to similar problems [Yos+14].

In the second part, the separation of overlapping slice content after SMS was performed by an artificial neural network. This novel reconstruction technique, termed *SMSnet*, does not require any reference data for calibration of the MR machine's receiver characteristics. Omitting the need for reference data could extend the use of modern accelerated imaging sequences to a broad spectrum of applications [Bil+18]. Potential and limitations of this approach were investigated in various experiments

accounting for image quality, robustness, sensitivity and how the network generalizes. The discussion at the end summarizes and relates the results of this work to state-of-the-art techniques and recent developments in MRI and gives an outlook to future work on SMS and DL-based reconstructions.

Part I

Introduction and Basic Concepts

1 The Role of MRI in Medicine

This chapter briefly reviews the historical development of radiology followed by an introduction to the *objects* investigated by MRI in this work. These can be structures like bones or organ-tissue or physiological processes, mainly blood-flow and perfusion.

1.1 Radiology: From X-Ray to Modern Imaging

In 1895, the physicist Wilhelm Conrad Röntgen entered a new age in medical diagnosis. He first published the discovery of X-rays and their ability to penetrate some materials while being absorbed by others. Six years later, Röntgen received the first Nobel Prize in physics for his remarkable work. He radiographed an assistant's hand live on stage [col00], and from these early times onwards radiology has become an important field of medicine where screening, diagnostics and monitoring lead to a detailed insight into the human body and its intricate physiology [SM14]. The ongoing development from glass plates over films to digital visualization of radiographic images has transited plain radiography into modern digital radiology providing not only tomographic images in versatile forms of visualization, but also information beyond plain anatomy serving as direct biomarkers or facilitating more accurate diagnoses in the clinical decision process [SM14]. This 'success' in more information should also be considered critically in some cases, because more information can sometimes lead to diagnostic confusion as well [SM14].

Aside the remarkable benefits of today's radiology, many imaging modalities come with additional risks associated with the ionizing radiation to which patients are exposed to. Radiation safety procedures began soon after clinical radiology had been established, but radiation-induced damage remains a critical point for X-ray, computer tomography (CT) or positron emission tomography (PET).

Ultrasound (US) and, from the early 1980s onwards, MRI extend the spectrum of available modalities and offer alternatives which are free of harmful ionizing radiation. Nevertheless, each modality has its individual (dis-)advantages and they all have found their place in modern radiological routine.

MRI, however, might have revolutionized the field of radiology more than any other technique after the discovery of X-rays. The ability to image without ionizing radiation, the option for selectable range of contrasts, its flexibility to be adjustable for a wide range of clinical questions may be unique properties and reasons for the increasing popularity and importance of MRI in anatomical and physiological imaging [Bae+05; Ope17].

1.2 Anatomy and Physiology

The following sections introduce the anatomical and physiological basics inside the human body. If not referenced explicitly otherwise, the given facts are based on [Ope17], where an extensive description can be found as well.

Anatomy (Greek *anatomē*, ‘to cut apart’ or ‘dissection’) is the study of the human body’s structure. These structures range in size from macro- to microscopic where microbiology ties in with the later one and observations require optical instruments. On the macroscopic scale unaided eyesight as well as modern radiological machinery are used to observe structures for pathological changes. While dissection and ex-vivo examination represent anatomy in a rather traditional manner, today’s in-vivo and often completely non-invasive anatomical observation is assisted by a number of imaging techniques including MRI.

Physiology (Greek *physis*, ‘nature ’ or ‘origin ’) can be considered a complementary discipline which studies the function of body’s structures. This includes the chemistry and physics of the structures of the body and how their interaction supports the functions of life. On one hand physiology can be macroscopic, e.g. to study the musculoskeletal system with focus on the movement of the body. On the other hand it can take processes on a smaller base into account and investigate, for example, molecular exchange or fluid dynamics like the blood flow and its distribution. As for anatomy, physiological observations can be radiologically aided by machines where MRI, among others, plays an essential role thanks to its high general flexibility.

1.2.1 Blood

Most functions for (human) life are non consciously controlled processes, but driven by a complex interplay of electrochemical, chemical or physical factors. Almost all physiological processes relate directly or indirectly to the cardiovascular system made up of the heart, vessels and blood. An intact cardiovascular system guarantees the primary functions of a healthy biological system. Therefore, imaging of responses of the cardiovascular system to physiological processes serve as a measurable parameter and sometimes direct biomarker for changes in the body. Blood, acting as the mediator of this system, delivers oxygen, transports nutrients, removes cellular wastes and other byproducts to removal organs, assists the immune response and preserves homeostasis. Blood can also transmit information through hormones released by endocrine glands into the bloodstream.

Blood itself is a connective tissue and unlike other connective tissues unique in a way because it is fluid. By being a connective tissue it is made up of cellular elements, including red and white blood cells, and an fluid extracellular matrix, the plasma. The plasma itself consists to about 8% of suspended substances, mostly proteins, and to 92% of water making it an excellent candidate to be imaged with MRI. Under

normal, healthy conditions blood has a stable temperature of about 38°C , slightly above body temperature and a viscosity of $1.4 \text{ mN} \cdot \text{s}/\text{m}^2$.

1.2.2 The Vascular System and Perfusion

The heart pumps blood in a closed network of differently sized blood vessels. This subpart of the cardiovascular system which carries the blood throughout the body is called vascular system. Starting at the heart, blood streams away in the aorta, where arteries connect to and distribute blood to tissue, organs and even bones. The arteries branch into even smaller vessels, the arterioles, which finally branch into thin capillaries with a diameter of $5 \mu\text{m} - 10 \mu\text{m}$. The exchange of oxygen, nutrients and wastes between blood and tissue takes place in these finest structures of the vascular system, the so-called capillary bed. The transportation of blood through the capillary bed is known as perfusion measured in $\frac{\text{ml}}{\text{s} \cdot \text{mg}}$. The capillaries combine later on the venules which themselves merge into veins and through which the blood returns to the heart (Fig. 1.1).

The different vessels share many features, but also differ in some structural properties. The heart ejects blood into the major aorta and then surging in the vascular system. The differences in pressure let the blood flow and as such, this requires stronger vessel walls for the higher pressure at the beginning of the closed vascular system than at its end. Blood streams through the lumen, a hollow passageway inside the vessels, that is smaller in diameter in the arterial than the venous partition of the system to ensure correct pressure. The complex interaction of pressure, blood velocity, blood volume, vascular resistance and others is called hemodynamics. A simplified approach is to formulate the vascular blood flow by the law of Hagen-Poiseuille as laminar fluid dynamics. The role of the vessels diameter, the total cross-sectional area, blood pressure and velocity can be described well on a macrovascular scale. However, since blood cells with a approximate sizes of $6 \mu\text{m} - 15 \mu\text{m}$ and the capillaries are of similar size, fluid dynamics disappear. The mass movement of fluids into and out of the capillary bed requires additional transport mechanisms. As depicted in Figure 1.1, hydrostatic and osmotic pressure move fluid or suspension from the capillaries into the interstitial fluid, also known as tissue fluid, and vice versa. The osmotic concentration gradients are not determined by the erythrocytes, leukocytes and thrombocytes in the blood, rather, it is the plasma proteins that play the key role.

1.2.3 Angiogenesis

Angiogenesis is the creation of new vascular structure, i.e. blood vessels from existing ones. It is responsible for most blood vessel growth during development and vascularization of new formed tissue, but also in disease. The term cancer is broadly used to describe diseases caused by mutated, abnormal cells accompanied by uncontrolled cell division, fast proliferation and vessel growth. While mutations not

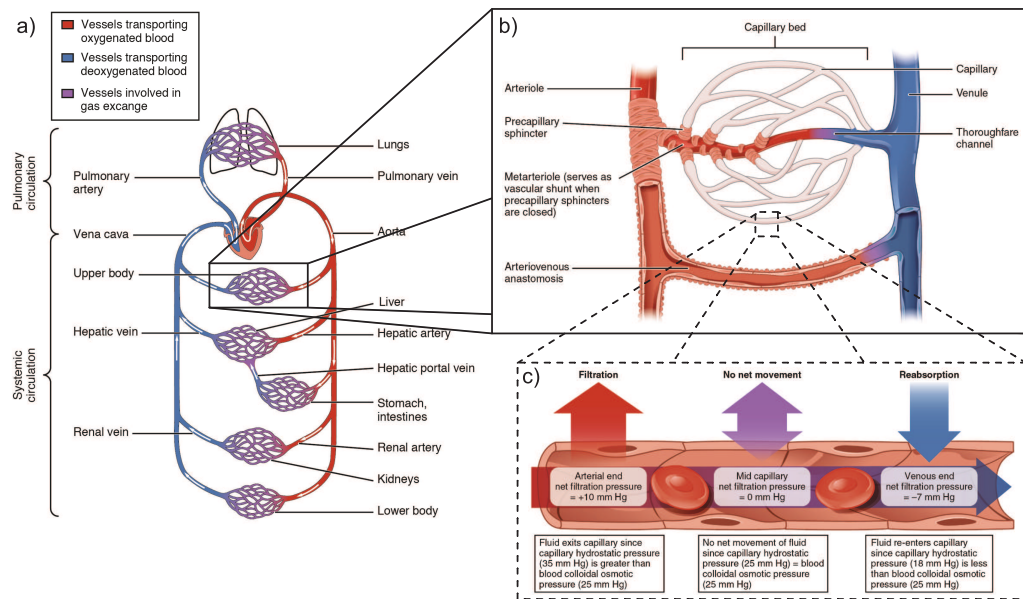


Figure 1.1: a) The cardiovascular and pulmonary circulation where the heart center moves blood through the lungs and the vascular system. b) A zoomed, schematic illustration of the capillary bed with its connections to the arterial and venous vessel system. c) Interplay of hydrostatic and osmotic pressure driving the exchange processes in the capillary bed. Adapted from [Ope17] licensed by CC BY 4.0.

necessarily chase noticeable change in the cell function, mutations affection the key proteins directly impact the cell's properties. These abnormal cells often lose the ability to proliferate orderly, which results in the formation of irregular tissue and vascular structures. Accumulations of abnormal cells and the resulting formation of tumors are often benign, but can become malignant, or cancerous. Cancerous tumors breach neighboring tissue, promote irregular angiogenesis, in particular on the capillary level and metastasize to other organs later on. Despite their chaotic order, tumors are not merely disorganized accumulations of cells, but have their own structures. Nevertheless, the fast growth of a tumor makes it vasculature porous with wide interendothelial junctions, heterogeneous and coarse in the capillary bed [Bae+05]. The vessels may also show discontinuous or even absent base membrane. All these factors favor leakage of solvents from the vasculature into the extravascular extracellular space (EES) [Jai87].

1.3 MRI in Radiation Oncology

Radiotherapy, a therapy where ionizing radiation is used to locally control or eliminate cancerous cells, is one of the most important therapies in nowadays cancer treatment [Bau+16]. Selection and contouring of the targeted tumor volume is an important challenge for successful radiotherapy [Bau+16]. Because of its excellent soft-tissue contrast, its harmlessness in terms of ionizing radiation and its versatility, MRI plays a key role for delineating the tumor volume, but also structures and organs at risk in

radiation therapy planning [Bae+05; Met+13]. While anatomical imaging has become an essential component in radiation oncology, the potential of physiological imaging to access radiobiological factors or biomarkers has only been partly revealed [Bau+16]. The so-called ‘Rs’ of radiotherapy determining the biological effectiveness of radiation are: radio-sensitivity or radio-resistance, hypoxia and reoxygenation, repopulation and redistribution. The reliable assessment of these ‘Rs’ is highly relevant for planning advanced radio-therapeutic treatments such as intensity-modulated radiotherapy (IMRT) and dose adaption between fractions to achieve tumor control and long-term survival [Bau+16].

By use of specific MRI techniques, physiological information such as tumor perfusion, vascular permeability, extracellular space tortuosity, metabolic status and hypoxia, which are potentially related to the ‘Rs’ can be obtained and support therapy planning [Des+09]. One essential component to assess physiological information by MRI is dynamic imaging, which requires fast acquisition methods to reflect physiological processes with timescales of a few seconds (Cha. 1.4). In particular, for MRI techniques where an exogenous substance, the so-called contrast agent, is injected, rapid sampling of the fluid dynamics in major vessels is crucial. Additionally, accelerated magnetic resonance (MR) acquisition strategies are desirable for most sorts of imaging protocols, either anatomical or physiological because the availability of MR machines is limited and clinical workflow is strict.

1.4 Accessing Physiological Parameters

As introduced in Section 1.2, blood flow and perfusion represent essential parameters of nearly all physiological processes and ,therefore, often serve as a biomarker for various clinical diagnoses [Sam16]. MRI techniques to access physiological parameters may be divided into exogenous and endogenous methods. In the first ones, an exogenous substance, a so-called contrast agent (CA), is injected into the vascular system and its distribution is traced. dynamic contrast-enhanced (DCE) and dynamic susceptibility contrast (DSC) are well known methods to measure perfusion by contrast-enhanced MRI as described in more detail in Section 1.4.1. Contrary, methods which trace endogenous substances work non-invasively. Blood-oxygenation-level dependent (BOLD) imaging, which will be introduced in Section 1.4.2, is a well-known technique to access brain activity in functional magnetic resonance imaging (fMRI). For perfusion imaging, arterial spin labeling (ASL) is a MRI technique which used magnetically labeled blood to trace supply of tissue with blood [Det+92]. Although, many properties of ASL, e.g. non-invasive and repeatable, make it an appealing method, clinical ASL has still a limited spectrum of applications, such as brain or kidney perfusion [Als+15].

1.4.1 Contrast-Enhanced Perfusion MRI in Oncology

The following section will give an brief introduction to dynamic contrast-enhanced MRI in research and clinical oncology. If not explicitly cited differently, this section refers to [Bae+05]. Further reading suggestions for image analysis from the beginning of CA-enhanced MRI [Ros+90], to the comprehensive issue of the so-called arterial input function (AIF) sampling [Cal13] as well as basic and advanced pharmacokinetic modeling [SB13] and perfusion MRI [Jah+14] can be found in the references. Yet, this work focuses on the acquisition of the MR signal rather than on its detailed analysis.

The first injection of a Gadolinium-based CA for MRI in a human volunteer was conducted in Berlin in 1983 to show resulting signal enhancement in the bladder [Loh+16]. The motivation for contrast-enhanced MRI and, in particular, its value for oncology arises from the variations in temporospatial enhancement patterns after CA-administration. Figure 1.2 depicts the temporal changes in the MR signal (a) and the diffusion by which CA-molecules may pass vessel walls and enter the EES to equalize intra- and extravascular CA-concentration (b). Over time, excretion by the kidneys reduces intravascular CA-concentration and the concentration gradient changes direction which results in back-diffusion of the tracer particles. This phase is called wash-out, because CA-molecules are gradually removed from the body.

The dynamics in the MR signal reflect (abnormal) changes in microvascular structure and pathophysiology. These can be affected by various physiological factors including regional blood flow, perfusion, vessel density, permeability and surface area of endothelial membranes or size of the EES and its CA-concentration difference to the plasma. All these factors change, to a certain extent, from healthy tissue to tumor. CAs are exogenous media shortening the so-called relaxation times, T_1 , T_2 and T_2^* , in MRI which will be introduced in Section 2.3. Therefore, they have an indirectly influence on the MR signal. Gadolinium (Gd)-based extracellular compounds are the most common type of intravenous MRI CAs. Gd belongs to the lanthanide series of elements and has strong paramagnetic properties with its 7 unpaired electrons. The Gd ion Gd^{3+} keeps its unpaired electrons when bound to a chelate structure to suppress its toxicity, its powerful magnetic moment is largely maintained [BV08]. Non-specific as well as (angiography-, liver-) specific CAs have medical approval and differ in their molecular structure, their distributional properties and their mechanism of excretion [BV08]. The CA used throughout this work is of extracellular type, named gadoterate meglumine and available under its brand name Dotarem (Guerbet, Villepinte, France). More information are available on the product's web-page [Gue18].

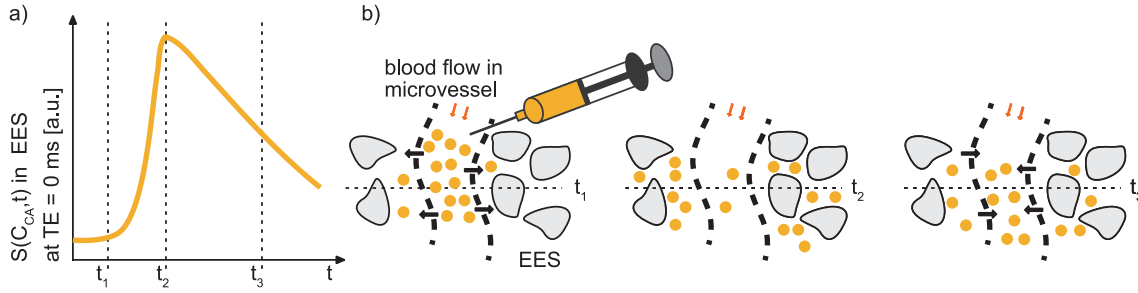


Figure 1.2: Schematic overview of the CA-exchange processes after bolus-injection. a) The dynamic MR signal in relation to local CA-concentration in the EES starts at baseline (t_1), before CA-concentration reaches a maximum in EES (t_2) and CA diffuses back into vasculature (t_3). b) The exchange of CA between vasculature and EES is depicted schematically. After injection (t_1), rapid CA-extravasation determined by vessel permeability, vessel-wall-surface-area and blood flow increases the signal when CA molecules accumulate in the EES (t_2). The CA-molecules do not penetrate intact cellular walls. The phase while CA diffuses back into vasculature and is excreted from there is called wash-out (t_3).

DCE and DSC MRI

Various methods for dynamic, CA-enhanced MRI have been proposed and have coexisted for perfusion imaging over the last decades. The two most widely used approaches for dynamic MRI with CA enhancement are: DCE, which relies on the so-called T_1 -weighted signal, and the DSC method, which measures changes in the so-called T_2 - or T_2^* -weighted signal over time [SB13]. DCE and DSC, i.e. T_1 - and T_2^* -weighted imaging methods, differ in the effect of CA on the acquired MR signal. The MR signal is increased in DCE, because of the reduced longitudinal relaxation time T_1 while the MR signal in DSC is decreased due to a shortened transversal relaxation time T_2^* . The differences between these methods regard as well the underlying mechanisms which reflect different physiological information. T_2^* -change is a long-range phenomenon where sensitivity is dominated by magnetic field gradients caused by magnetic susceptibility differences between regions of higher and lower CA-concentrations, i.e. intravascular space and EES or during bolus phase when CA-concentration rises fast and peaks inside the vascular system before extravasation [Lüd+09b]. By contrast, the T_1 -weighted contrast mechanism is more localized to the tracer molecules and performs well in leakage quantification [Lüd+09b]. The simultaneous acquisition of differently weighted MR signals allows removal of T_2^* -shortening effects from the T_1 -weighted DCE signal and vice versa during postprocessing [Miy+97; Von+00]. Hence, the separation of the measured MR signal into its T_1 - and T_2^* -dominated contributions reveals a more complete basis for physiological analysis. This increases the reliability of calculated parameters, e.g. blood volume which is commonly underestimated in DCE if the measured signal is only T_1 -weighted and T_2^* -contribution are neglected. A detailed description of this

approach can be found in Chapter 4.

After the MR measurement, one of the first processing steps is to translate the MR signal changes into CA-concentration and, only thereafter, tracer kinetics can be applied to translate concentration time curves to a domain in which they can be interpreted in a physiological sense, e.g. perfusion, blood volume or vessel permeability. The conversion from MR signal to CA-concentration is an additional and error-prone processing step for which accurate sampling of the AIF is essential [Cal13]. The pharmacokinetic modeling itself will not be addressed in detail in this thesis, because it rather focuses on MR physics and related methodical concepts of image acquisition and reconstruction. None the less, it should be emphasized, that dynamic MR data can provide valuable clinical information even if a pharmacokinetic analysis is not feasible [Bae+05]. This is underlined by the fact, that CA-enhanced MRI is an established method in clinical imaging of tumors [Jah+14].

1.4.2 BOLD Imaging in fMRI

There exist other physiological parameters besides perfusion in MRI. For example, BOLD imaging which is of particular interest in fMRI. Even though, neither fMRI nor the associated BOLD effect are the main focus of this work, they will be explained in brevity as the BOLD signal founds the background for experiments in Section 7.5. Neural activity induces variations in the blood oxygenation resulting in changes of T_2^* -signal. As hemoglobin becomes deoxygenated, it becomes more paramagnetic (hemoglobin's oxygen loading shields its ionic properties) which leads to stronger susceptibility effects and a shortened T_2^* relaxation time. The underlying mechanism of BOLD bases on the levels of (de-)oxygenated hemoglobin in the blood and the vascular system's overcompensation with oxyhemoglobin in case of increased oxygen demand. Therefore, an increased T_2^* -signal can be detected in neurological active areas.

Neural activation can be triggered, for example, by visual or auditive stimuli or motion tasks, i.e. finger tapping. The controlled switching between the trigger or active and rest phase is called design matrix or paradigm.

Hence, BOLD imaging is a non-invasive way to measure physiological responses dynamically and explore the sensitivity of the MR measurement and image reconstruction to small signal changes at the same time. The later, rather experimental aspect, relates to an experiment described and evaluated in Sections 7.5 and 8.1.3.

2 Basics of MRI

The following sections will briefly describe the principles of MRI based on [Haa+99; BKZ04; Lev09]. The extensive physics of nuclear magnetic resonance (NMR) and MRI in the classical and quantum mechanical picture, the vast range of MRI sequences and the versatile technical solutions in modern MRI systems can be found elsewhere in the literature. The basic principles presented in Section 2.1 are limited to relevant aspects for this work. It follows an account on the conceptual and technical basics of MRI. The so-called sequence controls the imaging process itself. This is basically formed by four ‘components’: the radio-frequency pulses for excitation and, optionally, preparation, the relaxation processes, the spatial encoding through a series of spatial (magnetic) gradients and the signal reception in the signal domain, also known as k-space. Basically, k-space and MR image are related directly by Fourier transformation. However, advanced image acquisition techniques often require more sophisticated post-processing and reconstruction methods as described later on in Chapter 3.

Section 2.1 starts with a quantum mechanical approach to motivate the underlying physics (Sec. 2.1.1) from which the basics of MRI are evolved in a semi-classical description (Sec. 2.1.2 ff.).

2.1 Nuclear Magnetic Resonance

This section introduces the quantum mechanical concept of nuclear spins and their associated magnetic moments. The phenomenon of NMR can be observed in any nucleus with a non-zero nuclear spin. However, the following description focuses on the importance of the proton spin in the hydrogen nucleus, its associated magnetic moment and its interaction with an external magnetic field, \vec{B} , in NMR and MRI. Because of the great abundance of hydrogen in the human body and its high gyromagnetic ratio (Sec. 2.1.2) it has become the most popular element for NMR in medicine.

2.1.1 Nuclear Spin

With 99.98%, ^1H is the most common, naturally occurring hydrogen isotope. Its nuclear spin \vec{J} has an absolute value of

$$|\vec{J}| = \sqrt{J(J+1)}\hbar = \frac{\sqrt{3}}{2}\hbar, \quad (2.1)$$

with $J = 1/2$, the nuclear spin quantum number for the ^1H nucleus. In an external B field, two spin states are observed. Therefore, the spin projection quantum number for $J = 1/2$ is $m_J = \pm 1/2$ for the two eigenstates. The two eigenstates degenerate in

absence of external magnetic field. Even though this quantum mechanical foundation allows a pictorial description to derive the magnetic properties from, it should be noted, that macroscopic magnetization effects dominate in MRI for medical applications [Han08].

2.1.2 Magnetic Moment and Magnetization

The nuclear spin \vec{J} is associated with an intrinsic magnetic moment $\vec{\mu}$ aligned along the direction of \mathbf{J} as

$$\vec{\mu} = \gamma \cdot \vec{J} \quad (2.2)$$

with the gyromagnetic ratio of $\gamma/2\pi = 42.58 \text{ MHz/T}$. For N nuclei, the magnetic moments in a volume V can be summarized to a total magnetization vector

$$\vec{M} = \frac{1}{V} \sum_{i=1}^N \vec{\mu}_i . \quad (2.3)$$

In presence of an external B field, i.e. the *main magnetic field* \vec{B}_0 , which w.l.o.g is aligned along the z-axis in MRI, the nuclear Zeeman effect or Zeeman splitting occurs. Meaning, that an energy difference ΔE associated with the (two) eigenstates ($m_J = \pm \frac{1}{2}$) exists. For a ^1H nucleus the energy gap is

$$\Delta E = \gamma \cdot \hbar \cdot B_0 . \quad (2.4)$$

with $B_0 = |\vec{B}_0|$. Combined with the Planck relation, this leads to

$$\Delta E = \hbar\omega = \gamma \cdot \hbar \cdot B_0 \Rightarrow \omega_L \equiv \gamma \cdot B_0 . \quad (2.5)$$

The frequency related to the energy difference is denoted as *Larmor frequency* ω_L . Low-energy eigenstates, parallel to \vec{B}_0 , are favored. However, with increasing temperatures, i.e. at body temperature, the probability to be in either energy-level is dominated by thermal energy described by Boltzmann statistics. At human body temperature ($T \approx 310 \text{ K}$) and with the Boltzmann constant $k_B = 1.38 \cdot 10^{-23} \text{ J/K}$, Taylor expansion for $\hbar\gamma B_0 \ll k_B T$ reveals an approximated net magnetization of [Haa+99]

$$\vec{M} \simeq \rho \frac{\gamma^2 \cdot \hbar^2}{4 \cdot k_B \cdot T} \cdot \vec{B}_0 = \chi \vec{B}_0 \quad (2.6)$$

with the proton density ρ and χ known as the magnetic susceptibility [Han08].

The general equation of motion for the clockwise precession of \vec{M} is described by a torque equation

$$\frac{d}{dt} \vec{M} = \gamma \cdot \vec{M} \times \vec{B}(t) , \quad (2.7)$$

valid for an ensemble of non-interacting protons in an effective magnetic field \vec{B} . Note that from Equation 2.7 follows that \vec{M} in equilibrium alignment does not precess since $\vec{B} = \vec{B}_0$ with $\vec{B}_0 \parallel \vec{M}$. However equilibrium alignment can be disturbed by injection of external energy in form of an oscillating magnetic field. The second magnetic field is typically termed B_1 field as introduced in the following section.

2.2 Rotating Reference Frame and Radiofrequency Excitation

The excitation process to generate a MR signal will be described in this section. For the description of the governing physics for MR signal formation, the concept of a second reference system besides the laboratory reference system will be briefly introduced. The so-called rotating reference frame (RRF) is a transformed right-handed Cartesian coordinate system, which rotates clockwise about the z -axis by an angular frequency ω_{rot} , with the z -axis chosen to be along longitudinal direction of main magnetic field \vec{B}_0 and x - y -axes which span the transversal plane. The rotation matrix

$$\mathbf{R} = \begin{pmatrix} \cos(\omega_{\text{rot}}t) & -\sin(\omega_{\text{rot}}t) & 0 \\ \sin(\omega_{\text{rot}}t) & \cos(\omega_{\text{rot}}t) & 0 \\ 0 & 0 & 1 \end{pmatrix} \quad (2.8)$$

can be employed to switch between the two reference frames. If \hat{x}' , \hat{y}' and \hat{z}' denote the orthogonal unit vectors in the Cartesian laboratory reference frame, these are transformed into unit vectors in the RRF by

$$\begin{aligned} \hat{x} &= \hat{x}' \cdot \cos(\omega_{\text{rot}}t) - \hat{y}' \cdot \sin(\omega_{\text{rot}}t) , \\ \hat{y} &= \hat{x}' \cdot \sin(\omega_{\text{rot}}t) + \hat{y}' \cdot \cos(\omega_{\text{rot}}t) , \\ \hat{z} &= \hat{z}' . \end{aligned} \quad (2.9)$$

The clockwise rotation of the RRF may be determined by a rotational angular velocity vector

$$\vec{\Omega} = \omega_{\text{rot}} \hat{z} . \quad (2.10)$$

Therewith, any vector \vec{p}' in the laboratory frame rotated by $\vec{\Omega}$ has a time rate of change given by

$$\left(\frac{d\vec{p}}{dt} \right)' = \vec{\Omega} \times \vec{p}' . \quad (2.11)$$

Moving the equation of motion in Equation 2.7 from the static laboratory reference frame to the RRF by

$$\frac{d\vec{M}}{dt} = \left(\frac{d\vec{M}}{dt} \right)' - \vec{\Omega} \times \vec{M} , \quad (2.12)$$

aligning the Larmor precession in Equation 2.5 along \hat{z} and inserting the definition of $\vec{\Omega}$ (Eq. 2.10) leads to

$$\frac{d\vec{M}}{dt} = (\omega_L - \omega_{\text{rot}})\vec{M} \times \hat{z} . \quad (2.13)$$

A complete derivation of the above expressions for the RRF can be found in [Haa+99]. With $\omega_{\text{rot}} = \omega_L$, descriptive equations for the spin dynamics simplify. The magnetization vector in Equation 2.13 becomes stationary, i.e. $\frac{d\vec{M}}{dt} = 0$, and the effect of \vec{B}'_0 (main magnetic field in laboratory reference frame) disappears. Under such conditions, a rotating reference system is said to be in resonance and is therefore termed *B₀ reference frame*. By comparison of the torque equation (Eq.2.7) for the laboratory reference frame and Equation 2.12, the *effective magnetic field* in the RRF can be defined as

$$B_{\text{eff}} = \vec{B}' + \frac{\vec{\Omega}}{\gamma} \quad (2.14)$$

with \vec{B}' being the effective magnetic field in the laboratory reference frame. An effective magnetic field results from superposition of multiple magnetic fields with respect to the chosen reference system, commonly the main magnetic field along z and the additional oscillating magnetic field of the radiofrequency (RF) pulse. The magnetization precesses about the direction of the effective magnetic field. The second magnetic field, the so-called B₁ field, may be realized as a quadrature field for which two identical, linearly polarized RF fields are added with a phase-shift of $\pi/2$, meaning

$$\vec{B}_1^{\text{circ}} = B_1(\hat{x}' \cdot \cos(\omega_{\text{rf}}t) - \hat{y}' \cdot \sin(\omega_{\text{rf}}t)) . \quad (2.15)$$

If the rotating frame frequency is set to the carrier frequency of the RF pulse, $\omega_{\text{max rot}} = \omega_{\text{rf}}$, the reference frame is referred to as the B₁ reference frame and Equation 2.15 simplifies to

$$\vec{B}_1^{\text{circ}} = B_1\hat{x} \equiv \vec{B}_1 . \quad (2.16)$$

Circularly polarized RF fields are advantageous compared to a single linearly polarized RF field because the generally time dependent B₁ field appears static in an appropriate RRF. Therewith, its full pulse amplitude is available for manipulation of the magnetization and RF power is used more efficiently.

The application of a RF pulse with an appropriate frequency ω_{rf} tips the magnetization vector \vec{M} about its equilibrium axis \vec{B}_0/B_0 . Temporal width and amplitude of the RF pulse determine the flip-angle (FA), also denoted as α , of \vec{M} . However, an idealized, instantaneous RF pulse with zero duration is usually assumed for formulations in the following sections which describe spatial encoding, imaging and relaxation.

2.3 Relaxation Processes

Most of the so far described physical processes are idealized, since no interactions of the individual hydrogen nuclei with its environment were considered. Macroscopic explanations including interactions of (local) magnetizations are non-static, i.e. $\vec{M} \Rightarrow \vec{M}(t)$, once an external magnetic field disturbed equilibrium (Eq. 2.7). The net magnetization \vec{M} can be separated into its vectorial components

$$\vec{M} = \vec{M}_{\parallel} + \vec{M}_{\perp} = \vec{M}_z + \vec{M}_{x,y} \quad (2.17)$$

referred to as longitudinal and transverse magnetization with respect to \vec{B}_0 . \vec{M}_z and $\vec{M}_{x,y}$ change dynamically until equilibrium is reached again. The relaxation time constant for \vec{M}_z is denoted as T_1 . It describes the restoration of magnetization along the longitudinal axis, which is also called spin-lattice relaxation. T_2 is the second relaxation time constant. It describes the decay, or dephasing, of the magnetization along the transverse axis, which is also termed spin-spin relaxation. In the RRF, both processes are covered by the phenomenological Bloch-equation

$$\frac{d}{dt}\vec{M} = \gamma \cdot \vec{M} \times \vec{B} - \begin{pmatrix} \frac{M_x}{T_2} \\ \frac{M_y}{T_2} \\ \frac{M_z - M_0}{T_1} \end{pmatrix} \quad (2.18)$$

which can be solved to

$$M_z = M_z(t) = M_0(1 - e^{-t/T_1}) \quad (2.19)$$

and

$$M_{x,y} = M_{x,y}(t) = M_{x,y}(0) \cdot e^{-t/T_2} \quad (2.20)$$

with the initial magnetization components M_0 along z and $M_{x,y}(0)$ in the transverse plane immediately after the excitation pulse.

Dephasing of $M_{x,y}$ happens typically on a shorter timescale than restoration of M_z , therefore $T_2 \leq T_1$. In addition, different magnetic susceptibilities, e.g. at tissue borders, lead to local inhomogeneities in the magnetic field which accelerate the decay of the transverse magnetization. The effective transverse relaxation time T_2^* is defined by the rate

$$\frac{1}{T_2^*} = \frac{1}{T_2} + \frac{1}{T_2'} \quad (2.21)$$

where T_2' is attributable to local magnetic field inhomogeneities ΔB

$$T_2' = \frac{1}{\gamma \Delta B}. \quad (2.22)$$

Therefore, if magnetic field inhomogeneities are not compensated appropriately, T_2^* replaces T_2 in Equation 2.20. The relaxation times T_1 , T_2 are tissue specific constants, while T_2^* depends on specific properties of the object being measured and the measurement process itself.

2.4 Gradients and Spatial Encoding

The formation of a MR signal as described in Section 2.2 was done globally in the entire object inside the MR machine. Three orthogonal gradient magnetic fields

$$\vec{G} = (G_x, G_y, G_z)^T = \begin{pmatrix} \frac{\partial B_z}{\partial x} \\ \frac{\partial B_z}{\partial y} \\ \frac{\partial B_z}{\partial z} \end{pmatrix} \quad (2.23)$$

generated by independent gradient coils can be superimposed to the main magnetic field \vec{B}_0 to obtain spatially resolved information.

Equation 2.23 is idealized and ignores the effect of higher-order concomitant magnetic fields, which are a consequence of the Maxwell equations. For a source free vacuum and if displacement current densities are negligible, the Gauss's and Ampère's circuital law simplify to

$$\nabla \cdot \vec{B} = 0 \text{ and } \nabla \times \vec{B} = 0. \quad (2.24)$$

These equations require additional magnetic fields with nonlinear spatial dependence when a linear gradient is activated. The resulting concomitant magnetic field terms are proportional to G^2/B_0 meaning that their effects (< 2 ppm at 1.5 T) can be commonly neglected in most imaging situations [Ber+98]. Potential image artifacts include geometric distortions, ghosting and intensity loss due to extra phase accumulation. A concomitant magnetic field represents a physics effect and is not a consequence of any hardware imperfections.

For 2D MRI, spatial encoding can be categorized into two steps. First, the slice selection gradient along z is applied. Simultaneously, the RF pulse manipulates a defined portion of magnetization as introduced in Section 2.4.1. This reduces the spatial distribution of relevant magnetization from 3D to 2D. Second, the in-plane encoding in x and y which is performed after the excitation process and encodes the remaining two orientations as shown in Section 2.4.2.

2.4.1 Slice Selective RF Excitation

As the Larmor frequency ω_0 is directly connected to the local magnetic field, it becomes a linear function of the position \vec{r} when an additional linear magnetic field (gradient) \vec{G} is superimposed to the static field \vec{B}_0 . Choosing z to be the static field direction, a simplified formulation of the Larmor frequency in a gradient field is

$$\omega(z) = \gamma(B_0 + z \cdot G_z) = \omega_0 + \gamma \cdot z \cdot G_z . \quad (2.25)$$

The desired slice thickness Δz is determined by the gradient strength G_z and centered around the position of the central frequency. Hence, with a given frequency bandwidth $\Delta\omega$ of the RF pulse the slice thickness is defined by

$$\Delta z = \frac{\Delta\omega}{\gamma \cdot G_z} , \quad (2.26)$$

as also illustrated for two different gradient amplitudes $G_{z,1}, G_{z,2}$ in Figure 2.1.

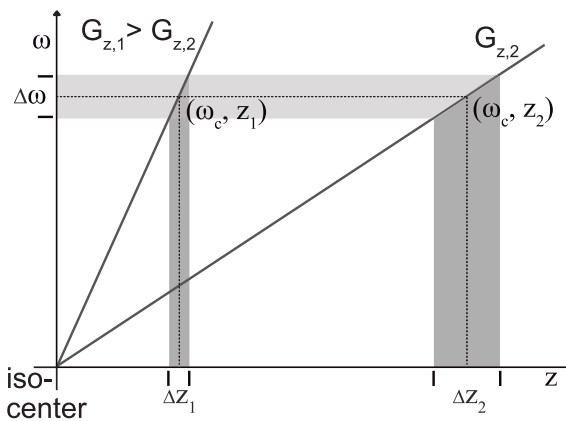


Figure 2.1: Slice selective RF excitation results from application of a specially tailored RF pulse which carries a defined bandwidth of frequencies $\Delta\omega$ around the center frequency ω_c and is simultaneously applied with a slice selective gradient ($G_{z,1}, G_{z,2}$). The gradient strength is inverse proportional to the finite slice thickness, i.e. $\Delta z_1 < \Delta z_2$ for $G_{z,1} > G_{z,2}$. The positions of the selected slices, z_1, z_2 , are defined by the center frequency and gradient strength.

2.4.2 In-plane Spatial Encoding

Once the MR signal has been created, spatially encoded data have to be collected before the signal decay is completed. Manipulation of the signal's frequency and phase by additional magnetic gradient fields is one key aspect of any MR sequence. The following parts introduce the concept of *k-space* which was patented in 1979 by Likes [Lik79] and its potential for MR sequence development was published in the early 1980's [Lju83; Twi83]. *k-space* represents the acquired signal with respect to the frequency history of the spins which is spatially modulated by the application of time-varying magnetic field gradients [Lik79].

k-Space Formalism

Knowing the concept of k-space, which is also known as Fourier domain, is rather fundamental to understand modern MRI. Although k-space can be expanded to a multidimensional scenario, only the 2D representations will be of interest in this section. For further reading, it is referred to standard books on MRI [BKZ04; Haa+99].

k-space can be considered as a coordinate system containing complex-valued numbers which represent spatial frequencies. Image domain and k-space are two representations of the acquired MR signal. Both can be converted to one another by the Fourier transform. By that, the spin density $\rho(\vec{r})$ can also be defined as a function of the k-space vector \vec{k}

$$\tilde{\rho}(\vec{k}) = \int_V \rho(\vec{r}) e^{-i\vec{k}\cdot\vec{r}} d\vec{r} = \mathcal{F}_{2D}(\rho(\vec{r})) \quad (2.27)$$

with the Fourier transform in 2D \mathcal{F}_{2D} . In mathematical practice, a discrete Fourier transform is required to process a finite number of data points which is computationally realized by the Fast Fourier transform (FFT) algorithm.

By the application of magnetic gradient fields along (one of) the three spatial directions, the MR pulse sequence encodes $S(t)$ along these orthogonal directions. The coordinates in k-space can be formulated as an integral description of the respective gradients

$$\vec{k} = \gamma \int_0^t \vec{G}(t') dt' . \quad (2.28)$$

The k-space trajectory is thus determined by the temporal integral of the gradient amplitudes between the RF excitation and the data collection. For the multidimensional case in volume V , the fundamental signal equation

$$S(t) = \int_V \rho(\vec{r}) \cdot \exp(-i\gamma\vec{r} \cdot \int_0^t \vec{G}(t') dt') d\vec{r} \quad (2.29)$$

can be written as [Lju83]

$$S(t) = \tilde{\rho}(\vec{k}(t)) . \quad (2.30)$$

From and 2.30 It can be seen, that Equation 2.27 describes the trajectory in k-space \vec{k} to assign the signal $S(t)$ to positions in the 2D k-space that corresponds to Fourier transform of the spin density (Eq. 2.30) [Lju83].

Sequences in MRI

The timing of RF pulses, magnetic field gradients and data acquisition can be graphically illustrated in a sequence diagram as shown in Figure 2.2. After RF excitation, transversal magnetization collects a phase from all applied gradient fields depending on gradient strength and timing as well as its polarity. The application

of gradients can accelerate dephasing, but can also rephase the manipulated phase in a controlled manner as illustrated in Figure 2.2. A correctly balanced de- and

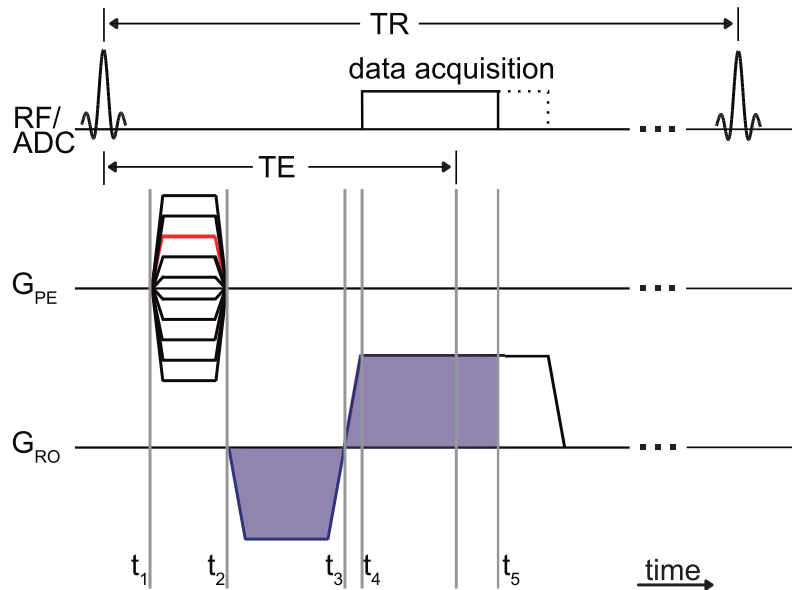


Figure 2.2: After RF excitation the timing of two orthogonal gradients G_{RO} and G_{PE} determines the k -space trajectory. The proceeding in k_y direction corresponds to the area under the phase-encoding gradient G_{PE} (red, $[t_1, t_2]$) while traveling along readout direction is determined by G_{RO} starting with the dephasing gradient at t_2 (blue). Often data is not sampled during ramp times, e.g. $[t_3, t_4]$, to yield equally distributed k -space data points. Here, data are sampled during readout period $[t_4, t_5]$ as indicated by the solid box in the ADC. The dotted area in the ADC represents the remaining readout for complete data sampling along one readout (RO) line. When the RO gradients are balanced, the central data point along RO at $k_{RO} = 0$ is acquired. The duration between RF excitation and the readout at $k_{RO} = 0$ equals TE. The period between successive RF excitations of the same magnetization is quantified by TR. Timing of the slice selection gradient G_z is not shown.

rephasing results in a so-called gradient echo (GRE), which is centered at $k_{RO} = 0$. The duration between RF excitation and readout at $k_{RO} = 0$ is denoted as echo-time (TE) (Fig. 2.2). The T_2 and T_2^* relaxation processes themselves are unaffected by this additional phase manipulation. Figures 2.2 and 2.3 schematically show the effect of applied gradients to the k -space trajectory. After the RF excitation, the phase-encoding (PE) gradient proceeds along the y -axis, also termed k_{PE} , during the interval $[t_1, t_2]$ followed by the prephasing gradient which sweeps the k -space in negative k_{RO} direction along the x -axis $[t_2, t_3]$. Signal is sampled during the application of the RO gradient $[t_3, t_4]$. The RO line in Figure 2.3 is not fully sampled yet which is indicated by the dotted line at the end of the analog-digital converter (ADC) event block (Fig. 2.2) and the dashed trajectory (Fig. 2.3). During data acquisition the signal is discretely sampled by the ADC, the sampling time per complex data point is named dwell time Δt . The dwell time is the inverse of the

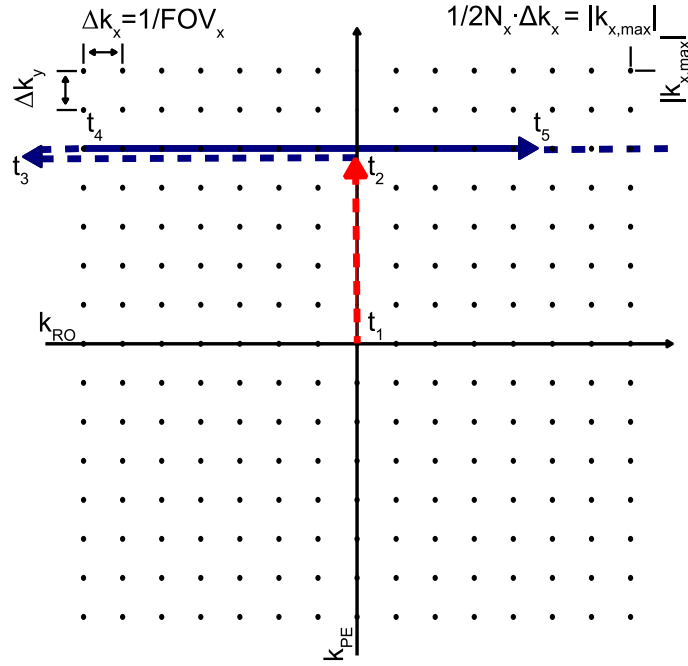


Figure 2.3: Schematic k-space trajectory according to the gradient timing diagram in Figure 2.2. G_{PE} (red) is the path resulting from the phase-encoding gradient. The blue path represents the RO line with dephasing (dashed, $[t_2, t_3]$), rephasing during ramp up time (dashed, $[t_3, t_4]$) and data acquisition (solid, $[t_4, t_5]$). The maximal frequency sampled or in the formalism of k-space the highest value of k along one direction ($k_{x,max}$ along RO, $k_{y,max}$ along PE) defines the image resolution (Δx , Δy) along this direction. For a desired spatial coverage of an object of length FOV_x (FOV_y) the distance of k-space data points Δk_x (Δk_y) has to be chosen accordingly.

receiver bandwidth in readout direction BW_{RO}

$$\Delta t = 1/BW_{RO} . \quad (2.31)$$

In data sampling the sampling frequency should fulfill the *Nyquist-Shannon* sampling theorem for discrete sampling. It states that the sampling frequency, also known as bandwidth (BW), has to be twice the maximal frequency (e.g. signal with maximal frequency component ω_{max}) to correctly reconstruct a band limited signal without aliasing artifacts [ZWZ10], thus

$$BW \geq 2\omega_{max} . \quad (2.32)$$

This has to be taken into account for the ADC during readout as well as for the bandwidth in PE direction. The receiver unit demodulates $S(t)$ along RO, meaning that the Larmor frequency of the transverse magnetization is removed. Similar to the quadrature field for excitation (Sec. 2.2), the receiver unit converts the real signal induced in the receive coils into a complex signal by quadrature detection. Therefore, a quadrature receive coil is made up of a pair of coils S_{re} and S_{im} which is

arranged such that a phase-shift of $\pi/2$ in the signal is realized between them. This gives the complex-valued signal

$$S = S_{\text{re}} + iS_{\text{im}} \quad (2.33)$$

saved to k-space. The application of a RO gradient simultaneously to data acquisition linearly varies the precession frequency in such way that data can be 1D-spatially encoded (Fig. 2.2). The full range of frequencies across an object is proportional to the gradient strength and size of the object. The bandwidth along RO can be quite high and readout oversampling is commonly used to avoid aliasing along this direction. Contrary to data acquisition along RO, oversampling along PE is expensive in terms of sampling duration. Herewith, aliasing artifacts are a prominent issue along this axis.

Even though, locations in k-space do not have a direct geometric correspondence to pixel locations in the image, the spatial frequencies in k-space have a relation to the image contrast and image details. Low spatial frequencies in the k-space's central region mainly determine the image contrast while high spatial frequencies in k-space's periphery correspond to image details, i.e. edges.

The sampling density, i.e. distance of adjacent points in k-space Δk_x , Δk_y , and the maximum extent of the k-space, $k_{x,\text{max}}$, $k_{y,\text{max}}$, define the spatial coverage of the field of view (FOV) and the spatial resolution along these directions as depicted in Figure 2.3. Spatial resolution is linked to the gradient integral (Eq. 2.28) and therefore depends on the gradient's amplitude and duration of the active gradient. Both are, however, limited in MRI, gradients' peak amplitudes and slew rates are technically limited, but constrained because of physiological interactions, too. The available readout time might also be limited, not only by the overall imaging time, but also by unavoidable signal decay for long readout trajectories as described in Section 3.1.

2.5 Image Contrast

In Section 2.4.2, the concept of GRE sequences was introduced. A second, basic type of echo-forming sequence is known, if the free induction decay (FID) after RF excitation is manipulated by an additional RF pulse. A second RF pulse is inserted between the excitation RF pulse and the readout at $TE/2$. Because many of the T_2^* -processes which accelerate the FID are symmetrically reversible, the second RF pulse regenerates some of the spin phase information [Els18]. Accordingly, the signal after such two RF pulses at TE is denoted as spin echo (SE). The second RF pulse may have a FA of 180° to maximize compensation for T_2^* -effects. The type of echo, either GRE or SE, is connected to the image contrast. Hence, GRE sequences acquire signal suffering from T_2^* -dephasing, while signal from SE sequences decays with T_2

only.

The imaging parameters, repetition-time (TR) and TE, which were introduced in Section 2.4.2 are important to control the image contrast. The term *weighting* is commonly used to characterize image contrast. Intrinsic tissue parameters, such as ρ , T_1 , T_2 and the relaxation time T_2^* dominate the observed image contrast. However, their influence in the image can be manipulated by choice of the imaging sequence and the selected imaging parameters.

If a chosen relaxation time allows full recovery of the longitudinal magnetization and transverse magnetization decay is minimized, the acquired signal is dominated by the spin density. In this case, the image is called ρ -weighted. The abbreviation PD-weighted, where PD stands of proton density, is also commonly used.

The exponential functions for recovery of the longitudinal magnetization (Eq. 2.19) and decay of the transversal magnetization (Eq. 2.20) reveal how the sensitivity to either relaxation time is connected to sequence timing. If M_z does not recover completely and TE is shortened, the sensitivity of the signal to T_1 -changes is increased. The acquired image is called T_1 -weighted. Later acquisition of the central k-space data leads to so-called T_2 - (SE) and T_2^* -weighted images (GRE).

3 Acceleration Techniques in MRI

This chapter introduces techniques by which imaging speed has been significantly increased. As the focus of this work is on simultaneous multislice imaging (SMS) and the combination of SMS with multi-shot EPI, the fundamentals of these techniques are described as well as accompanying concepts for image reconstruction and evaluation. The historical background is also given in brief to put different developments in technical and chronological context.

3.1 Echo Planar Imaging

In 1977, Sir Peter Mansfield unveiled EPI during a symposium at the University of Nottingham just some years after the initial principles of MRI have been invented. At that time imaging times typically ranged around one hour and the EPI method was about to enter a completely new world for fast imaging techniques [SST98]. Extreme demands on hardware components, i.e. gradients and RF, and new aspects in sequence design and image reconstruction decelerated the breakthrough of EPI. Germinating in Nottingham, EPI research spread out in 1982 when Ian Pykett and Richard Rzedzian set up *Advanced NMR Systems, Inc.* to create a commercial product. Years later in 1985 the so-called *blipped* technique introduced by Johnston and Edelsertein formed another basic element for genuinely single-shot acquisition and by 1986 most of the early problems had been solved [SST98]. Siemens in Germany and General Electric in the United States embarked the development of EPI in the late 1980s either in their own laboratories (Siemens) or by established collaborations (General Electric and Advanced NMR Systems) and latest after Phillips, Picker and Toshiba followed in the early 1990s EPI became commercially and thereby clinically available [SST98]. Nowadays, EPI is common for various applications such as fMRI, angiography, cardiac and perfusion imaging.

After this short historical background, the concepts of single- and multi-shot EPI based on [SST98] are introduced in the following sections.

3.1.1 Theory of EPI

In contrast to standard pulse sequences which mostly acquire a single k-space line along RO direction per RF excitation, an EPI pulse sequence acquires (all or several) PE lines after a single excitation. Therefore, EPI accelerated measurements significantly and the short acquisition time offers great potential for fast and motion insensitive imaging.

A gradient with alternating polarity reverses the direction of the signal traversal in k-space according to Equation 2.28. In EPI, the typical direction of alternating gradients is along RO. Brief pulses, or *blips*, of the PE gradient assign the signal to

PE positions. These two components, alternating RO gradients and PE blips, are the essential elements to form the so called echo train in EPI sequences as shown in the sequence diagram in Figure 3.1. The resulting k-space sampling is illustrated in Figure 3.2. Two basic types of EPI sequences are commonly used. A spin echo EPI, where a 180° RF pulse is played before readout, forms a spin echo at TE and eliminates T_2^* -effects. In FID EPI, the RO follows the RF excitation directly without any further RF pulses. Only the later one is used in this work.

The readout BW is the sampling rate of the MR. A low BW allows higher frequency differences to evolve between pixels. For EPI sequences, the (effective) BW is an important parameter. Because of the EPI sampling scheme, the effective BW can be rather low as the BW along PE has to be considered (Sec. 2.4.2). The relatively long time between adjacent data points along PE leads to BW as low as 15-30 Hz/px. This, in turn, can result in a positional shift of fat and water signal. Because of differences in the molecular environment of fat and water, a chemical shift of 3.5 ppm exists between them. This corresponds to a shift of about 150 Hz/T or 30-15 px (15-7.5 px) at a 3 T (1.5 T). The chemical shift is spatially invariant, while another off-resonance effect is not. Local magnetic field inhomogeneities exist at intersections of substances with different susceptibility and lead to geometric image distortions [SST98]. Moreover, other sources of errors like distortions by concomitant field gradients are more severe in EPI because of the increased gradient amplitudes. Acquisitions with such a relatively long readout of some 10 ms to 100 ms suffer from signal decay and therefore blurring. Moreover, fast gradient switching can induce (peripheral) nerve stimulation yielding also physiological limitations.

Strategies of echo train segmentation have been introduced to reduce BW-related distortion artifacts, segmentation may be applied along PE (see 3.1.2) or RO [PH09]. Fast k-space traversal require high performance gradients with high peak amplitudes and rapid rise times, but also high accuracy. Fast ADC units are needed to handle this precision, accordingly. Even though, modern MRI hardware is at a high technological level, the fast switching rates generate secondary effects, which are not due to hardware limitations. Eddy currents are the dominant effect resulting from fast alternating gradient switching in combination with conducting surfaces. A particular common EPI artifact caused by eddy currents is the Nyquist or $N/2$ -ghosting. Because of the trajectory alternation during readout, alternate data lines must be reversed in time prior FFT, eddy currents commonly lead to a (small) temporal misalignment and line-by-line frequency shifts and phase modulation. Because a periodical phase modulation in k-space results in spatial shifts in the image domain, this has to be corrected before FFT in a phase correction procedure. Therefore, at the beginning of each measurement, additional phase correction data are measured. After the excitation pulse, three navigator lines (2x positive, 1x negative polarity of

RO gradient) without PE are acquired in a separate reference scan to extract phase information. The therewith determined misalignment between the bi-directional readouts is used compensate for odd and even echo alternation during the phase correction.

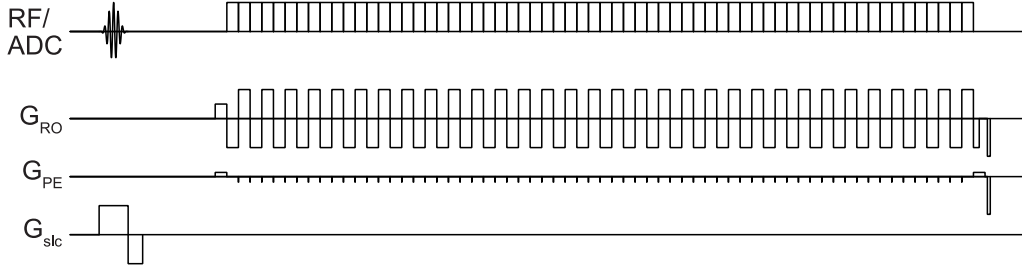


Figure 3.1: The sequence diagram for EPI acquisition shows the fast switching, alternating RO gradients and the gradient blips along PE following a slice selective excitation during FID. k-space data are sampled during the 64 readouts of the echo train. For illustration purposes the trapezoidal ramp up/down are not shown here.

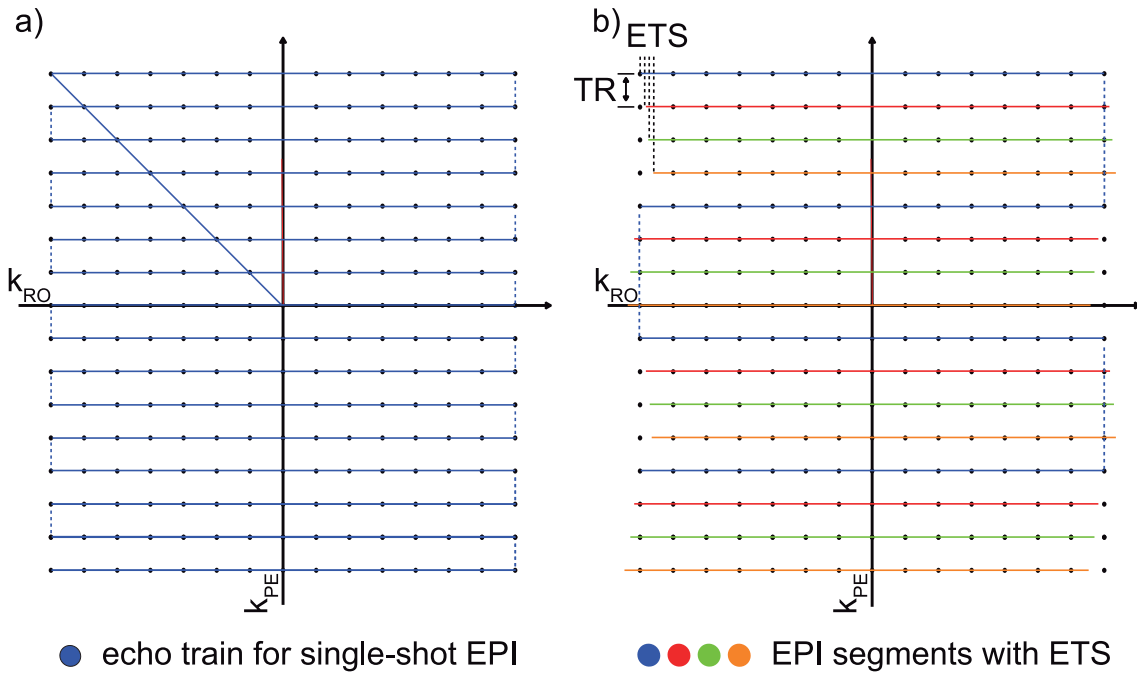


Figure 3.2: a) Zig-zag traversal of k-space of a single-shot EPI. The trajectory moves forth and back along RO while blips shift it from line to line along PE. b) Segmentation of k-space into shorter echo trains allow a flexible timing and shortened TEs. The duration between EPI segments equals TR, i.e. acquisition of adjacent k_y lines in the shown interleaved acquisition order. The meaning and benefit in SMS of the indicated phase modulation is described in Section 3.3.3 on CAIPIRINHA shifting.

3.1.2 Multi-Shot EPI

Typical limitations on spatial resolution, TE and distortions because of the long echo train in single-shot EPI can be addressed by segmentation of the echo train as illustrated in Figure 3.2. This type of acquisition scheme is known as *segmented*

or *multi-shot* EPI. The shorter echo-train length (ETL) yields less restrictions on resolution, possible values for TE and TR and reduces hardware demands. Even for signals with fast T_2^* -decay, multiple echoes can be acquired with segmented RO. Data of the individual segments are combined prior reconstruction into a complete k-space. Terminology differs in literature and sometimes regions of k-space divided up by each shot are called segments. However, here, a segment is formed by the zig-zag trajectory of the echo train after a RF excitation as shown in Figure 3.2. The flexibility of the readout requires longer overall scan time and, hence, an increased sensitivity to motion, which are the main drawbacks of multi-shot EPI compared to (single-shot) EPI. A long ETL accumulates off-resonance phase errors, which evolve continuously and map directly onto the k-space [FO94]. While the evolution of phase errors is reduced by shorter echo trains in multi-shot EPI, phase errors group together in adjacent segments and result in a stepwise phase discontinuities along k_y at $k_x = 0$. As shown in figure 3.2, slight temporal shifts of the successive echo trains, known as echo-time shifting (ETS), smoothen the k-space modulation function in the central k-space region and reduce image artifacts [FO94].

3.2 MRI with Multiple Receiver Coils

Phase manipulation by magnetic field gradients is one way to spatially encode the MR signal (Sec. 2.4). This is extensively employed in MR sequence design. Another way for spatial encoding is coil encoding [Bar+15]. The concept of coil encoding was presented theoretically by Hutchinson in 1988 [HR88] and first realized for imaging by Roemer in 1990 [REH90]. Since then, many accelerated acquisition techniques, e.g. parallel imaging (PI), omit time consuming gradient-based encoding steps, i.e. PE-encoding steps, and extract spatial information from the sensitivity patterns of the coil array [REH90; RR93]. Coil encoding then partially replaces PE encoding. The combination of both can also be considered as simultaneous encoding of several k-space data points. Furthermore, even if acceleration is not required, the detector's proximity to magnetization in the region of interest and distance to disturbing magnetization and noise from the rest of the sample increase signal-to-noise ratio (SNR) compared to signal reception with a (single) body coil inside the scanner's bore. In contrast to the advantages in SNR and encoding capability, multi coil arrays face additional challenges in their geometric design to balance local specificity and uniform (global) sensitivity.

The reception patterns of the individual coils form the so called coil sensitivity (CoS) profile. It describes the spatial B_1 dependence of the coil array. Typical CoS profiles of five representative coils in a 20-channel head coil are shown in Figure 3.3. The MR signal acquired with the individual coils after reconstruction (left) is compared

to the images of identical slices after sum-of-squares (SoS) combination of all 20 coils (right). Variations in the signal intensities represent spatial receiver characteristics. The SoS combination of the individual coil images results in a more homogeneous signal intensity.

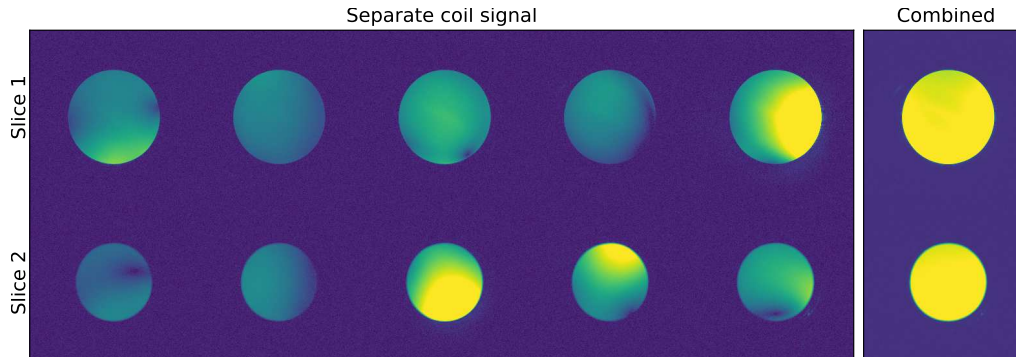


Figure 3.3: Two slices of a spherical phantom imaged with a 20-channels head coil (subset of five representative coils shown). a) The images of uncombined, individual coils show spatially discriminable, heterogeneous signal intensities contributing to the CoS profile. b) SoS coil combination gives a more homogeneous image of the object. For display purposes, the *viridis* colormap was used [Hun07] and colormap range was scaled differently for (a) and (b). A square-root mapping function was applied to account for the coil combination according to Equation 3.1 and to highlight local differences.

The SoS method to combine coil array signals or images is used throughout this work, because it has been shown that this simple but robust method approximates the theoretical upper bound if SNR is sufficiently high [Lar+03]. The signal contributions of all N_c individual coils, indexed with l , are combined by

$$S = \sqrt{\sum_{l=0}^{N_c} (S_l)^2} \quad (3.1)$$

to the final magnitude image.

The term *coil* is sometimes ambiguously used. A coil may refer to an individual coil element, but it commonly denotes the complete antenna unit as well, e.g. the head coil or the phased-array coil. In addition, the term *channel* is sometimes used synonymously for coil, although they can be differentiated technically. Channels are grouped coil elements in which signals are processed together to reduce the number of electronic components in the receiver chain [Els18]. This is mainly done for technical and financial reasons. The MR systems used for measurements in this work have separate circuitry for each coil and, therefore, the terms coil and channel are used interchangeably.

Sometimes PI as well as SMS are accounted as parallel imaging techniques since both utilize parallel or simultaneous signal acquisition from multiple coils and share similar reconstruction approaches. Therefore, the generalized autocalibrating

partially parallel acquisitions (GRAPPA) technique, which was first introduced for PI, will be described in Section 3.2.2, followed later on by modified GRAPPA-like methods to recover data which are undersampled along another dimension than PE.

3.2.1 Elimination of Noise Correlation in Coils

Multi coil arrays have an increased SNR compared to volume coils or large surface coils, because they can be placed in close proximity to the region of interest. Each individual detector response to signals from localized magnetization, but ignoring distant noise signal. However, the typically smaller diameter of the individual coils, with its reduced penetration depth, as well as interference between coils of the same coil array may have negative effects on the final SNR. The main source of image noise originates from the object to be imaged, because of its dielectric properties. Therefore, it is termed as (patient) loading or also called thermal or Johnson noise. In contrast, noise signal which is related to the electric circuitry is named electrical noise. Noise correlation occurs because coils receive partly identical thermal radiation if sensitivity regions of individual coils overlap [Pru+01]. Another source of signal correlation in coil arrays is the mutual induction between the coil elements. One can derive a noise covariance matrix from data of a noise-only measurement without RF excitation to determine the coupling of individual coils [Pru+01]. Typically, these calibration data to decorrelate coil signals are acquired once for a given configuration of object and coil array. Just like coil sensitivity, noise correlation between coils depends on coil positions and object and is assumed to be invariant over time. Coil arrays with a rigid structure, e.g. head coil, suffer less from noise correlation because of their optimized design and placement of the individual coils. However, if measurements are performed with flexible coil arrays or with a combination of coil arrays, noise decorrelation during signal processing is crucial as illustrated in Figure 3.4. The images show four slices of a pig's hip and leg region taken with two 18-channels body coil arrays and eight coils of the spine coil array before perfusion experiments (Part II). The SNR appears significantly reduced for reconstructions without consideration of noise correlation (Fig. 3.4, left) compared to reconstructions with it (Fig. 3.4, right). This is because some coils in this configuration exhibit strong mutual coupling as shown in Figure 3.5 (a). The benefit of considering noise statistics scales with the encoding redundancy and is more pronounced the less equivalent the coils are to each other with respect to coil load, gain, coupling and electronic noise [Pru+01]. In practice, a change of basis from a set of real, physical coils to a set of virtual coils is realized where transformed coil data are decorrelated. The resulting reduction of the receiver's noise-level increases final SNR. Therefore, a noise matrix Ψ of size $N_c \times N_c$ is determined experimentally by measuring samples in absence of a MR signal. For statistical reasons about $N_n = 10^3$ noise samples per coil, arranged in a

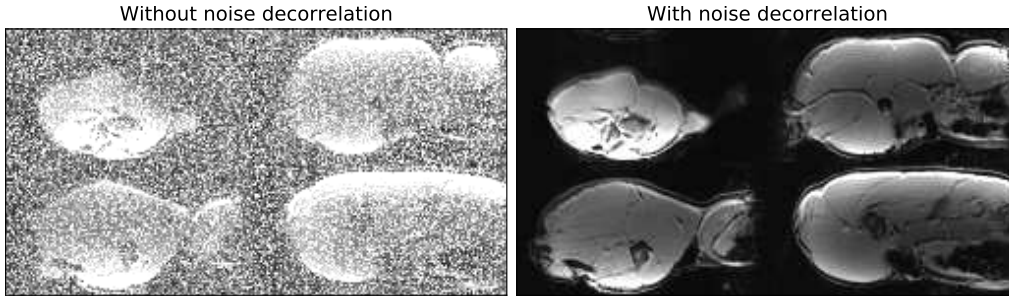


Figure 3.4: Example images of a pig's hip taken with flexible body and spine coil arrays elucidate the effect of noise decorrelation. Correlated noise in the coils propagates through the SoS combination into the final image (left). The decorrelation of raw data as one of the first processing steps lowers the noise-level dramatically and therefore increases SNR (right).

noise matrix $\boldsymbol{\eta}_l$ of size $N_c \times N_n$, should be averaged, indicated by the bar, yielding

$$\boldsymbol{\Psi} = \overline{\boldsymbol{\eta}_l \boldsymbol{\eta}_l^H}, \quad (3.2)$$

where H indicates the complex conjugate transpose of $\boldsymbol{\eta}_l$. Since $\boldsymbol{\Psi}$ represents the covariance matrix of the coils, the variance in each coil is along the matrix diagonal, while off-diagonal elements reflect noise correlation between samples in different coils as illustrated in Figure 3.5 (a).

The MR signal S_l measured with the l -th of N_c physical coils is then transformed to a set of N_c virtual coils by

$$S_l^{\text{decorr}} = \sum_{\nu=0}^{N_c} (\mathbf{L}^{-1})_{l,\nu} S_\nu, \quad (3.3)$$

where \mathbf{L} results from Cholesky decomposition of the noise matrix

$$\boldsymbol{\Psi} = \mathbf{L}\mathbf{L}^H. \quad (3.4)$$

The newly defined virtual coils exhibit unit noise levels and zero or only little mutual noise correlation as shown in Figure 3.5 (b). Besides transformation into a system of virtual coils, mathematical descriptions for signal and data processing remain unchanged and valid exactly as for the system of physical coils.

3.2.2 Parallel Imaging and GRAPPA

The use of PI reduces scan time by increasing the distance between PE-encoding steps in k-space by a reduction factor (R). By combining gradient and coil sensitivity encoding the number of serial encoding steps can be reduced to accelerate MR image acquisition. Therefore, the terms reduction factor and acceleration factor for R are often synonymously used in literature. In theory, only the number of receiver coils

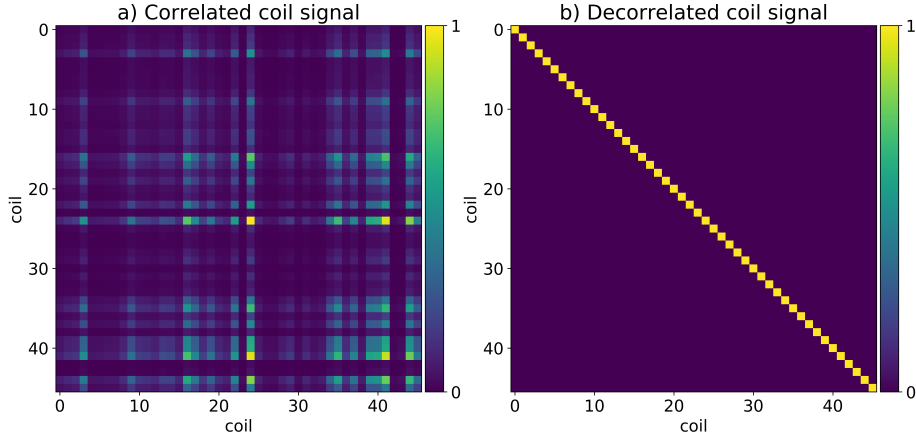


Figure 3.5: a) The covariance matrix shows the relative correlated signal of the 46 receiver coils (2 x 18-channel flex coils + spine coil) used for the measurement in Figure 3.4. b) After decorrelation according to Equations 3.2 and 3.3, the off-diagonal elements have values close to zero.

limits the maximal reduction rate along PE [RR93]. In practice, however, other effects like reduced SNR, coil cross-correlation and insufficient sensitivity variations between the separate receivers along the direction of acceleration, e.g. PE, limit the reduction rate. Therefore, R typically ranges from 2 to 6 for receiver arrays with 20 coils or more in 2D imaging [Des+12]. Generally formulated, the potential for acceleration in PI and related techniques is fundamentally limited by the amount of *spatial information* contained within the coil array and its arrangement to the object (Secs. 3.2.1 and 3.2.3).

Besides the design of the coil array itself, the dielectric properties of the measured object have an influence on the signal and change the CoS profile. Therefore, the unique CoS profile is determined by the scanner hardware, the object and their relative position. Positional changes, e.g. by patient motion, can directly change the CoS profile and the spatial information of the coil array for image encoding have to be recalibrated.

The present PI reconstruction methods can be classified into image and k-space based methods. Image based methods, such as sensitivity encoding (SENSE) [Pru+99], estimate the CoSs in image domain and recover the full image herein as well. k-space based methods like GRAPPA [Gri+02] use learned correlations between the coil signals and estimate a set of complex valued weights in k-space domain. Estimated GRAPPA weights to recover the full image are either directly applied as kernel weights in k-space or after Fourier transformation in image domain. Various hybrid methods have been suggested, but have not widely entered clinical protocols [Bla+04; Des+12]. Since GRAPPA-like approaches earned higher acceptance [Bar+15; Set+12b], the focus is turned to k-space based techniques in this work.

The basic assumption for GRAPPA is that omitted k-space data in a single coil

can be represented by a linear combination of their neighboring data in all receiver coils and that the discovered set of weights is shift invariant in k-space [Bra+08]. Calculated weights can be applied to the acquired signal either in k-space or image domain. Commonly, the calculated weights are transformed into image domain to replace time consuming mathematical convolution in k-space by multiplications. The obtained maps, also referred to as *unfold images*, do not correspond to a CoS profile in a strict physical meaning as in some SENSE-like variants. The unfold images rather reflects one solution of an overdetermined linear system which minimizes the reconstruction error [BB06]. Here, the term unfold image will be used to explicitly name GRAPPA weights in image domain, whereas the term CoS or CoS profile is designated for the physical properties of a given configuration of receiver coils and object.

Without loss of generality and because PE steps are more time consuming than encoding steps along RO, the following mathematical formulations of PI and description of the GRAPPA algorithm are reduced to a one-dimensional problem along the PE or y -direction. According to Equation 2.29 and reduced to 1D, the signal in k-space of an individual coil $S_l(k_y)$ received in component coil l is the Fourier transform of the spin density $\rho(y)$ and can be described as

$$S_l(k_y) = \int_{\text{FOV},y} C_l(y) \cdot \rho(y) e^{ik_y y} dy , \quad (3.5)$$

where $C_l(y)$ accounts for the corresponding local CoS. $C_l(y)$ weights the signal according to local receiver characteristics. The basic idea in k-space based strategies like GRAPPA is that signals from coil arrays can provide spatial information about the sample which would normally require the omitted PE data. Suppose to neglect coil dependencies at this point and define a new k-space \tilde{S} for the related signal. With a given reduction factor, e.g. $R = 2$, every other k-space line is skipped. For a total of N k_y -lines and indexing measured k_y^n from $n = 0, n = 2$ to $n = N - R$, the signal at n is

$$\tilde{S}(k_y^n) = \int_{\text{FOV},y} \rho(y) e^{ik_y^n y} dy , \quad (3.6)$$

whereas omitted signal at $k_y^n + \Delta k_y$ is given by

$$\tilde{S}(k_y^n + \Delta k_y) = \int_{\text{FOV},y} \rho(y) e^{ik_y^n y} e^{i\Delta k_y y} dy \quad (3.7)$$

with $\Delta k = 2\pi/\text{FOV}$ being the distance for neighboring PE lines. Appropriate combination of coil outputs may be configured to have a composite sensitivity in form of a complex exponential function as illustrated in Figure 3.6 [SM97]. Linear combinations of the CoSs weighted by $w_l^{(m)}$ emulate spatial modulations otherwise

produced by magnetic gradient fields [Bla+04]. Therewith, the missing spatial harmonics of order m in k-space can be generated by

$$\sum_{l=1}^{N_c} w_l^{(m)} C_l(y) \cong e^{im\Delta ky} \quad (3.8)$$

with N_c , the number of elements in the coil array. The combination of Equations 3.7 and 3.8 yields an expression to generate the signal S_j of shifted PE lines in a single, uncombined coil j from weighted combinations of measured coil signals $S_l(k_y^n)$ [Bla+04]

$$S_j(k_y^n - m\Delta k) \cong \sum_{l=1}^{N_c} w_l^{(m,j)} \cdot S_l(k_y^n) . \quad (3.9)$$

In GRAPPA, multiple k-space lines from all coils are used to determine the weights to synthesize signals for each coil. In other words, the uncombined images in each individual coil are obtained by applying multiple blockwise reconstructions to generate omitted k-space data [Gri+02]. This repetitive blockwise procedure extends Equation 3.9 by a block counter b to

$$S_j(k_y^n - m\Delta k) = \sum_{l=1}^{N_c} \sum_{b=0}^{N_b-1} w_{l,b}^{(m,j)} \cdot S_l(k_y^n - bR\Delta k_y) , \quad (3.10)$$

where N_b is the number of used blocks. A single block is defined as a single acquired PE line and $R - 1$ adjacent missing lines. In Equation 3.10, the omitted data at $(k_y^n + m\Delta k)$ in coil j are recovered by weighting the acquired data of all coils S_l by the discovered reconstruction weights $w_{l,b}^{(m,j)}$ and combine all contributions linearly. By these multiple blocks of data for each missing data point, GRAPPA incorporates extended information to robustly reconstruct unacquired data points [Gri+02].

GRAPPA Algorithm: From ACS to Reconstruction

The following description lists the typical steps done to recover PI-accelerated data. Literature provides extensive instructions suggested for further reading [Lar+01; Bla+04; Bre+09; Bra+08].

Additional calibration data are required to estimate the obligatory CoS information. The calibration data can be measured prior, during or after the actual scan, but with unchanged coil positioning. The acquisition of calibration data during the actual scan has become a frequent variant. Therefore, these methods are known as *autocalibration* methods and, hence, calibration data are called auto-calibration signal (ACS) [Des+12]. These fully encoded calibration data can be reduced to low resolution, e.g. an acquisition matrix of size 16×16 due to the naturally smooth variations of the CoS profile. GRAPPA weights are estimated from the

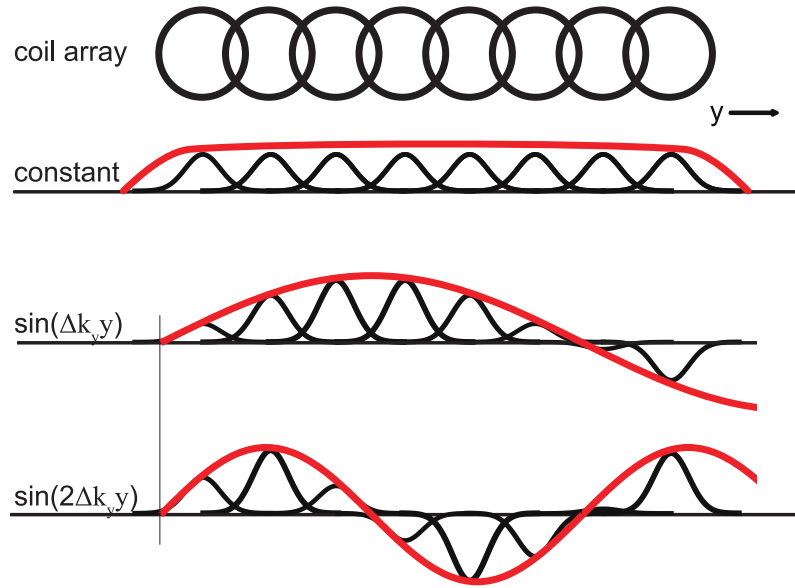


Figure 3.6: Some possible linear combinations of absolute values for coil sensitivities of eight receiver coils are schematically illustrated. Here, the weighted individual sensitivities approximate sinusoidal functions, cosinusoidal functions can be approximated analogously (Eq. 3.8).

ACS region, but can be applied repetitively to recover the full k -space. This can be proven by formulation of a calibration matrix and its null-space properties as done in comprehensive mathematical description in literature [Uec+14].

Implementations of GRAPPA may differ in block size, which is often set to $N_{b,x} \times N_{b,y} = 4 \times 4$ or 5×5 , inclusion of ACS data into the final image or the exact fitting algorithm used [Bla+04; Gri+02]. These blockwise reconstructions typically apply a sliding block along k_y and k_x that results in several possible combinations to solve the overdetermined problem.

Figure 3.7 illustrates the steps of the GRAPPA algorithm schematically. Calculation of the GRAPPA weights is formulated in matrix notation as specified in Equations 3.11 and 3.12. A selection kernel of predefined size, e.g. 4×4 , is slid through the ACS region to extract N_{src} source and N_{trg} target data points corresponding to the undersampling scheme, e.g. $R = 3$. This gives N_{rep} possible kernel repetitions to assemble ACS data into a source matrix \mathbf{S}_{src} (size: $N_c \cdot N_{src} \times N_{rep}$) and a target matrix \mathbf{S}_{trg} (size: $N_c \cdot N_{trg} \times N_{rep}$). The correlations between \mathbf{S}_{src} and \mathbf{S}_{trg} are encoded in a set of weights \mathbf{w} (size: $N_c \cdot N_{trg} \times N_c \cdot N_{src}$), i.e. GRAPPA kernel, which needs to be determined from [Bre+09]:

$$\mathbf{S}_{trg} = \mathbf{w} \cdot \mathbf{S}_{src} \quad (3.11)$$

This matrix equation can be solved for \mathbf{w} by estimation of a pseudoinverse [Bre+09]. A typical choice is the Moore-Penrose pseudoinverse, which is implemented in many

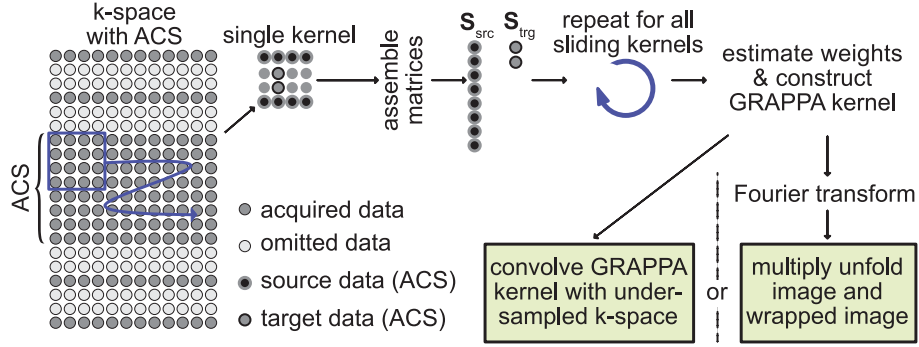


Figure 3.7: Schematic illustration of the GRAPPA algorithm: Exemplary undersampled k-space ($R = 3$) and central ACS region. Source \mathbf{S}_{src} and target \mathbf{S}_{trg} matrices are assembled from kernel slid through the ACS region and used to estimate weights. The final GRAPPA kernel can either be applied in k-space or after Fourier transform as unfold images to the wrapped image. Adapted from [Bre+09].

common numerical analysis software, e.g. in MATLAB (The MathWorks, Natick/US) where its computation is based on singular-value decomposition [Mat]

$$\mathbf{w} = \mathbf{S}_{\text{trg}} \cdot \text{pinv}(\mathbf{S}_{\text{src}}) . \quad (3.12)$$

Here, the term GRAPPA kernel for \mathbf{w} refers to the estimated, final and complete set of GRAPPA weights. Some literature uses the term differently to describe the kernel which selects data from ACS region.

The so gained reconstruction weights are then used to recover a full dataset S_k^{PI} from the accelerated and undersampled acquisition data S_l^{red} , either by convolution in k-space,

$$S_k^{\text{PI}} = \sum_{l=1}^{N_c} S_l^{\text{red}} \otimes w_{k,l} \quad (3.13)$$

or after 2D-FFT of signal and weights by multiplication of the unfold images W_{kl} with the reduced image I_l^{red} :

$$I_k^{\text{PI}} = \sum_{l=1}^{N_c} W_{kl} \cdot I_l^{\text{red}} \quad (3.14)$$

The indices k and l run from 1 to N_c , such that the unwrapped image I_k^{PI} in coil k contains contributions from all coils. The unfold images are not identical to coil sensitivities (Fig. 3.3) as exemplarily shown for a slice-GRAPPA (SG) reconstruction in Figure 3.9.

3.2.3 Signal-to-Noise and g-Factor

The SNR is the dominating limiting factor in MRI, in particular for accelerated acquisitions [Bre+09]. A global SNR defined as the mean signal divided by its

standard deviation will not characterize the true, spatially variant SNR in a final MR image acquired with multiple coils. In general, the SNR of an image after MR acquisition obeys the following relation,

$$SNR \propto V_{\text{voxel}} \cdot \sqrt{T_{\text{acq,total}}} \quad (3.15)$$

where V_{voxel} is the voxel volume and $T_{\text{acq,total}}$ is the total amount of time that the data acquisition window is open to sample data [BKZ04]. However, Relation 3.15 does not contain any detailed information about the MR system, e.g. B_0 , or any physical properties of the object, e.g. relaxation times, and many other influencing factors. One of these factors is of particular interest in accelerated MRI techniques which exploit spatial information of the receiver coils, i.e. PI and SMS. The g-factor, also known as the geometry factor, describes the spatially variant noise enhancement and thus the coils' influence on SNR.

g-factor

The g-factor can also be considered as a quantitative way to describe the ability to unwrap a particular aliasing pattern, given a specific coil geometry, object position and imaging region [Yan+15]. It describes reconstruction related uncertainties which also reduce SNR. The clearer signal contributions to a pixel can be associated with an individual coil, the more the g-factor for that location approaches 1. A larger uncertainty in the unwrapped signal results from pixels where the signals contributions can not be easily assigned to individual coils, e.g. in the case where two coils have equal distance to the signal source. For a R -fold accelerated acquisition, the g-factor, defined as

$$g = \frac{SNR_{\text{full}}}{SNR_{\text{acc}} \cdot \sqrt{R}}, \quad (3.16)$$

relates the local SNR in the final image SNR_{acc} to that of an unaccelerated image SNR_{full} .

The gold standard method for estimation of this spatially varying noise enhancement due to accelerated imaging is to acquire a series of fully encoded and accelerated images with identical parameters and derive thereof the respective SNRs [Bre+09]. Two alternative methods are commonly used as this gold standard method is time consuming and therefore inefficient, sensitive to instrument drifts and unfeasible for in-vivo measurements because of motion. On the one hand, multiple repeated measurements N_{reps} are simulated in a Monte-Carlo-like method, where correlated noise is added to a virtually noise-free dataset and is reconstructed thereafter. This so called pseudo multiple-replica method (PMRM) is illustrated in Figure 3.8 and was introduced in [Rob+08]. On the other hand, an analytical description for GRAPPA-like reconstructions exists, where the g-factor is derived directly from the

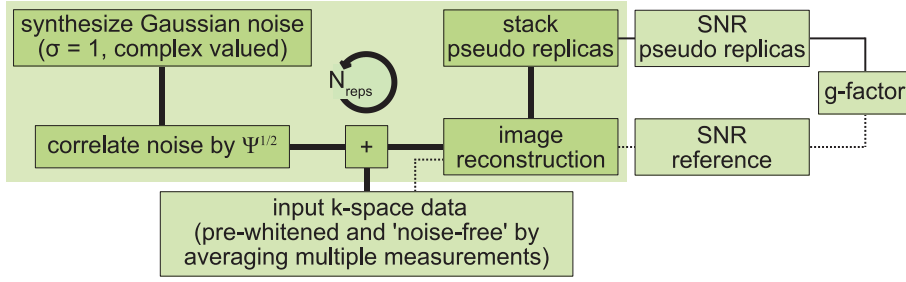


Figure 3.8: The PMRM was introduced to simulate spatially variant noise propagation through the image reconstruction processes and reduce experimental challenges such as motion or instrumental drifts. A single raw data measurement with high SNR or an averaged input severe as 'noise-free' reference to which correlated noise is added to create pseudo replicas.

reconstruction weights [Bre+09]. The g-factor of the k -th coil can be formulated as

$$g_k = \frac{\sqrt{|\mathbf{W} \cdot \Psi^2 \cdot \mathbf{W}^H|_{kk}}}{\sqrt{|\Psi^2|_{kk}}} \quad (3.17)$$

using the reconstruction weights in the image domain \mathbf{W} (Eq. 3.14) and the noise covariance matrix Ψ (Eq. 3.2). The g-factor after SoS combination is then

$$g = \frac{\sqrt{|(\mathbf{p}^T \cdot \mathbf{W}) \cdot \Psi^2 \cdot (\mathbf{p}^T \cdot \mathbf{W})^H|}}{\sqrt{|(\mathbf{p}^T \cdot \mathbf{1}) \cdot \Psi^2 \cdot (\mathbf{p}^T \cdot \mathbf{1})^H|}} \quad (3.18)$$

with the identity matrix $\mathbf{1}$ and the vector \mathbf{p} with $p_k = I_k^*/I$, which encodes the contribution of the complex-conjugated coil image I_k^* to the SoS-combined image I . As the analytical method requires GRAPPA weights explicitly, this approach is used in Part II while PMRM yields the g-factors in Part III.

3.3 Simultaneous Multi-Slice Imaging

The simultaneous excitation of multiple slices has been proposed already in the early days of modern MRI. In 1988, Souza and Müller independently published articles on the multislice technique which utilizes additional phase-labeling for the simultaneously excited slices, also known as Hadamard-labeling, to separate acquired data during reconstruction [Sou+88; Müll88]. In the same year, Weaver suggested a multislice MRI method in which the simultaneously excited slices appear side by side because of an additional frequency shift [Wea88]. Glover presented another encoding and reconstruction method in 1991. However, similar to the previous techniques, this type of multislice MRI increased SNR, but did not reduce the acquisition time [Glo91]. Larkman proposed a new reconstruction idea in 2001, which, for the first time, could effectively reduce the scan time by the use of multiple receiver coils [Lar+01]. From there on different improvements, e.g. by Breuer [Bre+05], Moeller

[Moe+10], Feinberg [Fei+11] and Setsompop [Set+12b], paved the way for SMS to various scientific and clinical applications.

As discussed in a review paper on SMS [Bar+15], the terms SMS and multiband (MB) are sometimes used synonymously. Nevertheless, both describe some sort of simultaneous slice excitation and readout. In this work, the term ‘SMS’ will be used in a rather general meaning to describe the technique, whereas the term ‘MB’ will refer to the number of simultaneously acquired slices or to the RF pulse exciting such a slice group.

3.3.1 Multiband Excitation

As described in Section 2.2, the basic idea of slice selective excitation is to linearly vary the precession frequency of the magnetization by the application of an additional gradient field and then apply a RF pulse which excites a defined BW $\Delta\omega_{\text{RF}}$. The simultaneous excitation of a group of slices can be done by the summation of phase modulated components. These simultaneously excited slices form a so called MB slice group as illustrated in Figure 3.10. A complex-valued RF pulse can be written as the product of a RF waveform, or RF envelope, $A(t)$, which defines the slice profile and a modulation function $P(t)$ [Bar+15; Abo+17a]:

$$RF(t) = A(t) \cdot P(t) . \quad (3.19)$$

For equidistant slices, the positions of the individual slices in MB slice group have a constant frequency offset, $\omega_s = \omega_{\text{offset}} \cdot s$, where s counts from $s = 1$ to the number of simultaneously excited slices MB . Thus, Equation 3.19 can be rewritten as

$$RF(t) = A(t) \cdot \sum_{s=1}^{MB} e^{i\omega_s t + \varphi_s} , \quad (3.20)$$

where an additional factor φ_s allows for a slice specific phase. Throughout this work, the basic RF waveform for $A(t)$ is a sinc function and no additional phase modulation by the RF pulse was done, $\varphi_s = 0$, such that all modulation functions are in phase with each other, which is also known as in-phase modulation [Abo+17a].

3.3.2 SMS Reconstruction

GRAPPA as introduced in Section 3.2.2 has probably become the most common k-space based reconstruction algorithm for PI [Yan+15]. As the reconstruction of SMS data can be interpreted as an undersampling problem like in PI, the herein used algorithms can be extended and applied to SMS.

The SG algorithm was introduced in 2012 to overcome limitation of k-space based methods to reconstruct slice-aliased data. By then, purely image based (SENSE) or hybrid methods (SENSE/GRAPPA) had been a common choice to reconstruct

data with simultaneously acquired and therefore overlapping slices. However, the vulnerability of CoS profiles to motion or other changes in the coils' reception characteristics restricted the application of image based method.

The following formulas and descriptions are taken from [Set+12b; Cau+14] and a review article on SMS [Bar+15]. The SG algorithm can be formulated similar to the GRAPPA algorithm in Equations 3.11 - 3.14. The collapsed image I_l^{colps} in coil l containing the MB simultaneously excited and acquired slices can be recovered by multiplication with an unfold image $W_{k,l,z}$. For a total of N_s slices, each unfold image slice-specifically reconstructs an image $I_{k,z}$ for coil k at position $z \in N_s$. Thus, Equation 3.14 is reformulated to

$$I_{k,z} = \sum_{l=1}^{N_c} W_{k,l,z} \cdot I_l^{\text{colps}} \quad (3.21)$$

with

$$I_l^{\text{colps}} = \sum_{s=1}^{MB} I_{l,s} \cdot \quad (3.22)$$

As in standard GRAPPA, SG returns one image for each of the N_c coils. The required unfold images $W_{k,l,z}$ can be calibrated by solving an inversion problem in k-space with the use of Equation 3.11 for ACS. The k-space data from ACS are then reorganized into a source matrix \mathbf{S}_{src} , holding the collapsed ACS data, and a target matrix \mathbf{S}_{trg} , with single slice ACS, similar as depicted in Figure 3.7. If done in practice, the pseudoinverse will be calculated like in Equation 3.12. Mathematically, the formulated inversion problem can be solved with

$$\mathbf{w} = \mathbf{S}_{\text{trg}} \cdot \frac{\mathbf{S}_{\text{src}}^H}{\mathbf{S}_{\text{src}} \cdot \mathbf{S}_{\text{src}}^H} \cdot \quad (3.23)$$

Reshaping the SG weights \mathbf{w} and transforming them to image domain leads to the unfold image for SMS:

$$W_{k,l,z} = \mathcal{F}_{2D}^{-1}(w_{k,l,z}) \cdot \quad (3.24)$$

In MRI, the inverse 2D Fourier transform \mathcal{F}_{2D}^{-1} commonly converts data from k-space to image domain and vice versa. Whereas the term FFT is usually used in here to describe either direction.

Remaining inter-slice leakage from one slice into another slice of the same MB slice group can restrain successful SG reconstructions. The split slice-GRAPPA (SSG) algorithm, also known as leak-block GRAPPA, addresses this issue by blocking contributions from all other slices apart from the slice z which is being reconstructed [Cau+14]. The explicit constraint in SSG is that the calculated weights cancel the

contributions of all slices at position $s \neq z$ for all coils $l = 1, \dots, N_c$:

$$0 = I_{l,s} \cdot W_{k,l,z}, \text{ if } s \neq z \quad (3.25)$$

The resulting unfold image(s) in SG or SSG differ from the physical CoS images as mentioned in the GRAPPA section above and shown in Figure 3.9.

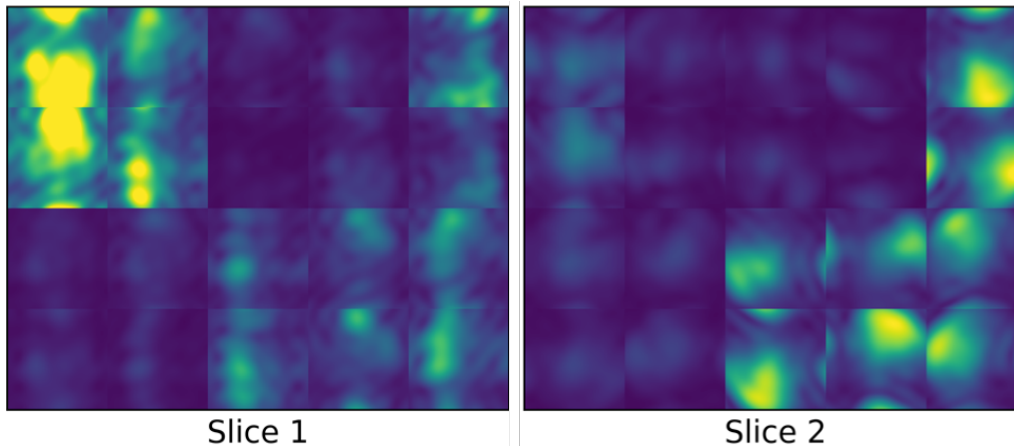


Figure 3.9: Slice-GRAPPA unfold images: The reconstruction weights as calculated in SG can be interpreted as unfold images $W_{k,l,z}$ in image domain as stated by the convolution theorem for FFT. These can be arranged in an array of size $[N_c, N_c, N_y, N_x, N_z]$. Here, the unfold images taken in a spherical phantom are shown. The absolute values for a SG reconstruction with $MB = 2$ after SoS along the first channel dimension are displayed for illustration purposes. Compare also to CoS exemplarily shown in Figure 3.3.

3.3.3 CAIPIRINHA Shifting

The concept of "controlled aliasing in parallel imaging results in higher acceleration" (CAIPIRINHA) was introduced in 2005 to address limitations in the variation of CoS along one direction, i.e. slice direction [Bre+05]. As introduced in Equation 3.5, signal from the sample's magnetization are weighted by the sensitivity of the receiver coil. In matrix notation and for SMS imaging, the local CoS can be written as the sensitivity matrix $\mathbf{C}_{l,s}$ of size $N_c \times MB$. $\mathbf{C}_{l,s}$ is then composed of the spatial sensitivity information from each coil l and slice s at in-plane location (x, y) [Bre+05]. Recovering the unaliased slices from a collapsed image is an inverse problem and corresponds to solving Equation 3.5 by matrix inversion. However, given that coil sensitivities of aliased pixels may not exhibit sufficient sensitivity variation, the linear equation system (Eq. 3.5) may not be solved mathematically robust, yielding

$$\det(\mathbf{C}_{1,s}) \approx 0. \quad (3.26)$$

In these cases, the direction of acceleration in combination with geometric constraints in coil design or unfortunate positioning of the imaging volume do not allow reliable

un-aliasing of the image. CAIPIRINHA introduces additional aliasing patterns in a controlled fashion and therefore often increases the CoS variation between overlapping pixels. In this work, the term CAIPIRINHA will be employed to describe the controlled shifting along directions, other than in [Bre+05], where it was introduced as a sequence type. For SMS, in which the distance of slices in one MB slice group inherently determines variations in CoS, the CAIPIRINHA shifting is typically applied along PE direction, if a more pronounced CoS profile is required. The amount of introduced CAIPIRINHA shift is given in fractions of the FOV and is called shift factor FOV_{shift} , or sometimes CAIPIRINHA factor. This is illustrated in Figure 3.10 for a SMS acquisition with $MB = 4$ and $FOV_{\text{shift}} = 1/4 \hat{=} FOV/4$ shift between adjacent slices of the same MB slice group. As the Fourier shift theorem

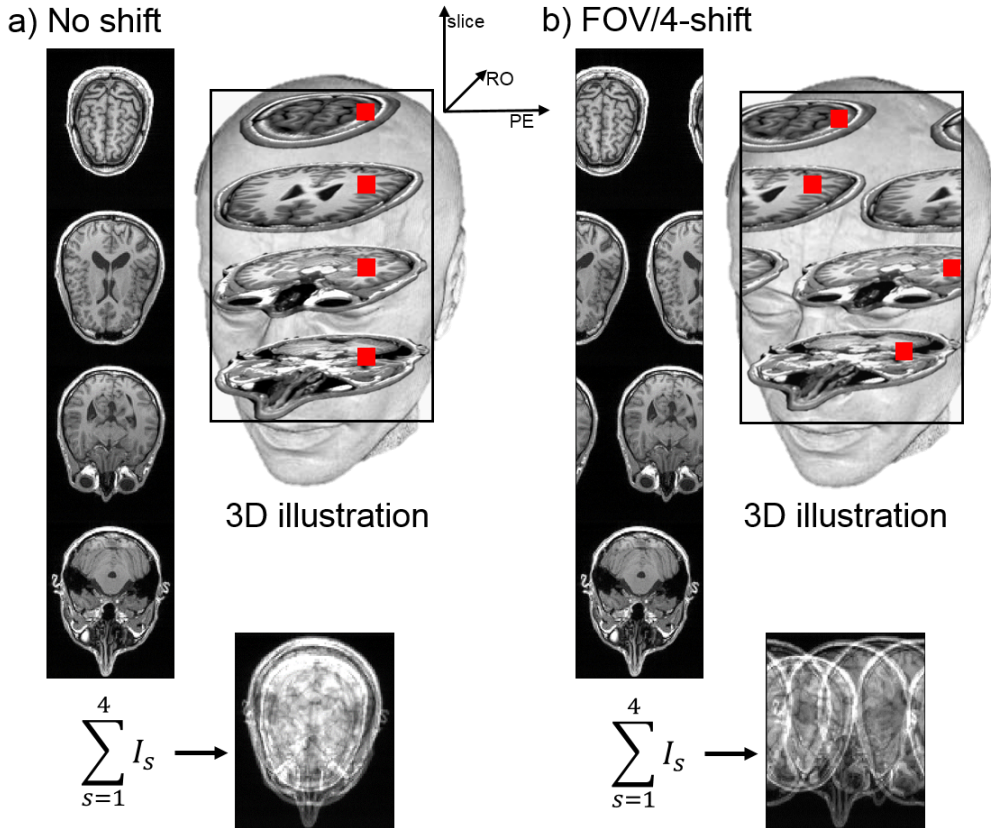


Figure 3.10: a) Four slices which are simultaneously excited by MB RF pulse are illustrated in separated transversal view and as 3D illustration. The collapsed image is shown in the bottom. b) CAIPIRINHA shifting, in here by $FOV/4$, induces a slice-depended shift of the image signal along PE. This usually increase variations in the CoS, which are beneficial during reconstruction. The 3D perspectives are given to illustrate the increased distance between pixels at identical x-y positions (red marker) after CAIPIRINHA shifting.

states, the desired shifts in image domain can be introduced by phase modulation when acquiring the k-space signal. Hence, a modulation of the signal phase ϕ by $\Delta\phi = \pi$ for neighboring PE lines results in a $FOV/2$ shift. Another, extended phase

modulation pattern for shifts of $\text{FOV}/4$ is depicted in Figure 2.3 (b). Modified MB RF pulses with slice specific phase modulation or modified gradients realize the desired shifting patterns in MRI. Various gradient based techniques have been proposed [Bre+06; Bil+15]. In particular, for single-shot EPI, where RF modulation is not feasible, [Nun+06; Set+12b] suggested schemes that made SMS also applicable to fMRI.

Part II

SMS for Dynamic Imaging

4 Material and Methods: Simultaneous Multislice Imaging for Dynamic Imaging

In MRI sequence design there is a trade-off between high temporal resolution, which can typically be achieved by using e.g. a single-shot EPI readout, and short echo times. Shortened TEs, e.g. below 10 ms, which provide sufficient T_1 -weighting whilst maintaining a high temporal resolution, can be accomplished by segmentation of the EPI readout. Furthermore, the extension of segmented EPI to multi-echo readout allows a flexible choice of crucial imaging parameters, such as temporal resolution, echo times and number of echoes. The optimal values of these parameters might vary for different anatomies and expected dynamic ranges of T_1 and T_2^* . Different parameter settings will be used in this chapter depending on the intention of the particular experiment.

In this part of the work, the acceleration of MRI by SMS is combined with the measurement of multiple gradient echoes in a flexible sequence design. This allows dynamic imaging of relatively large volumes, also outside the brain and the signal separation into dominantly T_1 - and T_2^* -weighted MR signal contributions for advanced pharmacokinetic modeling. This chapter begins with required background in CA-enhanced MRI. Later on it provides details on the developed MR sequence and its application in dynamic in-vivo measurement followed by an account of different reconstruction approaches with slice-GRAPPA (SG) and split slice-GRAPPA (SSG). The sequence's performance was tested in various, additional ex- and in-vivo experiments to address different aspects which may impact the results.

Parts of the following experiments have been previously published in [ELG15; Eic+16; Eic+18].

4.1 Combined DCE and DSC

The physiological fundamentals and the clinical relevance of CA-enhanced MRI were introduced in Section 1.4.1. One limitation of DCE and DSC is that T_1 and T_2^* -related effects can not be separated reliably, if only a single echo is acquired. In particular, in low perfused tissue it is difficult to separate intravascular and extravascular signal contributions by one echo alone, e.g. with DCE imaging [Hin+17]. The simultaneous acquisition of multiple echoes at different TEs allows separation of signal into mainly T_1 - and T_2^* -weighted signal components. This reveals a more complete basis for physiological analysis.

This work presents a novel MR sequence where SMS imaging is incorporated into a multi-shot EPI to address the demand for simultaneous acquisitions of multiple contrasts with a sufficiently high temporal resolution. Insufficient temporal resolution

often restricts advanced quantitative pharmacokinetic modeling in particular for dynamic MRI of large volumes under the CA-administration [Lüd+09b; Bae+05; Sou+09]. During the early phase of the bolus arrival or for CAs with high molecular weight, the tracer remains (mainly) intravascular and high susceptibility gradients dominate the formation of the MR-signal [SB13; Hin+15]. Thus, T_2^* -weighted imaging allows the quantification of the AIF with a temporal resolution of $\Delta t \leq 1.5$ s which is suggested as an upper limit for accurate sampling [Lüd+09b; Sou+09; Hei+07; KC10]. CA with low molecular weight diffuses into the surrounding tissue soon after injection and required a two-compartment kinetic model to correctly describe the T_2^* -effects [Von+00; Jah+14]. T_2^* -dependencies to the signal can be removed by extrapolation of the MR signal to TE = 0 ms [Miy+97]. The calculated signal, S_0 , is dominantly influenced by T_1 and the localized, short-range character of the T_1 -relaxation reveals insight into extravasation of the CA and permeability between vessels and EES [SB13; Lüd+09b; Miy+97]. Both contrasts, T_2^* and S_0 , can be used for pharmacokinetic modeling, thus providing additional information for different phases.

4.2 Segmented EPI for Multiple Contrasts with SMS

Here, a sequence is presented suited for dynamic CA-enhanced MRI. The sequence allows the acquisition of multiple echoes to address dominantly T_1 and T_2^* related changes in the image contrast. Therefore, SMS was introduced to a multi-shot, multi-echo EPI sequence.

Therefore, different components of the sequence were changed. As shown in Figure 4.1, the singleband (SB) RF pulse was replaced by a MB RF pulse as proposed in Section 3.3.1. Therewith, several equally spaced slices can be excited simultaneously to form a slice group. Segmentation of the readout along the PE direction offers a flexible choice readout duration and, hence, the minimal TE [Pol12]. The looping scheme for MB excitation and RO iterates over all slice groups before the next RO segment is acquired as indicated by different colors in Figure 4.1 [Eic+16]. The sequence allows a CAIPIRINHA-like shifting of individual slices of the same slice group to increase the slice-dependent variations in the CoS profile. This improves the slice separation by a reduced g-factor as introduced in Section 3.3.3. A slice-dependent phase modulation is realized by incomplete rephasing of the slice selection gradient. The modified slice rephasing gradients $G_{z, \text{re}}^{n_{\text{seg}}}$ are highlighted (gray and orange) in Figure 4.1. Hence, overlapping slices of the same MB slice group are shifted along PE direction. The phase modulation depends on the gradient moment difference for the current EPI segment n_{seg} at $t_{n_{\text{seg}}}$, counting from 0 to the number of segments $N_{\text{seg}} - 1$, the selected CAIPIRINHA shift factor FOV_{shift} (Sec. 3.3.3) and the slice position within the MB slice group $s \cdot z_{\text{gap}}$ [Eic+18]. Here, s counts the slices of a MB

slice group from 0 to $MB - 1$ with a given slice distance of z_{gap} . As n_{seg} is usually not identical to FOV_{shift}^{-1} , n_{seg} is replaced by a modulation factor $m = n_{\text{seg}} \bmod FOV_{\text{shift}}^{-1}$. With these, the phase modulation is defined as

$$\varphi_s^m = \gamma \cdot s \cdot z_{\text{gap}} \left(\int_{t_{n_{\text{seg}}}}^{t_{n_{\text{seg}}} + T_{\text{ss}}} G_{z,\text{ss}} dt - \int_{t_{n_{\text{seg}}} + T_{\text{ss}}}^{t_{n_{\text{seg}}} + T_{\text{ss}} + T_{\text{re}}} G_{z,\text{re}}^m dt \right), \quad (4.1)$$

where $T_{\text{ss}}, T_{\text{re}}$ are the durations of the slice selection $G_{z,\text{ss}}$ and slice rephasing $G_{z,\text{re}}$ gradients, respectively. An example of the resulting phase modulation pattern for $FOV_{\text{shift}} = 1/4$ is shown in Figure 4.2. By this, each slice of the MB slice group is shifted by $FOV/4$ with respect to its neighboring slice of the MB slice group.

As described in Section 3.1.1, a phase correction of the bi-directional readout in EPI is required. In here, the three navigator lines are acquired after a MB excitation and used for a MB slice group specific phase correction of the image data. The correction procedure is provided by the vendor's image reconstruction system and consists of a linear phase correction succeeded by correction of the constant phase [Hei00]. Furthermore, the interleaved EPI acquisition scheme in multi-shot EPI suffers from discontinuities in k-space along PE (Sec. 3.1.2). The phase evolutions demonstrate a stair-step pattern, which might lead to severe image artifacts [FO94]. ETS of $150 \mu\text{s}$ between adjacent EPI segments is used to reduce this artifact [MB96].

The following definitions for the repetition time TR and temporal resolution Δt will be used. The duration between successive excitations of the same volume, which allows longitudinal relaxation, is referred to as TR while the time, needed to acquire one complete set of data to reconstruct the individual slices, is defined as the temporal resolution Δt .

For successful reconstruction of SMS data, ACS similar to conventional PI are needed for the calculation of the reconstruction weights in SG [Bar+15]. The dependence of the SG reconstruction weights on the underlying images has been reported [Set+12b]. Therefore, additionally acquired ACS data serve for the weight calculation in SG, where all parameters which define the image contrast, i.e. TE, FA and TR are identical for SMS (ACS source) and SB (ACS target) data. In the following section, the reconstruction process is described systematically. Moreover, additional details on ACS handling can be found in Section 4.3.4.

4.2.1 Slice Profiles in SMS

The importance of slice profiles and their relevance for quantification in MRI have already been reported in early publications [You84; McR+86], but often little attention is paid on this topic, when it comes to concepts and protocols for quantitative perfusion measurements. If T_2 - and T_2^* -effects can be neglected, because of a short RF pulse duration, the key parameters interacting and influencing the slice profile are

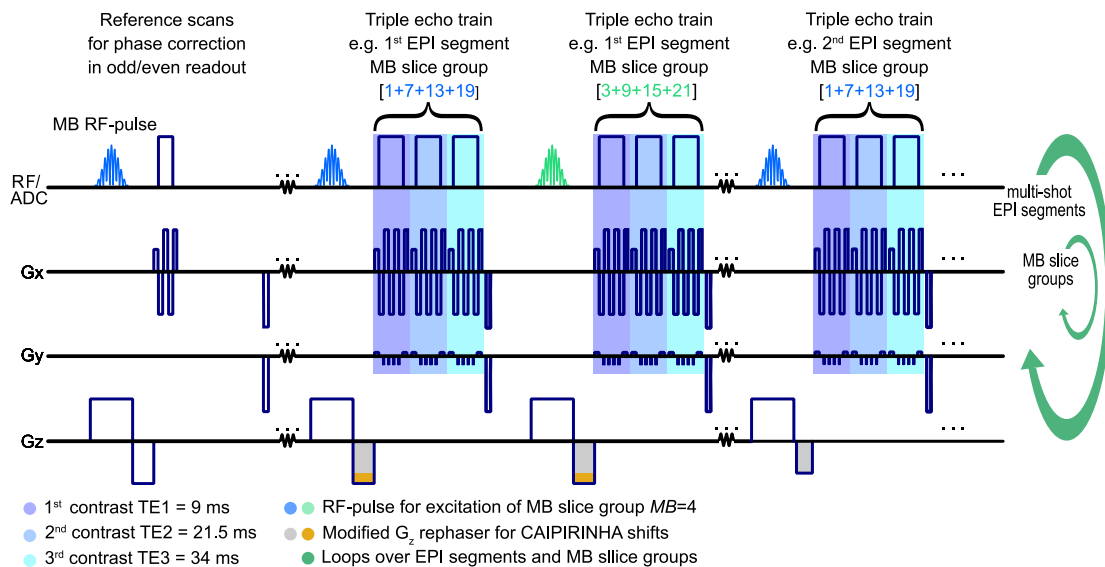


Figure 4.1: Sequence diagram for SMS acquisition using a segmented EPI with multiple contrasts. Looping is done over MB slice groups first, before looping over the EPI segments to prevent from inter-slice contrast variation. An interleaved acquisition scheme was chosen to reduce cross-talk between MB slice groups. CAIPIRINHA shifts: The orange area in G_z indicates the phase difference between EPI segments resulting in a phase modulation along PE depending on the z -position. Duration between identically colored RF pulses is TR.

the object's T_1 and the protocol parameters TR and FA. A particular combination of these parameters may result in an undesired slice profile which degrades the signal and may avoid reliable imaging, e.g. for T_1 -mapping. For small FA, the RF pulse shape and the slice profile are related by the Fourier transform if T_2^* -effects are neglected. In this case, sinc-modulation of the RF pulse approximates a rectangular slice profile [BKZ04]. A main source of imperfections in slice profiles comes with temporal constraints on the RF pulse length in MRI sequences. On one hand, it becomes obvious from the theory of the Fourier transform that finite RF pulses can not produce perfectly sharp edges for the slice profile. On the other hand, simple truncation of the RF pulse to the intended duration will result in ripples. Therefore, apodization of the RF pulse with smoothing functions has been established as a strategy to improve slice profiles [McR+06]. Other sources for an imperfect slice profile can be local field inhomogeneities or absorption effects especially for in-vivo MRI of subjects with high mass.

An interleaved slice acquisition scheme is often used in 2D MRI to prevent saturation effects from neighboring slices and maximizes the relaxation for a given TR. Albeit, this is generally beneficial, there exists some constraints when an interleaved acquisition order is selected in SMS. For an even number of MB slice groups, some slices of the edge MB slice groups may suffer from mutual saturation effects [Set+12a; Bar+15]. The presented SMS sequence with multi-contrast segmented EPI readout

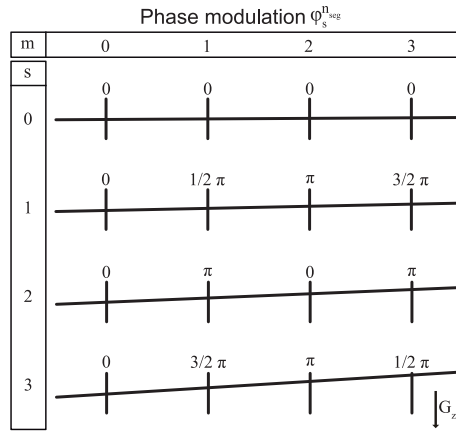


Figure 4.2: According to Equation 4.1, the phase modulation depends on the current segment n_{seg} and the resulting modulation factor m and the position of the slice s within the MB slice group. Here, the modulations in case of $FOV_{\text{shift}} = 1/4$ are depicted. The slices are arranged vertically, whereas the EPI segments are ordered along horizontal axis. The oblique lines illustrate the additional local phase according to position and segment.

can also be run in an interleaved slice acquisition order as depicted by differently colored RF pulses in Figure 4.1. Therefore, apart from the slice profile because of the quality of MB excitation, the interplay or cross-talk of adjacent MB slice groups has to be considered if the chosen inter-slice gap is little.

The used MB RF pulses were investigated for different parameter settings as described in Section 4.5 and experimental data were evaluated in Section 5.3 to underpin the above issues in the context of signal stability and quantification.

4.3 In-vivo Perfusion Experiments

The performance of the MR sequence under preclinical conditions was evaluated by dynamic in-vivo imaging of adult pigs (German Landrace, approximately 20 weeks old, body weight of 52 kg to 64 kg, no food restriction). Six subjects were investigated, whereby four experiments could be run successfully without any experimental complications.

4.3.1 Subjects and Experimental Setup

MR perfusion imaging in adult pigs has been evaluated in previous studies [Lüd+09a] and their anatomical and physiological proximity is well known in medical research [Sau+14]. However, MRI perfusion studies were limited to highly perfused organs, i.e. kidney, and the expected low tumor perfusion was not represented. Herein, muscle tissue with low baseline perfusion in the hip- and leg-region was investigated. To focus on the experimental details relevant to MR physics, specifications on animal handling and care as well as information on the surgical techniques applied for preparation before the MRI examinations will only be referenced [Sau+14]. All experiments were performed at University Hospital Essen, Essen, Germany (UKE)

in accordance with the German animal protection law and ethical approval was provided by Landesamt fuer Natur, Umwelt und Verbraucherschutz Nordrhein-Westfalen, Germany (Number: 84-02.04.2012.A208). The animals' heart rates and oxygen saturations during surgery and MRI examinations were monitored with a MRI-compatible device (Verdis, Medrad, Germany). The pigs were euthanized under high level of anesthesia by injection of T-61 (0.3 ml/kg) after the experiments. The total duration from beginning of anesthesia before surgery till euthanasia was about 13 ± 2.5 hours.

4.3.2 Imaging Parameters and Protocol

These preclinical in-vivo measurements were performed at 1.5 T using a commercial MRI system (MAGNETOM Aera, Siemens Healthcare, Erlangen, Germany) in a clinical environment. Subjects were set in supine position allowing placement of two phased-array coils (18+12 channels) around the hip and leg region. Additionally, four 4-channel spine coils were used, giving a total of 46 receiver channels. High resolution T_1 -weighted turbo-spin-echo (TSE) images (TR = 559 ms, TE = 9.7 ms, resolution: $0.8 \times 0.8 \times 5 \text{ mm}^3$) in coronal, transversal and sagittal orientation were acquired to ensure correct positioning of the FOV. ACS data were collected before bolus injection of CA. To ensure steady-state conditions, only the last one of three directly repeated measurements was used as ACS data for calculation of the SMS reconstruction kernel.

To cover hip and leg on one side of the animals in a sagittal orientation, a FOV of $400 \times 200 \text{ mm}^2$ was selected similar to the illustration in Figure 4.3. With respect to the desired temporal resolution of $\Delta t \leq 1.5 \text{ s}$ [Lüd+09b; Sou+09; Hei+07; KC10], the designed sequence allowed the acquisition of $128 \times 68 \text{ px}$ in-plane at a spatial resolution of $3. \times 3.1 \text{ mm}^2$ in 24 slices of 5 mm thickness (40% gap). The 4-fold accelerated imaging speed ($R = 4$) was achieved by SMS with $MB = 4$ only, without any in-plane undersampling. Therefore, TR could be also be reduced from TR = 1044 ms to TR = 261 ms with acquisition of a triple echo train (TE₁ = 9 ms, TE₂ = 21.5 ms, TE₃ = 34 ms). This yielded a temporal resolution of $\Delta t = 1.305 \text{ s}$ for a single acquisition of the navigator for phase correction and four EPI segments with ETL = 17 each. A CAIPIRINHA shift of FOV/4 between slices in one MB slice group was applied. The sequence design was optimized to reduce inter-slice contrast variation (Fig. 4.1) and to keep TR sufficiently long to recover more magnetization before the next excitation. Therefore, data of MB slice groups was acquired before segments were iterated (Figs. 4.1 and 2.3). Other sequence parameters were: $\alpha = 90^\circ$, echo-spacing = 0.61 ms and a BW of 2056 Hz/Px.

The CA (Dotarem, Guebet, Villpinte, France) bolus was injected into the jugular vein through a central venous catheter after the 5th measurement and automatically

controlled by a power injector (Medrad Spectris Solaris EP, Bayer AG, Leverkusen, Germany) using a dosage of 0.1 mmol/kg at a flow rate of 5 ml/s followed by a 20 ml (5 ml/s) flush of saline solution (0.9%). The total scan time for 500 acquisitions was 10:52 minutes. An illustration of the workflow for the MR part of the experiment is given in Figure 4.4.

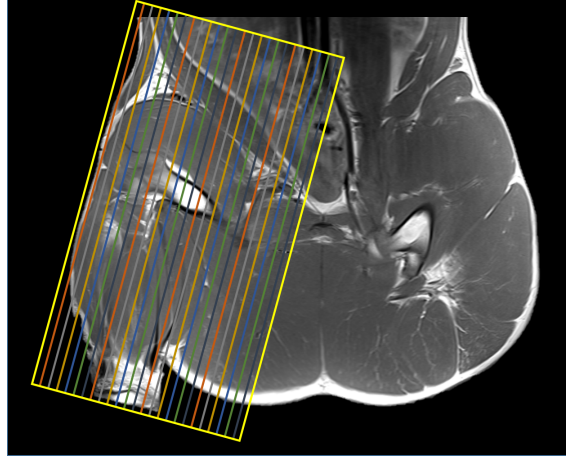


Figure 4.3: The slice were positioned in sagittal orientation as illustrated in a high resolution T_1 -image. The FOV covers the aorta and femoral artery for AIF detection.

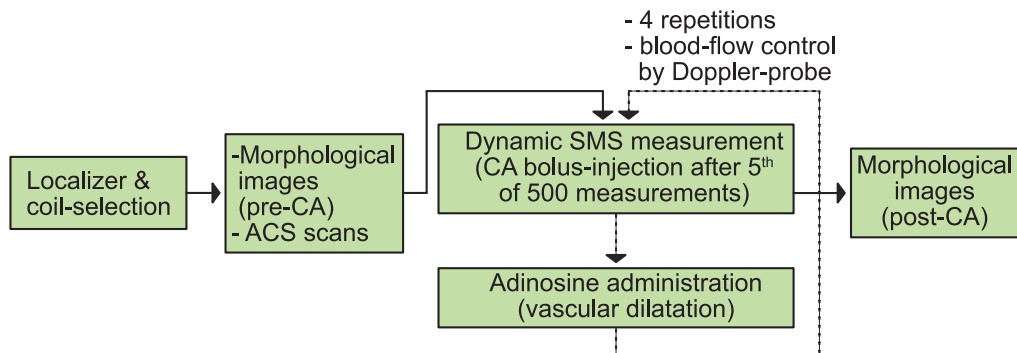


Figure 4.4: The different steps in the defined protocol are illustrated above. The dashed line depicts the repetitive MR measurements as described in Section 4.3.2.

Vasodilation and Flow-Control

Muscle perfusion varies widely during physical activity, thus, muscles are well suited to investigate how well different perfusion levels can be measured by MRI [Sau+14]. Mimicry of physical activation was achieved by a locally injected vasodilator. Adenosine, a clinically known antiarrhythmic drug, has a short plasma-half-life (≤ 10 s) and hence, allows direct control of the regional blood-flow, if continuously administered into the femoral artery. The response of the blood flow was recorded by a ultrasound flow probe (T206, Transonic Systems Inc. Ithaca, NY/US) implanted to the feeding femoral artery during pre-MR-experimental surgery [Sau+14]. During a single experiment, dynamic, multi-contrast MR measurements were four times

repeated for different levels of blood-flow after adenosine administration at different dosage.

4.3.3 Postprocessing

The postprocessing of the in-vivo data was performed offline in several steps and some of the individual components of the postprocessing chain shown in Figure 4.5 have been introduced in other chapters.

Offline reconstruction was chosen for two reasons. First, because online reconstruction for SMS was not available for the system's software (syngio MR D13A, Siemens Healthcare, Erlangen, Germany) at the time when experiments were conducted. Second and mainly, offline postprocessing ensures full control of the reconstruction and comparison of various reconstruction approaches, which are also part of this work. As depicted in Figure 4.5, MR raw data were preprocessed in the vendor's image calculation environment (ICE, Siemens Healthcare, Erlangen, Germany). Preprocessing included Nyquist ghost correction of the collapsed SMS data. An export tool saved the preprocessed data of all receiver channels for further image computing.

Data reorganization, preparation of ACS, calculation of the SMS reconstruction kernel and unfolding of the measured SMS datasets were performed in MATLAB (MathWorks, Natick, MA/USA). Implementations of two algorithms to separate overlapping pixel contributions in the MB slice group were compared: SG and SSG. Both algorithms are described in detail in Section 3.3.

After the SMS reconstruction the images of the individual receiver channels were merged by SoS combination. The unfold images were passed to MeVisLab (MeVis Medical Solutions AG, Bremen, Germany) for further image processing. The images with three different TEs were fitted to a mono-exponential T_2^* -decay

$$S(\text{TE}) = S_0 \cdot e^{-\frac{\text{TE}}{T_2^*}} \quad (4.2)$$

to provide the extrapolated dynamic T_1 -weighted MR-signal S_0 at $\text{TE} = 0$ ms and the corresponding T_2^* -dynamics [Miy+97]. The implemented fitting routine uses a Levenberg-Marquardt algorithm provided by the MPFIT library [Mar09]. Initial values were automatically estimated by linear regression.

4.3.4 Image Reconstruction and Quality Assessment

As in [Set+12b; Bar+15; Cau+14], SB data were acquired with the same in-plane imaging parameters as the SMS measurements and serve for calculation of the reconstruction kernel. For the dynamic SMS data, full resolution SB data were downsampled in a postprocessing step (32×32 px) and used for ACS. Two different methods for the formation of the ACS were tested for the SG algorithm. In the first

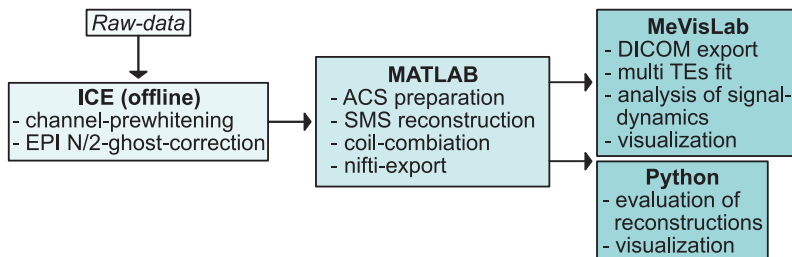


Figure 4.5: The workflow for MR raw data postprocessing is illustrated from top to bottom. The actual image reconstruction, i.e. SMS unfolding, is done in MATLAB. In MeVisLab, images are exported to DICOM to support compatibility to other software tools. For final analysis and visualization of the resulting images Python and MeVisLab offer different tools.

method ACS target data were derived from an SB acquisition (TR = 1500 ms) and shifted according to the CAIPIRINHA scheme. Measured data of an SMS acquisition with $MB = 4$ (TR = 1500 ms) were used as ACS source data. For the second method, ACS source and target data were delivered by the same SB acquisition (TR = 1500 ms) and, in contrast to the first method, ACS source data were not measured directly as SMS, but created by collapsing specific slices into a synthesized MB slice group. Furthermore, we compared the performance of the SSG to the SG algorithm. The ACS for SSG was chosen as in the second method only as proposed in [Cau+14], because the SSG algorithm can not use unseparated, measured ACS source data for kernel calculation. See also Section 3.3 for details.

The reconstructed SMS images I_{SMS} for the different reconstruction approaches and the reference SB images I_{SB} were compared. Normalized, absolute subtraction maps revealed local reconstruction errors

$$E_{\text{diff}} = M_{\text{b,H}} \left| \frac{I_{\text{SMS}} - I_{\text{SB}}}{I_{\text{SB}}} \right| \quad (4.3)$$

and after removal of background noise by binary masking, the mean error across the volume quantifies the exactness of the reconstruction. A Huang threshold was applied to the image volume to derive a binary mask $M_{\text{b,H}}$ [HW95]. Localized differences between the reconstructed SMS and the reference SB data might have severe impact on the quantitative analysis and should be minimized while homogeneous differences are acceptable and a constant offset can be easily removed.

Furthermore, the g-factor [Bar+15; Bre+09], as a quantitative measure to describe the unfolding process and related noise amplification, was computed for the different approaches and its mean and standard deviation across the object were calculated. Both metrics, the normalized subtraction error and the g-factor, are displayed exemplarily as maps for one MB slice group together with histograms and the corresponding mean values for all 24 slices.

It should be noted, that the performance of SMS reconstructions is directly related to the positioning of the receiver coils which is not fully reproducible if flexible phased-array coils are used as in the presented in-vivo experiments. Therefore, the chosen reconstruction method may perform differently in the individual experiments.

4.4 Dependency of slice-GRAPPA on Image Contrast Variations

As reported in previous publications [Set+12b], reconstructions in SMS imaging with SG or SSG may have some dependency on the image contrast of the training data. This is of special interest in case of CA-enhanced measurements where SMS image data vary contrast throughout the dynamic scan. An analysis of the reported contrast dependency of SG/SSG was conducted in additional experiments on a phantom. Specifically, possible dependencies on the image parameters of interest, namely base signal S_0 and T_2^* (Eq. 4.2), were closely investigated. One reconstruction where ACS and SMS data have identical contrast, which is considered as ground truth, was compared to another reconstruction where the image contrast of ACS and SMS data differed. The normalized difference in the image signal ΔI , defined as

$$\Delta I = \frac{I_A - I_B}{I_A}, \quad (4.4)$$

was considered where indices A, B indicate differences in the ACS data used for reconstruction. Because of different flip angles ($\alpha_A = 5^\circ$, $\alpha_B = 90^\circ$), ACS data for A and B differed in their image contrast. The multi-echo data were separated into S_0 and T_2^* components as previously described (Eq. 4.2). By this, differences in the reconstructed image signal ΔI can be related to a range of S_0 and T_2^* values. The observed discrepancies between the reconstructions, with (A) and without (B) identical image contrast in ACS and SMS data, were evaluated by a linear model (b_0 , b_1). The influence of image contrast and SNR from the type of ACS data used were compared. Different levels of SNR were achieved by averaging. Single slice measurements of a structured phantom ($T_1^{\text{pha}} = 289$ ms) containing CA-doped sub-volumes ($T_1^{\text{subVol}} = 211 / 434 / 556 / 953 / 1257$ ms) were used for evaluation. SMS data with CAIPIRINHA shifts were synthesized (see above) to analyze effects of the SG and SSG algorithms independently from the SMS sequence or other experimental fluctuations. The signal levels for the sequence parameters to vary, i.e. FA, were simulated beforehand to estimate resulting image contrast variation, compare Figure 5.9. Data with $\alpha = 5^\circ$, TR = 30 ms were reconstructed with SG/SSG using kernels calculated from either ACS with the same imaging parameters ($\alpha = 5^\circ$, TR = 30 ms) as suggested by [Set+12b] or from ACS with different image contrasts ($\alpha = 90^\circ$, TR = 30 ms). In addition, a comparison between individual kernels for each TE (ACS123) and a single reconstruction kernel (ACS111) derived only from the first

echo, TE_1 , with highest SNR was performed.

4.5 Slice Profiles and MB RF Pulse Imperfections

2D multi slice acquisition methods are sensitive to B_1 errors, i.e. incorrect local FAs, in particular if acceleration techniques are accompanied by a reduction in TR [Tof09]. Variation in TR alters the locally achieved value of FA and thus, the effective slice profile also depends on TR/T_1 due to the relaxation and saturation effects [You84]. Consequently, mapping of B_1 and a careful choice of imaging parameters are important for signal quantification.

SMS accelerates the acquisition process by grouping individual slice encoding steps and acquire their signals simultaneously, thus it allows a reduction of TR for a fixed number of slices. However, as stated above, a reduced TR affects the local B_1 . Therefore, slice profiles of MB RF pulses were compared with corresponding profiles after SB excitations. Different experiments were run to determine potential cross-talk between adjacent slices and TR-related changes in the slice profile as well as effects due to FA variations.

4.5.1 Slice Profiles: Experiments

A homogeneous, cylindrical phantom was placed inside a 20-channels head-coil in central axial position. The object's center was positioned at isocenter. The relaxation constant of the phantom is $T_1 = 106 \pm 1.4$ ms which was determined by an inversion-recovery experiment with eleven different inflow times (TIs) between 30 ms and 1400 ms at TR= 1500 ms.

A RF pulse duration of $T_{RF} = 7008 \mu\text{s}$ was chosen to guarantee the required amplifier power below maximal transmitter voltage of the MRI system. The RO gradient was aligned along slice direction to sample the slice profile with a resolution of $\Delta_{z,RO} = 0.104$ mm ($FOV_z = 143$ mm, $N_{\text{samples}} = 1376$ px) which ensures accurate sampling of details. Slice thickness was kept constant at $\Delta z = 5$ mm for all measurements.

Each measurement was repeated twice to avoid non-equilibrium effects and guarantee steady-state conditions in the longitudinal magnetization.

The experiments were evaluated on the MR raw data. First, the mean values along k_y were calculated, before the signal was transformed into image domain via FFT. The images of the individual receiver coils were then combined by the SoS method. For some evaluations the signal was slice-wise normalized to peak signal to separate effects on the absolute signal strength, e.g. due to saturation, from these directly affecting the slice profile.

To evaluate the slice profiles and allow a quantitative comparison, the full-width half-maximums (FWHMs) of the slices were determined. The mean signal of the FWHMs across all slice profiles were calculated and assigned as \bar{S}_{FWHM} . Since, the

pulse profiles after SB excitation were considered as reference, the left and right limits, z_l and z_r , of FWHM at a single slice position centered at z_i were defined as:

$$\begin{aligned} z_l : S(z_l) &= \frac{1}{2} \max (S(z_i)) , \text{ for } z_l < z_i \\ z_r : S(z_r) &= \frac{1}{2} \max (S(z_i)) , \text{ for } z_r > z_i \end{aligned} \quad (4.5)$$

These limits were set identically for the SB and the MB slice profiles. Hence, after determination of the limits, the mean signal \bar{S}_{FWHM} for all slice profiles N_s in both cases was calculated as:

$$\bar{S}_{\text{FWHM}} := \frac{1}{N_s} \sum_{n=1}^{N_s} \int_{z=z_l}^{z_r} S_n(z') dz' \quad (4.6)$$

\bar{S}_{FWHM} was evaluated in different experiments, which were performed to

- compare MB ($MB = 4$) and SB slices profiles in 24 slices (1 mm gap) for $\alpha = 90^\circ, 60^\circ, 30^\circ$ at $\text{TR} = 1800$ ms to simulate the slice configuration of the perfusion experiments in Section 4.3,
- consider effects of cross-talk between adjacent slice locations in a set of eight slices ($MB = 4$, 1 mm gap) acquired at $\text{TR} = 261$ ms with $\alpha = 68^\circ$,
- explore the influence of variations in TR ($\text{TR} = 32$ ms, 100 ms) and FA ($\alpha = 15^\circ, 30^\circ, 42^\circ, 90^\circ$) to the slice profiles of two slices ($MB = 2$, 30 mm gap), where the setup with $\text{TR} = 32$ ms approximates $\text{TR}/T_1 \approx 0.3$ which is similar to the perfusion experiments.

4.5.2 Effects of Excitation Imperfections

Two different methods for the formation of the ACS data were proposed and evaluated as described previously in Section 4.3.4. Measured ACS source and ACS target data can be considered for the calculation of the reconstruction weights in SG, whereas the SSG algorithm only processes ACS data from a SB acquisition. In standard approaches, the ACS data acquired with SB excitations are either synthesized in a MB dataset as ACS source (SG) or kept separated and zero-filled (SSG) [Set+12b; Cau+14]. However, if the MB RF pulse is calculated in a straightforward manner as defined in Equation 3.19, RF power amplifier's non-linearity and memory effects will distort the real MB RF pulse which is transmitted [Sco12]. In particular, the rapidly-varying envelopes for excitations with high MB factors experience these limitations [Gri+10]. Different optimizations in the RF pulse design have been proposed to tackle hardware related imperfections, but they usually come at a cost of flexibility and generality [Abo+17b].

As described in detail in the above Section 4.2.1, the transmitted MB RF pulse was analyzed and the slice profiles were evaluated. Moreover, the effects of distorted MB RF pulses were investigated on a compound phantom made up of a structured phantom (background filling: $T_1 = 289 \pm 4$ ms) and a bottle phantom ($T_1 = 290 \pm 20$ ms). T_1 -values of the phantoms were determined by inversion-recovery experiments. Measurements were run with $\alpha = 90^\circ$, TR= 400 ms and slice settings similar to the animal experiments. 24 slices of 5 mm thickness (1 mm gap) of SB and MB MRI data with $MB = 4$ (CAIPIRINHA shift of FOV/4) were acquired. These were reconstructed with/without measured MB ACS source data according to the two methods for SG and SSG presented in Section 4.3.4.

5 Results: Simultaneous Multislice Imaging for Dynamic Imaging

This chapter presents the relevant results concerning dynamic SMS MRI in-vivo accompanied by various auxiliary experiments, ex- and in-vivo, which address different aspects of SMS, the MB RF excitation and the introduced novel sequence and its reconstruction in particular.

Significant parts of the presented results have been published previously in [EGL14; ELG15; Eic+16; Eic+18].

5.1 In-vivo Perfusion Experiments

Since this work focuses on the general method, only results of a single experiment are presented in detail. The findings are consistent with data derived from four similar experiments which are summarized in Appendix A.1.

5.1.1 Signal Separation and Dynamic Imaging

500 repeated measurements from the dynamic protocol under CA-administration were reconstructed with a fixed, precalculated SG kernel. The SG kernel was based on separate ACS source ($MB = 4$) and target (SB) data with identical image contrast parameters (method 1, ACS111, Sec. 4.3.4) which were acquired before CA administration. Figure 5.1 (top row) shows a high resolution morphological TSE image, acquired prior to the dynamic scans with identical slice positioning to ease the definition of region of interests (ROIs). The figure on the left displays the signals taken from a single voxel (ROI1). ROI1 is located in a major vessel where a direct response to the inflowing CA can be easily identified in the signal time course for all three echoes (TE_1, TE_2, TE_3) in the early phase (200 s). During the CA-bolus, the T_2^* -effects dominate and reduce the signal amplitude even in the early echo, TE_1 , which has stronger T_1 -weighting. By the signal separation procedure based on Equation 4.2, T_2^* -contributions are removed and an essentially T_1 -weighted signal, S_0 ($TE = 0$ ms), can be recovered. The red curve in Figure 5.1 shows the increasing S_0 time course despite the exponential reduction by a shorted decay time, T_2^* , in presence of a high CA dosage (blue curve).

Two additional ROIs were selected from homogeneous regions in muscle tissue as depicted in the morphological image in Figure 5.2. The time courses for ROI2 (solid) and ROI3 (dotted) as well as the resulting S_0 -dynamics are shown in the left subfigure. The measured signals for TE_1, TE_2, TE_3 are consequently lower than S_0 at $TE = 0$ ms. The corresponding T_2^* -values in both ROIs for the complete measurement (10:52 min) are shown in the right subfigure. The signal decreases

compared to S_0 because of susceptibility effects during CA arrival. This reveals the measurements sensitivity to CA-effects. After some time (> 100 s), the T_2^* -signal continues at a constant level when CA distribution reached an equilibrium state between intra-vascular regions and EES.

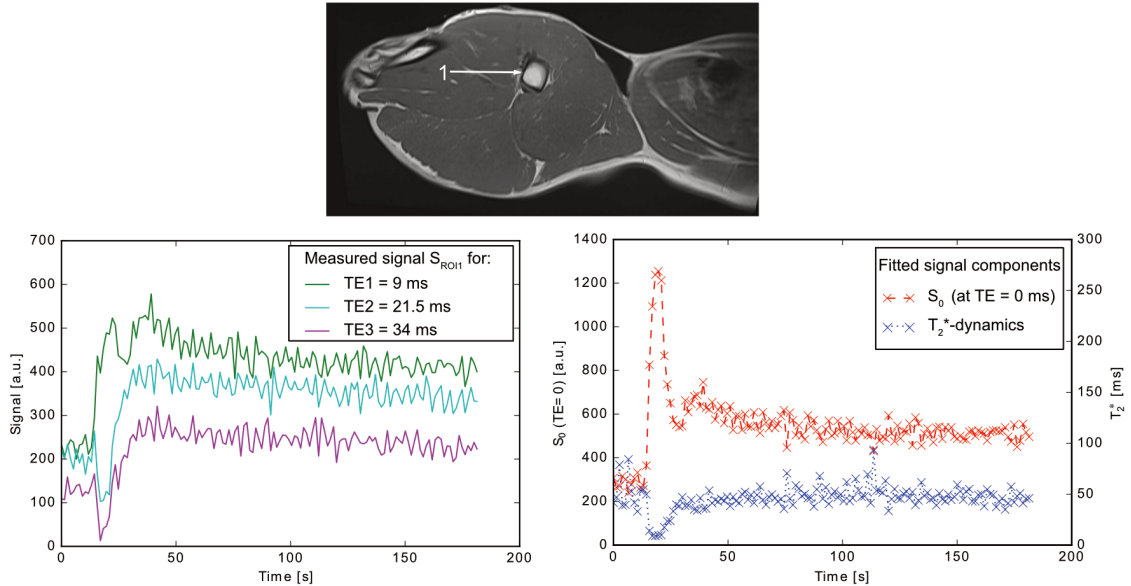


Figure 5.1: The selected ROI represents a single voxel (ROI1, slice 15) dominated by intravascular signal. The intravascular signal describes typical AIF curve characteristics. High resolution morphological images (TSE, sagittal) were used for selection and positioning of the ROI. The diagrams show the signal dynamics in a major vessel for all three acquired contrasts (left) as well as for the separated signal components, S_0 and T_2^* (right).

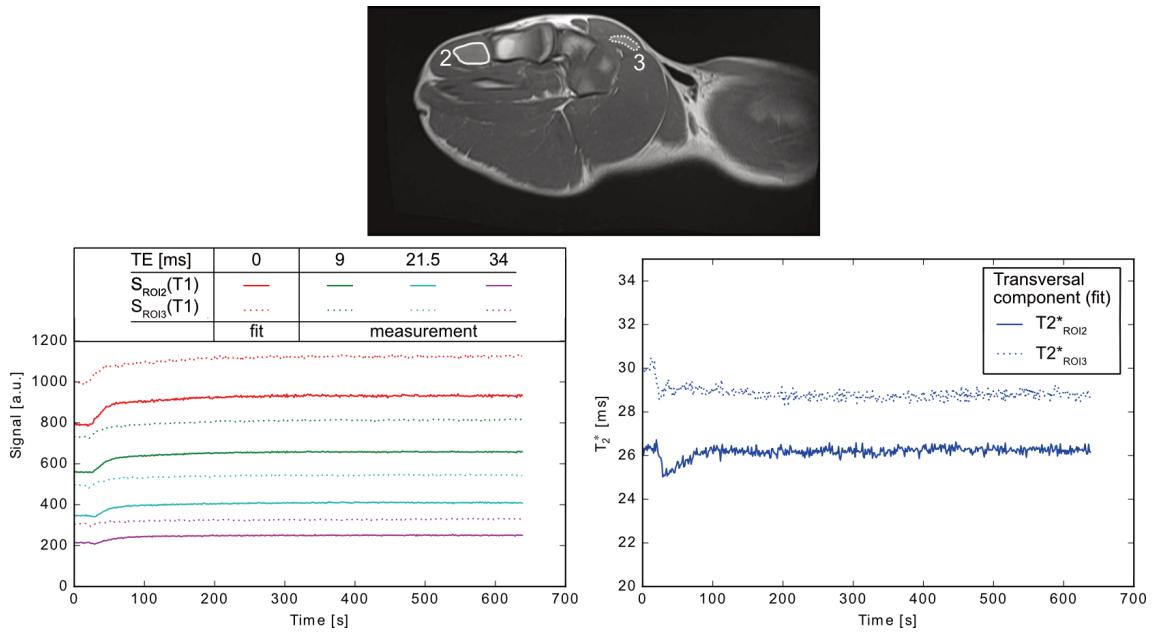


Figure 5.2: Two representative regions in muscle tissue were selected for dynamic signal curves in muscle tissue (slice 19, ROI2 (solid), ROI3 (dotted)). For ROI2 (solid) and ROI3 (dotted) the three acquired contrasts (TE_1 , TE_2 , TE_3) and the extrapolated signal for $TE = 0$ ms are depicted in the left diagram. The changes in T_2^* are shown in the right diagram. The sensitivity of T_2^* to inflow effects of CA leads to a decreased signal, which recovers to a constant level when CA is distributed inside the ROI.

5.1.2 Reconstruction Performance and Image Quality

Figure 5.3 shows the four times accelerated SMS acquisitions after unfolding and reconstruction. All 24 slices of the volume are displayed for completeness. In the later figures only representative slices from one MB slice group are selected for clarity. This MB slice group is highlighted by the green box in Figure 5.3.

The quality of the SMS images is comparable to the SB images which were acquired with the same image contrast of $T_1 = 9$ ms and $TR = 1500$ ms (Fig. 5.3, right top row). A similar reconstruction performance could be achieved for the later echo times as depicted in Figure 5.3 (right bottom row). No image normalization was applied, so signal inhomogeneities, reflecting the reception field and positioning of the phased array coils, appear in all cases.

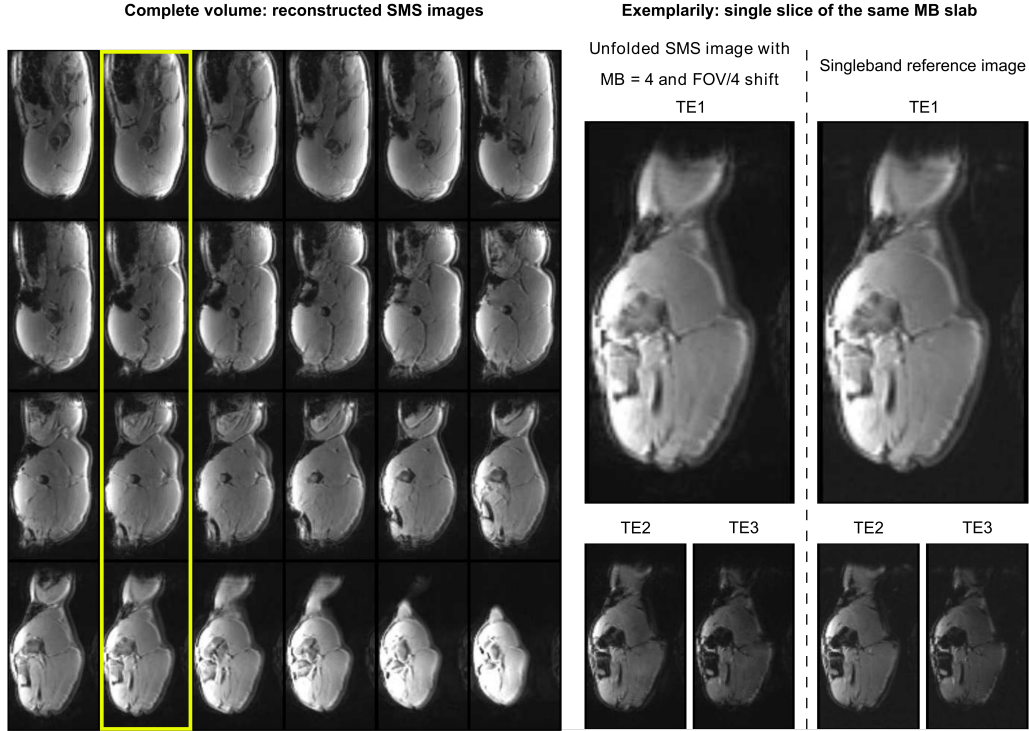


Figure 5.3: SMS image reconstruction of the complete volume (24 slices, $MB = 4$, $FOV/4$ -shift) performed with SG [Set+12b]. For kernel training, measured SMS and SB data with identical imaging parameters were used. Four representative slices from on MB slice group are selected for further illustration (yellow box). A single slice with a $TE_1 = 9$ ms of the reconstructed SMS image (center) and the reconstruction of the SB reference data (right) are shown in zoomed view. The results for the other echoes, TE_2 and TE_3 , are depicted below the first contrast images, accordingly.

In Figure 5.4, the two alternative reconstruction methods for SG and the reconstruction with SSG (method 2 only), as described in Section 4.3.4, are compared. Method 1 (left), where ACS source data were measured with SMS ($MB = 4$) and the same protocol parameters as for the SB acquisition, results in the most accurate reconstruction in terms of subtraction differences. The normalized subtraction map shows a homogeneous reconstruction of the signal throughout the recovered slices. For the SMS reconstruction with SG (method 1), the mean error across the volume is $\bar{E}_{\text{diff,SG},1} = 0.06$. In comparison, the reconstruction with method 2 for SG (center) suffers from localized intra- and inter-slice differences. A mean error of $\bar{E}_{\text{diff,SG},2} = 0.1$ was determined in this case. The use of the SSG algorithm (right) addresses reconstruction errors due to slice leakage and reduces inhomogeneity, but remaining local errors with a mean of $\bar{E}_{\text{diff,SSG},2} = 0.09$ can be identified.

In PI and related techniques, the g-factor is a standard metric for evaluation as introduced in Section 3.2.3. Reconstruction-related noise enhancement, is depicted in Figure 5.6. g-factors larger than one indicate that SNR was (locally) reduced by the reconstruction procedure. The mean g-factor for the compared reconstruction methods are summarized as histograms in Figure 5.7. All values are in close range,

with 1.8 ± 0.4 for method 1 (SG) and 1.5 ± 0.3 for method 2 (SG), respectively. While the g-factor for the SSG reconstruction (method 2) is 1.6 ± 0.3 .

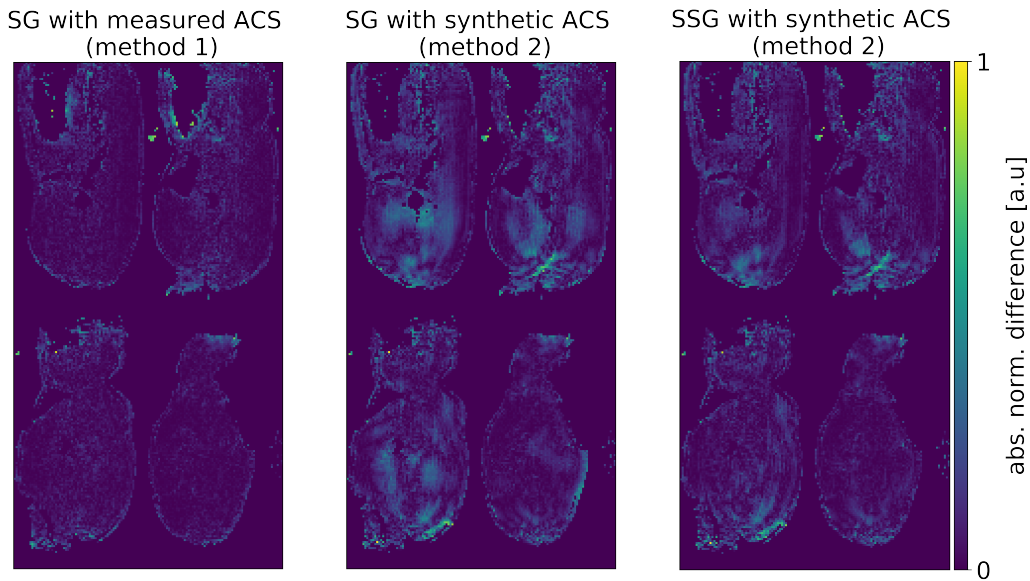


Figure 5.4: The normalized subtraction maps of the different reconstruction methods as described in Section 4.3.4 are shown. From left to right: Method 1, where the SG algorithm with measured data for ACS source ($MB = 4$) and ACS target (SB) was used for reconstruction. Method 2 (center), where the reconstruction is performed with synthesized ACS source data and, for comparison, a reconstruction by the SSG algorithm [Cau+14]. The most homogeneous reconstruction result can be achieved by method 1 (left), while method 2, especially for the SG algorithm, shows strong localized differences. The corresponding histograms in Figure 5.5 help to assess the mean subtraction error across the complete volume.

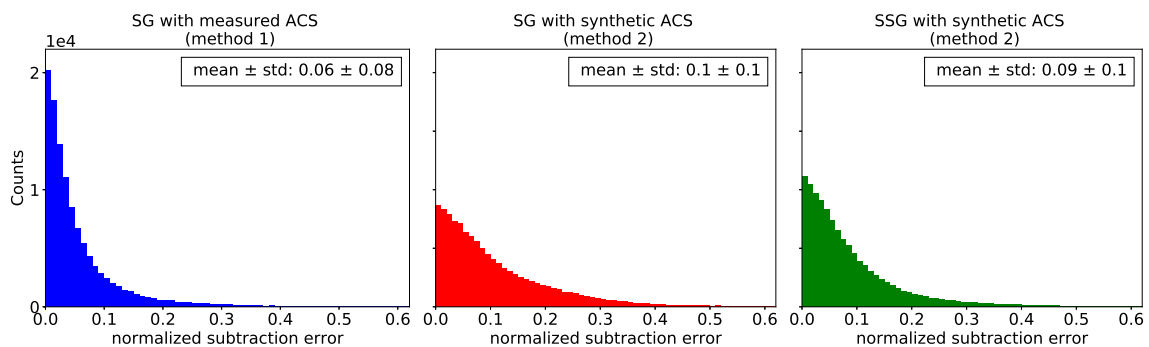


Figure 5.5: The corresponding histograms to Figure 5.4 allow assessment of the mean errors across the volume of 24 slices. Masking was applied to remove noise in the background for histogram and statistical calculations.

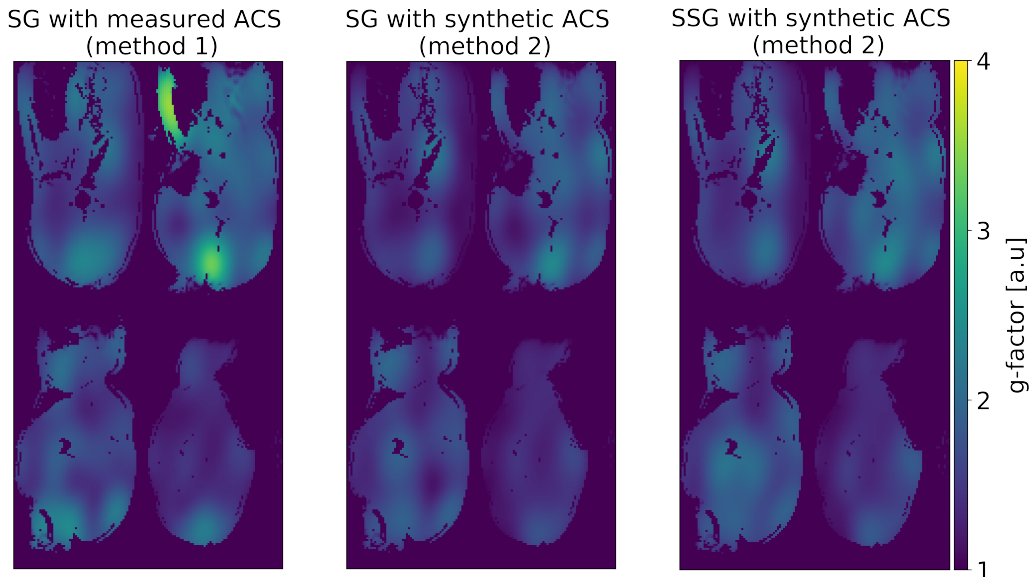


Figure 5.6: The g-factors of the different reconstruction approaches were derived from the SG/SSG weights as suggested in [Bre+09]. The corresponding histograms and the mean g-factor for all slices are displayed in Figure 5.7.

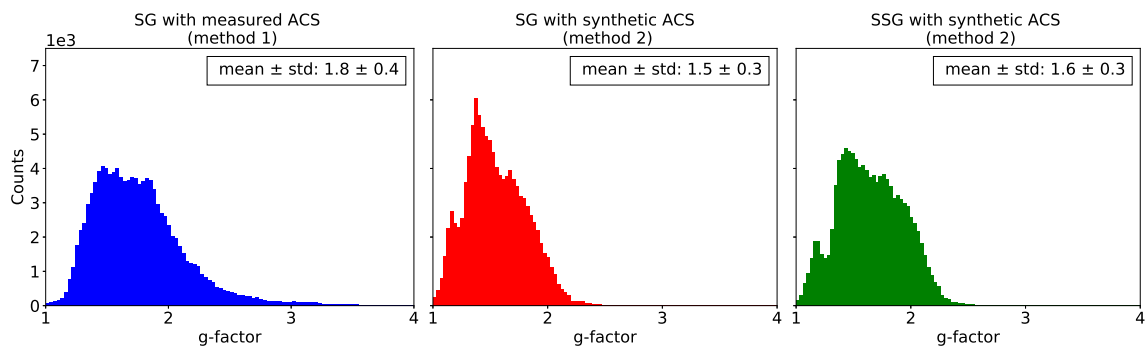


Figure 5.7: The mean g-factor across the object region, 24 slices, are in the same range for the compared approaches, with the chosen reconstruction strategy (left) indicates a slightly higher g-factor as the two others. Masking to remove background noise was applied before calculation of the histograms and statistics.

5.2 Dependency of slice-GRAPPA on Image Contrast Variations

As mentioned in Section 4.4, reports on the dependency of the SMS reconstruction on changes in image contrast between ACS scan and actual measurement were investigated. Phantom data acquired with $\alpha = 5^\circ$ and $\alpha = 90^\circ$ exhibit different image contrasts as shown in Figure 5.8. Figure 5.9 gives an overview of the range in image contrast in the used phantom with its CA-enhanced sub-volumes, first the expected contrast by a simulation of the signal equation for a GRE sequence (left) and then, as histogram after the measurement (right). The blue curve and bars indicate the data acquired with $\alpha = 5^\circ$, while the red color shows the simulated and measured signal for an excitation with $\alpha = 90^\circ$.

ACS with different image contrast were compared in their performance and influence

on the reconstruction result to experimentally evaluate potential dependencies of the SMS reconstruction on image contrast. Figures 5.10 and 5.11 display the S_0 and T_2^* dependency for different combination of ACS for SG and SSG reconstructions. For each combination different color-coded SNR levels were also plotted: no average (black), five averages (blue), and ten averages (red). The robustness of the tested reconstruction strategies was quantified by a linear model (b_0, b_1) , where the resulting fitted parameters are shown in the respective figures. A detailed overview of the results is given in Figure 5.12.

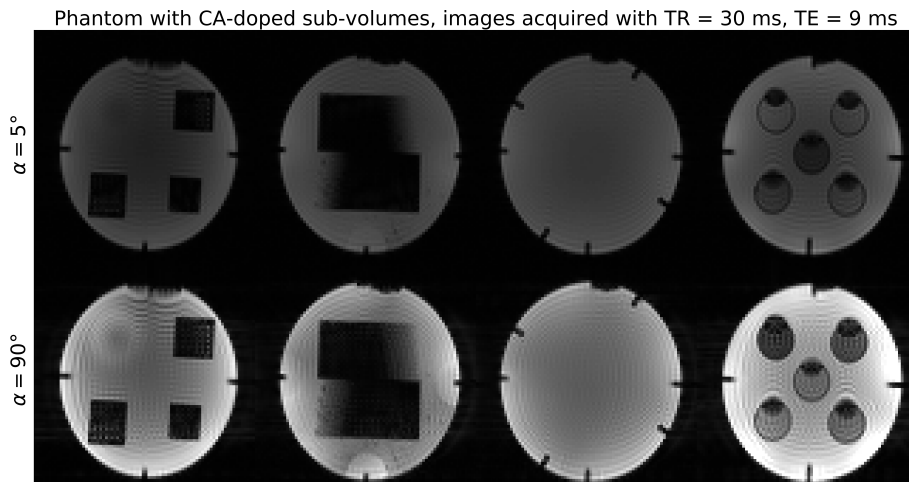


Figure 5.8: Images of GRE acquisitions with two different FAs, $\alpha_1 = 5^\circ$ (top) and $\alpha_2 = 90^\circ$ (bottom), but identical TR = 30 ms and TE = 9 ms. The contrast behavior under changed FA was investigated as shown in Figure 5.9 and a potential influence on reconstructions with SG or SSG is analyzed, see Figures 5.10, 5.11 and 5.12. Measurements were not optimized for image artifacts, e.g. so-called Gibbs ringing, because these are considered irrelevant for these investigations on SMS reconstruction.

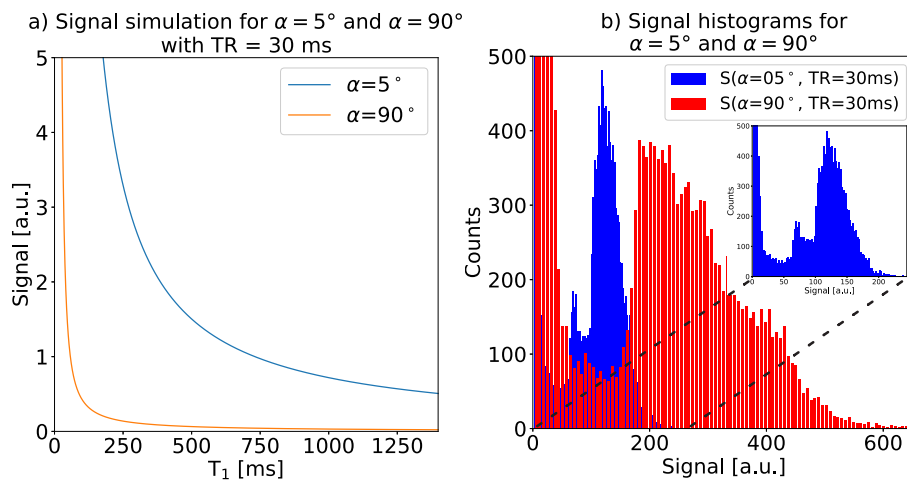


Figure 5.9: Simulation and corresponding measurement to evaluate changes of the image contrast related to variation in the flip angle. a) Simulation of gradient echo signal to estimate changes in image contrast for different flip angles. b) Histograms of acquired images to compare the image contrast change in dependency of flip angle variation. A phantom with differently CA-doped sub-volumes was used to evaluate contrast dependency of the SMS reconstruction algorithms. Data acquired with $\alpha = 5^\circ$ (blue) serves as SMS image and ACS data, while data taken with $\alpha = 90^\circ$ is only used as ACS to calculate SG and SSG kernels, respectively. All other imaging parameters were kept constant, i.e. $TR = 30$ ms

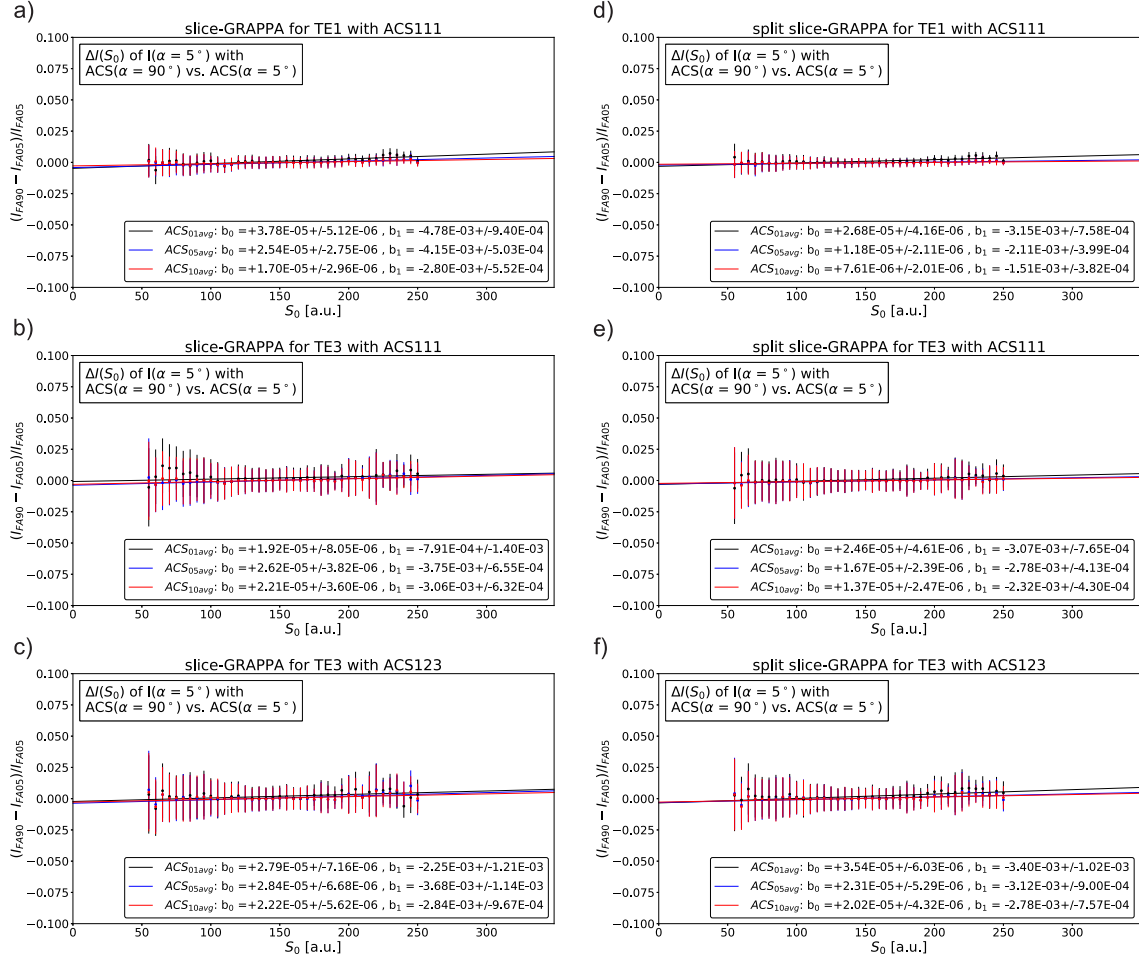


Figure 5.10: S_0 -dependency: Synthetic SMS images ($\alpha = 5^\circ$, $TR = 30$ ms) were disentangled with reconstruction kernels trained on either ACS with identical ($\alpha = 5^\circ$, $TR = 30$ ms) or different image contrast ($\alpha = 90^\circ$, $TR = 30$ ms). The resulting normalized signal differences for SG (left) and SSG (right) with respect to the base signal S_0 are shown for three levels of SNR in the ACS (no, five and ten averages). Subfigure a) and b) depict the first (TE_1) and third echo (TE_3) when reconstructed with a single, constant kernel (ACS111). In c) each echo is reconstructed with its corresponding echo in the ACS (ACS123). The subfigures d), e) and f) illustrate these dependencies for SSG. S_0 values along x-axis were binned to a width of 5. On the y-axis are the normalized differences between both reconstructions as formulated in Equation 4.4, the vertical bars represent the standard deviation of the mean value after binning.

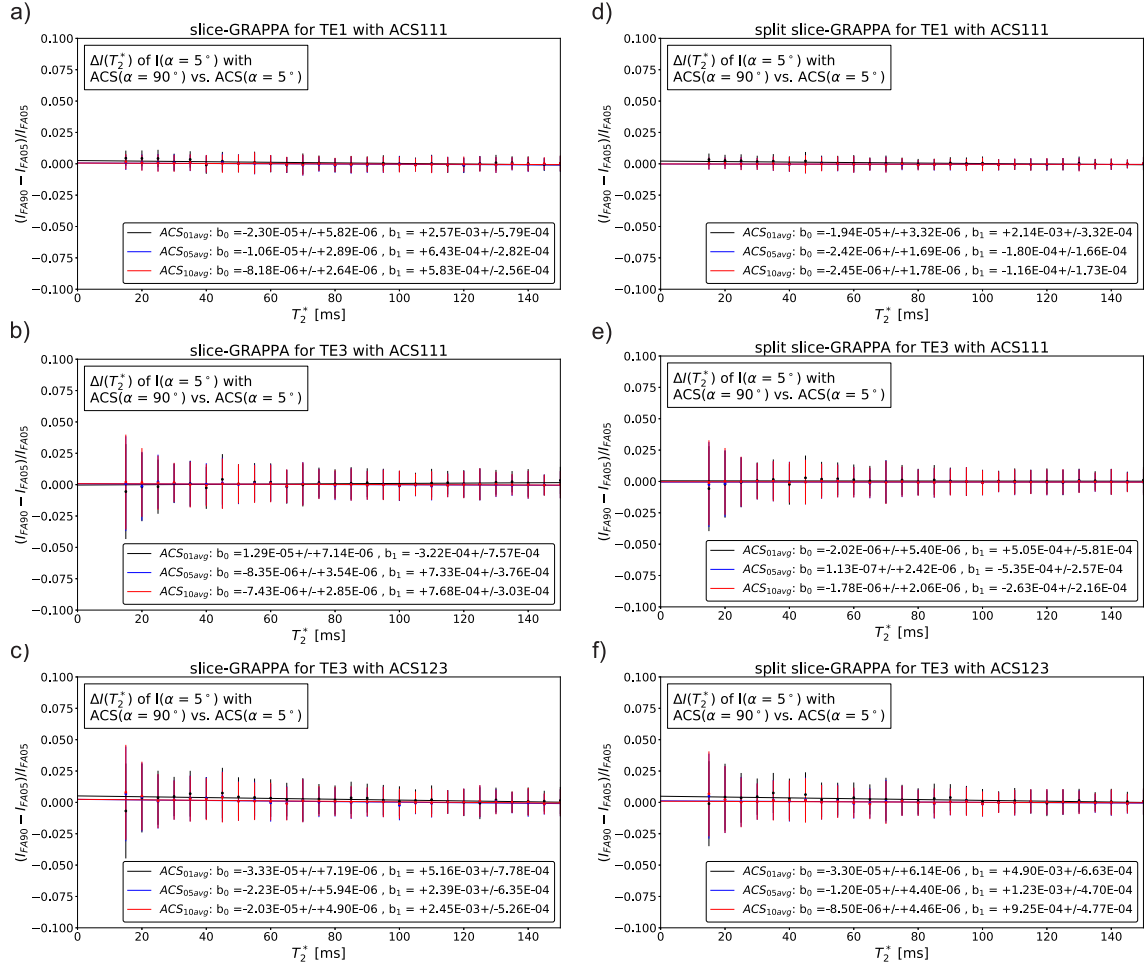


Figure 5.11: T_2^* -dependency: image signal for unwrapped, synthetic SMS images ($\alpha = 5^\circ$, $TR = 30$ ms) is shown for SG (left) and SSG (right). As in Figure 5.10 the reconstruction results of different ACS are compared by subtraction. While a), b), d) and e) represent reconstructions where the ACS is from the first echo only (ACS111), the subfigures c) and f) show SG and SSG reconstructions for TE_3 when each echo receives its own reconstruction kernel (ACS123). The bin-width is 5 ms. On the y-axis are the normalized differences between both reconstructions as formulated in Equation 4.4, the vertical bars represent the standard deviation of the mean value after binning.

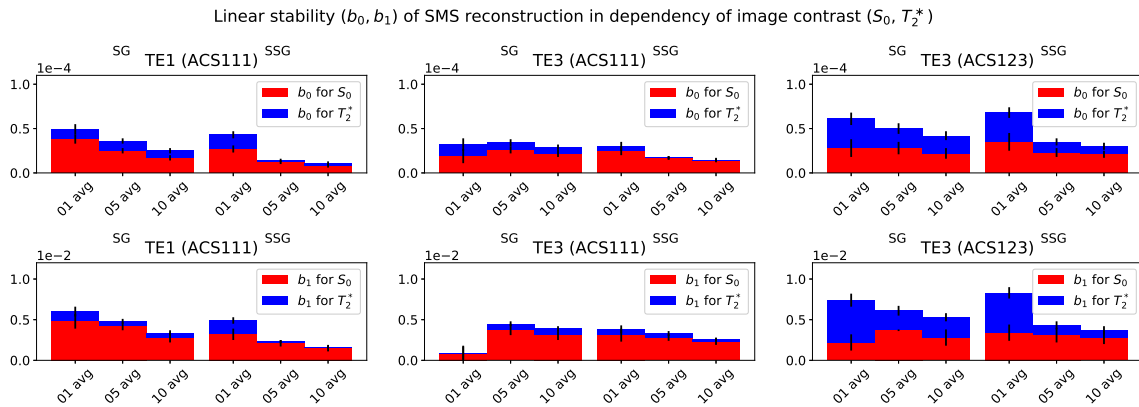


Figure 5.12: As shown in Figures 5.10 and 5.11, the robustness of the reconstruction with respect to S_0 (red) and T_2^* (blue) was quantified by a linear model (b_0, b_1). Besides different combinations of the ACS training data, three different SNR levels of the ACS data are shown (no, five and ten averages) for SG (left) and SSG (right). The slopes, b_0 , for both contrasts, S_0 and T_2^* , are visualized in the top row for the compared training configurations and TEs. The bottom row displays the offsets, b_1 , of the linear model.

5.3 Slice Profile after MB Excitation and Imperfections of MB RF Pulses

To investigate the slice profiles of MB excitation pulses these were compared to slice profiles after excitations with vendor's SB RF pulses. Signals of the slice profiles are shown for experiments with 24 slices (Figs. 5.13, 5.14, 5.15), eight slices (Fig. 5.16) each for $MB = 4$ and for two slices ($MB = 2$) in Figures 5.17 and 5.18. The temporally different excitations are plotted color-coded, such that slices of the same MB slice group appear in identical color in all the figures below. The reference slice profiles resulting from SB excitations have a dashed line style, while these after MB RF pulses are displayed as solid lines. The Tables 5.1 and 5.2 provide the mean signal \bar{S}_{FWHM} as defined in Equation 4.6 for quantitative comparison.

The slice profiles of 24 slices measured with $TR = 1800$ ms exhibit nearly identical shape and signal strength after a $\alpha = 90^\circ$ excitation, independent of the kind of RF pulse, SB or MB, as shown in Figure 5.13 (top). Multiple side lobes at different positions can be seen in a zoomed view closer to noise-level for the MB RF pulse, but these do not exist after SB excitation (Fig. 5.13, bottom). These side lobes are near 1% of the peak signal of the nearby slice and distinctively above noise-level for $\alpha = 90^\circ$ (Fig. 5.13) and $\alpha = 60^\circ$ (Fig. 5.14). The mean signal is slightly higher, $\bar{S}_{\text{FWHM,MB}}/\bar{S}_{\text{FWHM,SB}} = 101.6\%$, in case of MB excitation compared to the SB reference. While the side lobes decrease for a smaller FA, $\alpha = 30^\circ$ (Fig. 5.15), the peak signal between slice profiles after SB and MB RF pulses differs more clearly, albeit the shape of the slice profiles themselves remains similar. For $\alpha = 60^\circ$ (30°), the mean signal after the MB excitation drops to 98% (96.2%) of the SB excitation.

Potential cross-talk was investigated in the measurement with eight slices (SB and MB ($MB = 4$), $\alpha = 68^\circ$, $TR = 251$ ms) shown in Figure 5.16. The unscaled signals in (a) appear with similar slice profiles, but reduced peak signal (96.8%) in case of MB excitation. Side lobes for the MB RF pulse are at about 1% of the peak signal in the corresponding MB slice group as depicted in the zoomed inset, but these are not present in case of a SB excitation.

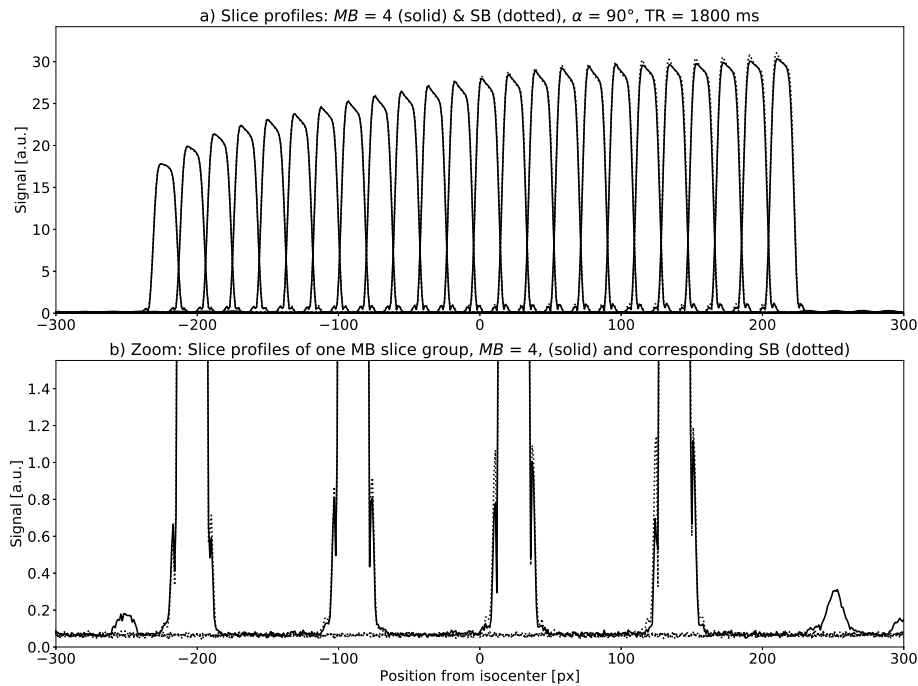


Figure 5.13: a) The slice profiles of 24 slices after excitation with MB (solid) and SB (dotted) RF pulses are displayed. Signal was acquired with a 20-channel head coil. The slice profiles in of both experiments are almost identical for $\alpha = 90^\circ$ and $TR = 1800$ ms (Tab. 5.1). b) A closer look into the low signal region reveals side lobes of the MB RF pulse, which do not occur in SB excitation.

\bar{S}_{FWHM} [a.u.] for $MB = 4$ with total number of slices	24	24	24	8
MB, \bar{S}_{FWHM} [a.u.]	23.41	19.6	11.33	215.69
SB, \bar{S}_{FWHM} [a.u.]	23.04	19.99	11.69	222.74
MB/SB	101.6 %	98.0 %	96.2 %	96.8 %
FA [deg]	90	60	30	68
TR [ms]	1800	1800	1800	251

Table 5.1: Comparison of slice profiles after MB excitation for $MB = 4$ and a reference SB RF pulse. The mean signal \bar{S}_{FWHM} for both types of excitation across all slices is listed. The ratio between MB and SB pulses quantifies the averaged attenuation of the MB RF pulse.

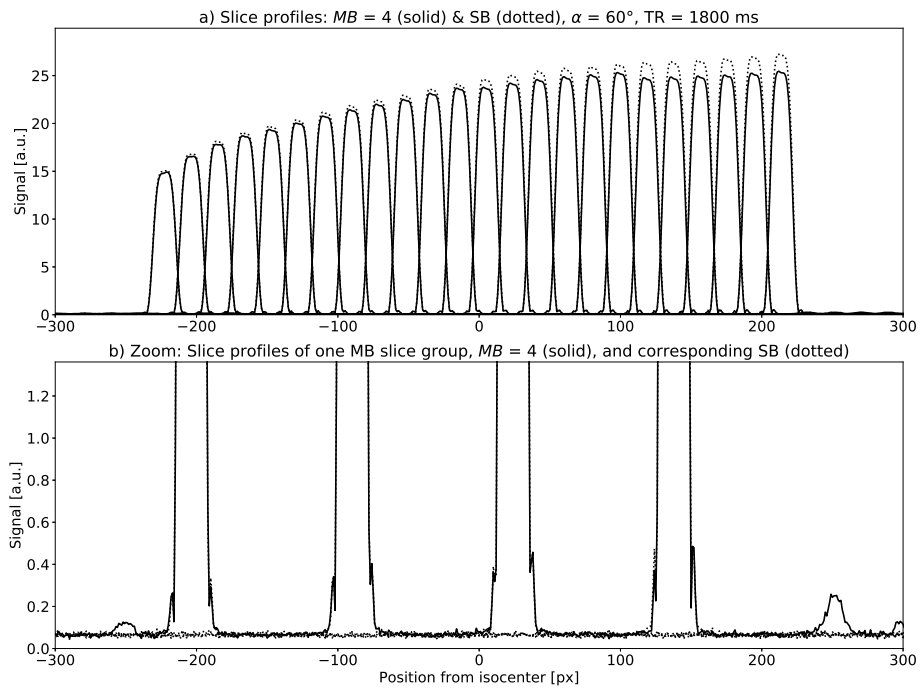


Figure 5.14: a) Direct comparison of slice profiles for excitations with MB (solid) and SB (dotted) RF pulses acquired with a 20-channel head coil similar to Figure 5.13 and 5.14. Excitations were done with $\alpha = 60^\circ$ and TR = 1800 ms, in this case the SB excitation yield higher absolute signal. b) The zoomed view of the slice profiles of one MB slice group and the corresponding SB shows side lobes which occur after MB excitation only.

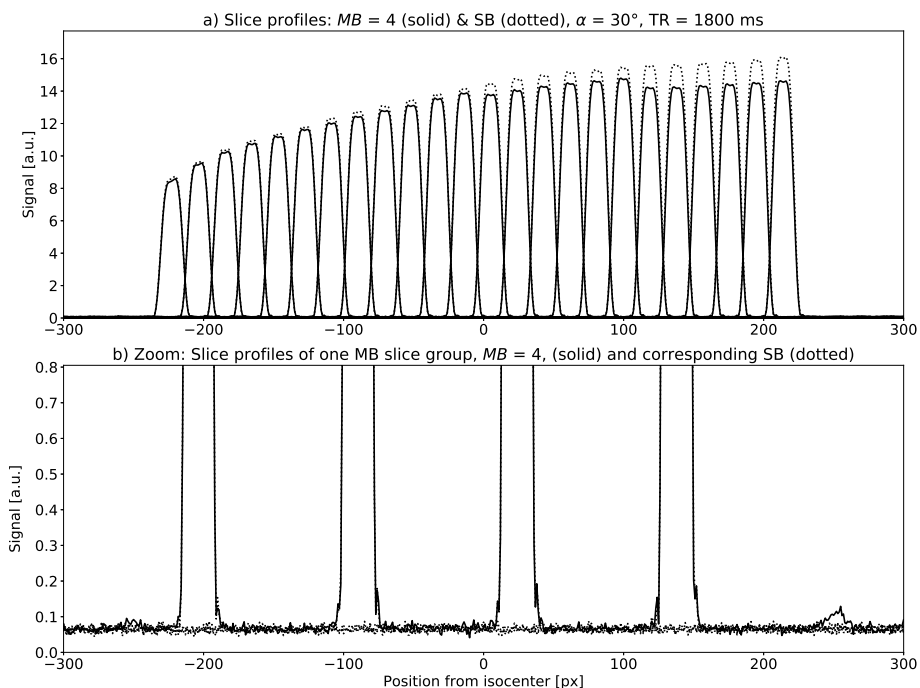


Figure 5.15: a) Direct comparison of slice profiles for excitations with MB (solid) and SB (dotted) RF pulses acquired with a 20-channel head coil similar to Figures 5.13 and 5.14. Excitations were done with $\alpha = 30^\circ$ and TR = 1800 ms. The absolute peak signal is reduced in slice profiles after MB excitations. b) Strength of the side lobes is reduced for $\alpha = 30^\circ$ when compared to Figures 5.13 and 5.14.

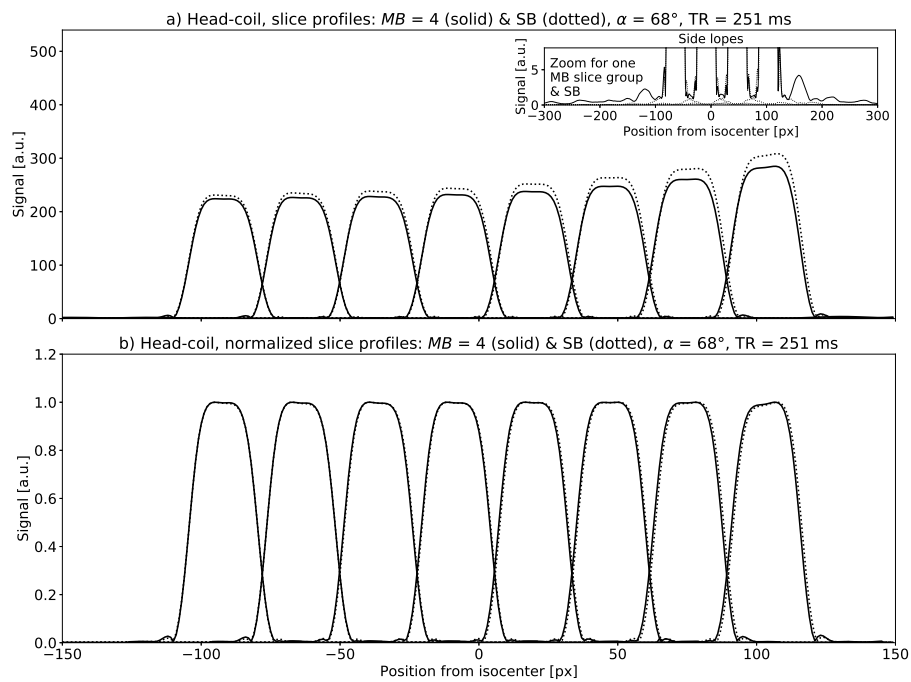


Figure 5.16: a) Comparison of slice profiles for excitations with MB (solid) and SB (dotted) RF pulses for eight slices to investigate cross-talk between the MB slice groups. Two MB excitations pulses for $MB = 4$ are played out in contrast to eight SB RF pulses. b) The signal level after SB excitation is higher, but cross-talk effects do not deteriorate neighboring slice profiles as shown after slice-wise normalization. For all excitations the FA was set to $\alpha = 68^\circ$ for $TR = 251$ ms.

As described in section 4.5, a slice-wise normalization was done for the measurements with eight slices (Fig. 5.16 bottom) and the experiments for two slices with variations in the FA (Figs. 5.17, 5.18) to investigate effects on the slice profile independently of the absolute signal strength.

Comparisons of normalized slice profiles at the identical spatial locations resulting from two separate SB excitations versus a MB RF pulse ($MB = 2$) are given in Figures 5.17 and 5.18. The variation of the slice profiles on changing FAs for rather short $TR = 32$ ms is demonstrated in Figure 5.17. The ratio of $TR/T_1 = 0.3$ was similar to the configuration in the animal experiments with an expected, averaged $T_1 = 870$ ms for muscle tissue at 1.5 T [BKZ04] and $TR = 261$ ms. The obvious distortion of the slice profile disappears when TR is prolonged. Changes in the FA affect the resulting slice profiles much less with a $TR/T_1 = 9.4$ ($T_1 = 106$, $TR = 1000$ ms) as displayed in Figure 5.18. The results for these measurements for two different TR s and varying FAs are summarized in Table 5.2.

Phantom imaging was performed to investigate the effects of the above described discrepancies or imperfections between SB RF and MB RF excitations. Figure 5.19 shows the reconstruction of 24 slices in a compound phantom made up of a structured phantom and a bottle phantom. Images of a standard SB excitation serve as reference and are given in (a). The colored maps show the absolute difference of SG and SSG reconstructions if compared to the reference. Images were reconstructed from the same data, but with different data used for ACS as described previously in Sections 4.3 and 4.5.2. The proposed SG reconstruction method with separately measured ACS source and ACS target data exhibits slice leakage from other simultaneously excited slices of the same MB slice group (b), but results in more correct recovery of the signal intensity and image contrast as the SSG reconstruction (c), where only SB ACS data were considered for the calculation of the reconstruction weights. No masking was applied to keep signal leakage visible in regions outside the volume because of the CAIPIRINHA shifts.

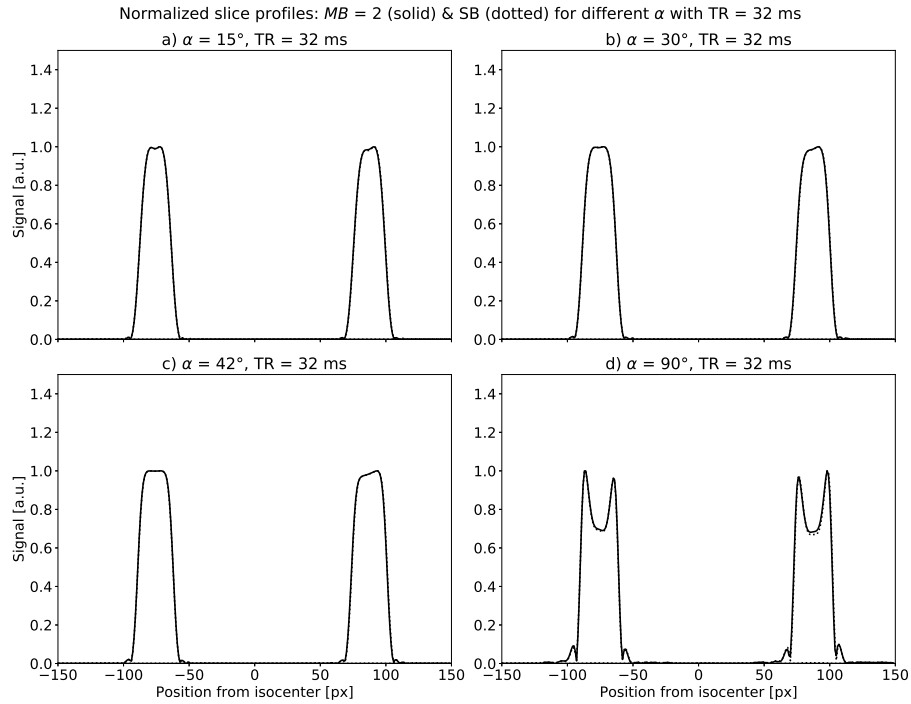


Figure 5.17: Slice profile effects of increased FAs for a fixed $TR/T_1 \approx 0.3$ are illustrated for $\alpha = 15^\circ$ (a), $\alpha = 30^\circ$ (b), $\alpha = 42^\circ$ (c) and $\alpha = 90^\circ$ (d). In (c), the FA ($\alpha = 42^\circ$) is the Ernst angle for the given TR/T_1 , while the slice profile for $\alpha = 90^\circ$ (d) approximates the parameters (FA, TR , T_1) of the in-vivo experiments in Section 5.1.

TR = 32 ms, Figure 5.17	α [deg]	15	30	42	90
\bar{S}_{FWHM} [a.u.]	MB	61.86	95.73	105.91	90.33
	SB	61.96	97.55	108.6	91.8
	MB/SB	99.8 %	98.1 %	97.5 %	98.4 %
TR = 1000 ms, Figure 5.18	α [deg]	15	30	42	90
\bar{S}_{FWHM} [a.u.]	MB	62.88	121.05	161.77	243.96
	SB	61.94	119.41	160.13	242.22
	MB/SB	106.4 %	101.4 %	101.0 %	100.7 %

Table 5.2: A series of measurements for two slices, $MB = 2$ and SB , with varying FA ($\alpha = 15^\circ, 30^\circ, 42^\circ, 90^\circ$) was conducted for $TR = 32$ ms (Fig. 5.17) and repeated for $TR = 1000$ ms (Fig. 5.18).

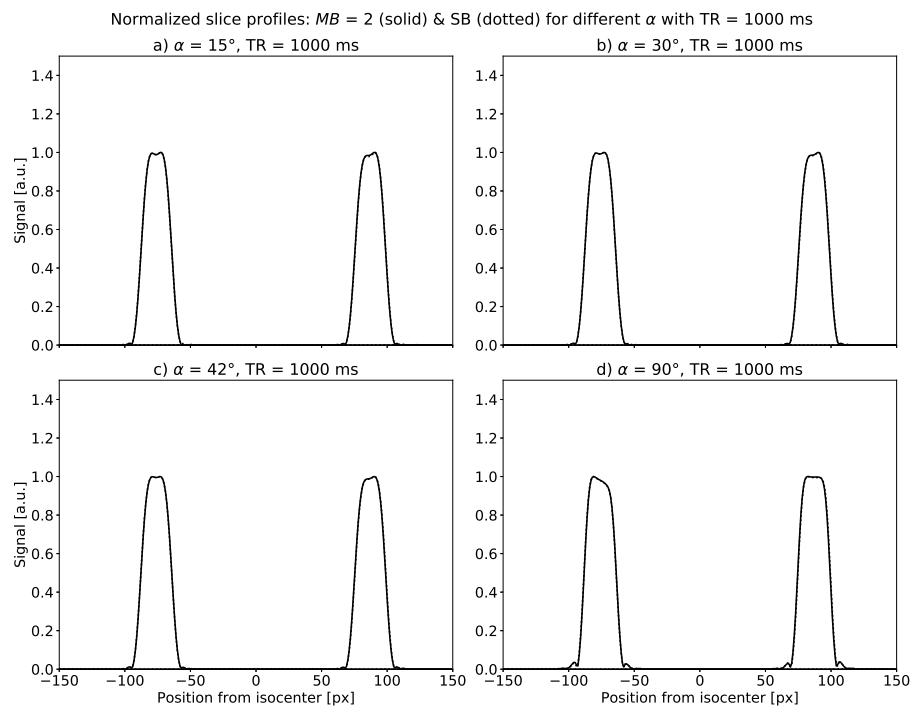


Figure 5.18: a-d) For $TR = 1000$ ms full relaxation of the magnetization with $T_1 = 106$ ms is ensured and the slice profiles are not distorted even for high flip angles in contrast to results in Figure 5.17 where high flip angles degrade the slice profiles.

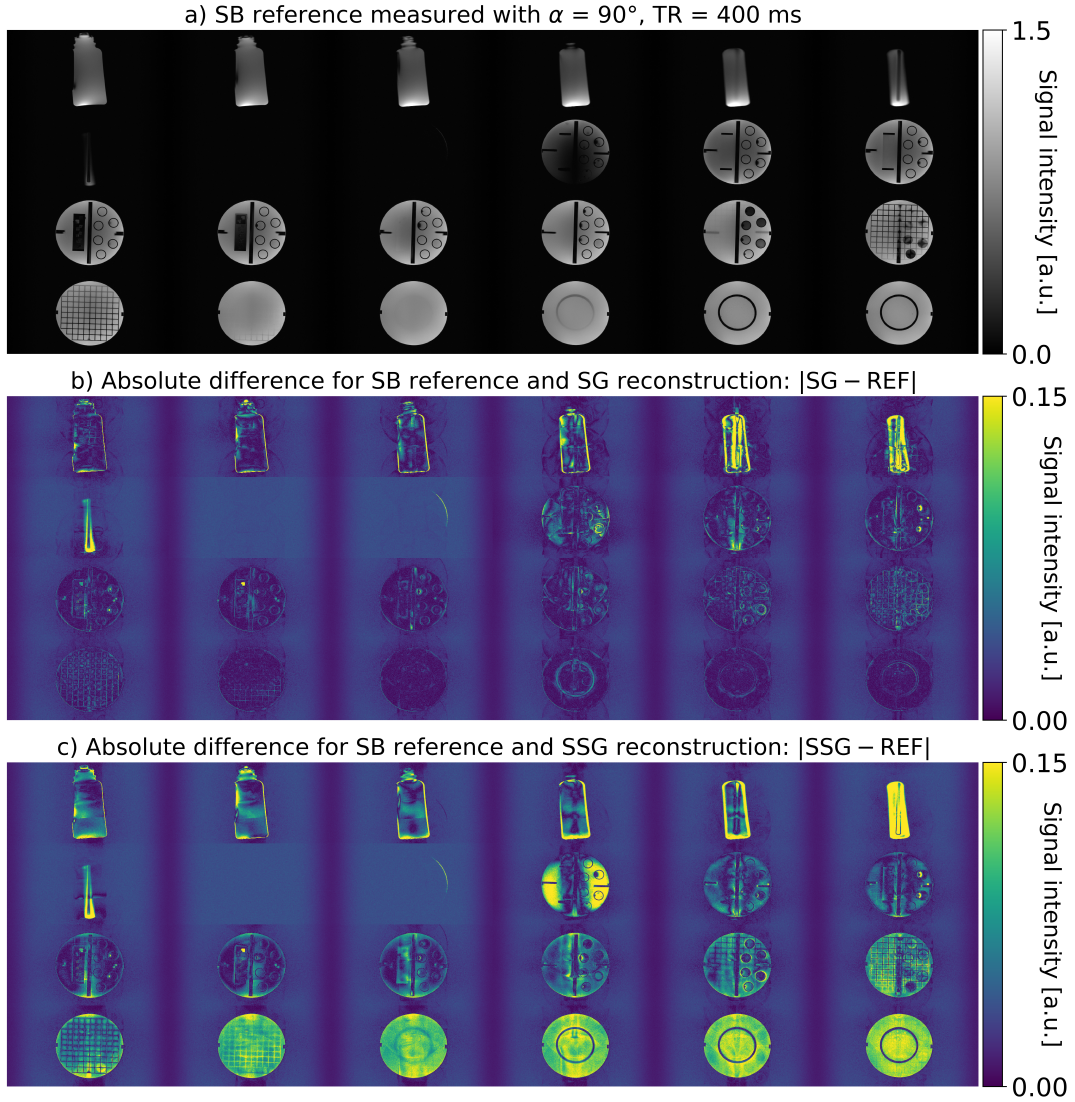


Figure 5.19: a) Acquisition of 24 slices in a compound phantom made of a structured phantom (background filling: $T_1 = 289 \pm 4$ ms) and a bottle phantom ($T_1 = 290 \pm 20$ ms). Images of SB excitation are given as reference. The slice thickness was set to 5 mm (1 mm gap). b-c) Show the absolute difference between SB and SMS images. b) SG reconstructions with measured source ACS and c) SSG reconstructions with synthesized source ACS. Both based on identical SMS data after MB excitation ($MB = 4$, $FOV_{\text{shift}} = 1/4$).

Part III

Deep Learning in MRI

6 Neural Networks and Deep Learning

“Machine-learning technology powers many aspects of modern society: from web searches to content filtering on social networks to recommendations on e-commerce websites, and it is increasingly present in consumer products (...). Machine-learning systems are used to identify objects in images, transcribe speech into text, match news, posts or products with users’ interests, and select relevant results of search. Increasingly, these applications make use of a class of techniques called deep learning.” [LYH15]

As stated by LeCun, Bengio and Hinton, deep learning (DL) has accessed a wide range of modern life technologies, but also entered different disciplines in science and research.

This chapter introduces the concepts of neural networks and, in particular, deep neural networks based on [Nie15], if not cited otherwise.

6.1 Deep Learning

Deep learning is a method of representation learning [LYH15] and it is inspired by nerval system in the human brain which is mimicked by an artificial neural network (NN). In 1949 Donald Hebb formulated the Hebbian Theory on how human learning can be interpreted on neuron level. Synaptic interactions compete and consolidate neural connections which finally lead to learning and memory [Heb49]. Similar principles have been successfully transfered to artificial NN such that a model can be trained to learn ‘something’ and accomplish a defined task.

In particular, the human visual system processes sensory input on multiple stages, also termed as levels, of representation. These representations are realized by neurons which are assumed to be organized in a layer-like structure. In visual detection, the human brain semantically perceives a scene. Likewise to visual detection, high-level representations are generated from low-level features, such as edges or colors, in DL [Hin07]. Which features are represented in the layers is self-determined by a general-purpose adaption procedure of the network without human feature engineering during the so-called *learning* phase [LYH15]. Abstract levels of representation are obtained by stacking multiple layers on top of each other accompanied by non-linear transformation of the input signal to the output in each or some of the layers. The signal transformation is usually denoted as activation function or just activation. A NN associates an input to its output similar to a mathematical function. However, a NN with a sufficiently large number of layers and non-linear activations has *universal function approximation capabilities* [HSW89] to approximate arbitrary complex functions [LYH15]. These principles, self-determined learning and universal

function approximation, are key advantages of DL. In particular, because these dominantly benefits from high computational power, i.e. graphics processing unit (GPU)-accelerated computing, and increasing amounts of available training data.

6.1.1 Terminology and Network Structures

This section introduces terminology and ruling principles used later on in this work. As NNs are a re-emerging technology in computer science there exists a mixture of well-established and recently introduced, less familiar methods and terms. Figure 6.1 gives an overview how the terms artificial intelligence (AI), machine learning (ML) and DL relate to each other.

NNs and, in particular, deep neural networks (DNNs) are nowadays associated with

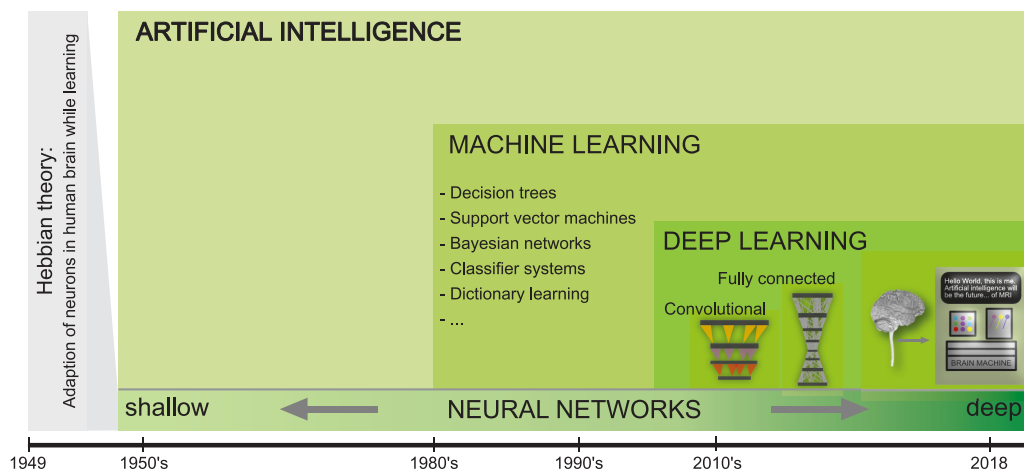


Figure 6.1: Deep learning embedded in a (historical) context of artificial intelligence and machine learning from the early 1950’s until today. Starting with a theoretical framework, i.e. the Hebbian Theory, ideas of brain-like machines and general artificial intelligence have arisen across the decades of digitalization. Neural networks, which are inspired by the brain’s biology, have been discussed since the early days of AI, but recently obtained attraction because of increasing computational power, availability of significant amounts of data and improved methods for efficient learning.

the DL. Both terms, NN and DNN, are used in this work and are often interchangeable. However, whereas NN is a rather general term, DNN describes NNs with multiple ($>$ two) layers, which have gained high interest, recently.

A NN is built up of individual components, denoted as nodes or neurons. Each of them forms a simple functional unit with one or more inputs x_i and one output y as depicted in Figure 6.2. The sum of the weighted inputs x_i connected to a neuron,

$$X = \sum_i x_i w_{ji} , \quad (6.1)$$

forms a linear input passed to an activation function f

$$y = f(X) . \quad (6.2)$$

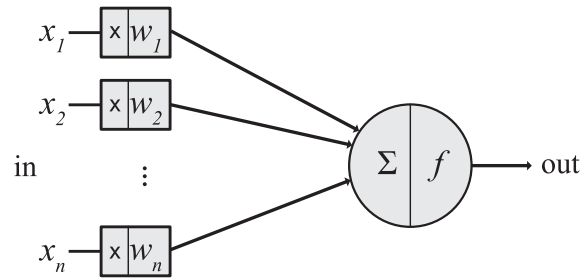


Figure 6.2: The input vector x_1, \dots, x_n (left) is multiplied, \times , by corresponding weights w_1, \dots, w_n . The sum, Σ , of weighted inputs is fed into the activation function f of the neuron.

If the neuron's output y is not the final output of the NN, it will be connected to one or more successive neurons. The interconnected neurons in a NN are typically organized in a layer-like structure where a layer represents a collection of neurons, which are not connected to each other, but have some kind of connection to its preceding and successive layers' neurons as shown in Figure 6.3. NNs in which layers receive inputs from previous layers and yield outputs to successive layers are named *feedforward neural networks* as they have no circular connections between neurons. DNNs have at least one hidden layer that is not directly connected to the in- or output. At the network's output, the output layer yields a prediction y which

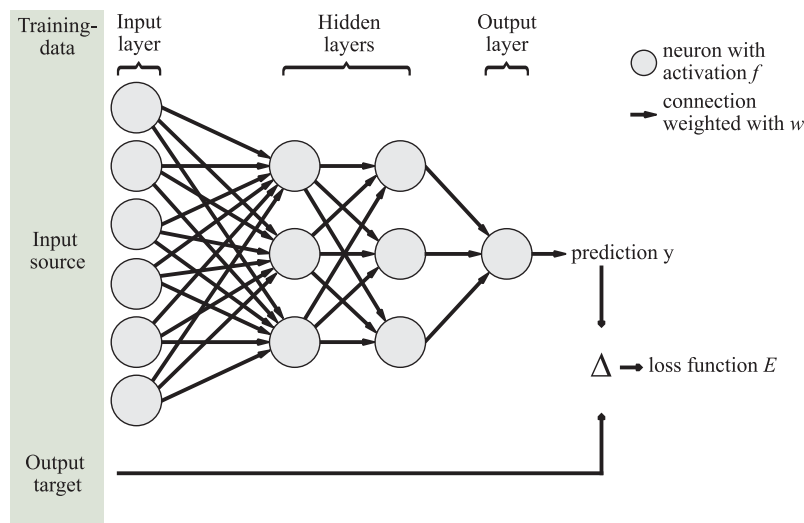


Figure 6.3: If all neurons of adjacent layers are connected to each other by a weighted connection (weights not shown), the network is called fully connected. There are no connections between neurons of the same layer. The source data fed into the input and passed forward through the network to produce the predicted output y , the correct output, e.g. target image is compared to y by the loss function.

is compared to the target. Prediction and target can be multi dimensional data, however, NNs in this work are limited to 2D outputs. Data that pass through a NN are organized as tensors which are often described as vectors for N dimensional data in literature.

If all neurons of adjacent layers are connected to each other, the layers are referred to as *fully connected* as illustrated in Figure 6.3. Another type of connection is present for *convolutional* layers. These layers apply a convolution operation to the input. The size of the convolution kernel defines the size of the receptive field and the number of weighted connections. Further details on the principles of connecting operations will be given in Section 7.1.

Independent of their connection type, the neurons map their input to the output as defined by their activation function. In order to approximate arbitrary functions, non-linear activations are needed after the linear operations, i.e. weighting and summation of the input [HSW89]. A common choice for the activation function in the hidden layers of a DNN is the rectified linear unit (ReLU) function [LYH15]:

$$f_{\text{ReLU}}(X) = \max(0, X) = \begin{cases} 0 & , \text{ for } X < 0 \\ x & , \text{ for } X \geq 0 \end{cases} \quad (6.3)$$

The strictly monotonic hyperbolic tangent

$$f_{\text{tanh}}(X) = \frac{e^{2X} - 1}{e^{2X} + 1} \quad (6.4)$$

can be an option to produce negative and positive values, but limit their range to $] - 1, +1[$. Whereas, the linear identity function

$$y = f(X) = X \quad (6.5)$$

is a common choice for the activations in the last layer(s), i.e. output layer. These linear output units are common in regression models where the prediction has to match continuous values [Hin+12]. Many other activation functions exist. In this work, the above-mentioned activations are used exclusively.

The shape and dimensionality of the training data define the shapes of the in- and output layers, whereas the design and architecture of the hidden layers is developed depending on the confronted problem or class of tasks. Often heuristic, less simple designs combine different types of layers to get a desired behavior of the net [Nie15]. The convention for the following sections will be a bottom-up or left-right design (Fig. 6.3), where the bottom/left-hand side layers in a given network serves as the visible input layers, stacked by a desired number of hidden layers and visible output layers on top/right-hand side.

The networks implemented for this work are setup with *Keras* [Cho+15] using a *TensorFlow* backend [Aba+16]. TensorFlow organizes data in tensors as common interchange and data structure format to compute on GPU, therefore the term tensor will be used for data objects processed by a network. In contrast to the chapters

before, the tensor and vector notation will not be in bold letters throughout the following chapters.

6.2 Training of a Neural Network

The aim of training is to find a set of weights which ensures that the trained NN predicts for each input tensor an output tensor which is identical or sufficiently close to the correct output [RHW86]. Such a training, termed as *supervised learning*, based on example input-output pairs lead to a model which maps an input to an output similar to a classical deterministic function. However, while conventional mathematical models are predefined, NNs are data-driven models which adjust while training.

6.2.1 Weight Adjustment by Backpropagation of the Loss Function during Learning

At the end of a successful learning, the predictions y by a trained model should equal the target output a . The loss function, or just loss, quantifies the (dis-)agreement of both by a prior defined metric. Note, that the literature also refers to the loss function as cost or objective function.

Training algorithm tries to find a set of weights w that minimizes the loss

$$\begin{aligned} & \text{minimize} && E(w, b) \\ & \text{subject to} && w \in \mathbb{R}, b < \epsilon, \end{aligned} \tag{6.6}$$

where b denotes an optional bias with its upper limit ϵ , which may be added to the summed inputs before the activation function.

A common choice for the loss function in regression problems is the mean squared error (MSE). The L2 norm compares a predicted output y to a target a , by

$$E_{\text{MSE}}(w, b) = \frac{1}{n} \sum_{i,j=1}^{N,M} \|y_{i,j} - a_{i,j}\|^2 \tag{6.7}$$

where $N \times M = n$ is the size of the output. If data are images, $N \times M = n$ is the 2D extension in pixels.

Another metric to guide the training can be total variation (TV), which is well known in image processing [ROF92] and MRI, i.e. compressed sensing [Lus+08]. TV or more precisely, TV denoising, is a L1 related norm to remove noise from images while yielding edges and structural content of the image [ROF92]. The two dimensional

TV in [Aba+16] is formulated as

$$TV(w, t) = \sum_{i,j=1}^{N,M} (|y_{i+1,j} - a_{i,j}| + |y_{i,j+1} - a_{i,j}|) . \quad (6.8)$$

Alternatively, loss functions might also be combined to mix their individual properties as considered in Chapter 7.

Once a loss is defined, the training procedure itself has to be determined. The most common method to control the training is *backpropagation*. Backpropagation was introduced in 1986 [RHW86] and names an algorithm which describes how to transfer the result of a loss function back into the network to adapt weights and bias. Being more precise, backpropagation repeatedly adjusts the weights $w \rightarrow w'$ and bias $b \rightarrow b'$ to change the loss ΔE :

$$w \rightarrow w' : \Delta E \quad \text{and} \quad b \rightarrow b' : \Delta E . \quad (6.9)$$

Therefore, it optimize the output by controlled adjustment of these networks parameters to minimize the loss. As a result, the hidden units come to represent important features of the training data and capture regularities by the interaction of these units [RHW86]. The central expression in this context is the gradient of the loss function

$$\nabla E = \left(\frac{\partial E}{\partial w_i}, \frac{\partial E}{\partial b_i} \right)^T \quad (6.10)$$

with respect to any weight w and bias b . While inputs and intermediate states yield predictions at the output in forward direction, *learning* is realized by backpropagation. It propagates the derivatives in Equation 6.10 from the output to the input. Therefore, the loss function must satisfy two aspects. First, it can be written as an average of all individual training samples k

$$E = \frac{1}{K} \sum_{k=1}^K E^k \quad (6.11)$$

of the set of training data K . With this, the total gradient can be recovered from the computed partial derivatives for a single training sample [Nie15]. Second, the loss can be written as a function of only the predicted output y

$$E(w, b) \leftrightarrow E(y) \quad (6.12)$$

without being a function of the target output a . This is because the source input and the target output a are fixed for a sample of training data. Consequently, the

loss is explicitly not a function of these [Nie15], but depends on the predicted output y which is a function of the network parameters w and b to be learned.

The training of a NN starts with the forward propagation of the input data. Commonly several samples of training data are processed simultaneously and referred to as *batch* of size N_b . The predictions at the output, the evaluation with a loss function and the backpropagation to associate a local error value to each neuron follow. Then, weights and biases are updated according to a predefined update rule. After the update a new batch is fed into the forward path of the NN. The local error of a (hidden) neuron is calculated by repeated application of the chain rule to compute multi-variable derivations of the loss function [RHW86]. At present, different implementation and variants of backpropagation have been developed. They define the rules in which way, how often and how much the weights are adjusted and hence, the particular learning process. One class of extensions of the backpropagation algorithm will be presented below, because of its popularity in up to date application of and research on DL. Gradient descent and precisely, stochastic gradient descent (SGD) is a basic optimization algorithm which updates the parameters for every batch to minimize the loss in opposite direction to the gradient of the loss function ∇E . SGD performs one parameter update w' , b' per batch

$$\begin{aligned} w &\rightarrow w' = w - \eta \nabla E^{N_b}(w, b) \\ b &\rightarrow b' = b - \eta \nabla E^{N_b}(w, b) \end{aligned} \tag{6.13}$$

where the learning rate η and batch size N_b are adjustable hyper-parameter to control the training. For a given number of training data N_{TB} , a larger batch size reduces the number of parameter updates. Processing the entire training data once is denoted as *epoch*. It requires multiple iterations:

$$N_I = \frac{N_{TB}}{N_b} . \tag{6.14}$$

Therefore, iterations N_I is the number of batches needed to complete one epoch. Many iterations result in frequent parameter updates in SGD which implicate a large variance according to the variations in the training data. These cause the loss to fluctuate and jump by which trapping in local minima is avoided, but exact convergence hampered as well [Rud16]. By today, many modified versions of SGD have been published to improve its performance [Rud16]. Adaptive Moment Estimation (Adam) is an efficient stochastic optimization derived from SGD [KB15], that realizes adaptive learning rate, damping to counter overshooting and adaptive momentum estimation. As Adam uses a different learning rate for every parameter w_i at a single time step t , the gradient of the loss function with respect to the

parameter w_i at t is [KB15]

$$g_{t,i} = \nabla E_t(w_i) , \tag{6.15}$$

or simply $g_t = g_{t,i}$ in vectorized notation. The algorithm applies exponentially updated moving averages of the past gradients. The decay is controlled by the hyper-parameters $\beta_1, \beta_2 \in [0, 1]$ to estimate the first moment m_t , or the mean, and second moment v_t , or the uncentered variance, of the gradients [Rud16]:

$$\begin{aligned} m_t &= \beta_1 m_{t-1} + (1 - \beta_1) g_t \\ v_t &= \beta_2 v_{t-1} + (1 - \beta_2) g_t^2 \end{aligned} \tag{6.16}$$

These averaged updates stabilize the decay and yield the Adam update rule at time t :

$$w_{t+1} = w_t - \frac{\eta}{\sqrt{v_t} + \epsilon} m_t \tag{6.17}$$

where $\epsilon = 10^{-8}$, as well as, $\beta_1 = 0.9$ and $\beta_2 = 0.999$ are the suggested default values for a wide range of parameter values [KB15]. For clarity, the terms for m_t and v_t have been kept in the non-bias-corrected form (see [Rud16]). To date, Adam is a commonly preferred choice compared with alternative optimizers [Rud16]. Its frequent update rate requires little GPU memory and is as computationally efficient [KB15] as Adam's parent methods, ADAGRAD [DHS10] and RMSProp [TH12]. Other gradient descent methods update the parameters less often, e.g. once per batch in case of batch gradient descent, and trade parameter oscillations for memory and computational power. Although, these attributes might sometimes be beneficial, stochastic gradient descent and its derivatives are of core practical importance in DL [Nie15]. A detailed mathematical description of the original backpropagation algorithm and some algorithmic features of the Adam optimizer can be found in the literature [RHW86; Nie15].

6.2.2 Overfitting and Regularization

Once training of a NN has been started, data flow and calculations inside the NN are somewhat black-box-like due to the vast amount of parameters, i.e. weighted connections between neurons. Intermediate outputs connected to hidden layers help to control and visualize the different representations, but complexity and multi-dimensionality of data do not allow a strict tracing. This lack of traceability poses an important drawback of NNs, especially in DL where the number of trainable parameters is often as large as $10^5 - 10^7$. Quoting Nobel prize winner Enrico Fermi, who said: "I remember my friend Johnny von Neumann used to say, with four parameters I can fit an elephant, and with five I can make him wiggle his trunk." [Dys04] rushes DL into a dilemma. Therefore, the problem of overfitting and how to control it are under ongoing development in computer science. A model

suffering from overfitting loses generality to the problem and performs weakly on new, unseen data. In this section some regularization strategies to prevent overfitting will be motivated and described, these are: data splitting into training, validation and test sets, L1/L2 regularization, dropout, batch normalization and training data expansion.

Data Splitting: The data fed into a model mark the basis for every learning. An often applied rule for data selection claims that data should be independent, identically distributed in the defined problem space [Vap99]. This means that no data has any preferences with the problem in mind and all are identically representative. It allows to find a model which generalizes well for a defined problem. In medical imaging, where the data availability is limited, the selection of suitable data is crucial. Despite a potentially limited amount of data not all data are used for the training explicitly. Data is rather split into three categories [Nie15]:

- **Training data** contain the majority of data. These data are presented to the model for learning. The input paired with the known output is compared to the calculated output of the NN and weights are adjusted iteratively during training to find optimal sets.
- **Validation data** represent a subset of data files used to evaluate model performance during training and optimize hyper-parameters, e.g. learning rate or batch-size to increase training performance. Validation data do not directly influence weight adjustments, but rather validate the model-performance with its tuned parameters.
- **Test data** are separated from the training processes and only presented to the model after training. The predicted output allows an evaluation of the quality, generality and potential of the trained NN.

Besides counteracting direct overfitting of the weights by evaluation on data not involved in the training process themselves, the split into separate validation and test data additionally prevents the overfitting of the hyper-parameters [Nie15].

L1/L2 Regularization: Another way to combat overfitting are L1 and L2 regularization of the loss function. Both limit the growth of single weights by adding an extra term to the loss function. The L1 approach regularizes the loss function to

$$E_{L1} = E_0 + \frac{\lambda}{n} \sum_w |w| , \quad (6.18)$$

where E_0 is the unregularized, previously defined loss function. The influence of the summed absolute values of the weights w can be tuned by the hyper-parameter

λ normalized by the size of the training set n . Analogously, the L2 regularization, sometimes also named weight decay, is formulated as

$$E_{L2} = E_0 + \frac{\lambda}{n} \sum_w w^2 . \quad (6.19)$$

Both regularizations, L1 and L2, act similarly and counter rapid weight growth, but their regulatory regime differs. L2 penalizes larger weights stronger than L1, but optimization might slow down during training. The partial derivatives for both scenarios are

$$\frac{\delta E}{\delta w} = \frac{\delta E_0}{\delta w} + \frac{\lambda}{n} \text{sgn}(w) \quad (6.20)$$

with

$$\text{sgn}(w) = \begin{cases} -1 & , \text{ for } w < 0 \\ 0 & , \text{ for } w = 0 \\ +1 & , \text{ for } w > 0 \end{cases}$$

for the L1 regularized loss function and

$$\frac{\delta E}{\delta w} = \frac{\delta E_0}{\delta w} + \frac{\lambda}{n} w \quad (6.21)$$

for L2 regularization of the loss function. With these and as addressed in Section 6.2.1, backpropagation is applied to define the update rule for weights in the NN. The weights in a L1 regularized network with a learning rate η are updated by

$$\text{L1: } w \rightarrow w' = w - \frac{\eta\lambda}{n} \text{sgn}(w) - \eta \frac{\delta E_0}{\delta w} , \quad (6.22)$$

which shrinks the weights by a constant value towards zero. By comparison, the weights are updated by an amount proportional to the current weight in case of L2 regularization

$$\text{L2: } w \rightarrow w' = w \left(1 - \frac{\eta\lambda}{n} \right) - \eta \frac{\delta E_0}{\delta w} . \quad (6.23)$$

NNs which are regularized with L1 tend to concentrate weights and connections to a relatively small number of high-importance connections [Nie15]. This is because the update rule in Equation 6.22 shrinks large weights $|w|$ much less than Equation 6.23. For updates where the weight values are small, e.g. close to zero, the L1 regularization will continue shrinking the weights without slowing down and reinforce zeroing weights, i.e. disconnecting neurons. In summary, regularization prevents overfitting by slowing down weight growth. Small weights, in turn, make the response of the NN robust against changes in only a few inputs, e.g. activation by noise [Nie15].

Dropout: A different approach to reinforce generalization during the training is dropout. Dropout can be considered as a binary selector for neurons in one or more layers. As depicted in Figure 6.4, dropout randomly and independently drops a defined percentage of neurons in that layer and thus randomly disconnects parts of adjacent layers [Hin+12]. A typical choice is the temporal and random omission of 50% of the neurons, e.g. neurons in the same layer which is affected by dropout. By the randomized disconnection of neurons, overfitting is reduced by prevention of complex co-adaptation of weights [Sri+14]. Adapting the weights on the incoming connections is the essential part of the learning processes and it enables prediction of an output with a given input [Hin+12]. Since in a suitable NN different settings of weights show equal accuracy of the model during training, but result in worse performance for the unseen data, the co-adaptation of weights to one of these specific sets reduces the general predictive capabilities of a NN. Another point of view is to consider dropout under certain circumstances as a form of data augmentation [Sch15].

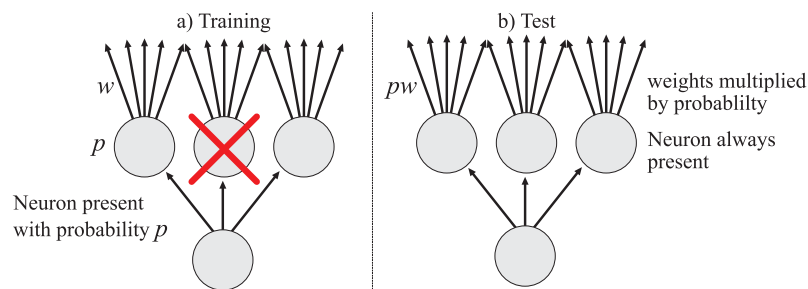


Figure 6.4: a) Neurons in a layer with dropout are disconnected from the next layer with a specified probability p . Training of weights w is only possible during training steps where neurons are present. b) At test time these randomly omitted neurons are always present and their corresponding weights are multiplied by the probability p , giving the same output as expected while training.

Batch Normalization: Batch Normalization (BN) was introduced to increase training speed. Moreover, its regulatory attitude helps to avoid overfitting and is beneficial for generalization. A sample of training data is seen in conjunction with other samples of the same batch, all trained simultaneously in the same batch. The variance of the samples of one batch hampers the DNN to produce deterministic parameters for a single sample [Sze15]. The principle behind BN is to reduce variance and inhomogeneity of a layer's inputs. The variance of training data leads to a range of differently distributed numbers not directly relevant for the features or information to be learned, but difficult for the DNN to capture and therefore, with negative impact on learning rate and training speed [Sze15]. In addition, varying input distributions propagate from layer to layer and hamper optimal parameter adjustment. Normalizing a layer's input is a tool to accelerate training and, furthermore, it stabilizes

parameter growth by its scaling property on gradients during backpropagation [Sze15]. The BN algorithm transforms the input of a batch $B = \{x_1, \dots, x_m\}$ of size m trained at a time according to Equation 6.24 [Sze15]:

$$\begin{aligned}
 \mu_B &\leftarrow \frac{1}{m} \sum_{i=1}^m x_i && , \text{ batch mean} \\
 \sigma_B^2 &\leftarrow \frac{1}{m} \sum_{i=1}^m (x_i - \mu_B)^2 && , \text{ batch variance} \\
 \hat{x}_i &\leftarrow \frac{x_i - \mu_B}{\sqrt{\sigma_B^2 + \epsilon}} && , \text{ normalization} \\
 \tilde{x}_i &\leftarrow \gamma \hat{x}_i + \beta \equiv \text{BN}_{\gamma, \beta}(x_1, x_2, \dots, x_m) && , \text{ scaling and shifting}
 \end{aligned} \tag{6.24}$$

The trainable parameters γ, β are adjusted per batch while the constant ϵ guarantees numerical stability.

6.2.3 Generalization by Randomness

Randomness is a key aspect of the generalization capabilities of DNNs. This can be identified in a variety of strategies from which some important ones will be explained in this section to underline the general understanding of *learned* generalization versus memorization during training, i.e. overfitting.

For a DNN with unchanged architecture, two trainings will not happen in exactly the same way. One reason for this is how the data handling routines provide the training and validation data during training. Typically, a batch of predefined size is randomly drawn from the data collection [Bro16a].

Furthermore, randomness is introduced during initialization of the trainable parameters, i.e. the weights. If every weight on the neurons' connections in the DNN would be same, all neurons computed the same output. This symmetry of all neurons in the layers leads to the same gradients during backpropagation and therefore all parameters undergo the exact same updates. In other words, there is no source of asymmetry between neurons if their weights are initialized to exactly the same values. Therefore, the weights have to be very close to zero to not emphasize any input right from the beginning, but not identically zero. As a solution, it is common to initialize the weights of the neurons to small numbers and refer to doing so as symmetry breaking, as such, a random state of the total DNN is established at first [Joh17; Bro16a].

The idea of generalization in supervised learning is inevitable connected to the bias-variance dilemma describing the trade-off between accurate modeling and generalization [Bro16b]. Since natural collections of training data contain fluctuations, a non-zero variance always exists. A low or high bias counteracts a high or low variance, hence biases are essential trainable parameters in DNNs [Bro16b]. A bias

as introduced in Equation 6.6 adds an additional input to a neuron and allows its activation even in case of zero input on all other connections and makes it easier for neurons to saturate [Nie15]. Its noise-like influence is almost complementary to dropout and fosters generalization [Bro16b]. During training the optimizer adjusts the bias' values to influence the model complexity. To avoid assumptions on the model before training, biases may be initialized by zero, e.g. default in Keras [Cho+15]. An account on the bias-variance dilemma is given in Appendix A.3 for further reading.

With regard to the aforementioned, a remark on reproducibility has to be made. Seeking for generalization by the mentioned strategies invoking randomness intuitively prevents reproducibility. However, reproducibility is an important concept to evaluate and proof scientific work. In order to reduce variance in training when reproducibility is to be tested, the generators used for (pseudo-)random initialization are fed with identical seed values.

7 Materials and Methods: Neural Networks for SMS Reconstruction

The following chapter moves the focus from the general introduction of NNs and DNNs to the materials, in form of software tools and data base, and methods, i.e. the developed DNN architectures and conducted experiments, used throughout this work.

Relation of SMS Reconstruction Methods to SMSnet: The efforts to accelerate MRI measurements lie mainly in three areas. These are: The signal processing for reconstruction, the scanner hardware and the physics behind an imaging sequence. As introduced in Chapter 3, established reconstruction methods for accelerated MRI commonly involve the spatial information inherent to the MR machine itself, i.e. from multi coil receiver arrays, to recover omitted data after the measurement [Bla+04; Lar+01]. Two main strategies have been established and coexist for the past 20 years. These are image domain based approaches such as SENSE [Pru+99] which utilize the coil sensitivities explicitly and methods such as simultaneous acquisition of spatial harmonics (SMASH) [SM97] or GRAPPA [Gri+02] which extract the missing information implicitly from k-space correlations in the coil elements [Uec+14]. Although, these methods share the same principles, sub-types of these strategies have been adapted to the different problems. Specific tasks are, for example, the recovery of in-plane undersampled data, typically along PE direction, or the reconstruction with an undersampling along the slice direction in SMS, but also a combination of both. While SENSE- and GRAPPA-like techniques basically solve an ill-conditioned linear system by numerical inversion other approaches accomplish reconstruction by iterative nonlinear inversion techniques, e.g. regularized nonlinear inversion (NLINV) for PI [Uec+08] and SMS-NLINV in case of SMS [Ros+17]. Both, linear and non-linear techniques, use reference data to estimate the coil sensitivities even though their density distribution (along k-space trajectories), point of acquisition and processing in the reconstruction differ.

A completely novel approach is presented here [WE16]. Instead of solving the problem of overlapping image content by a deterministic algorithm, a trained DNN recovers the separated slices. A new network architecture referred to as *SMSnet* was developed for this task. Generally speaking, SMSnet is designed and trained in such way that it *learns* information of the imaging system as one unit incorporating the hardware, i.e. the MR machine, and the imaging processing. The properties learned are, in case of SMS, probably best associated with the CoSs. The dielectric properties of the object under investigation directly influence the CoS [Uec+08],

therefore, a conventional calculation of an universal profile can not be done a priori. Even for objects which are often positioned similarly in an identical receiver array, e.g. the head coil, individual reference data are required to explore the CoSs and to compensate for these changes [Uec+08].

Here, a DNN interprets CoSs as a feature to be extracted. The generated output masks are merged with the preprocessed SMS image data in an extended channel domain. Both, the path to generate the masks and the path to handle the image data, receive only SMS data. In particular, no SB or ACS data, neither in image domain nor in k-space domain, are provided to the DNN. SMSnet learns an input-output mapping during supervised training, therefore pairs of source (in k-space and image domain) and target data (image domain) are available at the network's inputs and output.

7.1 Software and Architecture

The design of a NN is often motivated by existing architectures for related tasks or classical algorithms for the governing question. A combination of both approaches inspired the model designed in this work. The final architecture of SMSnet was mainly inspired by deterministic PI and SMS reconstruction methods.

The python based deep learning library, Keras, was used [Cho+15]. Its layer-based organization offers versatile types of layers and various derivatives of the most common types. Keras' high-level application programming interface (API) allows rapid development and prototyping of NNs and can be run with a TensorFlow backend. Layer parameters, such as type of the activation function or dimensionality, as well as hyper-parameters for training are specified during model definition. The compiled model can be saved for archiving or re-training. Jupyter Notebook was employed for programming and to run trainings and save evaluations [Jup18].

At this point, relevant types of layers will be introduced. The developed architecture will be described later on in Section 7.2.

- A *fully connected layer* connects all k inputs $x^n = \{x_1^n, \dots, x_k^n\}$ of the n -th layer to all l activation functions which results are passed to all l neurons in the $n+1$ -th layer (Fig. 6.3). For the 2D case, as typical for images, the constructed tensors have four axes: $[N_b, N_x, N_y, N_c]$, where the N_b images, i.e. the batch size, of size $N_x \times N_y$ are loaded simultaneously to the GPU. N_c specifies the number of channels, or features. Keras allows a fully connection limited to the channels axis only, resulting in $N_c^n \times N_c^{n+1}$ connections as illustrated in Figure 7.1. The tensor's shape of the first three axes remains unchanged for these type of fully connected layers.
- NNs containing *2D convolutional layers* are favored for many tasks involving

images and often called convolutional NNs or, if all connections in the NN are convolutions, fully convolutional NNs, respectively. The key advantages why convolutional NNs perform well on (natural) signals are: their sensitivity to local connections, i.e. patches of an image, and shared weights by the receptive field, their pooling properties by which neighboring inputs are fed as a pooled input to the next layer and the reduced number of trainable parameters which allow deep network architectures [LYH15]. The detection of image features such as edges is not locally limited as the convolution kernel is slid through the complete plane of the input as shown in Figure 7.2. This shift invariance is another important property of convolutional layers in the domain of image processing.

- *BN layers* in Keras allow the normalization of the previous layer's output. A common choice to apply BN on a four dimensional tensor is to normalize for mean and variance in first three dimensions separately for each channel (Eq. 6.24).
- A *dropout layer* randomly drops a specified rate $r_{\text{drop}} = [0, 1]$ of all input connections and passes the remaining connections without any modification to the next layer.
- A *2D upscaling layer* repeats the rows and columns, i.e. pixels in N_x, N_y , of the data as defined by the size parameter. E.g., a size of (2, 2) doubles the extend of the input along both axes.

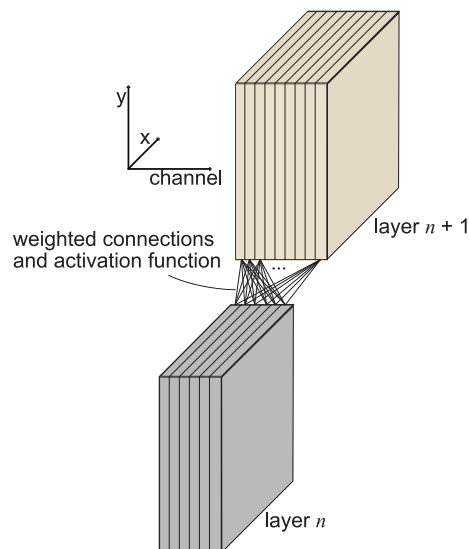


Figure 7.1: A fully connected layer can maintain its 2D shape in Keras. The fully connections are between channels of successive layers (layer n and layer $n + 1$) as illustrated. No x-y specific weights are involved.

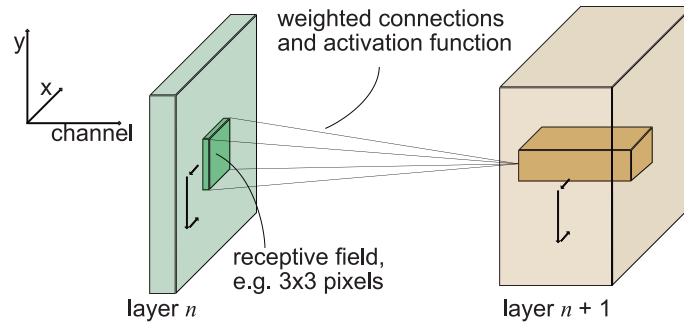


Figure 7.2: The receptive field is similar to a convolution kernel, here 2D, which is slid through the input. Pixel values at the input pass through weighted connections which accumulate in an activation function. Sliding of the receptive field in layer n indicated by arrows, yields an output pixel at a corresponding position in layer $n + 1$ also indicated by arrows. The results of different kernels, i.e. kernels with different trainable weights, are dumped along the channel dimension in the output. The number of channels is also called filter size or filters.

7.2 Architecture of SMSnet

The architecture of SMSnet is layer-based as common for networks created with Keras. It involves different types of layers which were introduced in Section 7.1. Figure 7.3 illustrates the arrangement of the layers. Two inputs are shown. One is for SMS data in k-space domain with a reduced resolution of 32×32 px and 40 channels to account for the complex valued data. The second input requires image data with a matrix size of 128×128 px in 40 channels. These two inputs are proceeded separately in the CoS- and the Im-path before the merge layer (light green).

The CoS-path employs fully-connected layers (blue) including dropout (black-white) to improve robustness and regularization. These are followed by a set of 2D convolutional layers (green) accompanied by two up-sampling (2, 2) layers (orange). Batch normalization (gray) is applied to regularize activations and improve training. The normalized and up-sampled output passes a fully-connected layer with tanh activation which allows negative values required for complex valued data. These are Fourier transformed before another fully-connected layer with linear activation rearranges the channels similar to a superposition. The number of independent CoS-paths in the final model equals the number of slices per MB slice group, e.g. two independent CoS-paths were created for $MB = 2$ as shown in Figure 7.4.

The image data in the Im-path passes fully-connected layers only. The first layer uses a leaky ReLU activation to keep a minimal sensitivity to negative values and to reduce vanishing gradient issues [Cho+15]. It follows a second layer with ReLU activation and a third layer which connections are passed through a tanh activation to, again, allow negative values. Batch-normalization is inserted after activations here, too. At the end of the Im-path, a fully-connected layer with linear activation rearranges the channels before the merge-layer as well. In contrast to the CoS-path,

the Im-path was not repeated in the final model architecture.

Preprocessed data from the CoS- and Im-path are then merged by element-wise multiplication. Since the next fully-connected layers have ReLU activations, the network has the chance to cancel out possible negative values during training. The merge layer is succeeded by some fully-connected layers which essentially reduce the channel dimensions yielding a single channel image at the output. The last three fully-connected layers with filter-sizes of 62, 31 and 1, are not followed by Batch normalization such that the output yields reasonable positive values similar to magnitude images after SoS coil combination.

The filter sizes for the layers were determined heuristically. Starting with a sophisticated guess for the initial number of network parameters and assuming that there exists a lower boundary for the number of trainable parameters for a configuration. Where configuration embraces the available training data and the chosen hyper-parameters for SMSnet. The layers initially had about 2x as many filters as they have in Figure 7.3. The therefore higher number of trainable parameters was successively reduced until the reconstruction worsened. Thereafter, an about 10% re-increased number of parameters provided robust reconstructions for different test data.

A filter size of 250 at each input was considered appropriate for the multiplicative merge, because it ensured enough complexity to represent channels and their weighting in the given dataset. A larger filter size did not improve the reconstruction noticeably, but required additional GPU memory.

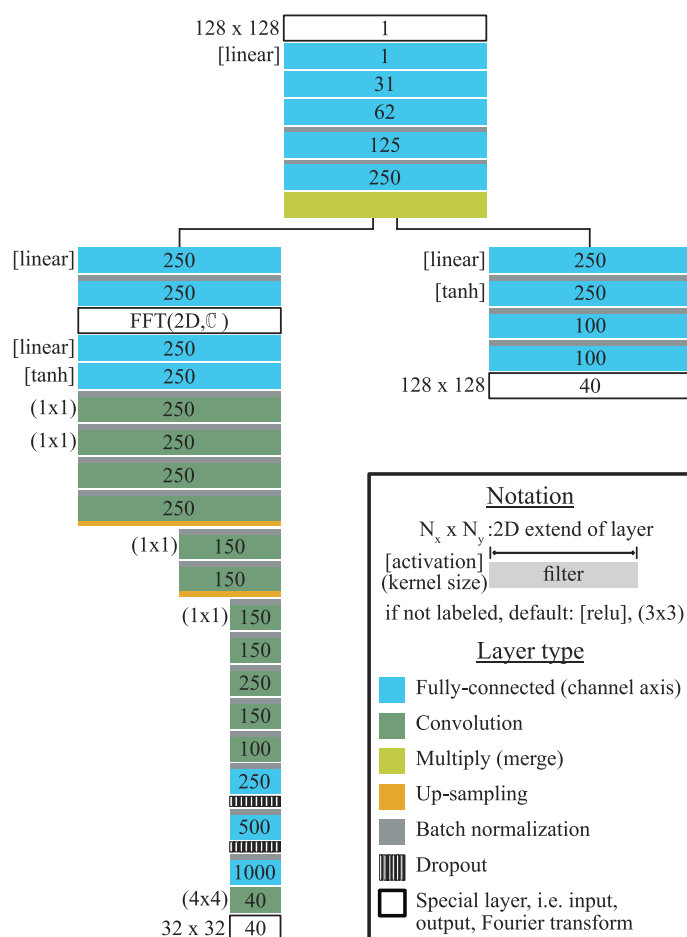


Figure 7.3: Architecture of SMSnet. The 20-channel complex input data are split into their real and imaginary components which are then concatenated along the channel dimension resulting in 40 input channels. In the left branch, CoS-path, features similar to coil sensitivities are derived from reduced k-space data (size: $32 \times 32 \times 40$). These are then merged by element-wise multiplication with the input image data (size: $128 \times 128 \times 40$) after passing the right branch, Im-path, similar to the unfolding process in SG. The last section, Merge-path, reduces the number of channels. The combined channels yielding a single magnitude image per slice at the output (size: 128×128) of SMSnet.

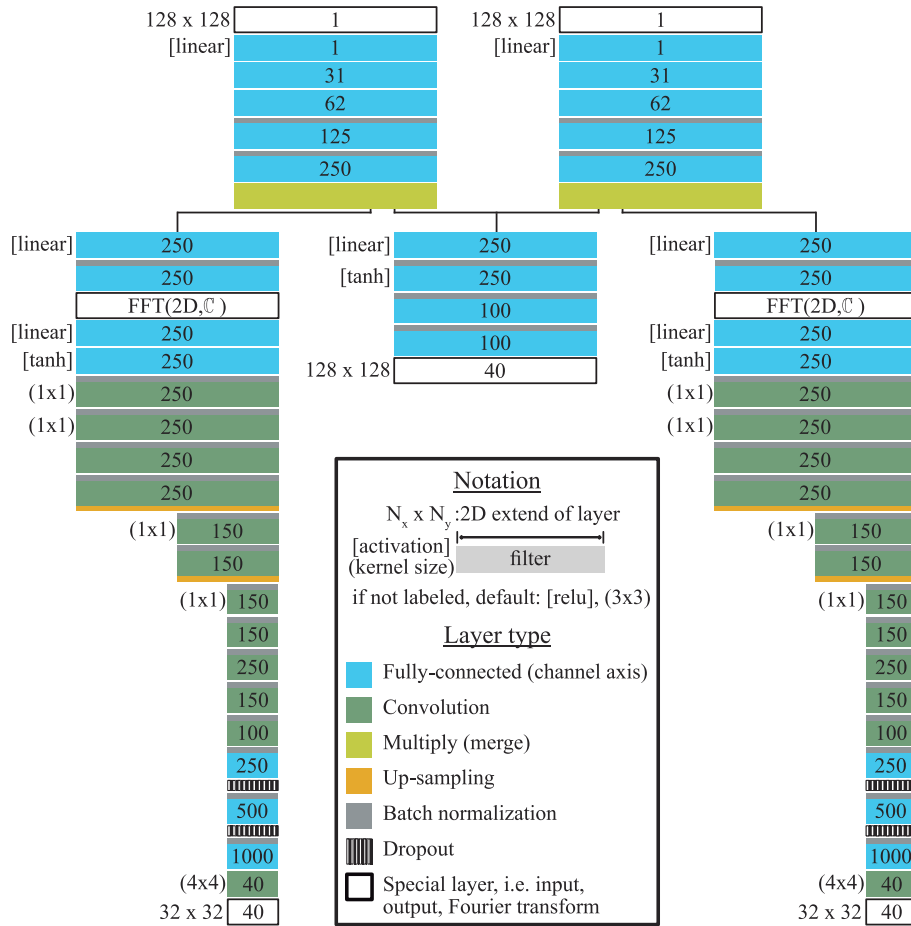


Figure 7.4: Architecture of SMSnet for $MB = 2$. Therefore, the network is extended to two CoS-paths and two Merge-paths while the single image input remains.

7.3 Data for Training and Testing

The presented technique for SMS reconstruction requires a sufficiently large amount of data for training, validation during training and testing of the trained NN.

All data were acquired with the identical 20-channel head coil which was positioned centrally to B-field isocenter. Data were acquired with SB measurements (without SMS) to focus on the reconstruction itself and reduce interference, i.e. artifacts related to the SMS acquisition sequence. The scanned objects can be categorized into two groups:

1. Data taken from a wide range of different phantoms which contrasts and dielectric properties are expected to differ significantly. The phantoms have been made of five different fruits (banana, cucumber, grapefruit, grapes, pomelo), three water phantoms (with and without structured elements), one oil-phantom, two geometric (cylindric, spherical) and one structured precision phantom(s) manufactured by the MR system's vendor (Siemens Healthcare, Erlangen, Germany) and another structured precision phantom (Pro MRI, Pro-Project, Okszow, Poland).

2. In-vivo data, in particular, MR-measurements of human heads which have been acquired in five healthy volunteers (25 - 47 years of age). Ethical approval was provided by the ethics committee of the University Bremen on 10. Mai 2011 ("MR-Messungen im Rahmen der Lehrveranstaltungen").

Data of group 1 were arranged geometrically different and in various combinations. In total, 33 pseudo different objects were scanned separately and used for training ($N_{\text{train,p}} = 22$) and validation ($N_{\text{val,p}} = 6$). Data of the spherical phantom ($T_1 = 290$ ms) and the Pro MRI structured precision phantom were used exclusively for testing ($N_{\text{test,p}} = 2$). Repositioning and sequence changes during in-vivo measurements for group 2 yielded a total of ten scans ($N_{\text{train,iv}} = 6$, $N_{\text{val,iv}} = 4$). Datasets of two volunteers were restrained from training and served as test data ($N_{\text{test,iv}} = 7$). The conducted measurements were carried out as 2D GRE SB acquisitions with six slices ($\Delta z = 5$ mm, 300% gap) or as 3D scans (1 mm isotropic). Volumetric 3D data, acquired with a magnetization prepared rapid gradient echo (MPRAGE) sequence, were preprocessed into pseudo 2D data with 202 slices. An overview of the protocol parameters and the objects associated with either sequence is give in Appendix A.4. It is assumed, that data used for training 'share the same MR system specific properties'. In particular, CoS are related, whereas the objects themselves differ in shape, volume and positioning as well as signal strength, image contrast and homogeneity.

The steps for data preparation are illustrated in Figure 7.5. First, source data were generated. Therefore, slices which correspond to the same MB slice group were selected from the loaded dataset. Data were synthesized to SMS source data in k-space and image domain with $\text{FOV}_{\text{shift}} = 1/2, 1/3, 1/4, 1/5, 1/6$ for $MB = 2$, $\text{FOV}_{\text{shift}} = 1/3, 1/4, 1/5, 1/6$ for $MB = 3$ and $\text{FOV}_{\text{shift}} = 1/4, 1/5, 1/6$ for $MB = 4$, respectively. k-space data were reduced from a size of 128×128 to 32×32 to mimic ACS and account for the smooth variation of the CoS. Source data in image domain were stored with a resolution of 128×128 , which was considered 'full resolution'. Second, the corresponding counterpart of SB slices serving as target data were CAIPIRINHA-shifted accordingly. Third, the procedures above were repeated in a data augmentation step. In order to augment data to the nine fold, the resolution of the full raw data (128×128 k-space matrix) was reduced to 90%, 80%, 75%, 70%, 60%, 50%, 40%, 30%. Cropped k-space data were filled with zeros to recover consistent image matrices of 128×128 for all data. Finally, pairs of source and target data were saved under a unique identifier to allow the data handler to randomly select training and validation data during training. A summary of the database generated can be found in Appendix A.6.

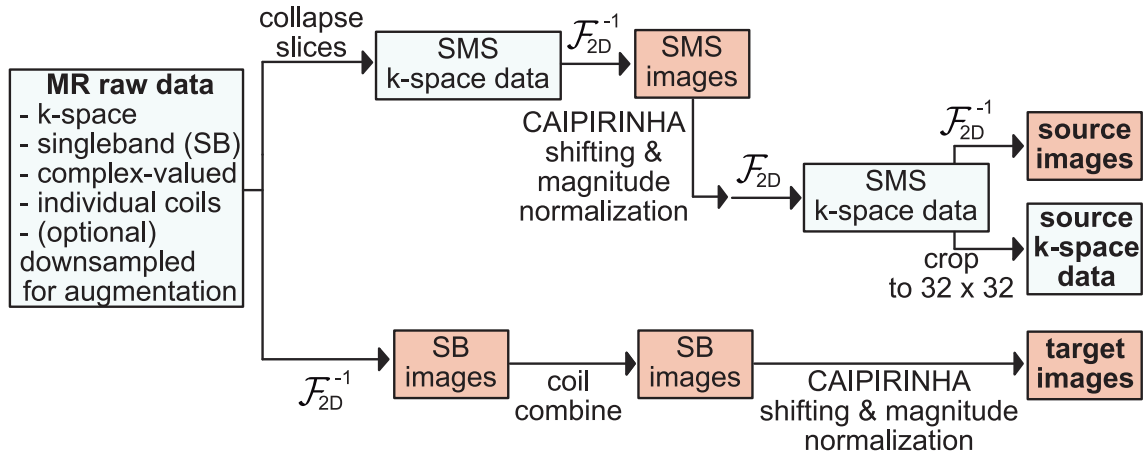


Figure 7.5: MR raw data were prepared in several steps to provide normalized and CAIPIRINHA-shifted source and target data for SMSnet. The preparation steps were repeated for different resolutions. Therefore, MR raw data were downsampled beforehand in k-space yielding different image resolutions.

7.4 Training of SMSnet

Data were randomly selected in pairs (source and target) by a data handler. The data handler normalized input and output data according to

$$|I| = \frac{|I| - \min(|I|)}{\max(|I|) - \min(|I|)} \quad (7.1)$$

to ensure a consistent range of values, where $|I|$ represents the magnitude of the complex-valued images for all coils. Normalization was performed in image domain, therefore, the k-space data are Fourier transformed twice. The network itself was loaded into the GPU’s memory before start of the training. Thereafter, a predefined number training and validation data pairs were loaded and processed simultaneously. The size of the training and validation batch varied with the MB factor due to the GPU’s memory limit of 8GB. Weights were initialized with a so-called *glorot uniform* distribution and identical seeds for all trainings [GB10]. Trainings were run with Adam (Sec. 6.2.1). Therefore, the definition of a global learning rate decay is unnecessary [KB15]. The MSE loss is a common choice for regression problems. It was combined to a multiplicative loss function

$$E_{TV \times MSE} = TV \times E_{MSE} \quad (7.2)$$

according to Equations 6.7, 6.8. Both norms, MSE and TV, are known in MRI reconstructions to account for pixel-by-pixel difference and sparsity [Lus+08]. No weight regularization was applied during the final trainings. Table A.6 in the appendix gives a tabular overview of the trainings.

7.5 Evaluation of Reconstructions with SMSnet

The evaluation of SMS reconstructions predicted by SMSnet was done in a visual manner, i.e. maps which show a representative set of slices, and quantitatively by mean values of specific metrics in analogy to the evaluation in Part II (Eq. 4.3). These were compared to different reconstructions with SSG.

Images were slice-wise normalized according to Equation 7.3 before plotting. Magnitude images after coil combination I_s for slice s are hence scaled to

$$I_s = \frac{I_s - \min(I_s)}{\max(I_s) - \min(I_s)} . \quad (7.3)$$

This ensures similar ranges of values also for non-SMSnet images to be compared. The reference images a and the images after SMS reconstruction y , either by SMSnet or with SSG, were compared with four metrics.

First, absolute pixel-wise differences normalized to

$$D = \left| \frac{y - a}{a} \right| \quad (7.4)$$

were plotted as maps and, in relation to the absolute difference, the MSE between a and y was calculated (Eq. 6.7) and averaged across all slices of a volume.

The second metric is introduced to assess the perceptual image quality by taking advantage of characteristics of the human visual system [Wan+04]. The structural similarity index (SSIM) is defined as

$$SSIM(y, a) = L(y, a) \cdot C(y, a) \cdot S(y, a) \quad (7.5)$$

where L , C , S are luminance, contrast and structure comparison for a and y [Wan+04]. These components are derived from the mean intensity over all N pixels

$$\mu_I = \frac{1}{N} \sum_{i=1}^N I_i , \quad (7.6)$$

the standard deviation

$$\sigma_I = \sqrt{\frac{1}{N-1} \sum_{i=1}^N (I_i - \mu_I)^2} \quad (7.7)$$

for the reference image $I = a$ and the reconstructed SMS image $I = y$ and the covariance of a and y

$$\sigma_{y,a} = \frac{1}{N-1} \sum_{i=1}^N (y_i - \mu_y)(a_i - \mu_a). \quad (7.8)$$

Therewith, for tow images, luminance comparison is taken from

$$L(y, a) = \frac{2\mu_y\mu_a + C_1}{\mu_y^2 + \mu_a^2 + C_1}, \quad (7.9)$$

contrast comparison is calculated with

$$C(y, a) = \frac{2\sigma_y\sigma_a + C_2}{\sigma_y^2 + \sigma_a^2 + C_2} \quad (7.10)$$

and structure is compared by

$$S(y, a) = \frac{\sigma_{y,a} + C_3}{\sigma_y\sigma_a + C_3}. \quad (7.11)$$

C_1 , C_2 and $C_3 = C_2/2$ are constants to regularize for division with weak denominator and scale the components with respect to the range of discrete values in the images. As above, SSIM was slice-wise determined before a mean SSIM across all slices of a volume was calculated. SSIM is a quality measure and a value of 1 represents the maximum equality of the two input images a and y . For visualization purposes, the SSIM maps were recalculated to $|1 - SSIM|$ to be in agreement with the subtraction maps, where low values correspond to a high agreement between reference and SMS reconstruction.

The third metric is the mean correlation between the reconstructed slice image I_s and the corresponding reference slice image $I_{s,\text{REF}}$. This is denoted as intra-slice correlation $\text{corr}(I_s, I_{s,\text{REF}})$.

Finally, the fourth metric is the inter-slice correlation, which is only available for $MB = 2$. It calculates the mean correlation between the two simultaneously acquired slices after the separation procedure $\text{corr}(I_s, I_{s+(N_s/MB),\text{REF}})$. FOV-shifts have to be considered for this inter-slice correlation calculation.

Metrics were computed with the scikit-image toolkit [Wal+14] (MSE, SSIM) and SciPy [JOP+01] ($\text{corr}(I_s, I_{s,\text{REF}})$, $\text{corr}(I_s, I_{s+(N_s/MB),\text{REF}}$). Results were given in tabular form as mean values. For objects with a significant oversampling along the slice direction, many slices did not contain a true signal. Hence, statistics were additionally calculated for 'inside object slices'. Meaning slices which covered the object were considered while slices in oversampling regions were neglected.

The predicted SMS reconstructions by SMSnet were compared to SSG. Different

scenarios for SSG were considered to address the 'referenceless reconstruction' aspect of SMSnet which is one of the key ideas behind and motivation for it. Therefore, SSG reconstructions with correct ACS were performed as well as reconstructions where correct ACS data were missing or corrupted. Missing or corrupted ACS data were replaced by ACS from other measurements but with similar protocol settings. The following scenarios on 'how ACS are provided' were compared:

- SSG_{std} , with correct ACS of the same acquisition indicated by the subscript 'std'.
- SSG_{01} , with averaged ACS data of multiple measurements (phantom and in-vivo). The subscript '01' indicates this setting.
- SSG_{avg} , with averaged ACS data of other head scans indicated by the subscript 'avg'.

ACS data used for averaging were identical to training and validation data for SMSnet. Two sets of averaged ACS were available, one set for which a GRE sequence acquired 6 transversal slices with a inter-slice distance of 15 mm ($\Delta z = 5$ mm, 300% gap) and another set acquired with a MPRAGE sequence transferred to 202 transversal slices (1 mm isotropic). All data processed for averaging were normalized to ensure equal influence in the compound ACS.

The basic reconstruction principle of SMSnet was examined on in-vivo test data taken from a MPRAGE measurement of a volunteer (male, 33 years). Furthermore, different experiments on phantom and in-vivo data were investigated as described below. SMS data were synthesized for $MB = 2$ with $FOV_{\text{shift}} = 1/4$, if not mentioned otherwise, to guarantee significant slice overlap also for smaller objects. However, higher MB factors ($MB = 3$, $MB = 4$) were explored as well in Section 7.6. The following, experiments were conducted to investigate different aspects of SMSnet reconstructions.

Phantom Experiments: Different phantom data were reconstructed by SMSnet. A spherical phantom (GRE, $T_1 = 290$ ms) was measured and its reconstruction analyzed to evaluate potential overfitting of the network. Therefore, SMSnet was trained twice, with and without, training data of a cylindrical phantom (GRE, $T_1 = 106$ ms). Improved reconstruction performance of SMSnet if cylindrical data were included during training would indicate overfitting, because slices of both phantoms appear similar in 2D. A structured phantom (MPRAGE) was used to evaluate the reconstruction of homogeneous objects with sharp edges and defined structures. An artificial spherical phantom with noise-like structure was generated from real data (spherical phantom above, GRE) to reflect true receiver characteristics to which

complex Gaussian-like noise was added to challenge SMSnet reconstruction with fine, irregular and unknown patterns. The fourth phantom consisted of two oval bottles filled with water-based (shower-) gel placed bilateral at the outer border of the head coil (ears region) to mimic an extreme object variation. Gel phantoms were scanned with the GRE sequence.

Noise propagation and Signal Sensitivity: The spatially varying, reconstruction related noise amplification in SMS can be characterized by the g-factor delivered by the PMRM [KM05; Rob+08]. Coverage of the acquired test data mimic a whole head scan in 6 slices ($\Delta z = 5$ mm, 500 % gap). Five repeated GRE measurements yielded a ‘noise-free’ ground truth image REF after averaging. PMRM was run for 100 repetitions from which SMS data were synthesized with $MB = 2$, $FOV_{\text{shift}} = 1/4$. These SMS data were fed into four different reconstructions: SMSnet, SSG_{std} , SSG_{01} and SSG_{avg} .

In contrast to signal stability, the sensitivity of the reconstruction to small signal variations was evaluated in two successive fMRI experiments. Time series of BOLD signal induced by bilateral finger tapping were compared for successively acquired SB and SMS ($MB = 2$, $FOV_{\text{shift}} = 1/2$) data. A multi-echo (TE = 8.6 / 19.1 / 30 ms), segmented EPI sequence (ETL = 13) was run in SB (3 slices, $\Delta z = 5$ mm, 100 % gap) and SMS (6 slices, $\Delta z = 5$ mm, 100 % gap) mode for 132 s (TA = 1.1 s, 120 measurements) while the volunteer (male, 31 years) performed finger tapping (paradigm: 20 s [rest] / 20 s [active]). Image time series were reconstructed for SB, SSG_{std} and SMSnet, respectively. BOLD dynamics were calculated after signal separation into S_0 and T_2^* by a mono-exponential fit (Eq. 4.2) using the Levenberg-Marquardt algorithm implemented in MeVisLab (MeVis Medical Solutions AG, Bremen, Germany) [PN09; EGL14]. Resulting T_2^* -dynamics were analyzed in NeuroQLab (MeVis Medical Solutions AG, Bremen, Germany) using a design matrix corrected for hydrodynamic responses (DMhr) and statistical evaluation from the generalized linear model (GLM) ($p = 0.025$, no spatial or temporal filters, no linear detrending) [Wei+09; 18]. Pearson correlations of voxel-averaged signal dynamics were calculated pairwise for all three reconstructions.

In here, all reconstructed images were masked for plotting to remove distracting background.

Severe Changes in the Coil Sensitivity Profile: Experiments simulate changes in CoS profile which can also be induced, e.g. by objects with high susceptibility variations. The CoS was perturbed, i.e. by replacing the signal content of one and four coil(s) with Gaussian noise (noise-level 5 % of maximal signal strength). Affected coils were located in the top anterior positions of the head coil.

Motion: In-vivo experiments in which the volunteer (male, 33 years) simulated inter-repetition head motion. The volunteer turned his head in the transversal plane. The GRE scans were repeated for five different head positions, #0 to #4, and SMS data were synthesized for $MB = 2$ with $FOV_{\text{shift}} = 1/4$. ACS for SSG were taken from data at position #0.

Synthesized and Acquired SMS Data: SMS data used were synthesized from SB data, because this part of the work focuses on the mere reconstruction. Synthetic SMS data allow versatile CAIPIRINHA patterns and ensure correct reference data for evaluation. However, synthetic and acquired SMS data were compared here to validate real world scenarios. Images after SSG_{std} reconstruction were taken for reference to guarantee identical underlying data also for the acquired SMS data. Hence, subtraction and SSIM maps were produced to investigate possible influences of the acquisition process.

Cross-System Validation: Cross-system experiments were performed to explore the transferability of a trained DNN. Here, SMSnet was trained with data of one specific MR system (MAGNETOM Skyra at University Bremen, Siemens Healthcare, Erlangen, Germany) and used to reconstruct data which were acquired with another, but identically equipped MR system (3 T, 20-channel head coil, MAGNETOM Skyra at ZEMODI Bremen, Siemens Healthcare, Erlangen, Germany).

7.6 Higher Acceleration Factors

Synthetic SMS with higher acceleration factors were reconstructed with SMSnet. Therefore, SMSnet’s modular architecture was extended by additional CoS-paths according to the MB factor. Further details on training data and settings are given in Table A.5 in the appendix. In particular, data for $MB = 3$ with $FOV_{\text{shift}} = 1/3$ and $MB = 4$ with $FOV_{\text{shift}} = 1/4$ were tested and compared to the reference images for eight representative slices. Similar to the previous experiments in Section 7.5, the reconstructions with SMSnet were then compared to SSG reconstructions with and without correct ACS.

7.7 Layer Activations

To investigate the learned features in the hidden layers, the activations of the layers before and after the merge layer were extracted after training. As illustrated in Figure 7.3, the merge layer performs element-wise multiplication of tensors from the CoS- and the Im-path before the number of channels is reduced. Test data of a human head (MPRAGE) were synthesized to SMS data with $MB = 2$ ($FOV_{\text{shift}} = 1/4$) and shifted along posterior to anterior direction only. The CAIPIRINHA pattern in the

training data was reduced to the same direction, which is in contrast to trainings for previous experiments. However, the reduced complexity in FOV-shifting will ease recognition of any shift-depended patterns.

7.8 Manipulation of Input Data

The following experiments were conducted to analyze the robustness of a trained SMSnet to variations in the input data. Therefore, input data were manipulated in a controlled manner. Four cases of input manipulation were tested.

- Zeros for k-space: Input k-space data were set to zero $IN_{ks} = 0$.
- Ones for k-space: Input k-space data were set to one $IN_{ks} = 1$.
- Noise for k-space: Input k-space data were replaced with Gaussian noise.
- Noise for k-space and image: Data in both input tensors, k-space and image, were replaced with Gaussian noise.

8 Results: Referenceless SMS

Reconstruction by Neural Networks

This chapter summarizes the results from various in-vivo and phantom experiments which were run to explore the potential of SMSnet. Quantitative results were given in tabular form. The mean values across all slices of the acquired volume accompanied by the resulting standard deviation. Because CAIPIRINHA-related shifting may result in aliasing artifacts, masking was not applied. Therefore, background signal was included into the calculation of metrics which, in general, increased standard deviations.

A summary of the training details is given in Appendix A.6 in addition to information provided in Chapter 7.

8.1 Image Quality

This section covers the general reconstruction performance of SMSnet and how SMSnet was evaluated under various aspects. Figure 8.1 shows the collapsed and CAIPIRINHA-shifted slices at the Im-input are shown after coil combination (a). The target and reference images REF without SMS is displayed in (b) for direct comparison to the predicted reconstructions by SMSnet (c). CAIPIRINHA-shifting was reversed after reconstruction by SMSnet.

A reduced number of slices is shown for most of the later experiments in this section to guarantee plots with sufficient details. The input test data for SMSnet were taken from synthetic SMS data with $MB = 2$ and $FOV_{\text{shift}} = 1/4$ if not labeled otherwise. Despite the reduction of test data to $FOV_{\text{shift}} = 1/4$, SMSnet was trained with different CAIPIRINHA patterns simultaneously. However, training with shifts in opposite directions yield worse reconstruction results. Therefore, the combinations for training data were constrained to shifts either along anterior to posterior and left to right directions or both combinations vice versa.

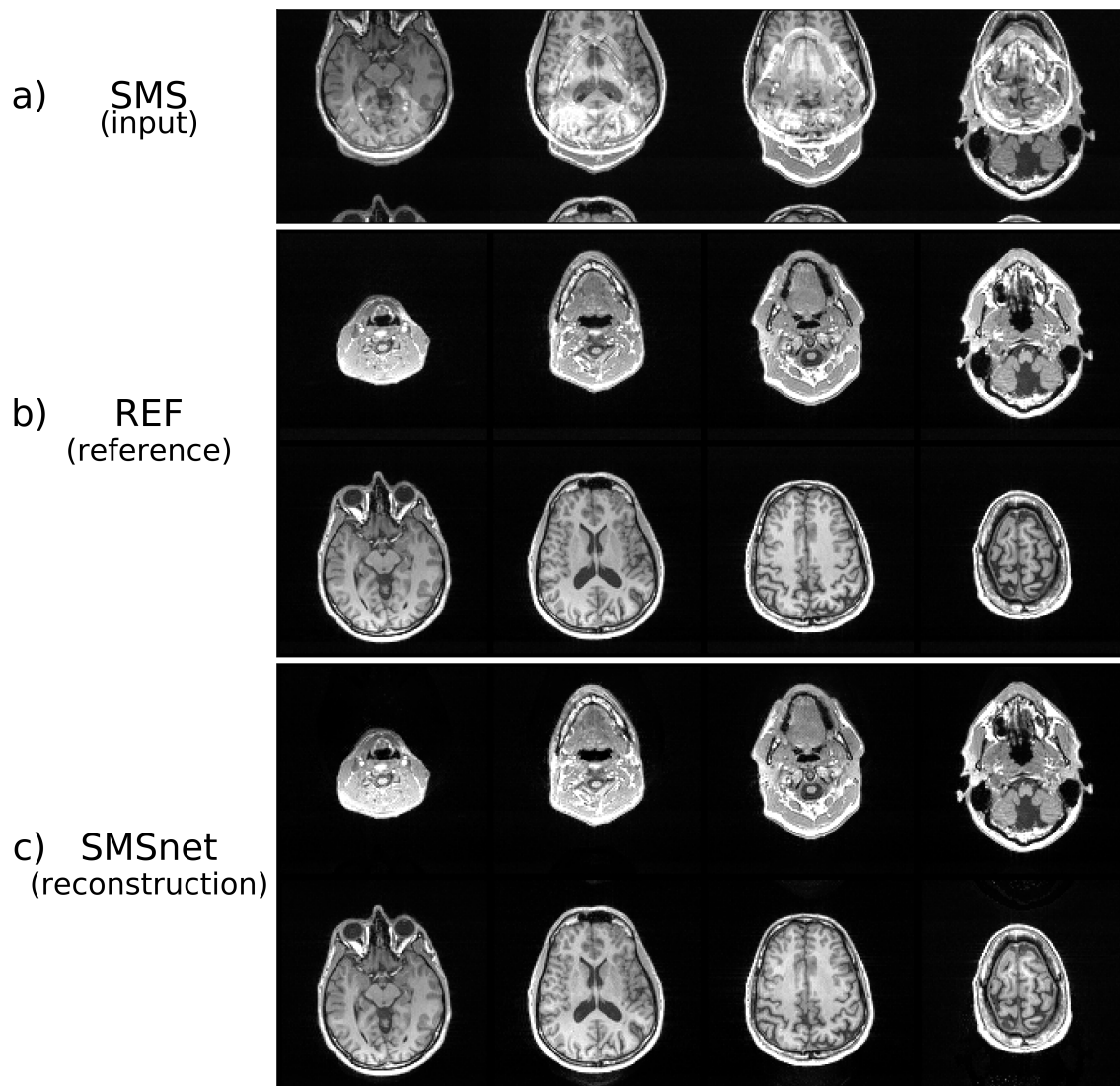


Figure 8.1: a) The coil combined input SMS images show the overlap of two simultaneously acquired slices with a CAIPIRINHA-shifting of $FOV_{\text{shift}} = 1/4$. b) The reference images REF were acquired and reconstructed without any SMS acceleration. Eight representative slices out of $N_s = 202$ slices are compared to the prediction made by SMSnet (c). CAIPIRINHA-shifting was reversed in (b) and (c). Data were acquired with a MPRAGE sequence ($\Delta z = 1$ mm, no gap).

8.1.1 Comparison with Established Reconstruction Strategies

The predictions of SMSnet are compared to SSG reconstructions. This allows evaluation of the reconstruction performance in relation to established methods.

Figure 8.2 shows the comparison of reconstructions with SMSnet and SSG in a single slice. As described in Section 7.5, the SSG reconstructions were performed for three different sets of ACS. These were: correct ACS (SSG_{std}), ACS averaged from phantom and in-vivo data (SSG_{01}) and ACS which originate from other in-vivo data, i.e. head scans, (SSG_{avg}) only.

The image quality for the reconstruction by SMSnet does not suffer from any obvious SMS artifacts and details, e.g. parts of the ears (Fig. 8.1) or shape of gyri (Fig. 8.2), are recovered correctly. Artifacts are visible in homogeneous regions without much contrast, for example in the white matter close to the ventricles in the zoomed view in Figure 8.2 (b). These are not observed in the standard SSG reconstruction. The reconstructions with SSG_{01} and SSG_{avg} show similar artifacts like SMSnet, but, in addition, more remaining additional signal from overlapping slices is visible in the background. This is clearly visible in the absolute difference maps in Figure 8.3. Pixel-wise subtraction reveals clear reconstruction errors for all cases apart from SSG_{std} . Figure 8.4 illustrates the SSIM of these slices and how similar reference and SMS reconstruction may be perceived despite artifacts. Here, SMSnet performs second best after SSG_{std} (Tab. 8.3).

The reconstructions are also quantified with the mean values of MSE and SSIM calculated across all slices of the volume. These values are listed along with results of other experiments in Table 8.3. In relation to SSG_{std} , these results correspond to 2% (1%, 11%) increase in MSE for SMSnet (SSG_{01} , SSG_{avg}). SMSnet performs best in terms of SSIM and results in a 3% increased mean SSIM in comparison to SSG_{std} . However, also SSG_{01} yields a 1% increment in SSIM compared with SSG_{std} while SSG_{avg} and SSG_{std} perform almost identically. The mean intra-slice correlation is highest for the SSG_{std} reconstruction with $\text{corr}(I_s, I_{s,REF}) = 0.98$ while all other reconstructions yield a mean value of about 0.97. However, slice leakage quantified by the intra-slice correlation $\text{corr}(I_s, I_{s+(N_s/MB),REF})$ is reduced in SMSnet (0.31) compared to SSG_{std} (0.33), SSG_{01} (0.38) and SSG_{avg} (0.37).

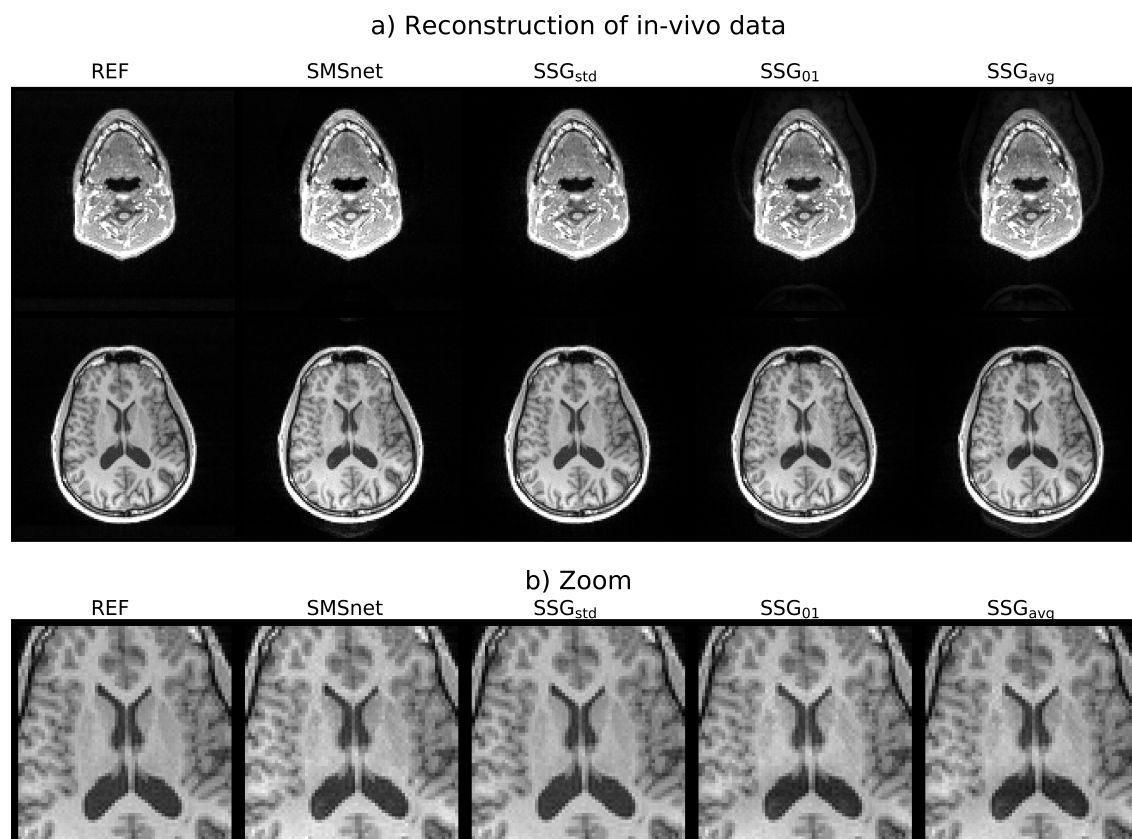


Figure 8.2: a) The comparison of predictions by SMSnet with the corresponding reference REF and different SSG approaches. Standard SSG with correct ACS data is shown in column three (SSG_{std}), whereas column four and five show reconstructions where correct ACS was not available and SSG was performed with ACS from other objects. These were averaged from phantom and in-vivo data (SSG_{01}), or in-vivo, i.e. head scans, (SSG_{avg}) only. b) The zoom allows inspection of some artifacts in proximity to the ventricles. Data were acquired with a MPRAGE sequence to synthesize SMS data with $MB = 2$ and $FOV_{shift} = 1/4$.

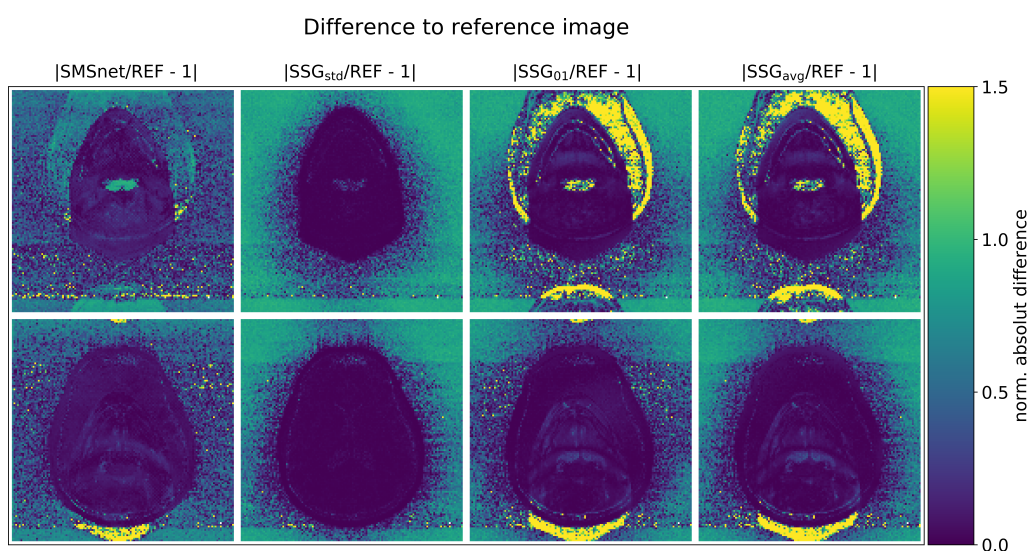


Figure 8.3: The absolute differences on pixel-level are shown for reconstructions with SMSnet and different SSG reconstructions. Images were normalized by REF.

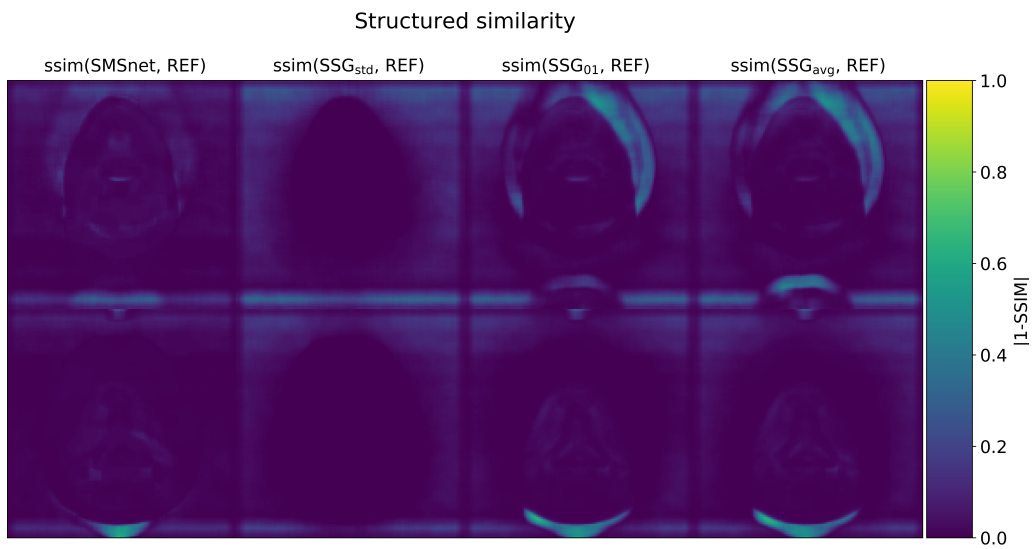


Figure 8.4: SSIM maps of the reconstructions with SMSnet and different SSG reconstructions are shown. These maps are recalculated to $|1 - SSIM|$ for intuitive visualization and, therefore, low pixel values correspond to a high agreement with respect to SSIM.

8.1.2 Reconstruction of Phantom Data

Images of four phantom objects were reconstructed with SMSnet and compared to SSG.

Data of a spherical phantom were acquired with a GRE sequence. For presentation, only one slice out of six slices is shown in Figure 8.5. The spherical phantom is homogeneously filled with doped water as seen in the reference image (REF). Shading from the overlapping slices appears in the reconstruction with SMSnet, which is not present in a correctly performed SSG reconstruction (SSG_{std}). However, if appropriate ACS is not available (SSG_{01} , SSG_{avg}), the slice separation with SSG is incorrect and overlapping signal leads to artifacts. The mean values of the introduced metrics confirm this observation. While MSE increases by several 100 % for SMSnet, SSG_{01} and SSG_{avg} (Tab. 8.1), the mean SSIM appears more robust and decreases by 1 % (SMSnet), 6 % (SSG_{01}) and 9 % (SSG_{avg}), respectively. The mean intra-slice correlations $\text{corr}(I_s, I_{s,REF})$ are about 1 for all cases (Tab. 8.3), but intra-slice correlation $\text{corr}(I_s, I_{s+(Ns/MB),REF})$ is reduced in SMSnet (0.18), compared to SSG_{std} (0.2), SSG_{01} (0.23) and SSG_{avg} (0.27). A second training without training data of a cylindrical phantom yielded similar results as listed in Table 8.1. Figures were omitted for these results as they were in agreement with the results shown.

The approaches perform well on test data of a structured precision phantom (Pro MRI, Pro-Project, Okszow, Poland), if inspected visually as depicted in Figure 8.6. Data were acquired with a MPRAGE sequence and unchanged protocol parameters, such that the FOV exceeded the object boundaries along slice direction. Thus, several transversal slices contain no true signal but only noise. All reconstructions of synthetic SMS data lead to reconstruction-related signal leakage into these regions outside the object, this results in higher mean error values. Inside-object slices were evaluated in a subset of 112 out of 202 slices to allow reliable calculation of MSE, SSIM, and $\text{corr}(I_s, I_{s,REF})$ for the phantom. However, for the calculation of $\text{corr}(I_s, I_{s+(Ns/MB),REF})$ all 202 slices were considered to quantify slice leakage into outside-object regions. The results in Table 8.2 indicate that SMSnet performs second best after SSG_{std} for MSE and SSIM. Furthermore, SMSnet shows high intra-slice correlation of 0.997 and low inter-slice correlation -0.172 .

An artificial phantom with fine, highly irregular (noise-like) structures is shown in Figure 8.7. The base-data derived from the spherical phantom above and the artificial noise-like patterns are unknown to SMSnet, but can be recovered reasonably well when compared to the other approaches. Quantitative evaluation, apart from the mean intra- and inter-slice correlations, as well as the subtraction maps were moved to the appendix (Fig. A.11, Tab. A.2), because the fine, irregular patterns can be compared well visually in a zoomed view (Fig. 8.7 (b)). Partial sub-patterns of gray-scale values can be directly identified in all four reconstructions for regions

without any overlapping slice signal. Even though the signal propagates correctly through the DNN, pixel values vary slightly in overlap regions, because of inter-slice signal leakage. While SSG_{std} recovers the patterns most accurately, SMSnet reconstruction shows minor variations in individual pixels whereas reconstructions with SSG_{01} and SSG_{avg} result in more pronounced signal leakage and, hence, changed patterns. The difference maps in Figure 8.8 show the remaining signal of overlapping slices for SMSnet, SSG_{01} and SSG_{avg} . However, in comparison to slice-GRAPPA approaches without correct ACS, SMSnet clearly reduces the leakage artifacts. The background signal of these data was on a low level, which led to different scaling after normalization and should be noticed for interpretation of the results. Intra-slice correlations are similar: 1 (SSG_{std}), 0.99 (SMSnet), 0.99 (SSG_{01}) and 0.99 (SSG_{avg}), while inter-slice correlation is reduced in SMSnet (0.2) compared to SSG_{01} (0.22) and SSG_{avg} (0.23).

Images of two gel phantoms placed at bilateral positions at the head coil’s borders as shown in Figure 8.9. While SMSnet and SSG_{std} reconstruct the objects without any obvious slice leakage, remaining signal from overlapping slices is visible for SSG_{01} and SSG_{avg} . Furthermore, the image contrast is attenuated in the right gel phantom after SSG_{01} and SSG_{avg} reconstructions. These artifacts are also reflected in the quantitative evaluation. SSG_{std} results in the lowest $\text{MSE} = 0.38 \cdot 10^{-4}$, this error is increased to $1.97 \cdot 10^{-4}$ for SMSnet, but SSG_{01} and SSG_{avg} yield higher mean values for MSE: $8.54 \cdot 10^{-4}$ and $27.5 \cdot 10^{-4}$. The mean SSIM is on comparable level for all reconstructions: 0.93 (SSG_{std}), 0.92 (SMSnet), 0.94 (SSG_{01}) and 0.92 (SSG_{avg}). Intra-slice correlation $\text{corr}(I_s, I_{s,\text{REF}})$ confirms that SMSnet (0.98) outperforms SSG_{01} and SSG_{avg} with correlations of 0.92 and 0.77, respectively. SSG_{std} yields an intra-slice correlation of 1. In contrast, absolute values of inter-slice correlations $\text{corr}(I_s, I_{s+(N_s/\text{MB}),\text{REF}})$ are comparable for SSG_{std} (-0.02) and SMSnet (0.02), but significantly higher for SSG_{01} (0.2) and SSG_{avg} (0.4).

Omitted evaluation results, e.g. plots and quantification, for all experiments in this part were available in Appendix A.5.1 to complete evaluation.

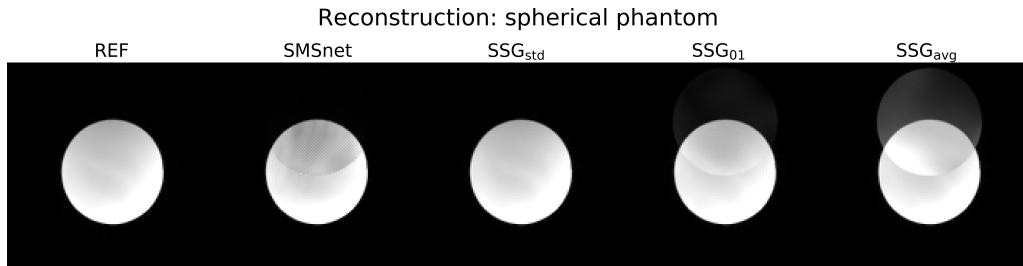


Figure 8.5: Phantom data were acquired on a homogeneous spherical phantom using a GRE sequence. SMS data were synthesized for $MB = 2$ and $FOV_{\text{shift}} = 1/4$. Images of only one out of six slices (300% gap, GRE) are shown above. The reference image is compared to the predicted reconstruction with SMSnet (columns 1 and 2). Images after SSG reconstructions, with and without correct ACS, are displayed as well (columns 3, 4 and 5).

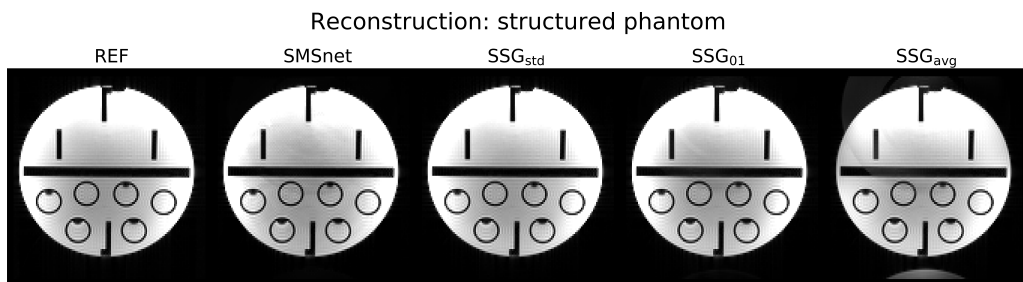


Figure 8.6: Reconstructions of data acquired in a structured, precision phantom are shown for one out of 202 slices ($\Delta z = 1$ mm, no gap, MPRAGE). The correct recovery of image details can be evaluated easily apart from SSG_{avg} where remaining signal of the overlapping slice is visible.

Spherical phantom					
Mean values across volume					
	SMSnet	SMSnet	SSG _{std}	SSG ₀₁	SSG _{avg}
	w/	w/o			
MSE [10^{-3}]	0.4 ± 0.15	0.26 ± 0.09	0.01 ± 0.002	0.49 ± 0.27	1.6 ± 1.18
SSIM [10^{-1}]	9.78 ± 0.11	9.8 ± 0.07	9.9 ± 0.07	9.22 ± 0.39	8.98 ± 0.4
$\text{corr}(I_s, I_{s,\text{REF}})$ [10^{-1}]	9.98 ± 0.005	9.99 ± 0.003	1 ± 0.0002	9.97 ± 0.023	9.91 ± 0.057
$\text{corr}(I_s, I_{s+(N_s/MB),\text{REF}})$ [10^{-1}]	1.83 ± 0.16	1.93 ± 1.8	2.02 ± 0.002	2.32 ± 0.22	2.7 ± 0.38

Table 8.1: Evaluation of SMSnet reconstruction in comparison with SSG on data acquired in a spherical phantom. The mean values of MSE and SSIM across all six slices are given as well as the intra- and inter-slice correlations. SMSnet was trained twice: with (w/) and without (w/o) training data of a cylindrical phantom.

Structured phantom				
Mean values across volume				
Inside-object slices only for MSE, SSIM and $\text{corr}(I_s, I_{s,\text{REF}})$				
	SMSnet	SSG _{std}	SSG ₀₁	SSG _{avg}
MSE [10^{-3}]	0.26 ± 0.515	0.05 ± 0.27	1.03 ± 6.42	14.91 ± 15.62
SSIM [10^{-1}]	9.88 ± 0.36	9.93 ± 0.27	9.81 ± 0.78	8.68 ± 1.33
$\text{corr}(I_s, I_{s,\text{REF}})$ [10^{-1}]	9.97 ± 0.16	9.99 ± 0.05	9.85 ± 1.02	9.4 ± 1.47
$\text{corr}(I_s, I_{s+(N_s/\text{MB}),\text{REF}})$ [10^{-1}]	-1.72 ± 0.59	-0.074 ± 0.86	1.26 ± 0.93	2.92 ± 1.32

Table 8.2: Evaluation of SMSnet reconstruction in comparison with SSG on data acquired in a structured precision phantom. The mean values of MSE and SSIM across 112 out of 202 slices are given. This subset of slices was selected to avoid prominent contribution of noise-only slices because of oversampling along slice direction. All 202 slices were considered for calculation of $\text{corr}(I_s, I_{s+(N_s/\text{MB}),\text{REF}})$ to quantify slice leakage into outside-object regions.

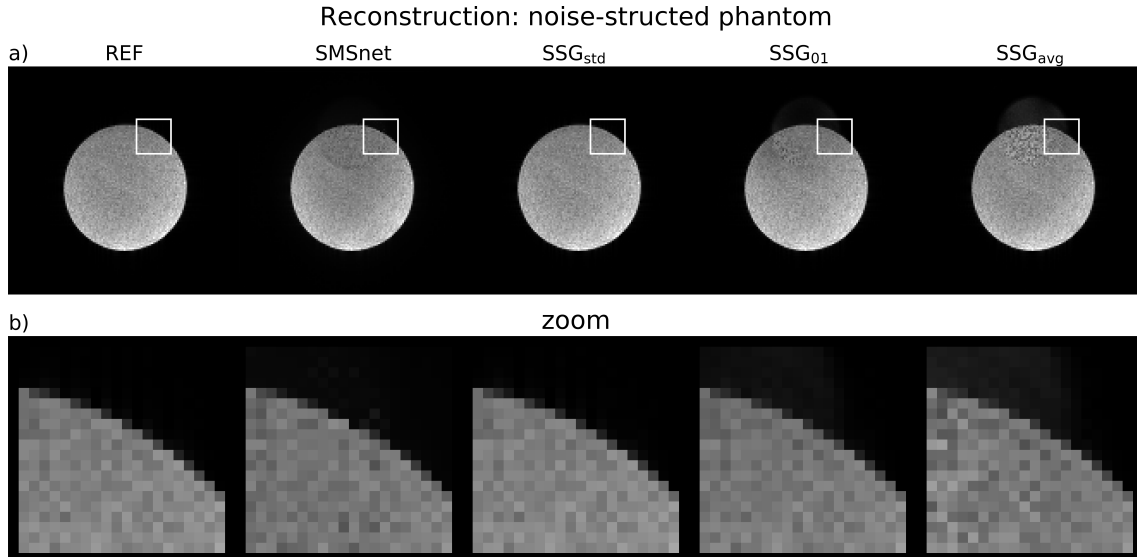


Figure 8.7: a) Results of noise-structured phantom with the different reconstruction methods are depicted. b) The zoomed views show correct recovery of fine, irregular patterns, i.e. noise structure where no slice overlap occurred. Non complete removal of leaked signal changes pixel-values and, hence, patterns locally.

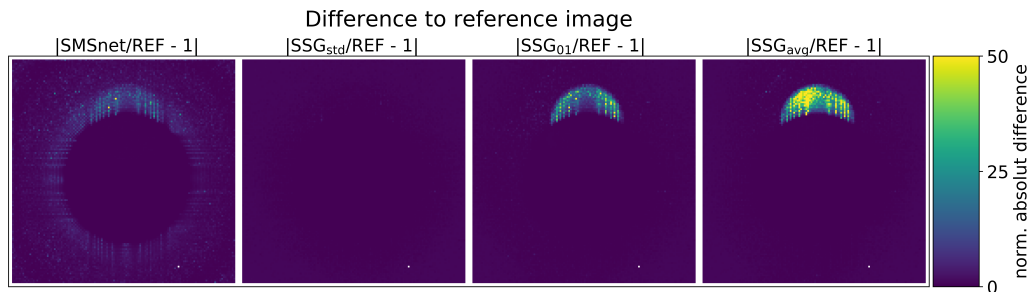


Figure 8.8: Normalization allows clear visualization of the remaining signal of overlapping slices in the difference map for the artificial noise-structured phantom. Background signal was on a low level, which resulted in scaling effects in background regions. Therefore, range of values was adjusted.

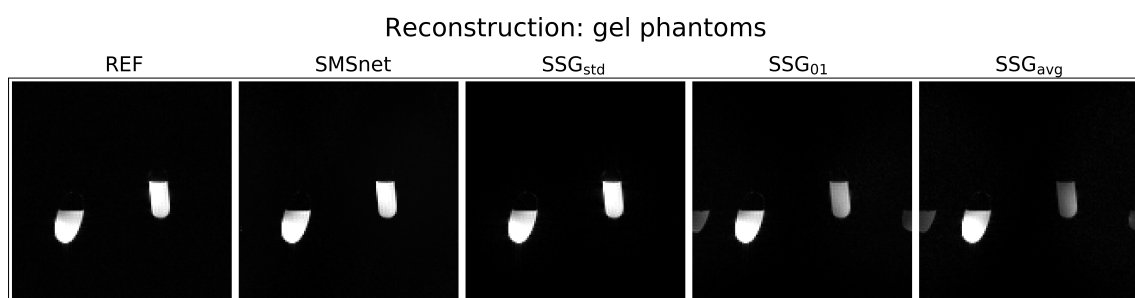


Figure 8.9: Data were taken of gel phantoms which were placed bilateral near the outer border of the head coil to mimic an extreme variation of the object volume and connected CoS profile.

8.1.3 Noise Propagation and Signal Sensitivity

Figure 8.10 shows the local, reconstruction-related noise-enhancement. While SMSnet and SSG_{std} perform almost equally in average (mean g-factors 1.71 and 1.72), higher local g-factors appear in SMSnet. Noise is clearly enhanced in SSG_{01} and SSG_{avg} (mean g-factors 1.92 and 2.15) which is in accordance with the observed leakage artifacts in Figure 8.11. Results of these experiment were also quantified. The different methods yielded a SSIM of 0.91 (SMSnet), 0.99 (SSG_{std}), 0.91 (SSG_{01}) and 0.87 (SSG_{avg}), respectively. MSEs were $7 \cdot 10^{-4}$ (SMSnet), $0.3 \cdot 10^{-4}$ (SSG_{std}), $17.8 \cdot 10^{-4}$ (SSG_{01}) and $61.3 \cdot 10^{-4}$ (SSG_{avg}).

Signal separation of finger tapping SMS data as shown in Figure 8.12 results in a time-series of T_2^* -maps (Fig. 8.12, a) Time courses of ten identical voxels indicated by red markers were averaged. Regions, where the BOLD effect induced T_2^* -changes with significant correlation to the applied paradigm, are identified by the generalized linear model and depicted in Figure 8.12 (b). Temporal signal changes in selected voxels reveal reasonable T_2^* -dynamics corresponding to the paradigm in all three cases as shown in Figure 8.12 (c). Temporally varying T_2^* -values of SB (green), SSG_{std} (blue) and SMSnet (red) reconstructions are shown for each measurement. The design matrix convolved with a hemodynamic response function is plotted for reference (solid black). Because data for SB and SMS were acquired in separate experiments, dynamics of these match less ($\text{corr}(\text{SB}, \text{SSG}_{\text{std}})$: $r = 0.73$ and $\text{corr}(\text{SB}, \text{SMSnet})$: $r = 0.7$) compared to a correlation of $r = 0.96$ between SSG_{std} and SMSnet reconstructions of the very same raw data.

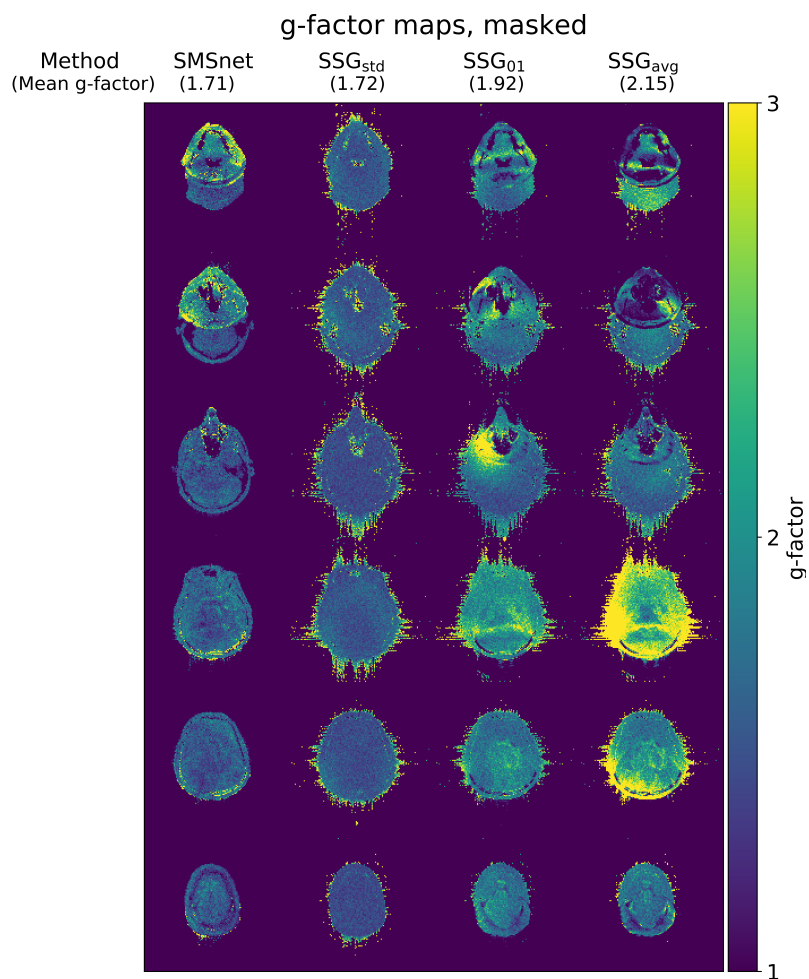


Figure 8.10: Monte-Carlo generated g-factor maps show the reconstruction-related noise-enhancement for all four reconstruction methods. Masks were applied to remove irritating background. Corresponding reconstructed images are displayed in Figure 8.11.



Figure 8.11: Reconstructions of mimicked whole brain MRI scan. Averaged, noise-free data were used for PMRM to calculate g-factor maps as shown in Figure 8.10. Images were slice-wise normalized for display.

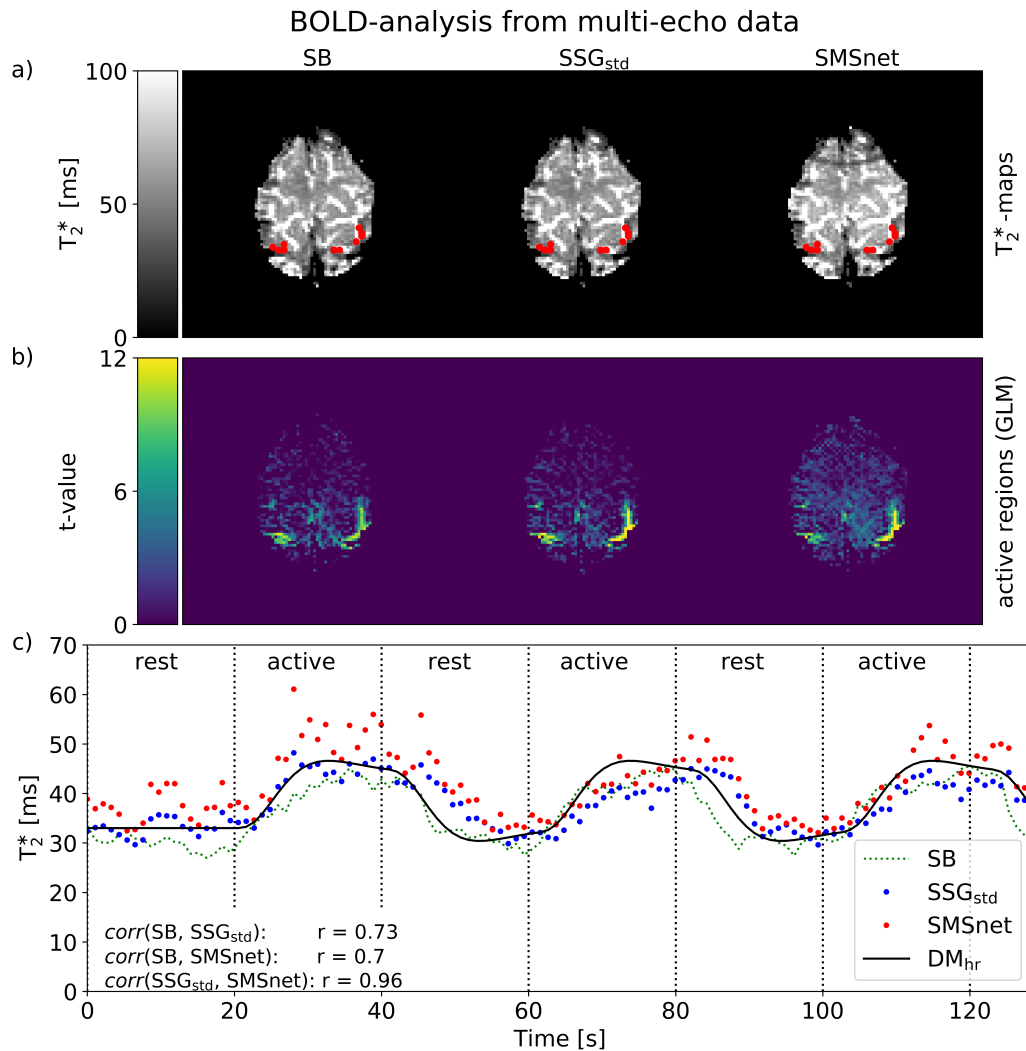


Figure 8.12: a) The identical slice of two repeated finger tapping experiments (three slices (SB scan) vs. six slices ($MB = 2$ scan)) is shown representing the T_2^* -contrast after mono-exponential fit of the multi-echo data. Red markers highlight selected voxels from which T_2^* -dynamics were delivered for SB, SSG_{std} and SMSnet. b) Activated areas are visualized by their t-values resulting from statistics of the generalized linear model. c) The averaged T_2^* -signals from ten representative voxels are plotted over time (SB (green), SSG_{std} (blue) and SMSnet (red)) and Pearson correlations are given. The time course rises due to the BOLD effect while performing bilateral finger tapping, the rest/activation paradigm is illustrated by vertical dotted lines. The applied design matrix corrected for hemodynamic response, DM_{hr}, is drawn as a solid black line.

8.1.4 Severe Changes in the Coil Sensitivities

Severe perturbation to the CoS profile was simulated by the replacement of signal with Gaussian noise (noise-level of 5%). If a single coil (coil number 5) contains only noise, the reconstructions result in a comparable image quality as with object signal in all coils (Fig. 8.2). In particular, the slice separation does not fail abruptly. However, SNR is reduced as shown in Figure 8.13 (a). This is also visible in the difference maps in Figure 8.14 (a) when compared to experiments where all coils contribute meaningful content to the reconstructed images (Fig. 8.3).

In another experiment four coils contain no true signal, but only noise. This simulates a more severe perturbation of the CoSs and signal attenuation over a larger region near the forehead. The reconstructed images are given in Figure 8.13 (b). As expected for MR acquisitions with a reduced number of coils, the image quality degrades in all cases. The increased noise at the input propagates into the reconstructed images, which appears more prominent for SMSnet than for the SSG approaches. A reduced noise-level is found in the background of the SSG reconstructions even if compared to the reference.

Table 8.3 lists quantitative results for both experiments and the results of Section 8.1.1, all separated by dashes. Noisy coil signal yields the following changes for SMSnet. The average MSE increases by 61% (222%), if one coil (four coils) contains only uncorrelated Gaussian noise and is compared to reconstructions without any artificial noise in the coils. The quality of the reconstructed images quantified by the mean SSIM reduces by -11% (-23%).

Likewise, this degradation in image quality is observed for all SSG reconstructions. The MSE changes by -9% (30%) for SSG_{std} , 72% (291%) for SSG_{01} and 67% (303%) for SSG_{avg} . The mean SSIM declines by -7% (-15%) for SSG_{std} , -15% (-35%) for SSG_{01} and -16% (-38%) for SSG_{avg} . Other metrics confirm the reduced image quality (Tab. 8.3).

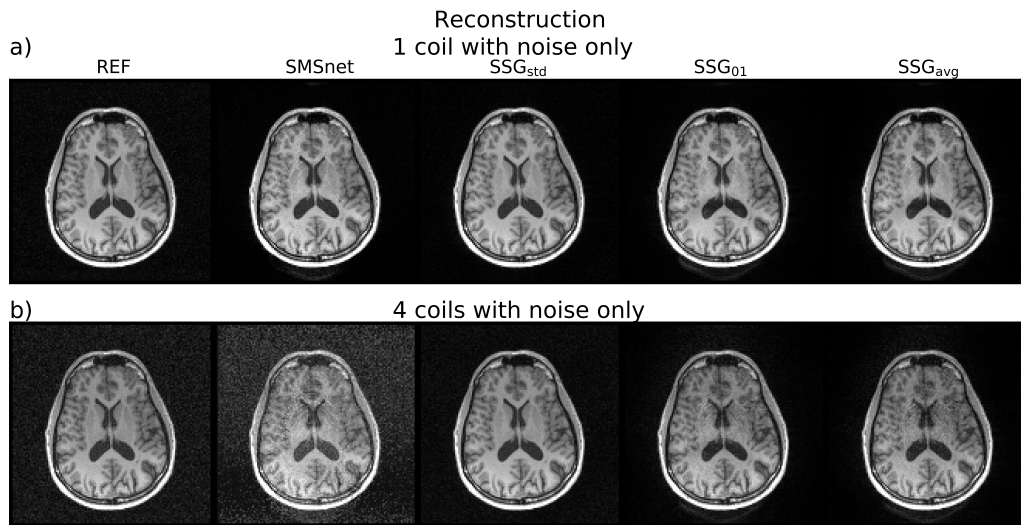


Figure 8.13: Effect on image quality, if sensitivities of one coil or four coils are severely perturbed. Here, noise-only signal (noise-level 5%) was inserted to this / these coil(s) before reconstruction.

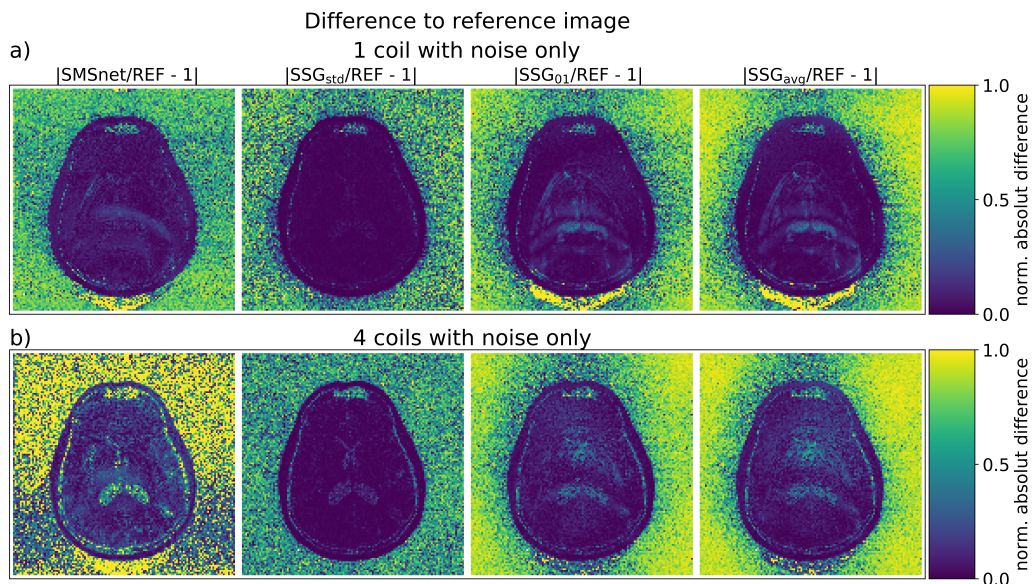


Figure 8.14: Normalized difference maps show clearly the effect of an lower overall SNR. Differences because of reduced SNR, should be distinguished from slice leakage artifacts.

Volunteer's head, severe changes in CoS				
Mean values across volume				
Noise only in: 0 coils / 1 coil / 4 coils				
	SMSnet	SSG _{std}	SSG ₀₁	SSG _{avg}
MSE [10^{-3}]	1.98 ± 8.86	1.92 ± 9.36	1.91 ± 8.82	2 ± 10
	3.4 ± 13.3	1.85 ± 7.68	3.5 ± 14.4	3.79 ± 15.8
	5 ± 10	2.65 ± 7.5	6 ± 18.5	6.9 ± 22.2
SSIM [10^{-1}]	9.4 ± 1.41	9.15 ± 1.59	9.22 ± 1.53	9.13 ± 1.66
	8.31 ± 1.67	8.52 ± 1.63	7.88 ± 1.68	7.7 ± 1.68
	7.22 ± 1.26	7.77 ± 1.55	6.12 ± 1.48	5.79 ± 1.45
$\text{corr}(I_s, I_{s,\text{REF}})$ [10^{-1}]	9.71 ± 1.19	9.84 ± 0.79	9.71 ± 1.17	9.73 ± 1.08
	9.52 ± 1.67	9.54 ± 1.93	9.52 ± 1.84	9.53 ± 1.82
	9.17 ± 1.46	9.3 ± 2.1	9.27 ± 2.06	9.26 ± 2.04
$\text{corr}(I_s, I_{s+(\text{Ns}/\text{MB}),\text{REF}})$ [10^{-1}]	3.13 ± 0.04	3.32 ± 0.04	3.75 ± 0.23	3.74 ± 0.21
	3.22 ± 0.03	3.14 ± 0.002	3.62 ± 0.28	3.62 ± 0.26
	3.18 ± 0.09	2.98 ± 0.02	3.45 ± 0.03	3.54 ± 0.07

Table 8.3: Results of the experiments with noise-only content in one coil or four coils can be directly compared to reconstructions without any artificial noise in any coil. Each cell contains values for mean and standard deviation of each metric for all three scenarios: no coil contains only noise, one coil contains noise only, four coils contain noise only.

8.1.5 Robustness to Object Motion

Measurements under simulated head motion result in SMS-reconstruction-related artifacts as depicted in Figure 8.15. The referenceless reconstructions with SMSnet are shown in the second row below the reference images REF. Conventional reconstructions, shown in the third row, are labeled as SSG_{p0} because ACS data are taken only from position #0 scans. Both reconstructions are free of pronounced leakage signal from simultaneously excited slices. However, SMSnet fails to suppress some signal in the left posterior region. In contrast, SSG_{p0} reconstructions show the typical signal of shifted, overlapping slices in that region.

The normalized difference maps in Figure 8.16 reveal leakage signal which is more pronounced inside the object for SMSnet. Remaining signal outside the object, is suppressed more completely by SMSnet than by SSG_{p0} . The mean values for MSE indicate that SMSnet ($MSE = 5.07 \cdot 10^{-4}$) results in higher difference to the reference images compared to SSG_{p0} ($MSE = 2.51 \cdot 10^{-4}$) while SMSnet yields a higher mean SSIM (0.96) than SSG_{p0} (0.95). Overall, neither reconstruction outperforms the other in all metrics (Tab. 8.4).

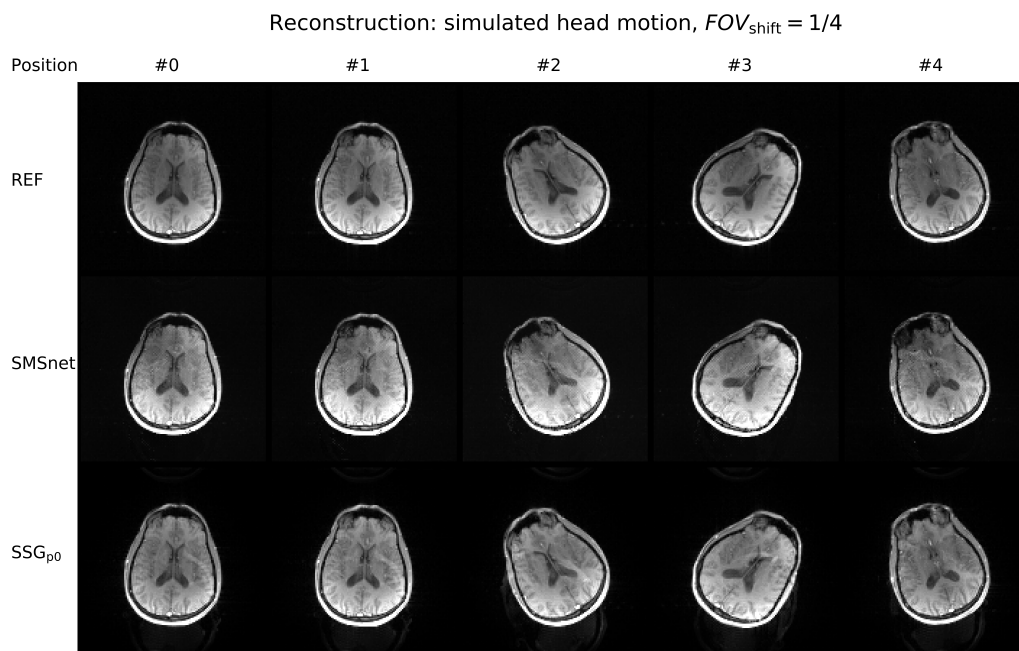


Figure 8.15: Different head positions (#0 to #5) are shown in each column for reference data without SMS and SMS reconstructions of two different methods, SMSnet and SSG_{p0} .

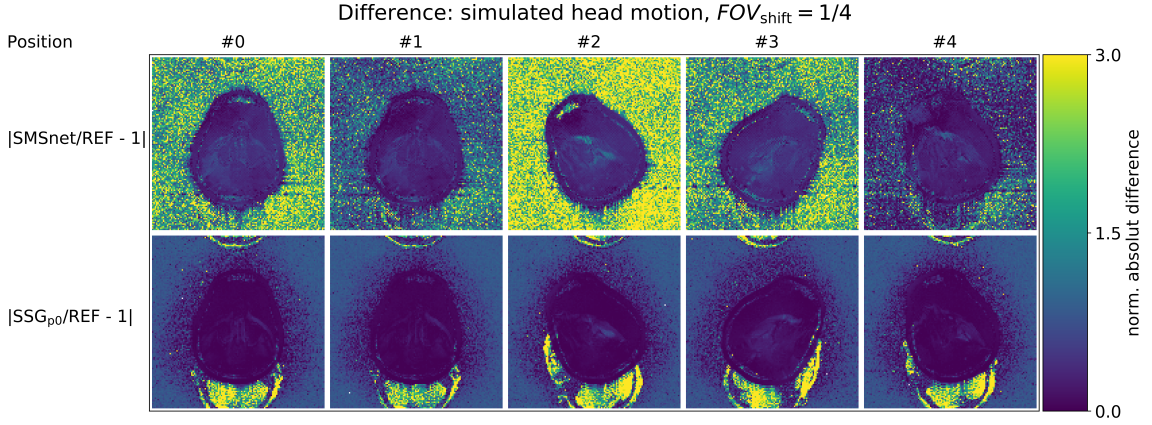


Figure 8.16: The normalized difference maps reveal remaining signal from the overlapping slices that leaks into the reconstructed slice for SMSnet (top row), but also for SSG reconstructions (bottom row).

Simulated head motion, $FOV_{\text{shift}} = 1/4$		
Mean values across volume and positions		
	SMSnet	SSG _{p0}
MSE [10^{-3}]	0.62 ± 0.55	0.25 ± 0.18
SSIM [10^{-1}]	9.21 ± 0.076	9.47 ± 0.028
$\text{corr}(I_s, I_{s,\text{REF}})$ [10^{-1}]	9.89 ± 0.03	9.88 ± 0.07
$\text{corr}(I_s, I_{s+(\text{Ns}/\text{MB}),\text{REF}})$ [10^{-1}]	1.96 ± 0.04	2.35 ± 0.18

Table 8.4: Mean values and standard deviation across all slices and five head positions are given.

8.1.6 Synthesized and Acquired SMS Data

To validate the efficiency of SMSnet for truly acquired SMS data, a comparison between synthesized and acquired SMS data was done. Assuming that a correctly performed SSG reconstruction SSG_{std} recovers the SMS data most reliably, images of this reconstruction serve as reference. Figure 8.17 shows the difference between reconstructions with missing/incorrect ACS (SMSnet, SSG_{01} , SSG_{avg}) and the reference images (SSG_{std}). All reconstructions perform similar for synthesized and acquired SMS data. However, the overall difference is about a order of magnitude smaller for SMSnet than for the conventional reconstruction approaches. In particular, regions outside the object are reconstructed more correctly with SMSnet. This is confirmed quantitatively in Table 8.5. SMSnet yields MSEs of $0.36 \cdot 10^{-3}$ to $0.87 \cdot 10^{-3}$ compared to MSE values between $1.33 \cdot 10^{-3}$ and $1.43 \cdot 10^{-3}$ for SSG_{01} and between $5.03 \cdot 10^{-3}$ and $5.26 \cdot 10^{-3}$ for SSG_{avg} , respectively.

SMSnet performs also better in SSIM. Mean SSIM values range from 0.94 to 0.97 compared to 0.914 for SSG_{01} and 0.87 to 0.88 for SSG_{avg} .

The corresponding reconstructed images were moved to Appendix A.5.

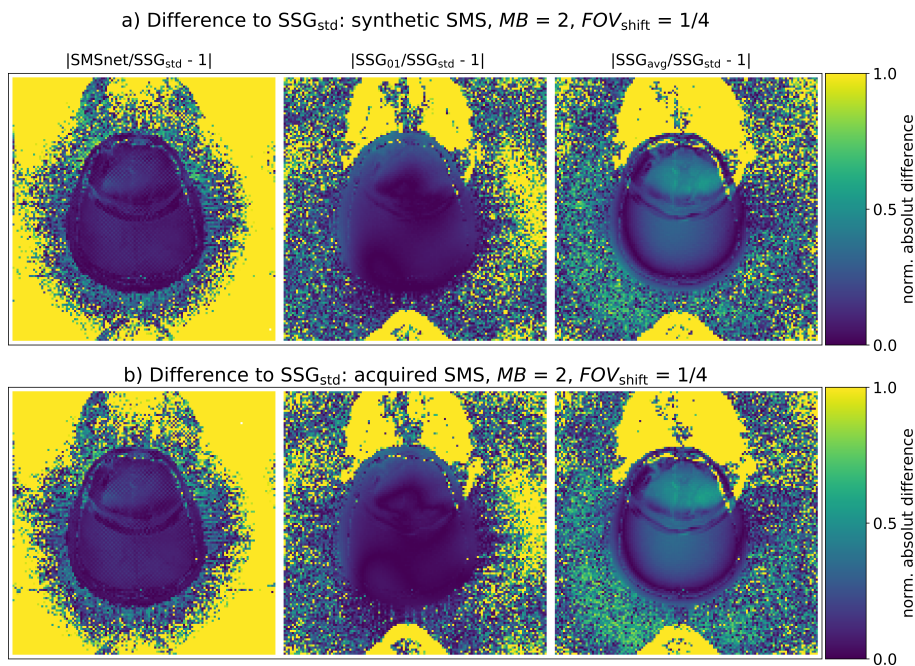


Figure 8.17: Normalized difference maps with respect to SSG_{std} as reference are shown for synthesized (a) and for actually acquired SMS data (b), both with identical parameters $MB = 2$ and $FOV_{shift} = 1/4$.

Reconstruction for synthesized and acquired SMS data			
Mean values across volume			
synthesized / acquired			
	SMSnet	SSG ₀₁	SSG _{avg}
MSE [10^{-3}]	0.36 ± 0.03	1.43 ± 1.62	5.26 ± 6.36
	0.87 ± 0.92	1.33 ± 1.52	5.03 ± 5.75
SSIM [10^{-1}]	9.4 ± 0.42	9.14 ± 0.63	8.74 ± 0.73
	9.66 ± 0.18	9.14 ± 0.63	8.75 ± 0.72
$\text{corr}(I_s, I_{s,REF})$ [10^{-1}]	9.98 ± 0.012	9.8 ± 0.22	9.19 ± 0.99
	9.92 ± 0.06	9.79 ± 0.24	9.16 ± 1.07
$\text{corr}(I_s, I_{s+(N_s/MB),REF})$ [10^{-1}]	2.66 ± 0.004	3.38 ± 0.67	4.49 ± 1.01
	2.7 ± 0.02	3.48 ± 0.68	4.59 ± 1.03

Table 8.5: Quantitative evaluation of results shown in Figures 8.17 and 8.18 is given for reconstructions with incorrect/missing ACS. Images after SMSnet, SSG₀₁ and SSG_{avg} reconstruction were compared to images reconstructed with SSG_{std}. Each cell lists values for mean and standard deviation for synthesized and acquired SMS data.

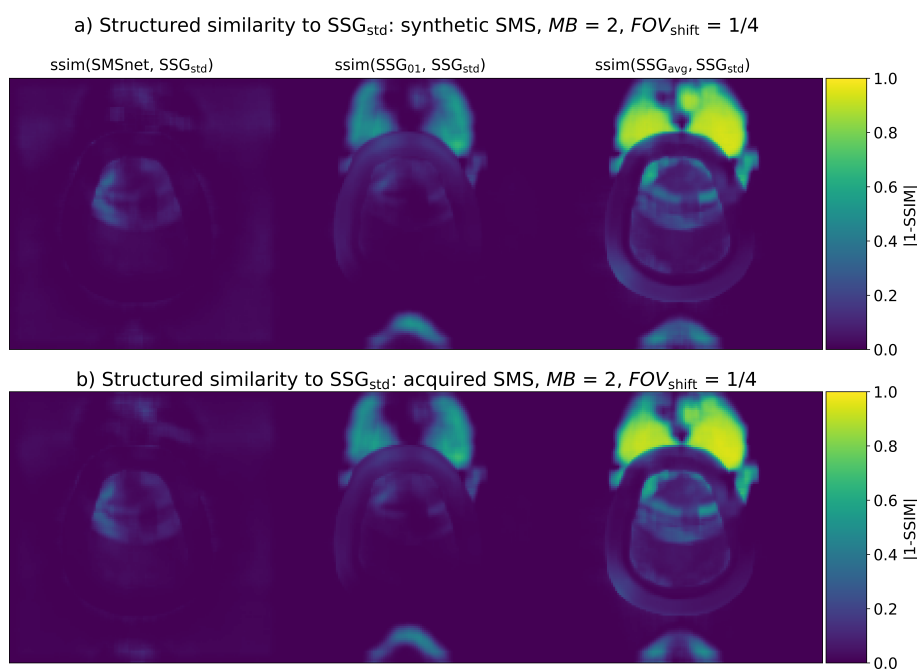


Figure 8.18: Inverted SSIM reveals a similar trend as the subtractions in Figure 8.17, where SMSnet produces the most accurate results. All reconstructions perform almost equally on synthesized (a) and acquired (b) SMS data.

8.1.7 Cross-System Transferability

Figure 8.19 shows the unsuccessful reconstructions of data acquired at another MR system (system A), while data for SMSnet or averaged ACS were derived from another system (system B). As shown, the reconstruction with SMSnet as well as the reconstructions with SSG_{01} and SSG_{avg} result in insufficient slice separation. The quantitative evaluation confirms this visual assessment. It is summarized in Table 8.6. The difference and SSIM maps can be found in Appendix A.5.



Figure 8.19: The approach to use a trained SMSnet to reconstruct SMS data acquired on another MR machine (cross-system) fails. The same is true if SSG is performed with unsuited cross-system ACS (SSG_{01} , SSG_{avg}).

Volunteer's head, cross-system				
Mean values across volume				
	SMSnet	SSG_{std}	SSG_{01}	SSG_{avg}
MSE [10^{-3}]	18.7 ± 18.1	3.92 ± 13.3	14.1 ± 18.2	14.3 ± 19.1
SSIM [10^{-1}]	6.31 ± 1.89	9.02 ± 1.95	6.71 ± 1.92	6.59 ± 1.94
$\text{corr}(I_s, I_{s,REF})$ [10^{-1}]	5.74 ± 1.21	9.68 ± 1.05	6.96 ± 2.17	6.95 ± 2.05
$\text{corr}(I_s, I_{s+(Ns/MB),REF})$ [10^{-1}]	6.04 ± 0.21	2.07 ± 0.13	6.42 ± 0.91	6.29 ± 0.96

Table 8.6: The quantitative evaluation confirms the visual assessment (Fig. 8.19). Values for mean and standard deviation are listed.

8.2 Higher Acceleration Factors

So far, the results in this chapter were limited to SMS data with $MB = 2$. Images from synthetic SMS data with $MB = 3$ ($FOV_{\text{shift}} = 1/3$) and $MB = 4$ ($FOV_{\text{shift}} = 1/4$) are shown in Figure 8.20 and compared to reference images and a reconstruction with SMSnet for $MB = 2$. Eight out of 202 slices are depicted to overview the reconstruction performance across the complete volume. Reconstructions for higher acceleration factors yield obvious signal leakage. However, the intensity of overlapping slice artifacts varies with spatial position along slice direction.

The signal leakage appears with similar intensity as for SSG reconstructions without correct ACS as shown in Figure 8.21. Besides leakage artifacts in SMSnet, SSG_{01} and SSG_{avg} , a structured difference appears after normalized subtraction for the reconstruction with SSG_{std} (Fig. 8.22). The difference between SSG_{std} and the reference images is also reflected in the quantitative evaluation summarized in Table 8.7.

For reconstruction of SMS data with $MB = 4$, the quantification yields reasonable results again in which SSG_{std} separates slices from MB slice groups most accurate. This is visually confirmed in Figure 8.23 and the difference maps in Figure 8.24. In contrast to the SSG_{std} reconstruction for $MB = 3$, no structured offset artifact is visible for the SSG_{std} reconstruction. SMSnet suppresses signal leakage outside the object slightly better than reconstructions with SSG_{01} and SSG_{avg} . However, all reconstructions without correct ACS suffer from overlapping slice signal. Results in Table 8.7 affirm these observations.

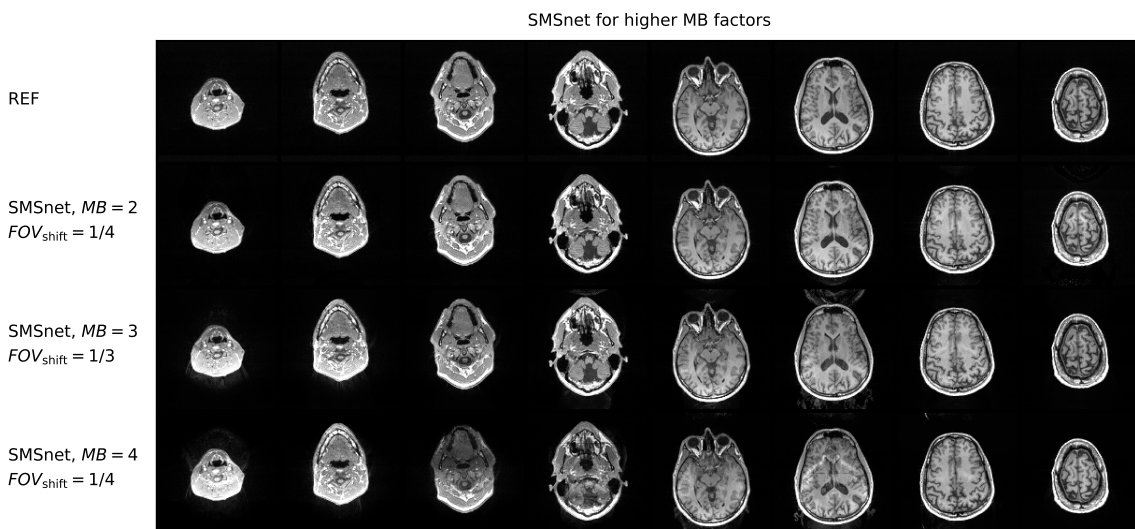


Figure 8.20: Reconstructions with SMSnet for $MB = 2$ (second row), $MB = 3$ (third row) and $MB = 4$ (fourth row) are shown for eight representative slices. All SMS data were synthesized from identical MPRAGE acquisitions.



Figure 8.21: Comparison of SMSnet for $MB = 3$ with the reference image REF and reconstructions with SSG. While the reconstruction with SSG_{std} shows no obvious leakage artifacts, these are visible in images after reconstruction with SMSnet, SSG_{01} and SSG_{avg} .

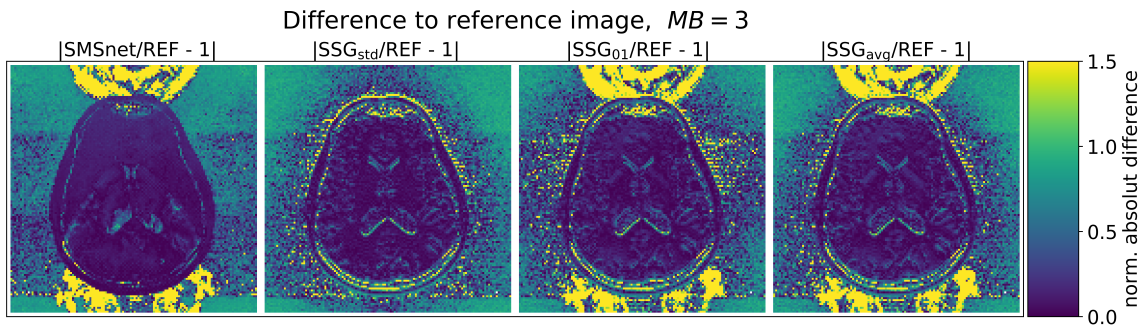


Figure 8.22: The difference maps for $MB = 3$ reveal leakage signal of other slices for SMSnet, SSG_{01} and SSG_{avg} . The reconstruction with SSG_{std} shows no inter-slice signal, but the recovered image signal differs from the reference image by an offset.



Figure 8.23: Comparisons for $MB = 4$, the slice signals are not well separated after reconstructions with SMSnet, SSG_{01} and SSG_{avg} .

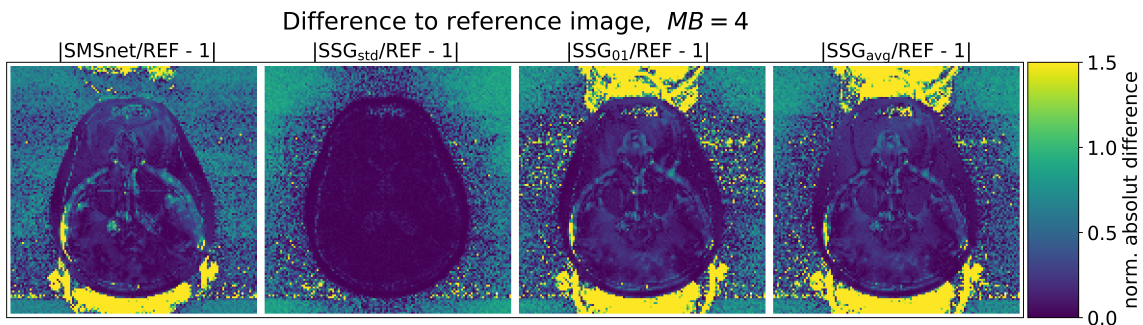


Figure 8.24: The difference maps for reconstructions of $MB = 4$ emphasizes the remaining slice artifacts for SMSnet, SSG_{01} and SSG_{avg} reconstructions. SSG_{std} results in an image with only little difference to the reference image.

In-vivo, volunteer's head, higher acceleration factors				
Mean values across volume				
$MB = 3 / MB = 4$				
	SMSnet	SSG _{std}	SSG ₀₁	SSG _{avg}
MSE [10^{-3}]	2.26 ± 9.48	3.76 ± 8.56	3.68 ± 7.66	3.9 ± 8.75
	3.37 ± 8.1	1.34 ± 7.26	1.83 ± 6.47	2.14 ± 7.49
SSIM [10^{-1}]	9.14 ± 1.69	8.63 ± 1.58	8.62 ± 1.41	8.5 ± 1.51
	8.62 ± 1.58	9.28 ± 1.42	8.91 ± 1.29	8.79 ± 1.38
$\text{corr}(I_s, I_{s,\text{REF}})$ [10^{-1}]	9.55 ± 1.73	9.25 ± 0.97	9.15 ± 1.16	9.15 ± 1.12
	9.28 ± 1.55	9.87 ± 0.67	9.64 ± 1.06	9.62 ± 1
$\text{corr}(I_s, I_{s+(N_s/MB),\text{REF}})$ [10^{-1}]	2.09 ± 0.35	2.02 ± 0.09	2.23 ± 0.08	2.24 ± 0.12
	3.41 ± 0.54	3.36 ± 0.03	3.46 ± 0.17	3.46 ± 0.22

Table 8.7: Reconstructions for higher acceleration factors were also quantified by the mean values across the volume. Results for $MB = 3$ and $MB = 4$ are listed in each cell. For the reconstruction of $MB = 3$ data, the above values do not confirm the visual appearance in Figures 8.21 and 8.22 which show leakage artifacts for SMSnet, SSG₀₁, SSG_{avg}, but reasonable reconstruction quality in SSG_{std}.

8.3 Layer Activations

Layer activations at the intersection of CoS-, Im- and Merge-path were investigated and shown together with activation maps of the network’s in- and output. For illustration purposes, activation maps of one MB slice group with $MB = 2$ are shown. A diverging colormap named *RdYlBu* was applied for range of values (negative and positive) [Hun07].

The input data available at the first layers for CoS- and Im-path are displayed in Figure 8.25. Only four out of 40 channels of k-space and image data were selected for illustration. Figure 8.26 shows the activation at the end of the CoS-path. A SMSnet trained for $MB = 2$ data consists of two CoS-paths. Therefore, the results for each path correspond to one of the two overlapping slices: slice #1 and slice #2. Slice #2 was shifted according to the CAIPIRINHA pattern. The activation maps show structured band patterns along the direction were slices were shifted. Only data with shifts along one direction, from posterior to anterior, were used for training in this experiment. Shifts were done by different amounts of FOV (FOV/2, FOV/3, FOV, FOV/5, and FOV/6). However, other structures like halo or fragmented patterns are visible as well. Figure 8.27 allows insight to the effect of the multiplicative merge-layers. The input image passed through fully-connected layers in the Im-path. Weighted connections were limited to the channel dimension, therefore, no in-plane shifts other than the input image shifts are visible. Nonetheless, non-linear activations in three of the layers allow an adjustable combination of complex channel data during training, such that image activations (Fig. 8.27, a) multiplied with CoS masks (8.27, b & c) yield slice position dependent signal changes. After merging, the activation maps for slice #1 (Fig. 8.28, a) and slice #2 (Fig. 8.28, b) differ more clearly in some channels, i.e. top left, than in others, i.e. center right. The successive layers of the Merge-path reduce the number of channels from 250 to a single channel output for each slice.

The activations in the last layer of SMSnet correspond to the reconstructed images as depicted in Figure 8.26. Here, the FOV-shift according to the CAIPIRINHA pattern was not reversed to ease comparison with the hidden layer activation maps.

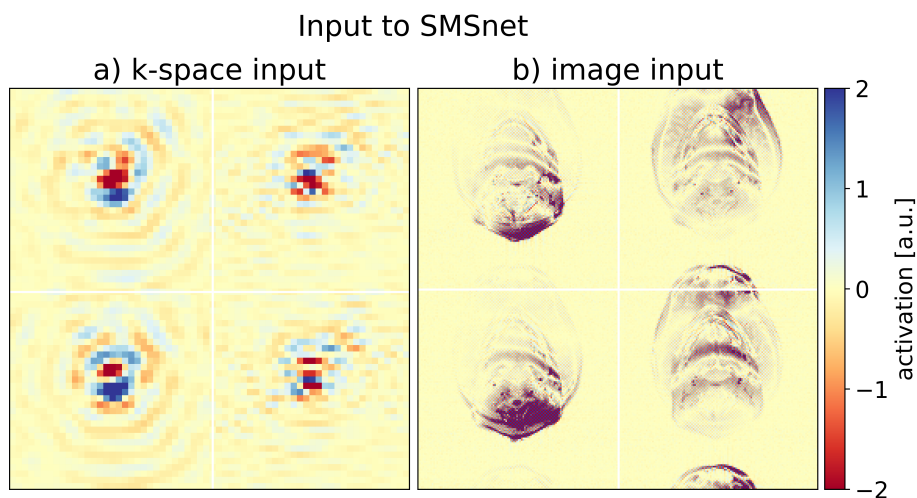


Figure 8.25: a) Low resolution k-space data of size $(32 \times 32 \times 40)$ were presented to the input of the CoS-path. b) Image data at the Im-path input had full resolution of size $(128 \times 128 \times 40)$. Four out of 40 channels are shown.

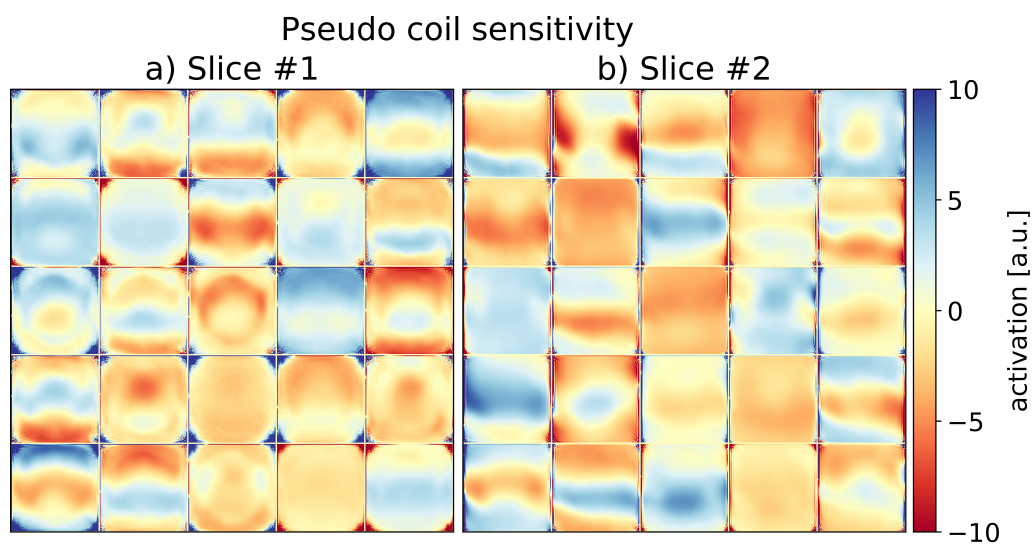


Figure 8.26: The activation of the hidden layers at the end of the CoS-path were extracted after training for $MB = 2$. Only every tenth channel of 250 channels is shown for each CoS-path (slice #1, slice #2). While objects in (a) are not affected by CAIPIRINHA shifts, objects multiplied with CoS mask of (b) were shifted by $FOV_{\text{shift}} = 1/2, 1/4, 1/4, 1/5, 1/6$.

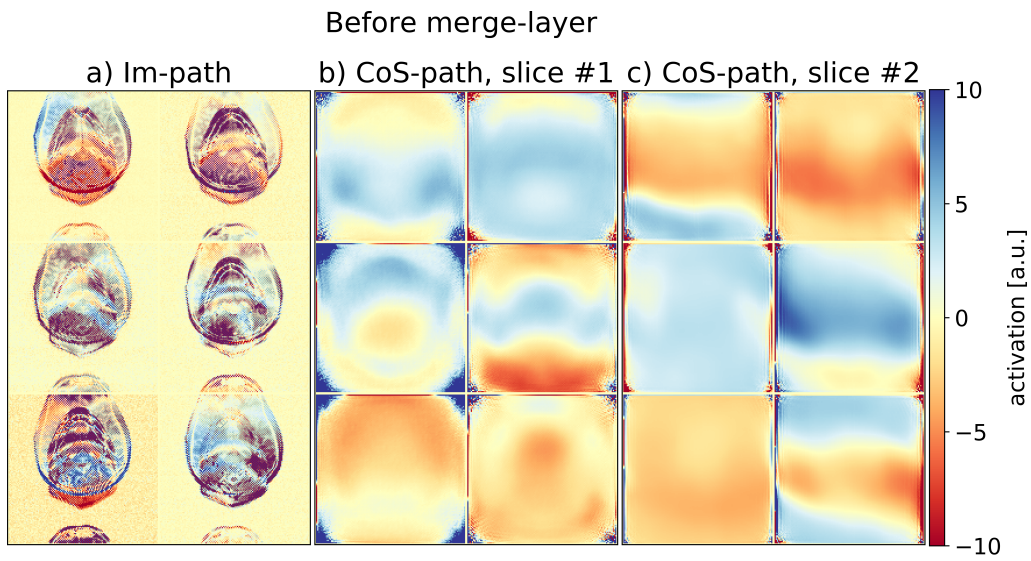


Figure 8.27: a) Image passed through three layers with non-linear activations in the Im-path before being merge with the masks from the CoS-path (b,c). The outputs of six out of 250 channels are illustrated.

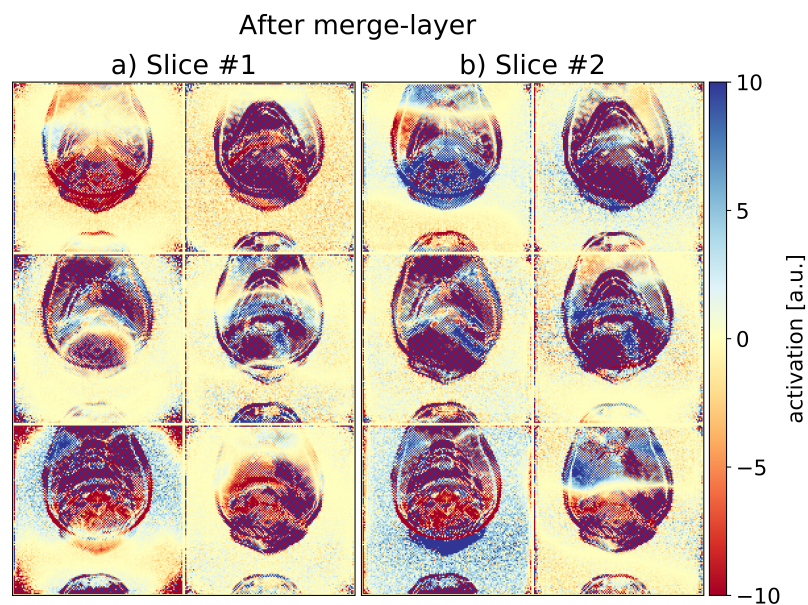


Figure 8.28: After the merge layer, the two images for slice #1 (a) and slice #2 (b) show different enhancement patterns. In some regions, activation values differed clearly and signal content of either slice is separated into a positive or negative range of values, e.g. central region in top left channel. The outputs of six out of 250 channels are illustrated.

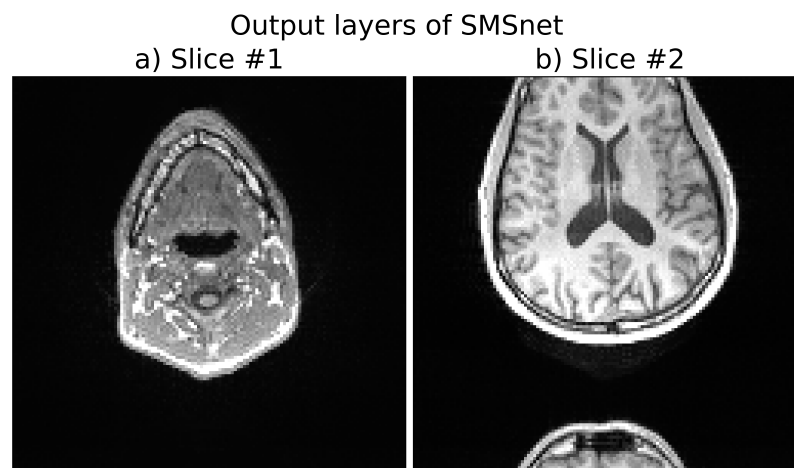


Figure 8.29: The number of channels is reduced to a single channel at the output layer of SMSnet. The images for slice #1 (a) and #2 (b) are shifted according to the CAIPIRINHA pattern of the test data. Shifts were not reversed for plotting to allow comparison with shifted CoS masks and hidden layer outputs in Figures. 8.27 and 8.28.

8.4 Manipulation of Input Data

Input data were manipulated to further trace the ruling principles of SMSnet. To assess all 202 reconstructed slices simultaneously, image slices were rebuilt to one volume and viewed in sagittal direction in Figure 8.30. The reference images (a) are compared to a standard SMSnet reconstruction where input data were not manipulated (b) and reconstructions with manipulated data at the k-space input and/or image input (c-f). While experiments in (b), (d) and (e) produce results without any obvious folding artifacts, signal leakage is visible in (c). If input data in both domains is replaced with Gaussian noise, the noise signal propagates through the network without any superimposed patterns. At the vertical center, a difference in the signal intensity appears where signal changes from slice #1 to slice #2 position. This is in particular visible for noise-only slices (f). Quantification of these results can be found in Appendix A.5.

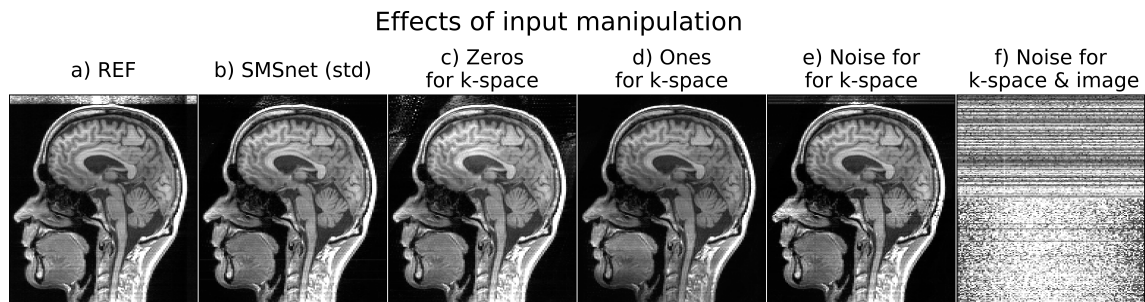


Figure 8.30: a-b) Reconstructions of SMSnet for manipulated input data are compared to reference data REF and a SMSnet reconstruction with correct k-space IN_{ks} and image IN_{ks} input data. c) Leakage artifacts corrupt the reconstruction if k-space input data are replaced with zeros ($IN_{ks} = 0$). These remaining signals are not visible if incorrect data other than zero are presented to the CoS-path. d) Shows the results if k-space input data replace with ones ($IN_{ks} = 1$) and (e) if data are replaced with Gaussian noise. f) If input data for both paths, CoS- and Im-path, are manipulated, the reconstruction fails.

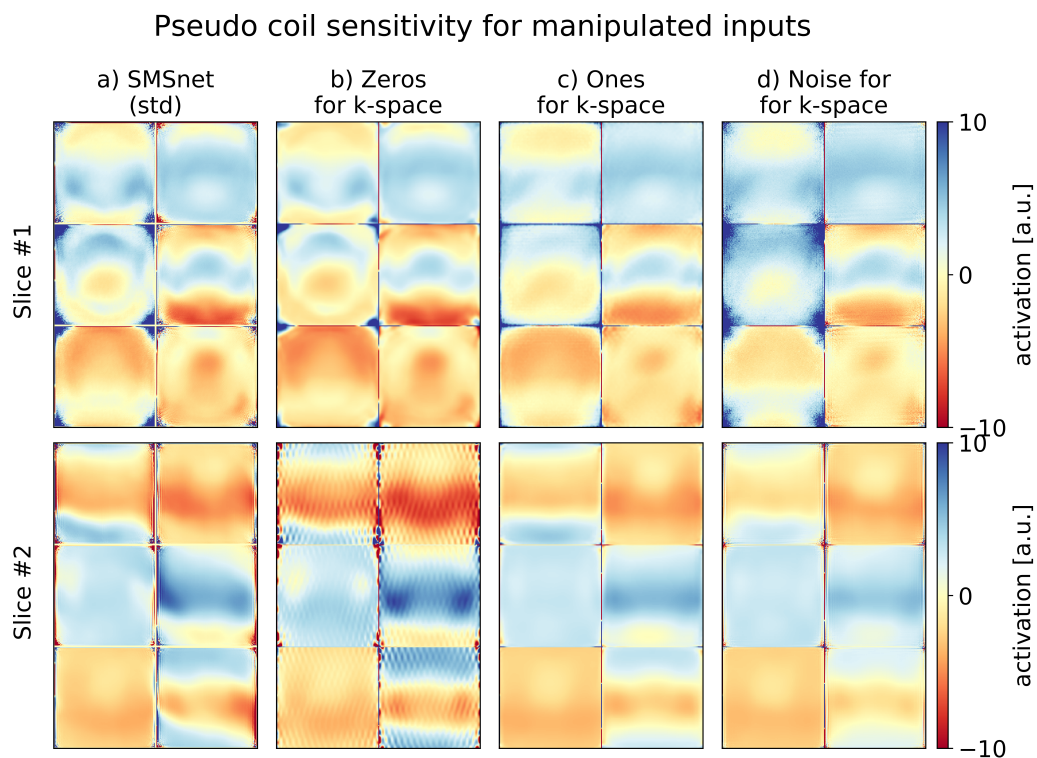


Figure 8.31: a) The activation maps in six representative channels for the complete input data are shown as reference (SMSnet (std)). b) With zero input to the CoS-path, the activation change. Additional structured patterns are visible in the pseudo CoSs for slice #2. c) Setting $IN_{ks} = 1$ changes the activations as well, however, additional patterns are less visible. d) In case of a noisy k-space input, noise-like fluctuations emerge also in the activation pattern and the CoS masks appear smeared compared to (a).

Part IV

Discussion & Conclusions

9 Discussion and Outlook

Because SMS in MRI is the overall subject of this work, the following discussion will summarize the findings of Part II and Part III.

First, the results in Chapter 5 on SMS MRI with a focus on the dynamic imaging are discussed, followed by an account on MB RF excitations and resulting slice profiles. The (re-)rise of AI and DNN in medical science and specifically MRI will be discussed in the second part of this chapter as well as its application and potential for SMS, which has been invented and investigated in Sections 7 and 8.

9.1 SMS for Dynamic Imaging

The presented SMS multi-contrast segmented EPI sequence as described in Section 3.3 allows fast, dynamic imaging of a large volume of interest. Its performance for dynamic MRI was tested in a preclinical perfusion study under CA administration. A multi-contrast segmented EPI sequence yields sufficient signal at late echo times for T_2^* -contrast, as well as providing short echo time data for T_1 -weighted contrast. The segmentation of the echo train offers an additional parameter, which allows flexible adjustment of the acquisition scheme with respect to both, the desired TEs and the temporal and spatial resolution for a given volume of interest. The results in Section 5.1 have shown that the combination of SMS and multi-contrast segmented EPI permits comprehensive dynamic imaging studies with scan times that would be acceptable in clinical practice. Here, a volume of $400 \times 200 \text{ mm}^2$ in 24 slices was covered within the upper limit for the temporal resolution of $\Delta t \leq 1.5 \text{ s}$ for accurate AIF detection. The SMS protocol used in this study is consistent with other perfusion protocols for DCE, DSC [Jah+14] or combined T_1/T_2^* -imaging [New+07; New+16], but offers an increased flexibility than, for example, single-shot EPI, which is often limited to DSC in the brain [New+16]. The reconstructed SMS images do not suffer from any obvious residual inter-slice artifacts of the collapsed slices (Fig. 5.4), which confirms the correct unfolding of the accelerated SMS data.

Image Artifacts: Nyquist ghosts occur in EPI sequences because of a temporal misalignment between alternating readout gradients and signal acquisition. If not corrected appropriately, this results in a $N_{\text{PE}}/2$ -ghost for single-shot EPI for a FOV of N_{PE} pixels along PE. In case of segmented EPI, the signal intensity of the ghost-artifacts is shared between the N_{seg} segments resulting in N_{seg} ghosts distributed along N_{PE} [Hen97]. The SMS reconstructions in this work do not suffer from obvious Nyquist ghosting. However, if Nyquist ghosts appear more pronounced, the slice separation procedure may precede the phase correction as suggested in [Moe+10]

which would change the order of the processing steps (Fig. 4.5).

Segmented sampling strategies have been restrained because of their severe vulnerability to motion, which, in particular, limits their application for abdominal or cardiac imaging by introduced structured artifacts. As structured artifacts due to motion are a drawback of all segmentation strategies, the achieved overall acceleration by SMS encounters motion related error to a certain level. Nevertheless, the intrinsic sensitivity to any motion between the segments of the same frame of EPI data will remain a clear disadvantage. If motion can be controlled, e.g. data are acquired under breath holding, the field of applications may be extended and further acceleration as described later on may help to reduce present restrictions in the application of segmented EPI. In here, the performed experiments can be considered as motion-free, since the animals were anesthetized and the imaging volume was in and near the lower extremities and not affected by respiratory motion.

Comparison to Parallel Imaging: Standard PI strategies in single-shot EPI as introduced in Section 3.2.2 apply in-plane undersampling either merely for acceleration or also to reduce distortion and echo time. In comparison to PI where an acceleration factor of $R = 4$ is selected, SMS measurements with $R = 4$ achieve a higher overall acceleration. The in-plane undersampling in PI only reduces the duration of the readout whereas SMS shortens the complete TR period including the excitation and the readout. If PI is combined with multi-shot EPI, the achieved acceleration is higher, because some of segments can be omitted completely. However, even with similar temporal and spatial performance, the introduction of SMS to multi-contrast perfusion MRI does not suffer from a \sqrt{R} -fold SNR penalty like PI [Bar+15].

It should be emphasized that PI can be easily incorporated into the presented type of sequence if further acceleration is desired, e.g. to reduce sensitivity to motion. PI accelerated acquisition of multi-contrast dynamic MRI has shown promising results in brain perfusion mapping [New+07]. Although, PI is an established technique, acceleration is limited due to inherent reduction in SNR by \sqrt{R} in addition to the reconstruction related SNR penalty (g-factor) [Des+12]. The shortened RO train and, therefore, a shorter TE are beneficial for some applications especially in single-shot EPI, but are less important if the readout is segmented as in the presented sequence. The reduction of image distortions is another important benefit of a reduced echo train length in PI-accelerated EPI. While the setup for the in-vivo MRI on animals included 46 receiver coils which would allow combined SMS and PI theoretically, this was not considered in the experiments. First, because the achieved temporal resolution met the prior defined requirements and second, because of potentially poor CoS profiles for the subjects' anatomical conditions due to difficult placement of the coils and resulting spatially inhomogeneous signal levels. Poor CoS profiles would

affect SMS and PI in a similar manner, but the SG/SSG reconstruction in SMS (with CAIPIRINHA) exploits sensitivity variations along two directions, PE and slice, which typically reduces the g-factor penalty compared to PI reconstructions in 2-dimensional (2D) MRI where only CoS variations along PE are used [Bre+05].

g-factor and Subtraction Maps: The relatively high g-factors for the evaluated reconstruction approaches (Fig. 5.6) lead to localized SNR penalties, which can be seen in the subtraction images for reconstructions where ACS data were synthesized (Fig. 5.4, method 2). These prominent localized differences do not occur if the ACS source data used for weights calculation in SG are the measured SMS data. This is because ACS data for the general signal equation (Eq. 3.21) will reflect MB RF pulse specific imperfections if ACS source data are measured. The SG algorithm will then optimize the solution for the signal equation to reduce the total reconstruction error, i.e. MSE, without any conditions on inter-slice artifacts [Cau+14]. Hence, the higher g-factor in method 1 than in method 2 was traded against a reduced reconstruction error. Method 1 provides a robust reconstruction with less localized inhomogeneities for the given experimental setups and no obvious inter-slice leakage was observed by visual inspection of the final images, which would have required slice leakage blocking. The dynamic dataset was reconstructed with SG unfold images calculated accordingly (method 1). The pixel-wise difference after subtraction (Fig. 5.4) and the g-factor (Fig. 5.6) represent two different metrics for the quantification of the reconstruction performance in SMS. Reasons for the disagreement in both metrics, i.e. lower g-factor vs. higher subtraction difference for method 2 (Figs. 5.4 and 5.6), might arise from the algorithm for the g-factor calculation itself. It derives the g-factor from the variances of the accelerated and reference images which are gained from identical data in method 2 [Bre+09].

slice-GRAPPA and split slice-GRAPPA: These results suggest that the image quality is improved by acquiring additional low resolution ACS data: SB data for ACS target and data from a SMS acquisition serving as ACS source. In particular, for perfusion imaging or other protocols with repeated measurements, the extra time spent might be acceptable. Additional experiments to analyze and verify this approach as well as an account on underlying reasons in real measurements are given in Section 5.3 and discussed in the Section 9.1.1. Note, that special care must be taken to avoid object motion between ACS scans. Motion and its artifacts are an issue which, in general, hamper dynamic MRI. Imaging methods where the reconstruction relies on reference data are inherently affected by motion. The repeated acquisition of reference data, for example during the extravasation phase some time after the bolus, when temporal resolution is less critical, could help to ensure a correct match

between reference and SMS data.

CAIPIRINHA Shift: A CAIPIRINHA-like shifting by gradient modulated phases along PE reduces the g-factor penalty [Set+12b]. Here, the modulation gradients were integrated into the rewinder of the slice-selection gradients. This method to introduce phase modulation can become an alternative to the z-blips commonly used in single-shot EPI, if the k-space is segmented along PE. A drawback of this strategy is a limitation in $\text{FOV}_{\text{shift}}$ -factors selectable with respect to a given number of EPI segments. On the other hand, omitting extra gradients for shifting reduces gradient switching and avoids additional gradient blips, which can have disadvantages such as eddy currents or increased echo spacing, as well as some signal loss due to intra-slice dephasing.

Reference Data for slice-GRAPPA: Influences of the SMS reconstruction process on the image contrast [Set+12b] have been addressed by the choice of ACS data with identical contrast and sufficient SNR (Figs. 5.10 and 5.11). Phantom experiments were carried out to investigate the influences of image contrast variations between ACS and SMS data which were to reconstruct. The evaluation of different strategies suggests that the reconstruction performance for either SG or SSG depend more on a sufficiently high SNR than on the image contrast (Fig. 5.12). Slice-GRAPPA with averaged ACS (five or ten averages) and, therefore, higher SNR tend to reconstruct SMS data independently of the image contrast (TE_1 , TE_3 , S_0 , T_2^*). SSG is slightly more robust than SG, but with sufficient SNR the methods are comparable. It should be noted, that the resulting parameters of the linear model (b_0 , b_1) which quantify this dependency are all relatively small and close to zero, indicating that there is no dependency on S_0 and T_2^* . Thus, by correct choice of ACS data, a scaling of the SMS image during reconstruction, which appears when source and target ACS have different contrast, can be avoided and the recovered SMS images exhibit the correct contrast according to their imaging parameters. However, the conducted experiments only cover a limited spectrum of image contrast variation (Sec. 5.2) and, therefore, these results may not be extrapolated to any changes in image contrast between ACS and measured SMS data.

No additional inter-slice leakage or ghosting was observed during or after CA administration, which locally and globally changed the image contrast. This confirms that the reconstruction method performed equally well throughout the dynamic protocol. This is in line with the results reported previously [Eic+14].

An interleaved acquisition scheme for the MB slice groups was used to reduce crosstalk between adjacent slice groups and saturation effects in the magnetization. This also ensures similar contrast characteristics across the volume.

Dynamic Imaging: Two major aspects motivating the sequence development part of this work were analyzed. First, the acquisition of multiple contrasts enables separation of the MR signal into multiple components by fitting a mono-exponential decay to the acquired contrasts: a resulting S_0 -signal, which depends mainly on T_1 , and a T_2^* -dependent signal which reflects different pharmacokinetic properties. The results in Section 5.1.1 qualitatively show that signal separation can be successfully performed and the expected dynamics of S_0 and T_2^* can be extracted. These parameters or related relaxation times provide additional information for perfusion and extravasation modeling (e.g. vessel size index describing the geometry might be calculated). Therefore, baseline measurements can be used for the quantification of the relaxation time change rates and offer data for advanced pharmacokinetic analysis in the future. Second, an accelerated MR sequence for dynamic contrast-enhanced imaging at a temporal resolution of $\Delta t \leq 1.5$ s with sufficient spatial resolution has been investigated. It allows sampling of the AIF in major vessels with a temporal resolution of $\Delta t = 1.305$ s per image. The FOV available covered the pigs' leg and hip, including the abdominal aorta. The segmentation of the EPI readout allows the acquisition of the desired (short and long) echo times. By the simultaneous measurement of multiple contrasts, separated signals at TE = 0 ms can be recovered to sample the AIF despite the fast signal decay during CA-bolus passage with its dominant T_2^* -effect (Fig. 5.1). The importance of these two major aspects have been recently verified for simultaneous perfusion and permeability assessment in brain tumors [Wu+18]. However, in contrast to the work presented here, the pharmacokinetic modeling itself and comparison of multi-contrast MRI to single-contrast acquisitions are addressed while SMS specific issues concerning the MR physics and the SMS reconstruction were not discussed in great detail.

Limitations: AIF detection in large major vessels allows the minimization of partial-volume effects in the case of voxels which are completely intravascular. The signal drop during bolus phase dominated in all three acquired contrasts (Fig. 5.1) and, thus, reliable separation of the signal contributions was difficult in the abdominal aorta with the chosen FA of $\alpha = 90^\circ$ and the given CA concentration. This suggests the use of a lower FA for a similar setting in future experiments, e.g. $\alpha \approx 30^\circ$ [Cal13]. By the acquisition of multiple contrasts and the signal fitting procedure, the resulting concomitant T_1 -changes during the bolus phase can be avoided [Cal13]. For other major vessels in the arterial tree the bolus dispersion allows detection of the AIF and signal separation as shown in Figure 5.1 and in Appendix A.1.

Furthermore, the suboptimal choice of the FA introduced severe B_1 errors. A reduction of the applied FA to a value below the Ernst angle for an averaged, assumed T_1 of muscle tissue plus expected CA shortening of the relaxation time, will

counteract additional B_1 errors. The occurring distortion effects of (too) large FAs on the slice profiles for a given TR/T_1 were analyzed on a homogeneous cylinder phantom and presented in Section 5.3 and in particular in Figure 5.17.

In addition to unavoidable B_1 errors corrupting an ideal slice profile [You84], inflow effects may influence the MR signal, most of all in larger vessels. Global inversion or saturation pulses are often applied to minimize these effects [Hei+07; Jah+14], but are at the expense of temporal resolution which was not acceptable for the required parameters and, in particular for segmented sequences, signal homogeneity between excitations may be deteriorated.

Relation to other Techniques: The segmented EPI sequence with acceleration by SMS is expected to achieve similar image quality in terms of spatial accuracy compared to a single-shot EPI sequence with PI yielding a similar overall acceleration. The desired TEs restrict echo-spacing. A shortened echo train in PI-accelerated single-shot EPI reduces distortions, which may then appear at a similar level in single-shot EPI with PI and multi-shot EPI with SMS. Despite spatial accuracy, the SNR penalty in PI remains a clear drawback when compared to SMS. For a further reduction of the scan time in the future, the SMS method described here could be combined with standard k-space (under-)sampling strategies such as PI or keyhole methods [Set+12b; Fei+11]. Because SNR losses in SMS are limited to the g-factor [Set+12b], additional in-plane undersampling could be combined with SMS as long as induced CAIPIRINHA shifts do not negatively interfere. A large number of receiver coils as well as their sophisticated positioning can achieve a well-defined CoS profile to reduce g-factor limitations which are of high importance for these types of reconstructions (Sec. 3.2).

Moreover, segmentation of k-space data could allow retrospective acceleration. The acquisition of the individual segments distributes equally over the volume as illustrated in the sequence diagram in Figure 4.1. This results in temporally discrete EPI segments. Temporal resolution could be improved by 25% for the parameters used in this in-vivo perfusion study by omitting every other EPI segment and performing a PI reconstruction.

A sliding-window approach could be another reconstruction strategy where the most recently acquired segments update the oldest ones [DAr+02]. In the segmented EPI acquisition scheme a portion of low and high spatial frequencies, reflecting global CA enhancement and local details, is acquired in each segment and therefore, a frequent update of a portion of k-space could yield useful dynamic information.

9.1.1 Slice Profiles and MB RF Imperfections

In 2D MRI, ideal properties of the slice profiles are often assumed, e.g. infinitely steep edges and zero signal beyond the slice region, i.e. no side lobes. However, an ideal slice profile which is invariant to the scanning procedure and to different imaging parameters is an often improperly addressed issue for the measurement of relaxation times [McR+86]. Errors in relaxation time calculations due to slice profile imperfections become more severe for smaller T_R/T_1 [You84; McR+86]. Already relatively small variations in TR alter the slice profile, unless $T_R \gg T_1$ [You84]. Therefore, protocols with TR variations are not qualified to measure T_1 reliably. This also suggests that larger FAs increase the effect of slice profile imperfections for a given TR and prevent quantification. It can be seen from Section 5.3 that for the chosen T_R/T_1 these physical properties severely corrupt the slice profile and therefore hamper quantitative analysis.

Slice Profile Analysis: If directly compared, the absolute signal strength differs for some settings between MB and SB RF pulses as determined by the mean signal across all slice profiles (Sec. 5.3). Larger side lobes in the MB pulses are likely to reduce available magnetization in neighboring regions and therefore lower the final signal. However, when normalized to peak signal, the slice profiles highly match each other as shown in the normalized plots in Section 5.3. Obvious signal attenuations at edge positions within a MB slice group as reported in [Set+12a; Bar+15] were not seen. These inter-MB-slice-group saturation effects appear because of an interleaved slice acquisition scheme in combination with an even number of MB slice groups. In the presented work, however, the chosen gap between slices may likely be sufficiently large, such that this type of cross-talk has no or only little effect.

Limitations of the MB RF Pulse: Special care has to be taken on specific absorption rate (SAR) limitations [Bar+15] and maximum output voltage capabilities of the transmission hardware [Abo+17b]. The simple summation of phase modulated single slice RF pulses to achieve a MB excitation comes at the cost of higher additional modulation frequencies and increases roughness of the RF pulse's envelope [Gri+10]. This might cause conflicts with some hardware components and limit the optimal performance of the transmitter unit [Sco12; Abo+17b]. As reported in Section 5.3, by taking B_1 imperfections due to the demanding MB RF pulses into account when calculating the reconstruction weights, the level of slice specific distortions can be reduced. The recovered signal intensity in the MB images matches the SB reference more correctly as if ACS are delivered by SB acquisitions only (Fig. 5.19). Reductions in TR, which are essential in SMS, will emphasize these effects because interference of off-resonance excitations with adjacent slices of other MB slice groups

may increase.

However, these variations caused by the MB excitation have to be traded against inter-slice leakage which can be reliably blocked by SSG and depends mainly on the spatial configuration of the receiver coils and the distance between the slices in one MB slice group [Cau+14]. In addition, the acquisition of separate MB ACS source and SB ACS target data is prone to any motion and might therefore result in a mismatch between ACS source and target if motion can not be controlled sufficiently.

9.2 Deep Learning in SMS

The presented, novel reconstruction technique for SMS explores DL aided MR data processing to allow SMS reconstructions without the need of any reference data. SMS as a cutting edge acceleration technique and DL as a versatile concept in modern computer science were combined and investigated. Reduced amounts of reference data are also considered in iterative reconstruction methods, such as SMS-NLINV [Ros+17], however, reference data can not be avoided completely and iterative algorithms may require scan specific adjustment. SMSnet disentangles overlapping slice signals without the need of any reference data and scan specific model adjustments. Acquired SMS data of all coil elements are presented to the network's input in k-space and image domain. At its outputs, magnitude images of the separated slices are then provided. The potential and limitations of SMSnet were investigated in various experiments in Chapter 8. In addition to visual inspection of the reconstructed images, different metrics have been calculated to quantify the results and allow comparison with split slice-GRAPPA. Until now, the introduced concepts have only been tested for a fixed configuration of receiver coils, i.e. a 20-channel head coil. The extension of this technique to flexible coil arrangements will be topic of future research.

Architecture: Overfitting is one of the most crucial aspects of DNNs [GBC16], this was closely considered during the design phase of SMSnet and was investigated carefully. SMSnet consists of at least three paths: the CoS-path and the Im-path which are fused into the Merge-path. No convolutional layers, which are well suited for image recognition tasks [LYH15], were inserted to the Im-path. Thereby, the risk of overfitting and memorization of image content is reduced. 2D convolution layers were inserted before the FFT in the CoS-path, where only data in k-space domain serve as input which have no spatial correlations. The majority of trainable parameters is in the CoS-path. With 17 layers with non-linear activation functions, this part certainly represents a *deep* neural network. In comparison, the Im-path (three layers) and the Merge-path (four layers) are rather shallow. The developed architecture was inspired by existing reconstruction algorithms for SMS that merge

pre-calculated unfold images and collapsed image signals to unwrap SMS data.

Image Quality: Chapter 8 begins with the examination of the image quality obtained after SMSnet reconstruction. This is compared to established SMS reconstruction strategies. As discussed in Section 9.1.1, reconstructions with SSG outperform these with SG if a perfect imaging process can be assumed and no additional bias because of the MB excitation is introduced [Cau+14]. In Part III, synthetic SMS data were used primarily. Therefore, the reconstruction can be considered as free from any SMS-sequence-specific bias. Hence, SSG reconstructions were compared with reconstructions of SMSnet. It was shown that a referenceless DL-based approach can separate overlapping image content in SMS data independent of the applied CAIPIRINHA pattern. Evaluations were performed on images taken from measurements of a volunteer’s head. SMS test data with $MB = 2$ and $FOV_{\text{shift}} = 1/4$ guaranteed significant overlap of slice contents. The general, non SMS-specific image quality is comparable with conventional approaches, however, signal from overlapping slices could not always be removed completely. Conventional SSG_{std}, with correct ACS outperformed SMSnet in any experiment. Results in Section 8.1.1 reveal that artifacts in the SMSnet reconstructions are more localized to regions inside the object and partly reflect signal offset between REF and SMSnet. Nevertheless, it was shown that SSG reconstructions where correct ACS data are missing exhibit SMS-specific leakage artifacts which can be eliminated better by SMSnet in most cases. These results were confirmed by a set of different experiments on phantom data.

Phantom Data: To investigate the quality of reconstructed images, but also potential overfitting of SMSnet, various phantom experiments were performed. Phantoms allow good control of the image content, in particular, defined and homogeneous contrast (spherical phantom), clear structures (structural phantom), fine patterns (noise-structure phantom) and variation in shape, symmetry and positioning (two gel phantoms). Data of a homogeneous cylinder phantom were included into the training data, because its 2D slices appear very similar to images of the sphere phantom used for testing. However, both objects are expected to have different characteristics in CoS and, therefore, experiments with these phantom data are interpreted as a counterevidence for overfitting. The predictions of SMSnet trained *with* data of a cylinder phantom did not improve the reconstructions of the spherical phantom test data any further. This suggests, that overfitting to shapes or structures during training is unlikely. SMS data from other phantoms could also be separated. In particular, the reconstructions of the noise-structured phantom and the gel phantoms confirm that SMSnet generalizes sufficiently.

Robustness and Signal Sensitivity: Noise propagation and reconstruction-related noise enhancement were investigated in form of g-factors to quantify the robustness of the technique to signal fluctuations. Moreover, severe changes in the coil sensitivities were mimicked by replacement of the true signal in some coil elements by artificial noise signal. This simulated imaging situations in which high local susceptibility gradients may degrade the MR signal. Despite an obvious reduction in SNR because of the reduced number of coil elements which contribute to the image, SMS slices can be separated robustly. In contrast to SNR in regions with object signal, average noise-level in background is reduced during SG reconstruction. Reduced noise-level in background results from decorrelation of signal content in the individual receiver coils inherent in the SSG algorithm and similar to pre-whitening. However, robustness is often traded for sensitivity. SMS data for BOLD imaging were reconstructed successfully which verifies the sensitivity of SMSnet to small signal changes. Its potential for fMRI may be of particular interest, because SMS has had a high impact in fMRI [Cau+14; Kun+17], e.g. SMS was used in fMRI protocols in the Human Connectome Project [Hea]. Acceleration in SMS benefits from reduced TR while keeping TE, which is essential in T_2^* -weighted imaging.

Motion: MRI is inherently sensitive to motion. Accelerated imaging reduces vulnerability to motion artifacts because the acquisition time and, hence, the risk of motion induced errors decline. Motion during data acquisition and its effect to SMSnet reconstructions was not investigated in this work. However, motion between repeated measurements as it can appear during long scan times, e.g. dynamic protocols, was simulated. Positional changes influence CoS and are therefore problematic for SMS reconstruction algorithms which rely on reference data. DL-based reconstruction methods may unveil their potential for these types of MRI protocols. Although, the given results for SMSnet do not outperform SSG, the extension of SMSnet to moving objects is appealing. Dynamic MR scans with controlled motion are easy to conduct and provide larger amount of training data compared to structural imaging.

Reconstruction Speed: Once trained, the network reconstructs prepared SMS data fast, because no time consuming calculations are required. For example, images of size (128 x 128) from measurements containing 101 MB slice groups with two slices each are separated in less than 30 seconds. Reconstructions with slice-GRAPPA are computational demanding and are thus likely benefit from fast hardware and parallelization, too. However, one main difference between both is that DL-based approaches without further training are reduced to basic operations while GRAPPA-like methods normally require numerical algorithms to solve an inverse problem. A main limitation for convenient application of the proposed method is data handling,

i.e. transfer to appropriated hardware. Further work could address these practical limitations which would also be beneficial for generalization of SMSnet to other coil configurations and MR machines.

Input Data Manipulation and Model Interpretation: Hidden layer activations were investigated. The results in Section 8.3 and 8.4 suggest, that weight and bias adapt to variations at CoS-path input during training, however, they adjust their values to be robust to these input variations. In general, non-zero activations, e.g. by a constant or noisy signal, seem to be more relevant than the correctness of input data. Therefore, k-space input may be handled as random input rather than as true k-space signal with a correlation to the image input. Because biases are also adjusted during training, these may dominantly determine the behavior of the CoS-path. From a computer science perspective, this can be interpreted as regularization complementary to dropout, because input is not captured as coherent signal but as rather erratic activations. Interpretation in a physical meaning is that weights and, in particular, biases in the CoS-path encode generic *unfold images* as known in GRAPPA (Sec. 3.2.2). Activations at the input layer may fine-tune these generic unfold images. The unfold images relate to the coil sensitivities which in turn vary for the different training data, but also share identical properties such as coil positions, reception characteristics and correlations (Sec. 3.2). DL is characterized by multiple levels of representation for an input which are detected automatically during training [LYH15; Hin07]. This makes it difficult to determine the cause of learned representations explicitly. However, because the architecture of SMSnet was inspired by conventional reconstruction algorithms for SMS, the observed properties of the trained network match the intended idea. On one hand, the CoS-path of SMSnet, which contains the majority of trainable parameters, creates generic masks similar to unfold images in GRAPPA. These adapt only weakly to a given input. On the other hand, the Im-path which operates only along the channel dimension transforms the physical input channels, i.e. coil signals, such that these match the CoS masks with respect to the slice position. After multiplication of both maps, CoS mask and image, the number of channels is reduced to a single channel output in the Merge-path. This can be interpreted as a coil combination procedure. Because target data during training were SoS combined images, the Merge-path might probably have approximated this coil combination. In this case, it is beneficial, that SoS is a robust combination method that approximates SNR optimum in many cases [Lar+03].

Limitations: Until now, SMSnet was only trained and tested for head coil data. Its performance for flexible coils is unknown. Because CoSs in flexible coils vary stronger and erratically, the complexity of the separation procedure will increase. Nonetheless,

as one key aspect of DL is its data driven model adjustment, appropriated training data may cover the complexity of CoS variations. Furthermore, mathematical transformation based on singular value decomposition or principle component analysis can be applied prior training to make data, and specifically their CoS attributes, more consistent. Transformations from the physical coils to another set of virtual coils were successfully utilized to improve reconstruction of undersampled MR data [Uec+14].

Reconstructions for higher acceleration factors did not perform well. Although, the mean values of MSE and SSIM suggest a decent performance of SMSnet, visual inspection reveals SMS specific artifacts which confirm that SMSnet performs weak on the tested data for $MB = 3$ and $MB = 4$. Therefore, reliable quantification should be considered carefully. It is likely, that the decreased number of available training data, because less pairs of source and target data can be synthesized (Tab. A.6) are too little. In particular, because the number of trainable parameters in SMSnet increases at the same time for SMSnet architectures for higher MB factors. Another data related issue may be the broad spectrum of phantom data used for training. Even though, large amount of data influence training, in general, positively, abstract phantom data for training may have negative influence on the performance on in-vivo data. For reconstructions of SMS data of the head it may be beneficial to primarily collect head data for training as the variance in structure and shape for heads may be considered as relatively small.

Further Comments: Trainings were also repeated with weight regularization as introduced in Section 6.2.2 to investigate the influence of regularized weight adjustment. However, weight regularization did not improve the training process, but reduced the prediction precision in the test data used for visual monitoring. Therefore, no weight regularization was applied in later trainings. In particular, because other mechanisms and ideas were in place to avoid overfitting and ensure generalization. Even if the test on cross-system transferability (Sec. 8.1.7) failed in terms of reconstruction quality, it might give insight into the 'what' was learned during training of SMSnet. As the nominal properties of the compared MR systems are identical or at least similar, and head coil and object were arranged similar, too, one crucial property which is likely to differ between both systems is B field shimming and the reception characteristic of the single coil elements which can vary within the product specifications. Both represent changes in the CoS profile of the MR system and this is what should be explicitly learned during training of SMSnet.

In summary, DL-aided and -based MR image reconstruction approaches promise significant advances as indicated in following paragraph. Accelerated imaging without acquisition of additional reference data may reveal untapped potentials of SMS MRI.

For example, in imaging situations where sampling of ACS is challenging because of respiration and motion [Pol+15] as well as for structural (single-volume) imaging where the acquisition of fully-sampled reference data has an unacceptable time penalty [Bar+15].

As highlighted at the beginning of this work, deep learning has rapidly gained interest in the MR community. For some years, DL has already been successfully applied to medical imaging [Wan16]. However, while typically problems in medical imaging are segmentation and classification of data in the image domain, DL-based reconstruction of sensory data, i.e. k-space data in MRI, was not available for a long time. For medical imaging in general, DL is already seen as a paradigm shift [Wan16] and it may affect MRI reconstruction similarly in the future. A selection of suggested publications will follow at the end of this discussion, because these works demonstrate the impact of DL to MRI. Recently published methods like AUTOMAP [Zhu+18], where the entire reconstruction from sensor domain to image is performed by a DNN raised attention for various image reconstruction tasks. Conversely, RAKI [Bil+18] only replaces the GRAPPA algorithm with a non-linear convolutional neural network. It is interesting that RAKI is trained on scan-specific ACS only to reconstruct data in parallel imaging. This appealing concept to avoid databases for training of a NN was also extended to SMS [Moe+18]. Recently, a DL-based approach for navigator-free phase estimation in multi-shot EPI called NEATR was presented [Bil+18]. It realizes a synergistic combination of a convolutional NN to estimate phase variations and physics-based reconstruction which use estimated solution of the neural network to improve reconstruction. Therewith, NEATR addresses the complexity of the input output mapping of neural networks, which are difficult to characterize.

The difficult interpretability of the processing steps inside a NN, i.e. the trained model, is a major point in current discussions [MSM18]. In particular, for clinical applications interpretability is important, because made decisions may have serious consequences. As described previously, the architecture of SMSnet addresses this issue. In comparison to the solutions above, SMSnet's approach with its double input for k-space and image data represents a novel architectural concept in which training may benefit from either domain. As for conventional reconstruction methods, a fair comparison between network architectures will be of interest to establish DL-based approaches for image reconstruction. However, data used for training and evaluation play an important role and generalization is closely linked to data quality. Therefore, shared data bases and challenges as in other computer scientific disciplines may be of particular interest in the MR community and an essential step to proceed with DL-based solutions for MRI reconstructions.

10 Conclusions

In conclusion, it has been demonstrated that the incorporation of SMS into multi-echo, multi-shot EPI can overcome existing limitations in dynamic MRI. The accelerated acquisition allows fast ($\Delta t \leq 1.5$ s), repetitive measurements of multiple echoes which are required for a signal separation procedure into its T_1 dominated S_0 and T_2^* components. The presented technique retains the temporal and spatial resolution even for relatively large FOVs that encompass a feeding artery for AIF detection. SMS is beneficial compared to in-plane acceleration, i.e. PI, because SNR is only reduced by the g-factor and not by the square-root of the acceleration factor \sqrt{R} . The effects of sequence imperfection, in particular the MB RF pulse interference, and the possible impact of the varying image contrast on reconstruction algorithms were evaluated. Based on these investigations, it was shown that a constant SG kernel, calculated from measured source and target ACS, reconstructs four-fold accelerated SMS data reliably ($MB = 4$) and avoids contrast dependencies of the reconstruction. This allows dynamic data to be successfully separated into individual signal contributions that provide additional information for comprehensive pharmacokinetic modeling. A novel deep learning-based reconstruction technique was introduced and systematically investigated. SMSnet demonstrates the reconstruction of collapsed SMS data in a referenceless approach. This overcomes the need to acquire scan-specific reference data to assess coil sensitivity information required for reconstruction of slice-undersampled data. This innovative part of the work entered a new field of research: the combination of SMS, an important MRI acceleration technique, with concepts of deep learning. Therefore, the presented methods have a strong exploratory character. Compared to acceleration factors realized in state-of-the art parallel imaging and SMS, the shown results for an acceleration by two may no impress, however, it can be claimed that SMSnet's potential has just been revealed.

Part V

Appendix

A Appendix

A.1 Signal-Dynamics in In-vivo Perfusion Experiments: Further Subjects

In this section, the signal dynamics and calculated S_0 - and T_2^* -dynamics for three further subjects are given. In addition, each figure provides an anatomical overview to show selected ROIs.

Signal dynamics for subject #2

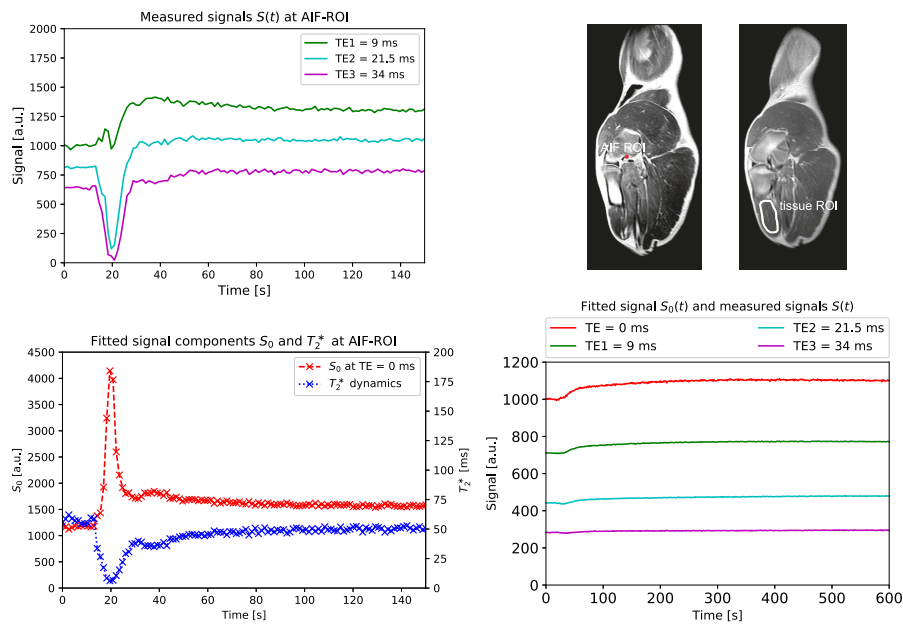


Figure A.1: Subject #2. Dynamics of the measured signal (TE_1 , TE_2 , TE_3) (top left) and separated signal components (S_0 , T_2^*) (bottom left) during the CA bolus phase in a single voxel (AIF ROI). In contrast to the AIF the extravasation process into muscle tissue is selected from a larger ROI (tissue ROI) removing underestimation of the dynamic signal ($TE=0$ ms) due to T_2^* -effects if compared to the directly measured signals (TE_1 , TE_2 , TE_3).

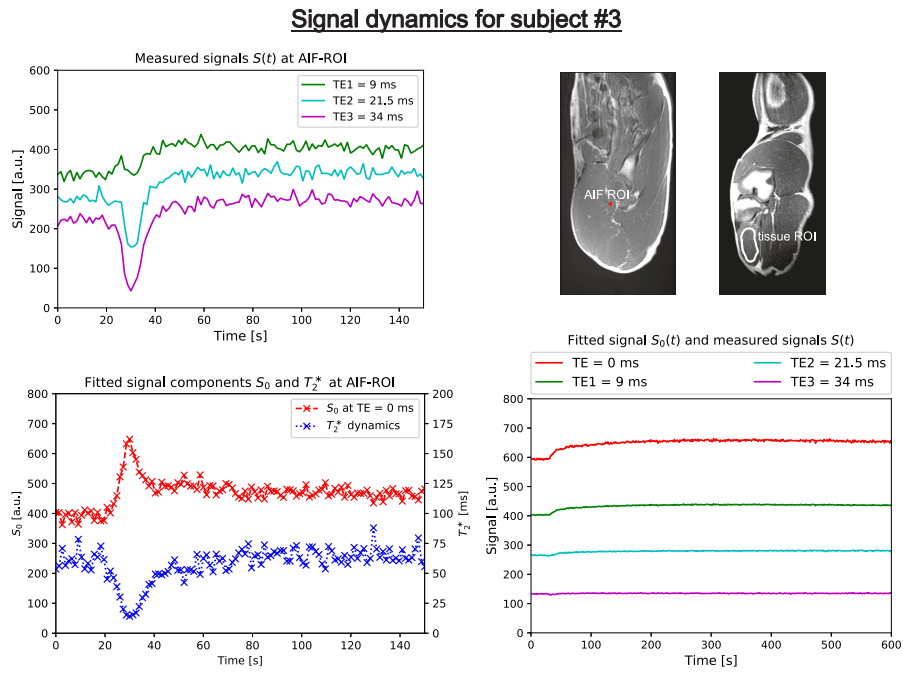


Figure A.2: Subject #3. Dynamics of the measured signal (TE_1 , TE_2 , TE_3) (top left) and separated signal components (S_0 , T_2^*) (bottom left) during the CA bolus phase in a single voxel (AIF ROI). In contrast to the AIF the extravasation process into muscle tissue is selected from a larger ROI (tissue ROI) removing underestimation of the dynamic signal ($TE=0$ ms) due to T_2^* -effects if compared to the directly measured signals (TE_1 , TE_2 , TE_3).

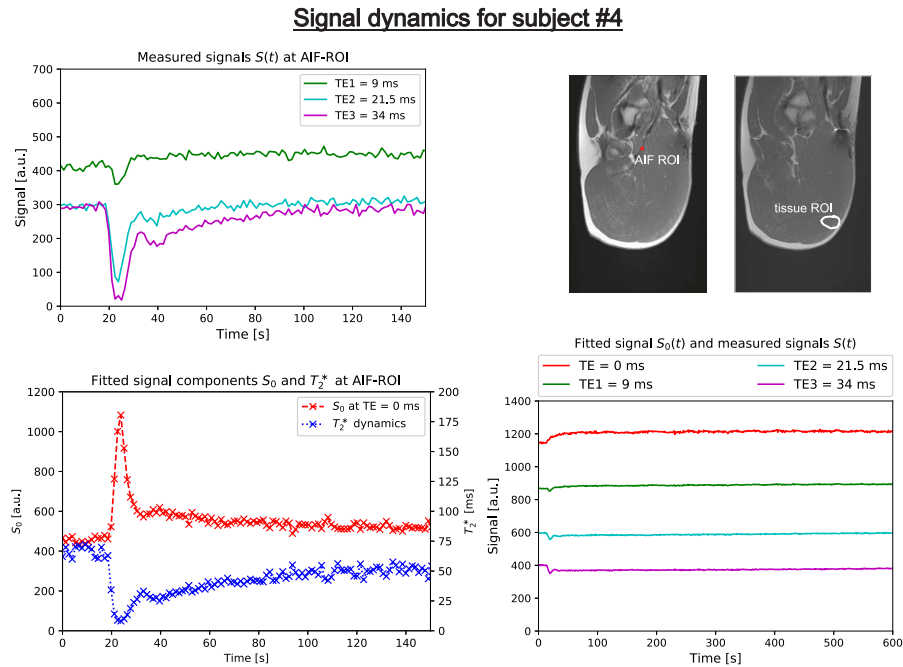


Figure A.3: Subject #4. Dynamics of the measured signal (TE_1 , TE_2 , TE_3) (top left) and separated signal components (S_0 , T_2^*) (bottom left) during the CA bolus phase in a single voxel (AIF ROI). In contrast to the AIF the extravasation process into muscle tissue is selected from a larger ROI (tissue ROI) removing underestimation of the dynamic signal ($TE=0$ ms) due to T_2^* -effects if compared to the directly measured signals (TE_1 , TE_2 , TE_3).

A.2 SMS Reconstruction for In-vivo Perfusion Experiments - Further Subjects

In the following section, the evaluations of the SMS reconstructions as described in chapter 4 are summarized for three additional subjects. Besides the normalized subtraction and g-factor maps, histograms are given to assess overall performance for the different reconstruction approaches.

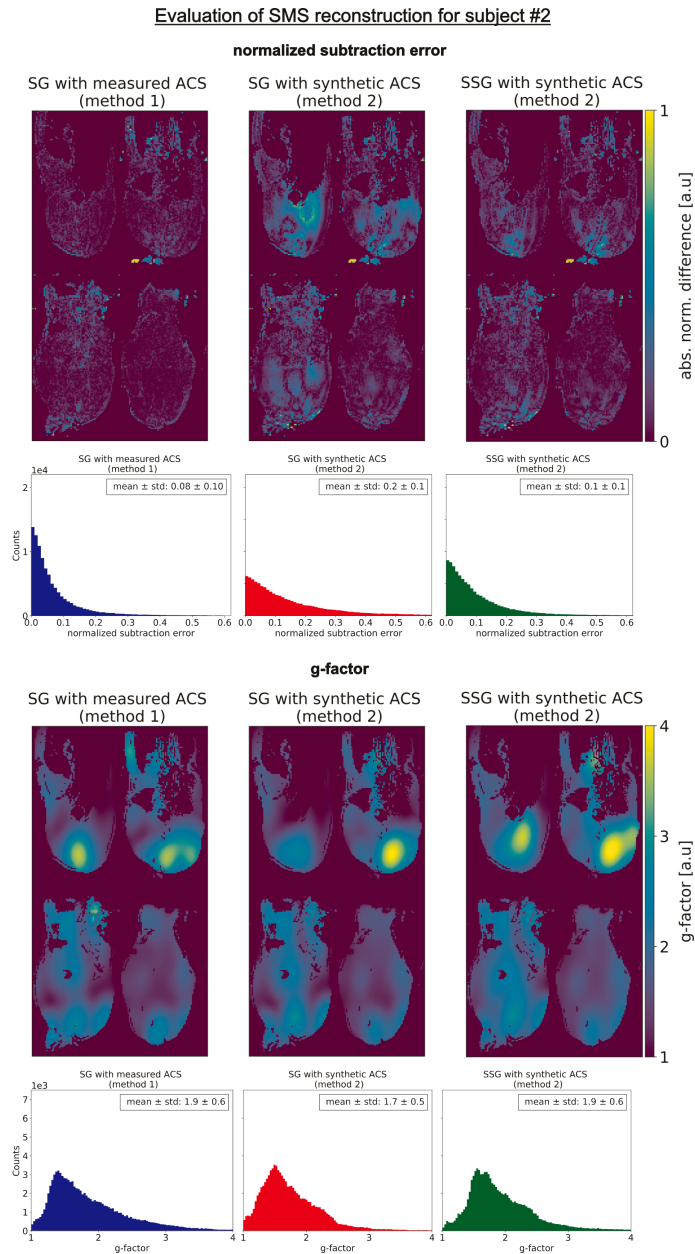


Figure A.4: Subject #2: Evaluation of different SMS reconstruction approaches. Four representative slices from one MB slice group are shown as maps for the normalized subtraction-error compared to a SB acquisition and for the g-factor resulting from the SMS reconstruction. Histograms below each map summarize the respective metric across all 24 slices. Mean and standard deviation are displayed in the top corner of the histograms.

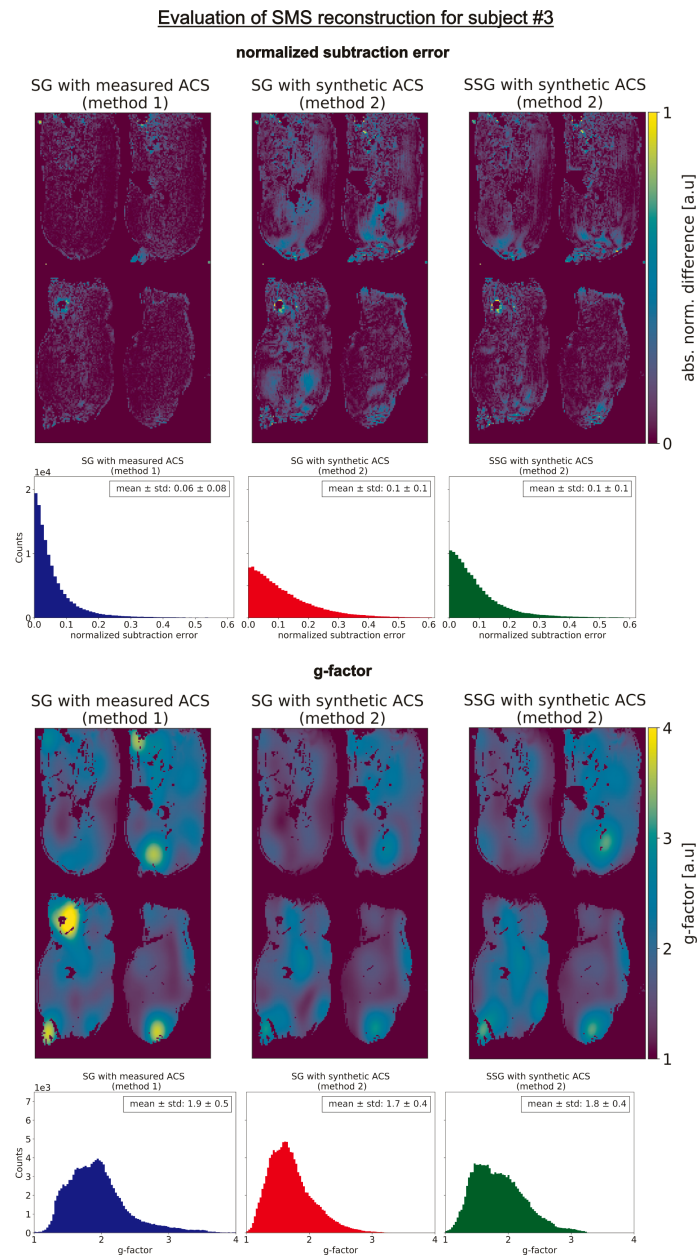


Figure A.5: Subject #3: Evaluation of different SMS reconstruction approaches. Four representative slices from one MB slice group are shown as maps for the normalized subtraction-error compared to a SB acquisition and for the g-factor resulting from the SMS reconstruction. Histograms below each map summarize the respective metric across all 24 slices. Mean and standard deviation are displayed in the top corner of the histograms.

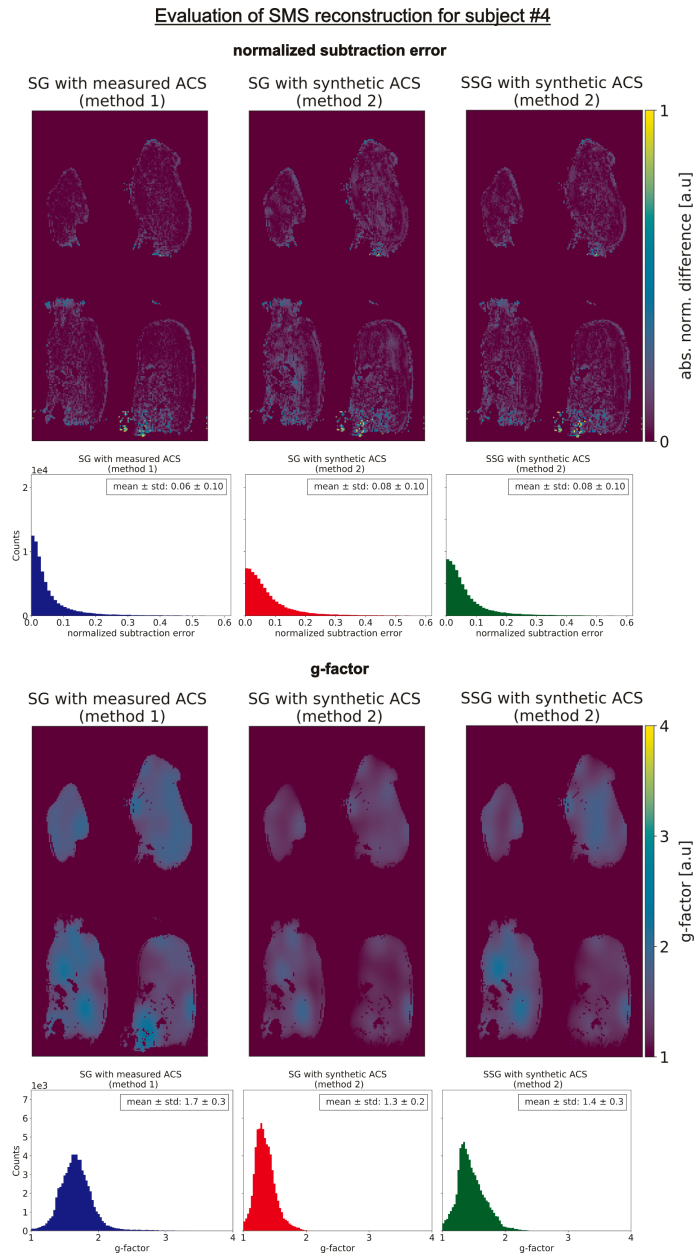


Figure A.6: Subject #4: Evaluation of different SMS reconstruction approaches. Four representative slices from one MB slice group are shown as maps for the normalized subtraction-error compared to a SB acquisition and for the g-factor resulting from the SMS reconstruction. Histograms below each map summarize the respective metric across all 24 slices. Mean and standard deviation are displayed in the top corner of the histograms.

A.3 Bias-Variance Dilemma

As discussed in Section 6.2.3, the bias-variance trade-off, or dilemma, describes the conflict in trying simultaneously minimize bias and variance. The essence of the dilemma is that a prediction error of a model can be decomposed into two components: bias, reflecting erroneous assumption in the model and variance, which accounts for the sensitivity of the model to small fluctuations, e.g. noise, in the training data. For an expected value of the $E[E_{\text{MSE}}]$, the decomposition follows as:

$$E[E_{\text{MSE}}] = \text{Bias}[y]^2 + \text{Var}[y] + \sigma_{\text{irr}}^2 \quad (\text{A.1})$$

with the bias

$$\text{Bias}[y] = E[y - a] , \quad (\text{A.2})$$

which can be seen as an incorrect model with too many simplified assumptions, and

$$\text{Var}[y] = E[(y - E[y])^2] , \quad (\text{A.3})$$

the variance describing the offset between the model prediction and the expected mean. Here, $E[\]$ denotes expectation values and have to be distinguished from the previously defined loss functions (Sec. 6.2.1) and σ_{irr}^2 represents the lower boundary of the model in form of an irreducible error term.

According to this dilemma, an (incorrect) model with high bias leads to low variance, and vice versa. Thereby, a model, i.e. a NN, which is sufficiently versatile to reasonably approximate a broad range of input to target mapping, is necessarily sensitive to the idiosyncrasies of the data used for its training [GBD92]. A (very) large data set will be required to reduce overfitting of the model to the particular training data, this is why data augmentation has gained large interest in the supervised learning, notably when access to large data bases is limited, i.e. for medical data due to privacy policies.

A.4 SMSnet: MR Protocol for Data Acquisition

MR protocols:	MPRAGE	Gradient-echo	SMS
Objects	head & phantom	head & phantom	head
Type	3D	2D	2D
N_z	202	6	3 x 2 (for MB=2)
Δz	1 mm	5 mm	5 mm
z_{gap}	0	300 %	500 %
$\text{FOV}_x \times \text{FOV}_y$	256×256	300×300	300×300
$N_x \times N_y$	128×128	128×128	128×128
FA	8°	70°	30°
TE	2.45 ms	4.9/9.68/14.46 ms	4.9 ms
TR	1900 ms	126 ms	126 ms
TI	900 ms	0	0

Table A.1: Data for training and evaluation of SMSnet were acquired with different MR protocols. Most data were measured with identical protocols. These protocol parameters are listed above.

A.5 SMSnet: Additional Figures and Tables

A.5.1 Phantom Data

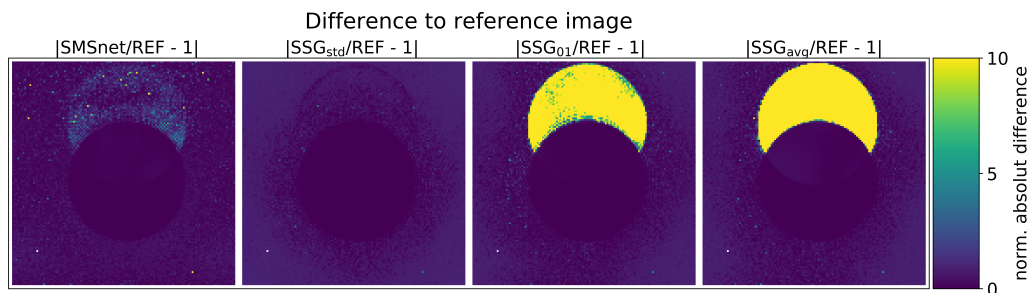


Figure A.7: Normalized difference maps for spherical phantom. Range of values adjusted to address scaling issues for low background signal.

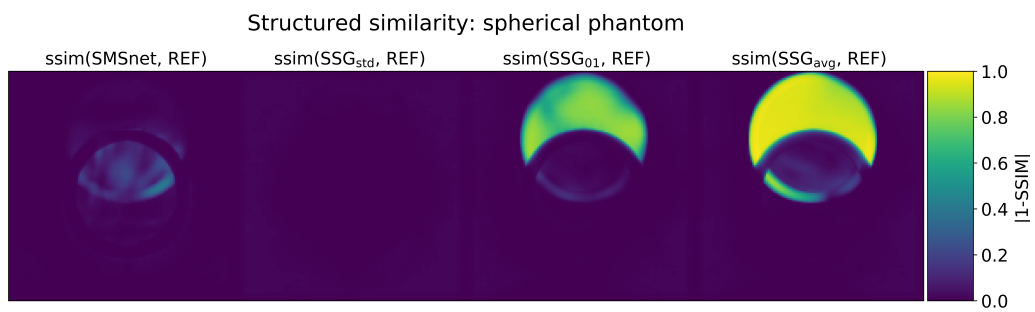


Figure A.8: SSIM maps for spherical phantom.

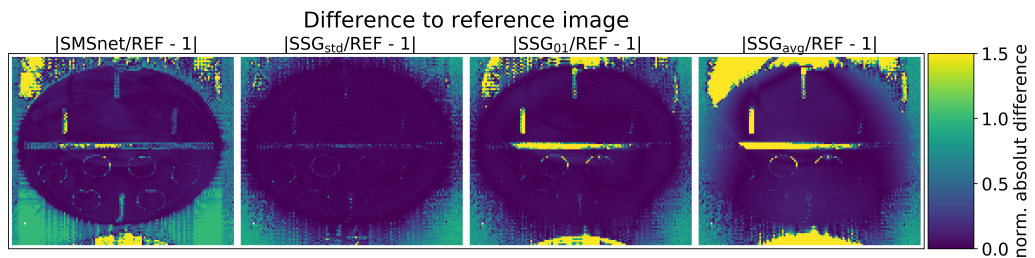


Figure A.9: Normalized difference maps for structured phantom.

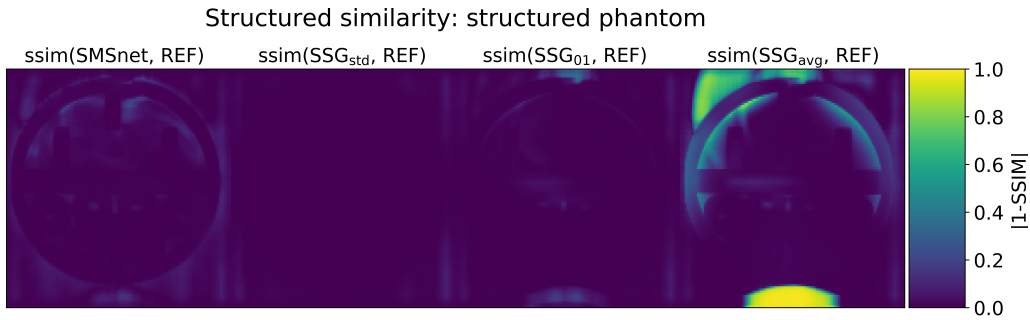


Figure A.10: SSIM maps for structured phantom.

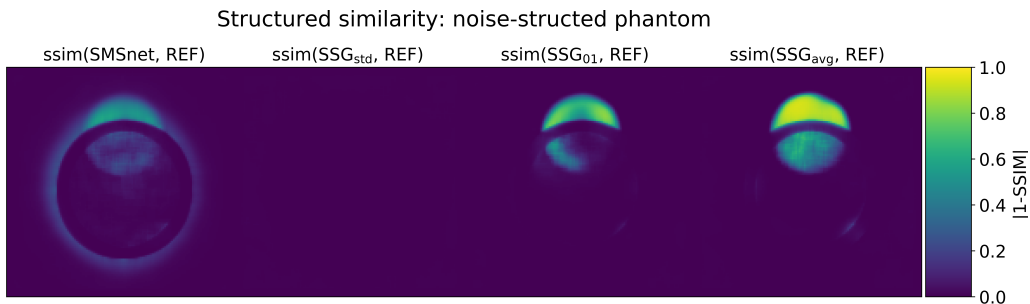


Figure A.11: SSIM maps for noise-structured phantom.

Noise-structured phantom				
Mean values across volume				
	SMSnet	SSG _{std}	SSG ₀₁	SSG _{avg}
MSE [10^{-4}]	11.7 ± 0.76	0.05 ± 0.008	8 <i>pm</i> 2.8	16 <i>pm</i> 15.3
SSIM [10^{-1}]	8.9 <i>pm</i> 0.53	9.9 ± 0.03	9 ± 0.45	8.8 ± 0.47
$\text{corr}(I_s, I_{s,\text{REF}})$ [10^{-1}]	9.9 ± 0.1	1 ± 0.001	9.9 ± 0.03	9.9 ± 0.01
$\text{corr}(I_s, I_{s+(Ns/MB),\text{REF}})$ [10^{-1}]	2.2 ± 0.35	1.96 ± 0.001	2.4 ± 0.29	2.6 ± 0.22

Table A.2: Evaluation of SMSnet reconstruction in comparison with SSG on artificial ex-vivo data. Base-data was acquired in a spherical phantom to which artificial noise-like structure was added. The mean values of MSE and SSIM across all 6 slices of the volume are given, as well as the intra- and inter-slice correlations.

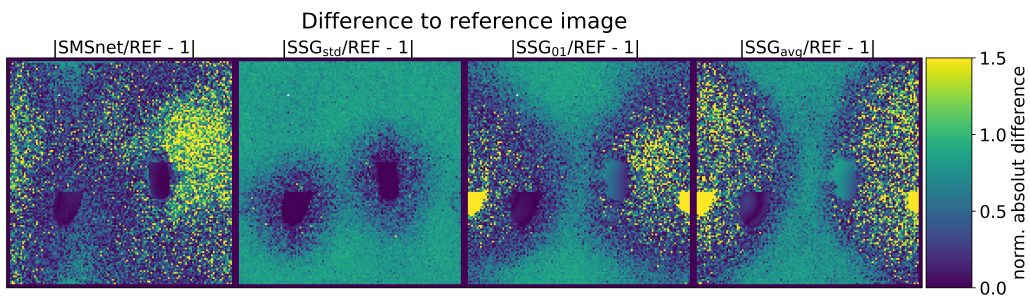


Figure A.12: Normalized difference maps for gel phantoms.

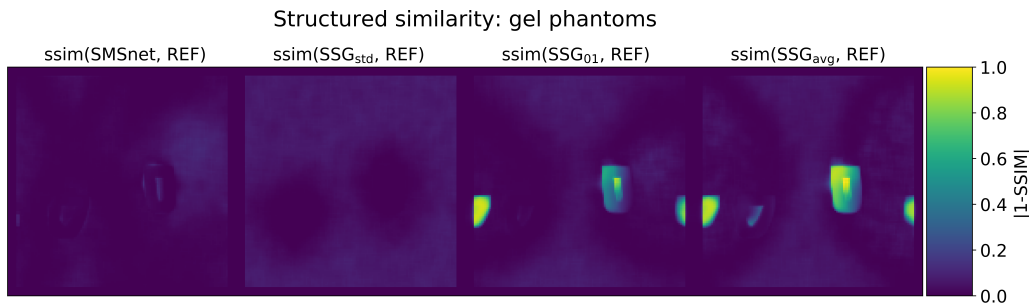


Figure A.13: SSIM maps for gel phantoms.

Gel phantoms				
Mean values across volume				
	SMSnet	SSG _{std}	SSG ₀₁	SSG _{avg}
MSE [10^{-3}]	0.21 ± 0.17	0.04 ± 0.02	0.91 ± 0.59	2.92 ± 2.28
SSIM [10^{-1}]	9.17 ± 0.54	9.3 ± 0.33	9.42 ± 2.32	9.25 ± 0.34
$\text{corr}(I_s, I_{s,\text{REF}})$ [10^{-1}]	9.81 ± 0.18	9.99 ± 0.01	9.16 ± 0.54	7.65 ± 2.1
$\text{corr}(I_s, I_{s+(\text{Ns}/\text{MB}),\text{REF}})$ [10^{-1}]	0.17 ± 0.31	-0.17 ± 0.01	2.07 ± 0.35	3.51 ± 0.14

Table A.3: Evaluation of SMSnet reconstruction in comparison with SSG on artificial ex-vivo data. Base-data was acquired in a spherical phantom to which artificial noise-like structure was added. The mean values and their standard deviation across all 6 slices of the volume are given, as well as the intra- and inter-slice correlations.

A.5.2 Robustness to Object Motion

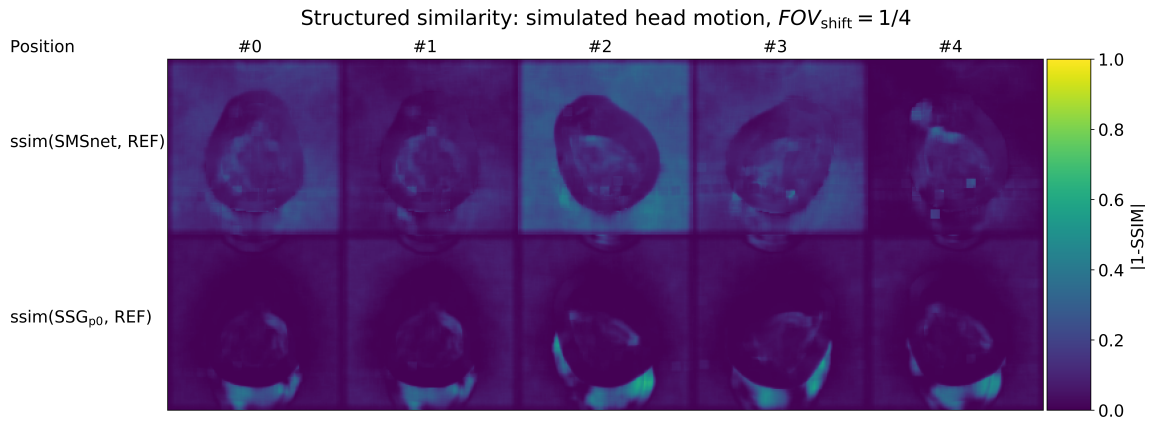


Figure A.14: Reconstruction of data with simulated head motion, SSIM.

A.5.3 Severe Changes in the Coil Sensitivities

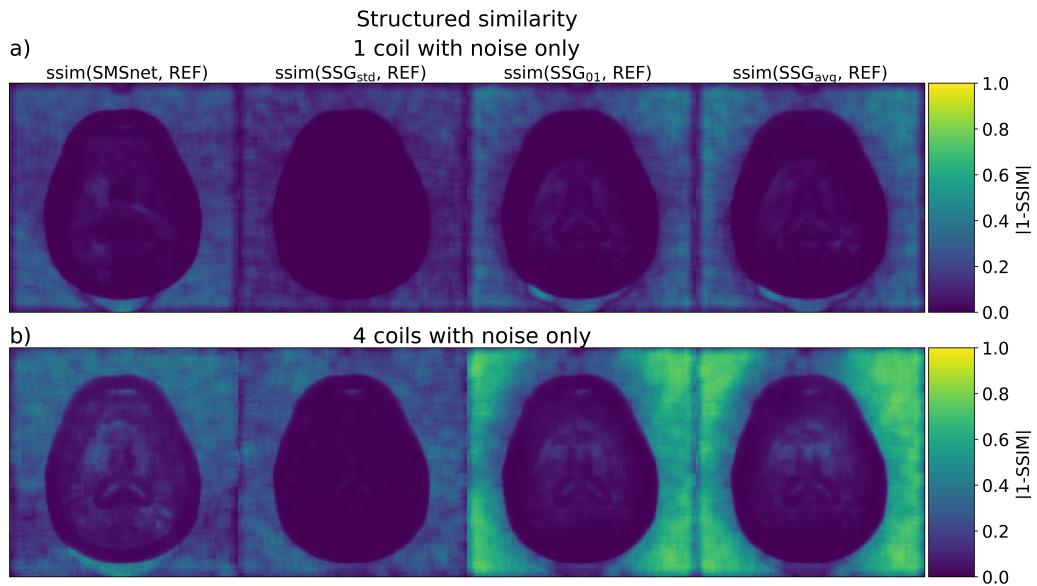


Figure A.15: SSIM maps for reconstructions in case of severe changes in the CoSs, e.g. by noise-only contributions in some coils.

A.5.4 Cross-System Transferability

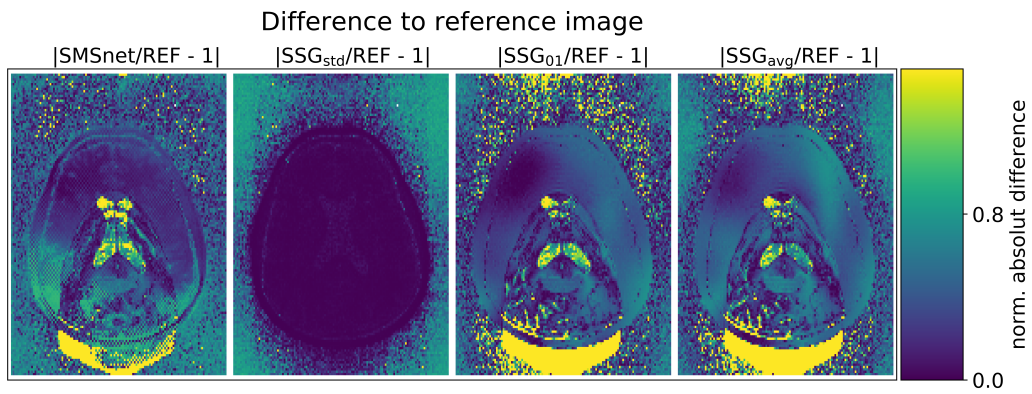


Figure A.16: Normalized difference maps for cross-system reconstructions.

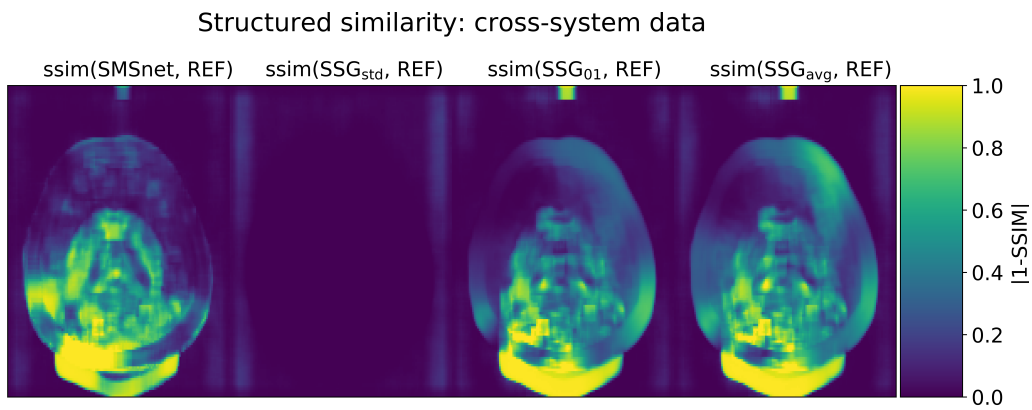


Figure A.17: SSIM maps for cross-system reconstructions.

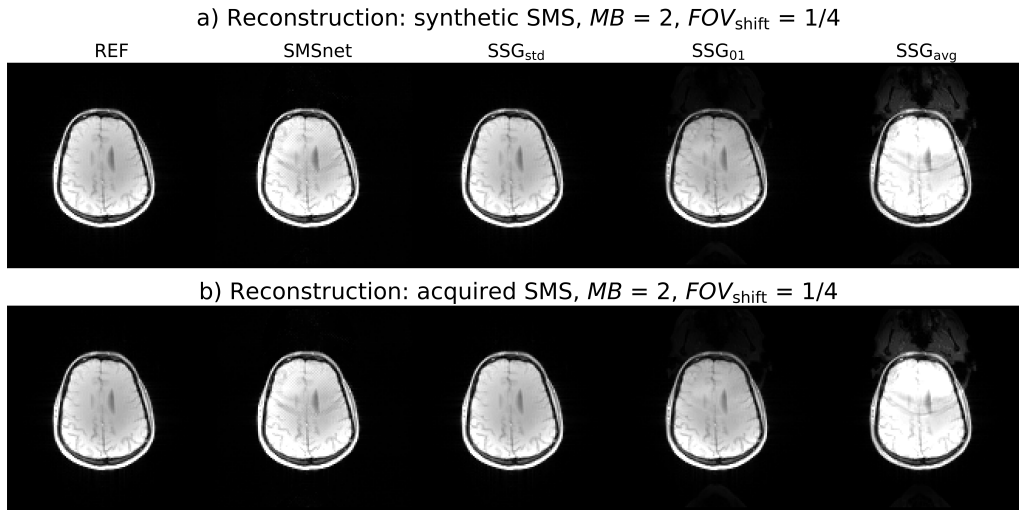


Figure A.18: Image reconstructions of synthetic and acquired SMS data are shown for direct comparison. Raw data were either synthesized (a) or acquired (b) representing SMS data with $MB = 1$ and $FOV_{\text{shift}} = 1/4$.

A.5.5 Higher Acceleration Factors

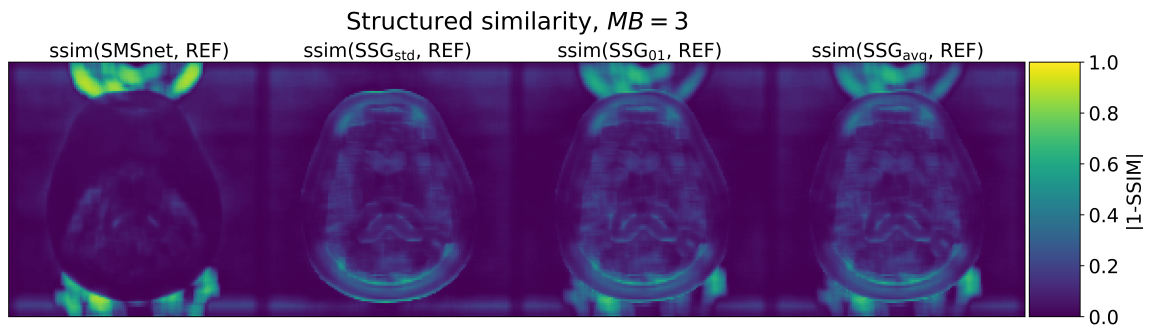


Figure A.19: SSIM maps for $MB = 3$ data.

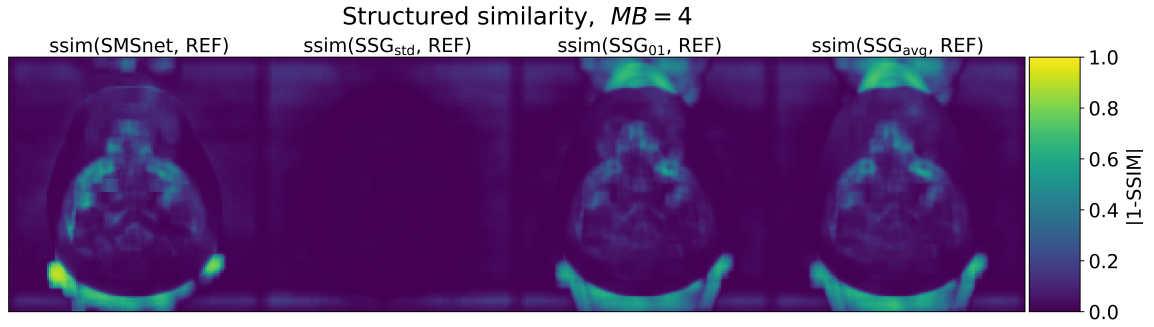


Figure A.20: SSIM maps for $MB = 4$ data.

A.5.6 Manipulation of Input Data

Controlled input manipulation					
Mean values across volume, SMSnet					
	std	$IN_{ks} = 0$	$IN_{ks} = 1$	IN_{ks} is noise	IN_{ks} & IN_{im} are noise
MSE [10^{-3}]	2.75 ± 12.61	3.03 ± 1.162	2.11 \pm	2.39 ± 9.89	96.5 ± 49.81
SSIM [10^{-1}]	9.19 ± 1.84	9.1 ± 1.81	9.23 \pm	9.13 ± 1.53	0.84 ± 0.71
$\text{corr}(I_s, I_{s,REF})$ [10^{-1}]	9.61 ± 1.62	9.52 ± 1.62	9.73 ± 1.17	9.67 \pm	1.42 ± 1.27
$\text{corr}(I_s, I_{s+(Ns/MB),REF})$ [10^{-1}]	3.43 ± 0.24	3.8 ± 0.59	3.54 ± 0.28	3.58 \pm	0.96 ± 0.8

Table A.4: Evaluation of the reconstruction results of SMSnet, if the k-space input data IN_{ks} and/or image input data IN_{im} were manipulated. Mean values across all 202 slices of the image volume are listed.

A.6 SMSnet: Summary of Trainings

SMSnet	$MB = 2$	$MB = 3$	$MB = 4$
Total no of par	6981108	10420562	13860016
No of trainable par	6964208	10395212	13826216
Pairs of training sets	20970	11088	5049
Pairs of validation sets	12330	4140	1998
Epochs	15	20	20
Batch size, training	5	3	2
Batch size, validation	2	1	1
Optimizer	Adam	Adam	Adam
Loss	TV x MSE	TV x MSE	TV x MSE
Direction of FOV-shift	P > A & R > L or A > P & L > R	P > A & R > L	P > A & R > L

Table A.5: Model learning by SMSnet was conducted in separate trainings for $MB = 2$, $MB = 3$, $MB = 4$. Each training consisted of a certain number of epochs in which all training and validation datasets were load once. Abbreviations: A = anterior, P = posterior, R = right, L = left, no = number, par = parameter

Glossary

- 2D** 2-dimensional. 145
- ACS** auto-calibration signal. 32
- Adam** Adaptive Moment Estimation. 91
- ADC** analog-digital converter. 19
- AI** artificial intelligence. 86
- AIF** arterial input function. 43
- API** application programming interface. 100
- ASL** arterial spin labeling. 43
- BN** Batch Normalization. 95
- BOLD** blood-oxygenation-level dependent. 46
- BW** bandwidth. 20
- CA** contrast agent. 43
- CAIPIRINHA** "controlled aliasing in parallel imaging results in higher acceleration".
39
- CoS** coil sensitivity. 26
- CT** computer tomography. 5
- DCE** dynamic contrast-enhanced. 43
- DL** deep learning. 85
- DNN** deep neural network. 86
- DSC** dynamic susceptibility contrast. 43
- EES** extravascular extracellular space. 8
- EPI** echo-planar imaging. iii
- ETL** echo-train length. 25

- ETS** echo-time shifting. 25
- FA** flip-angle. 14
- FFT** Fast Fourier transform. 18
- FID** free induction decay. 21
- fMRI** functional magnetic resonance imaging. 23
- FOV** field of view. 21
- FWHM** full-width half-maximum. 60
- Gd** Gadolinium. 44
- GLM** generalized linear model. 110
- GPU** graphics processing unit. 86
- GRAPPA** generalized autocalibrating partially parallel acquisitions. 27
- GRE** gradient echo. 19
- IMRT** intensity-modulated ratio therapy. 9
- MB** multiband. 37
- ML** machine learning. 86
- MPRAGE** magnetization prepared rapid gradient echo. 106
- MR** magnetic resonance. 9
- MRI** magnetic resonance imaging. vii
- MSE** mean squared error. 89
- NLINV** regularized nonlinear inversion. 99
- NMR** nuclear magnetic resonance. 11
- NN** neural network. 85
- PE** phase-encoding. 19
- PET** positron emission tomography. 5

- PI** parallel imaging. 26
- PMRM** pseudo multiple-replica method. 35
- PSNR** peak signal-to-noise ratio. 108
- R** reduction factor. 29
- ReLU** rectified linear unit. 88
- RF** radiofrequency. 14
- RO** readout. 19
- ROI** region of interest. 63
- RRF** rotating reference frame. 13
- SAR** specific absorption rate. 149
- SB** singleband. 53
- SE** spin echo. 21
- SENSE** sensitivity encoding. 30
- SG** slice-GRAPPA. 34
- SGD** stochastic gradient descent. 91
- SMASH** simultaneous acquisition of spatial harmonics. 99
- SMS** simultaneous multislice imaging. 23
- SNR** signal-to-noise ratio. 26
- SoS** sum-of-squares. 26
- SSG** split slice-GRAPPA. 38
- SSIM** structural similarity index. 108
- TE** echo-time. 19
- TI** inflow time. 60
- TR** repetition-time. 22
- TSE** turbo-spin-echo. 55

TV total variation. 89

UKE University Hospital Essen, Essen, Germany. 55

US ultrasound. 5

List of Figures

1.1	Vascular system schematically illustrated.	6
1.2	Exchange of contrast agent between vasculature and tissue	9
2.1	Slice selective RF excitation	17
2.2	Components of sequence diagrams	19
2.3	Concept of k-space	20
3.1	Sequence diagram for EPI	25
3.2	Travelling k-space in EPI	25
3.3	Coil sensitivities in spherical phantom	27
3.4	Correlated and decorrelated coil signal	29
3.5	Correlated and decorrelated coil signal, coil correlation matrix	30
3.6	Linear combination of coil sensitivities	33
3.7	Schematic description of GRAPPA algorithm	34
3.8	Pseudo multiple replica method	36
3.9	Examples for unfold images generated in slice-GRAPPA	39
3.10	Illustration of CAIPIRINHA shifting in SMS MRI	40
4.1	SMS sequence diagram	48
4.2	Phase modulation for FOV/4-shifting	49
4.3	FOV positioning in animal experiments	51
4.4	Workflow MR data postprocessing	51
4.5	Workfow MR data postprocessing	53
5.1	AIF detection in dynamic SMS imaging.	60
5.2	Signal dynamics in muscle tissue during CA-enhanced MRI.	61
5.3	Reconstruction of SMS images for hind leg and hip of domestic pig.	62
5.4	Normalized subtraction maps of different SMS reconstructions	63
5.5	Normalized subtraction of different SMS reconstructions, histograms	63
5.6	g-factor maps of different SMS reconstructions	64
5.7	g-factors of different SMS reconstructions, histograms	64
5.8	Images of phantom with CA-doped sub-volumes.	65
5.9	Simulation of GRE signal and histogram to estimate contrast variation in phantom data	66
5.10	S_0 dependency of SMS reconstruction.	67
5.11	Dependency of SMS reconstructions on variation in T_2^*	68
5.12	Summary: Dependency of SMS reconstruction on contrast variations.	69

5.13	Slice profile for 24 slices, $\alpha = 90^\circ$ with $MB = 4$ compared to SB. . . .	71
5.14	Slice profile for 24 slices, $\alpha = 60^\circ$ with $MB = 4$ compared to SB. . . .	72
5.15	Slice profile for 24 slices, $\alpha = 30^\circ$ with $MB = 4$ compared to SB. . . .	72
5.16	Slice profile for eight slices with $MB = 4$ compared to SB.	73
5.17	Slice profile for four slices with $MB = 4$ compared to SB for different FA at $TR = 32$ ms	75
5.18	Slice profile for four slices with $MB = 4$ compared to SB for different FA at $T_R = 1000$ ms	76
5.19	Effects of MB RF Pulse Imperfections	77
6.1	Schematic overview from artificial intelligence to deep learning	82
6.2	Principle structure of a neuron	83
6.3	Schematic example of a fully connected neural network	83
6.4	Droptout of neurons	91
7.1	Fully connected layers on 2D	97
7.2	2D Convolution in NN	98
7.3	Architecture of NN for SMS reconstruction	100
7.4	Architecture of SMSnet for $MB = 2$	101
7.5	Workflow data preparation for SMSnet	103
8.1	Reconstruction by SMSnet	112
8.2	Reconstruction of in-vivo head data, difference	114
8.3	Reconstruction of in-vivo head data, difference	114
8.4	Reconstruction of in-vivo head data, SSIM	115
8.5	Reconstruction of spherical phantom	118
8.6	Reconstruction of structured phantom	118
8.7	Reconstruction of noise-structured phantom	119
8.8	Reconstruction for noise-structured phantom, absolute difference . . .	120
8.9	Reconstruction of gel phantoms	120
8.10	g-factor maps generated by pseudo multiple-replica method	122
8.11	Pseudo multiple-replica method, reconstructions	122
8.12	Sensitivity of reconstructions to BOLD signal	123
8.13	Reconstruction in case of severe changes in coil sensitivities	125
8.14	Reconstruction in case of severe changes in coil sensitivities, difference	125
8.15	Reconstruction of data with simulated head motion	127
8.16	Reconstruction of data with simulated head motion, difference	128
8.17	Reconstruction of synthetic and aquired SMS data, difference	129
8.18	Reconstruction of synthetic and acquired SMS data, SSIM	130
8.19	Validation of SMSnet for cross-system transferability	131

8.20	Reconstructions with SMSnet for higher acceleration factors	132
8.21	Reconstructions for $MB = 3$ data	133
8.22	Reconstructions for $MB = 3$ data, difference	133
8.23	Reconstructions for $MB = 4$ data	133
8.24	Reconstructions for $MB = 4$ data, difference	133
8.25	Input data to SMSnet	136
8.26	Hidden layer activation at the end of CoS-path, pseudo coil sensitivity	136
8.27	Hidden layer activation before merge layer	137
8.28	Hidden layer activation after merge layer	137
8.29	Activation at output of SMSnet	138
8.30	Reconstructions of SMSnet for manipulated input data	139
8.31	Pseudo coil sensitivities for manipulated input data	140
A.1	Dynamic MR signal for subject #2.	161
A.2	Dynamic MR signal for subject #3.	162
A.3	Dynamic MR signal for subject #4.	162
A.4	Dynamic MR signal for subject #2.	163
A.5	Normalized subtraction maps and histogram for SMS reconstruction, subject #3.	164
A.6	Dynamic MR signal for subject #4.	165
A.7	Reconstruction for a spherical phantom, difference	168
A.8	Reconstruction for a spherical phantom, SSIM	168
A.9	Reconstruction for a structured phantom, difference	168
A.10	Reconstruction for a structured phantom, SSIM	169
A.11	Reconstruction for noise-structured phantom, SSIM	169
A.12	Reconstruciton for gel phantoms, difference	169
A.13	Reconstruction for gel phantoms, SSIM	170
A.14	Reconstruction of data with simulated head motion, SSIM	171
A.15	Reconstruction in case of severe changes in coil sensitivities, SSIM . .	171
A.16	Cross-system transferability of SMSnet, absolute difference	172
A.17	Cross-system transferability of SMSnet, SSIM	172
A.18	Reconstruction of synthetic and aquired SMS data	173
A.19	Reconstructions for $MB = 3$ data, SSIM	173
A.20	Reconstructions for $MB = 4$ data, SSIM	174

List of Tables

5.1	Evaluation of cross-talk in SMS and SB slice profiles.	71
5.2	Evaluation of SMS and SB slice profiles for different FA and TR.	75
8.1	Reconstruction of spherical phantom, quantitative evaluation	118
8.2	Reconstruction of structured phantom, quantitative evaluation	119
8.3	Reconstruction of in-vivo head data, quantitative evaluation	126
8.4	Reconstruction of data with simulated head motion, quantitative evaluation	128
8.5	Reconstruction of synthetic and acquired SMS data, quantitative evaluation	129
8.6	Validation of SMSnet for cross-system transferability, quantitative evaluation	131
8.7	Reconstructions for higher acceleration factors, quantitative evaluation	134
A.1	Summary of MRI acquisitions for data base	167
A.2	Reconstruction for noise-structured phantom, quantitative evaluation	169
A.3	Reconstruction for gel phantoms, quantitative evaluation	170
A.4	Controlled manipulation of input data, quantitative evaluation	174
A.5	Summary of Trainings for SMSnet	175

Bibliography

- [Aba+16] Martín Abadi et al. “TensorFlow: Large-Scale Machine Learning on Heterogeneous Distributed Systems”. In: (2016). arXiv: 1603.04467. URL: <http://tensorflow.org/>.
- [Abo+17a] Samy Abo Seada et al. “Optimized amplitude modulated multiband RF pulse design”. In: *Magnetic Resonance in Medicine* 78.6 (2017), pp. 2185–2193. ISSN: 15222594. DOI: 10.1002/mrm.26610.
- [Abo+17b] Samy Abo Seada et al. “Optimized amplitude modulated multiband RF pulse design”. In: *Magnetic Resonance in Medicine* 78.6 (2017), pp. 2185–2193. ISSN: 15222594. DOI: 10.1002/mrm.26610.
- [Als+15] David C. Alsop et al. “Recommended implementation of arterial spin-labeled Perfusion mri for clinical applications: A consensus of the ISMRM Perfusion Study group and the European consortium for ASL in dementia”. In: *Magnetic Resonance in Medicine* 73.1 (2015), pp. 102–116. ISSN: 15222594. DOI: 10.1002/mrm.25197. eprint: NIHMS150003.
- [Bae+05] A L Baert et al. *Dynamic Contrast-Enhanced Magnetic Resonance Imaging in Oncology*. Ed. by Alan Jackson, David L. Buckley, and Geoffrey J. M. Parker. Medical Radiology. Berlin, Heidelberg: Springer Berlin Heidelberg, 2005. ISBN: 978-3-540-42322-5. DOI: 10.1007/b137553. URL: <https://books.google.de/books?id=y8YNYmRUTqQC%20http://link.springer.com/10.1007/b137553>.
- [Bar+15] Markus Barth et al. “Simultaneous multislice (SMS) imaging techniques”. In: *Magnetic Resonance in Medicine* 00 (2015), n/a–n/a. ISSN: 07403194. DOI: 10.1002/mrm.25897. URL: <http://doi.wiley.com/10.1002/mrm.25897>.
- [Bau+16] Michael Baumann et al. “Radiation oncology in the era of precision medicine”. In: *Nature Reviews Cancer* 16 (Mar. 2016), p. 234. URL: <http://dx.doi.org/10.1038/nrc.2016.18%20http://10.0.4.14/nrc.2016.18>.
- [BB06] Philip J. Beatty and Anja C. S. Brau. “Understanding the GRAPPA Paradox”. In: *Proc Intl Soc Magn Reson Med* 14 (2006), p. 2467.
- [BV08] Marie France Bellin and Aart J. Van Der Molen. “Extracellular gadolinium-based contrast media: An overview”. In: *European Journal of Radiology* 66.2 (2008), pp. 160–167. ISSN: 0720048X. DOI: 10.1016/j.ejrad.2008.01.023.

- [BKZ04] MA Bernstein, KE King, and XJ Zhou. *Handbook of MRI pulse sequences*. Academic Press, 2004, p. 1017. ISBN: 978-0120928613.
- [Ber+98] Matt a. Bernstein et al. “Concomitant gradient terms in phase contrast MR: Analysis and correction”. In: *Magnetic Resonance in Medicine* 39 (1998), pp. 300–308. ISSN: 07403194. DOI: 10.1002/mrm.1910390218.
- [Bil+15] Berkin Bilgic et al. “Wave-CAIPI for highly accelerated 3D imaging”. In: *Magnetic Resonance in Medicine* 73.6 (2015), pp. 2152–2162. ISSN: 15222594. DOI: 10.1002/mrm.25347.
- [Bil+18] Berkin Bilgic et al. “Highly Accelerated Multishot EPI through Synergistic Combination of Machine Learning and Joint Reconstruction”. In: *ArXiv e-prints* (Aug. 2018). arXiv: 1808.02814. URL: [arxiv:1808.02814v1](https://arxiv.org/abs/1808.02814v1).
- [Bla+04] Martin Blaimer et al. “Smash, Sense, Pils, Grappa”. In: *Topics in Magnetic Resonance Imaging* 15.4 (Aug. 2004), pp. 223–236. ISSN: 0899-3459. DOI: 10.1097/01.rmr.0000136558.09801.dd. URL: <http://content.wkhealth.com/linkback/openurl?sid=WKPTLP:landingpage%7B%5C%7Dan=00002142-200408000-00002>.
- [Bra+08] Anja C S Brau et al. “Comparison of reconstruction accuracy and efficiency among autocalibrating data-driven parallel imaging methods”. In: *Magnetic Resonance in Medicine* 59.2 (2008), pp. 382–395. ISSN: 07403194. DOI: 10.1002/mrm.21481. arXiv: NIHMS150003.
- [Bre+06] Felix A. Breuer et al. “Controlled aliasing in volumetric parallel imaging (2D CAIPIRINHA)”. In: *Magnetic Resonance in Medicine* 55.3 (Mar. 2006), pp. 549–556. ISSN: 07403194. DOI: 10.1002/mrm.20787. URL: <http://www.ncbi.nlm.nih.gov/pubmed/16408271>.
- [Bre+09] Felix A. Breuer et al. “General formulation for quantitative G-factor calculation in GRAPPA reconstructions”. In: *Magnetic Resonance in Medicine* 62.3 (Sept. 2009), pp. 739–746. ISSN: 07403194. DOI: 10.1002/mrm.22066. URL: <http://doi.wiley.com/10.1002/mrm.22066>.
- [Bre+05] Felix a. Breuer et al. “Controlled aliasing in parallel imaging results in higher acceleration (CAIPIRINHA) for multi-slice imaging”. In: *Magnetic Resonance in Medicine* 53.3 (2005), pp. 684–691. ISSN: 07403194. DOI: 10.1002/mrm.20401.
- [Bro16a] Jason Brownless. *Embrace Randomness in Machine Learning*. 2016. URL: <https://machinelearningmastery.com/randomness-in-machine-learning/> (visited on 12/12/2017).

- [Bro16b] Jason Brownless. *Gentle Introduction to the Bias-Variance Trade-Off in Machine Learning*. 2016. URL: <https://machinelearningmastery.com/gentle-introduction-to-the-bias-variance-trade-off-in-machine-learning/> (visited on 12/12/2017).
- [Cal13] Fernando Calamante. “Arterial input function in perfusion MRI: A comprehensive review”. In: *Progress in Nuclear Magnetic Resonance Spectroscopy* 74 (2013), pp. 1–32. ISSN: 00796565. DOI: 10.1016/j.pnmrs.2013.04.002. URL: <http://dx.doi.org/10.1016/j.pnmrs.2013.04.002>.
- [Cau+14] Stephen F. Cauley et al. “Interslice leakage artifact reduction technique for simultaneous multislice acquisitions”. In: *Magnetic Resonance in Medicine* 72.1 (2014), pp. 93–102. ISSN: 15222594. DOI: 10.1002/mrm.24898.
- [Cho+15] François Chollet et al. *Keras*. <https://github.com/fchollet/keras>. 2015.
- [col00] desy collaboration. *desy.de*. 2000. URL: http://www.desy.de/expo2000/deutsch/dhtmlbrowser/webthemen/05%7B%5C_%7Droentgen/roentgen%7B%5C_%7Ddruck.htm (visited on 01/11/2018).
- [DAr+02] J. A. D’Arcy et al. “Applications of sliding window reconstruction with cartesian sampling for dynamic contrast enhanced MRI”. In: *NMR in Biomedicine* 15.2 (2002), pp. 174–183. ISSN: 09523480. DOI: 10.1002/nbm.755.
- [Des+09] I. M E Desar et al. “Beyond RECIST: Molecular and functional imaging techniques for evaluation of response to targeted therapy”. In: *Cancer Treatment Reviews* 35.4 (2009), pp. 309–321. ISSN: 03057372. DOI: 10.1016/j.ctrv.2008.12.001. URL: <http://dx.doi.org/10.1016/j.ctrv.2008.12.001>.
- [Des+12] Anagha Deshmane et al. “Parallel MR imaging”. In: *Journal of Magnetic Resonance Imaging* 36.1 (2012), pp. 55–72. ISSN: 10531807. DOI: 10.1002/jmri.23639. eprint: 15334406.
- [Det+92] John A. Detre et al. “Perfusion imaging”. In: *Magnetic Resonance in Medicine* 23.1 (Jan. 1992), pp. 37–45. ISSN: 07403194. DOI: 10.1002/mrm.1910230106. URL: <http://doi.wiley.com/10.1002/jmri.24382>
<http://doi.wiley.com/10.1002/mrm.1910230106>.
- [DHS10] John Duchi, Elad Hazan, and Yoram Singer. “Adaptive Subgradient Methods for Online Learning and Stochastic Optimization”. In: *Colt 2010* 12 (2010), pp. 2121–2159.

- [Dys04] Freeman Dyson. “A meeting with Enrico Fermi”. In: *Nature* 427.6972 (Jan. 2004), p. 297. ISSN: 0028-0836. URL: <http://dx.doi.org/10.1038/427297a>.
- [Eic+14] Cornelius Eichner et al. “Slice accelerated gradient-echo spin-echo dynamic susceptibility contrast imaging with blipped CAIPI for increased slice coverage”. In: *Magnetic Resonance in Medicine* 72.3 (2014), pp. 770–778. ISSN: 07403194. DOI: 10.1002/mrm.24960. URL: <http://doi.wiley.com/10.1002/mrm.24960>.
- [EGL14] Klaus Eickel, Matthias Günther, and Lutz Lüdemann. “Dynamic T2*-Mapping using Segmented EPI with Multi-TE”. In: *Dreiländertagung der Medizinischen Physik in Zürich 2014. SGSMP, ÖGMP, DGMP, Hrsg. Stephan Klöck*. (2014). Ed. by Stephan Klöck, p. 410.
- [ELG15] Klaus Eickel, Lutz Lüdemann, and Matthias Günther. “Dynamic Imaging using Multi-Contrast Segmented EPI with SMS Acquisition and Controlled Aliasing : First Results”. In: *Magnetic Resonance Materials in Physics, Biology and Medicine* 28.1 (2015), pp. 277–418. DOI: doi.org/10.1007/s10334-015-0489-0.
- [Eic+16] Klaus Eickel et al. “Simultaneous multi-slice acquisition with multi-contrast segmented EPI for dynamic contrast-enhanced imaging”. In: *Proc Intl Soc Mag Reson Med* 3244 (2016).
- [Eic+18] Klaus Eickel et al. “Simultaneous multislice acquisition with multi-contrast segmented EPI for separation of signal contributions in dynamic contrast-enhanced imaging”. In: *PLOS ONE* 13.8 (Aug. 2018). Ed. by Vadim E. Degtyar, e0202673. ISSN: 1932-6203. DOI: 10.1371/journal.pone.0202673. URL: <http://dx.plos.org/10.1371/journal.pone.0202673>.
- [Els18] Allen D. Elster. *MRI Questions*. Jan. 19, 2018. URL: <http://www.mriquestions.com>.
- [Fei+11] David A. Feinberg et al. “Multiplexed echo planar imaging for sub-second whole brain fMRI and fast diffusion imaging”. In: *PLoS ONE* 6.9 (Sept. 2011). Ed. by Pedro Antonio Valdes-Sosa, e15710. ISSN: 1932-6203. DOI: 10.1371/annotation/d9496d01-8c5d-4d24-8287-94449ada5064. URL: <http://www.pubmedcentral.nih.gov/articlerender.fcgi?artid=3004955%7B%5C%7Dtool=pmcentrez%7B%5C%7Drendertype=abstract%20http://dx.plos.org/10.1371/journal.pone.0015710%20http://dx.plos.org/10.1371/annotation/d9496d01-8c5d-4d24-8287-94449ada5064>.

- [FO94] David A Feinberg and Koichi Oshio. “Phase errors in multi-shot echo planar imaging”. In: *Magnetic Resonance in Medicine* 32.4 (1994), pp. 535–539. ISSN: 07403194. DOI: 10.1002/mrm.1910320418.
- [Fou16] NVIDIA Foundation. *DEEP LEARNING ADVANCES IN MEDICINE*. 2016. URL: <http://www.nvidia.com/object/deep-learning-in-medicine.html> (visited on 03/05/2017).
- [GBD92] Stuart Geman, Elie Bienenstock, and René Doursat. “Neural Networks and the Bias/Variance Dilemma”. In: *Neural Computation* 4.1 (Jan. 1992), pp. 1–58. ISSN: 0899-7667. DOI: 10.1162/neco.1992.4.1.1. eprint: arXiv:1011.1669v3. URL: <http://www.mitpressjournals.org/doi/10.1162/neco.1992.4.1.1>.
- [GB10] Xavier Glorot and Yoshua Bengio. “Understanding the difficulty of training deep feedforward neural networks”. In: *Proceedings of the 13th International Conference on Artificial Intelligence and Statistics (AISTATS) 9* (2010), pp. 249–256. ISSN: 15324435. DOI: 10.1.1.207.2059. arXiv: arXiv:1011.1669v3. URL: http://machinelearning.wustl.edu/mlpapers/paper%7B%5C_%7Dfiles/AISTATS2010%7B%5C_%7DGlorotB10.pdf.
- [Glo91] Gary H. Glover. “Phase-offset multiplanar (POMP) volume imaging: A new technique”. In: *Journal of Magnetic Resonance Imaging* 1.4 (1991), pp. 457–461. ISSN: 15222586. DOI: 10.1002/jmri.1880010410.
- [GBC16] Ian Goodfellow, Yoshua Bengio, and Aaron Courville. *Deep Learning*. <http://www.deeplearningbook.org>. MIT Press, 2016.
- [Gri+10] William A. Grissom et al. “Minimum envelope roughness pulse design for reduced amplifier distortion in parallel excitation”. In: *Magnetic Resonance in Medicine* 64.5 (Nov. 2010), pp. 1432–1439. ISSN: 07403194. DOI: 10.1002/mrm.22512. eprint: NIHMS150003. URL: <http://www.ncbi.nlm.nih.gov/pubmed/22083964><http://www.pubmedcentral.nih.gov/articlerender.fcgi?artid=PMC3319839><http://doi.wiley.com/10.1002/jor.22002><http://doi.wiley.com/10.1002/mrm.22512>.
- [Gri+02] Mark a. Griswold et al. “Generalized Autocalibrating Partially Parallel Acquisitions (GRAPPA)”. In: *Magnetic Resonance in Medicine* 47.6 (2002), pp. 1202–1210. ISSN: 07403194. DOI: 10.1002/mrm.10171.
- [Gue18] Guerbet. *DOTAREM, gadoterate meglumine injection*. 2018. URL: <http://www.guerbet-us.com/products/dotarem.html> (visited on 01/02/2018).

- [Haa+99] E. Mark Haacke et al. *Magnetic Resonance Imaging Physical Principles and Sequence Design*. 1st Edition. John Wiley & Sons, Inc., 1999, p. 914. ISBN: 0471351288.
- [Han08] Lars G. Hanson. “Is quantum mechanics necessary for understanding magnetic resonance?” In: *Concepts in Magnetic Resonance Part A* 32A.5 (Sept. 2008), pp. 329–340. ISSN: 15466086. DOI: 10.1002/cmr.a.20123. URL: <http://doi.wiley.com/10.1002/cmr.a.20123>.
- [Hea] National Institutes of Health. *Human Connectome Project*. URL: <https://www.humanconnectome.org/study/hcp-young-adult/project-protocol/pulse-sequences>.
- [Heb49] Donald Hebb. *The organization of behavior: A neuropsychological theory*. 1949. ISBN: 471367273.
- [Hei00] Oliver Heid. *Method for the phase correction of nuclear magnetic resonance signals*. 2000.
- [Hei+07] Melanie Heilmann et al. “Simultaneous dynamic T₁ and T₂* measurement for AIF assessment combined with DCE MRI in a mouse tumor model”. In: *Magnetic Resonance Materials in Physics, Biology and Medicine* 20.4 (Oct. 2007), pp. 193–203. ISSN: 1352-8661. DOI: 10.1007/s10334-007-0082-2. URL: <http://link.springer.com/10.1007/s10334-007-0082-2>.
- [Hen97] Franciszek Hennel. “Multiple-Shot Echo-Planar Imaging”. In: *Concepts in Magnetic Resonance* 9.1 (1997), pp. 43–58.
- [Hin+15] Stefan Hindel et al. “Validation of perfusion quantification with 3D Gradient echo dynamic contrast-enhanced magnetic resonance imaging using a blood pool contrast agent in skeletal swine muscle”. In: *PLOS ONE* 10.6 (June 2015). Ed. by Andreas-Claudius Hoffmann, e0128060. ISSN: 1932-6203. DOI: 10.1371/journal.pone.0128060. URL: <http://dx.plos.org/10.1371/journal.pone.0128060>.
- [Hin+17] Stefan Hindel et al. “Validation of blood volume fraction quantification with 3D gradient echo dynamic contrast-enhanced magnetic resonance imaging in porcine skeletal muscle”. In: *PLOS ONE* 12.1 (Jan. 2017), e0170841. ISSN: 1932-6203. DOI: 10.1371/journal.pone.0170841. URL: <http://content.wkhealth.com/linkback/openurl?sid=WKPTLP:landingpage%7B%5C%7Dan=00004424-900000000-99174%20http://dx.plos.org/10.1371/journal.pone.0170841>.

- [Hin07] Geoffrey E. Hinton. “Learning multiple layers of representation”. In: *Trends in Cognitive Sciences* 11.10 (2007), pp. 428–434. ISSN: 13646613. DOI: 10.1016/j.tics.2007.09.004.
- [Hin+12] Geoffrey E. Hinton et al. “Improving neural networks by preventing co-adaptation of feature detectors”. In: *ArXiv e-prints* (2012), pp. 1–18. ISSN: 9781467394673. DOI: arXiv:1207.0580. arXiv: 1207.0580. URL: <http://arxiv.org/abs/1207.0580>.
- [HSW89] Kurt Hornik, Maxwell Stinchcombe, and Halbert White. “Multilayer feedforward networks are universal approximators”. In: *Neural Networks* 2.5 (Jan. 1989), pp. 359–366. ISSN: 08936080. DOI: 10.1016/0893-6080(89)90020-8. URL: <http://linkinghub.elsevier.com/retrieve/pii/0893608089900208>.
- [HW95] Liang-Kai Huang and Mao-Jiun Wang. “Image Thresholding by Minimizing the Measure of Fuzziness”. In: *Pattern Recognition* 28.1 (1995), pp. 41–51. URL: [http://linkinghub.elsevier.com/retrieve/pii/0031320394E0043K%7B%5C%7D5Cnpapers3://publication/doi/10.1016/0031-3203\(94\)E0043-K](http://linkinghub.elsevier.com/retrieve/pii/0031320394E0043K%7B%5C%7D5Cnpapers3://publication/doi/10.1016/0031-3203(94)E0043-K).
- [Hun07] J. D. Hunter. “Matplotlib: A 2D graphics environment”. In: *Computing In Science & Engineering* 9.3 (2007), pp. 90–95. DOI: 10.1109/MCSE.2007.55.
- [HR88] Michael Hutchinson and Ulrich Raff. “Fast MRI data acquisition using multiple detectors”. In: *Magnetic Resonance in Medicine* 6.1 (Jan. 1988), pp. 87–91. ISSN: 0740-3194. DOI: 10.1002/mrm.1910060110. URL: <https://doi.org/10.1002/mrm.1910060110>.
- [Jah+14] Geon Ho Jahng et al. “Perfusion magnetic resonance imaging: A comprehensive update on principles and techniques”. In: *Korean Journal of Radiology* 15.5 (2014), pp. 554–577. ISSN: 12296929. DOI: 10.3348/kjr.2014.15.5.554. URL: <http://www.pubmedcentral.nih.gov/articlerender.fcgi?artid=4170157%7B%5C%7Dtool=pmcentrez%7B%5C%7Drendertype=abstract%20https://synapse.koreamed.org/DOIx.php?id=10.3348/kjr.2014.15.5.554%20http://www.ncbi.nlm.nih.gov/pubmed/25246817%20http://www.pubmedcentral.nih.gov/articleren>.
- [Jai87] R K Jain. “Transport of molecules across tumor vasculature.” In: *Cancer metastasis reviews* 6.4 (1987), pp. 559–93. ISSN: 0167-7659. URL: <http://www.ncbi.nlm.nih.gov/pubmed/3327633>.

- [Joh17] Justin Johnson. *CS231n: Convolutional Neural Networks for Visual Recognition*. 2017. URL: <https://cs231n.github.io/neural-networks-2/> (visited on 12/12/2017).
- [JOP+01] Eric Jones, Travis Oliphant, Pearu Peterson, et al. *SciPy: Open source scientific tools for Python*. 2001–. URL: <http://www.scipy.org> (visited on 12/02/2018).
- [Jup18] Project Jupyter. *Project Jupyter*. 2018. URL: <https://jupyter.org/about> (visited on 06/26/2018).
- [KM05] Peter Kellman and Elliot R. McVeigh. “Image reconstruction in SNR units: A general method for SNR measurement”. In: *Magnetic Resonance in Medicine* 54.6 (2005), pp. 1439–1447. ISSN: 07403194. DOI: 10.1002/mrm.20713.
- [KC10] Lucy E. Kershaw and H. L M Cheng. “Temporal resolution and SNR requirements for accurate DCE-MRI data analysis using the AATH model”. In: *Magnetic Resonance in Medicine* 64.6 (Dec. 2010), pp. 1772–1780. ISSN: 07403194. DOI: 10.1002/mrm.22573. URL: <http://www.ncbi.nlm.nih.gov/pubmed/20715059>.
- [KB15] Diederik P. Kingma and Jimmy Ba. “Adam: A Method for Stochastic Optimization”. In: *Iclr* (2015), pp. 1–15. ISSN: 09252312. DOI: <http://doi.acm.org.ezproxy.lib.ucf.edu/10.1145/1830483.1830503>. arXiv: 1412.6980. URL: <http://arxiv.org/abs/1412.6980>.
- [Kun+17] Prantik Kundu et al. “Multi-echo fMRI : A review of applications in fMRI denoising and analysis of BOLD signals”. In: *NeuroImage* 154.March (2017), pp. 59–80. ISSN: 1053-8119. DOI: 10.1016/j.neuroimage.2017.03.033. URL: <http://dx.doi.org/10.1016/j.neuroimage.2017.03.033>.
- [Lar+01] David J. Larkman et al. “Use of multicoil arrays for separation of signal from multiple slices simultaneously excited”. In: *Journal of Magnetic Resonance Imaging* 13.2 (2001), pp. 313–317. ISSN: 10531807. DOI: 10.1002/1522-2586(200102)13:2<313::AID-JMRI1045>3.0.CO;2-W.
- [Lar+03] Erik G. Larsson et al. “SNR-optimality of sum-of-squares reconstruction for phased-array magnetic resonance imaging”. In: *Journal of Magnetic Resonance* 163.1 (2003), pp. 121–123. ISSN: 10907807. DOI: 10.1016/S1090-7807(03)00132-0.

- [LYH15] Yann LeCun, Bengio Yoshua, and Geoffrey E. Hinton. “Deep learning”. In: *Nature Methods* 521.1 (2015), pp. 436–444. ISSN: 1548-7091. DOI: 10.1038/nmeth.3707. arXiv: arXiv:1312.6184v5. URL: <http://www.nature.com/doifinder/10.1038/nature14539%7B%5C%7D5Cnhttp://www.nature.com/doifinder/10.1038/nmeth.3707>.
- [Lev09] Malcolm H. Levitt. *Spin Dynamics : Basics of Nuclear Magnetic Resonance*. 2nd. Wiley, 2009, p. 724. ISBN: 9780470511183. DOI: 10.1007/978-1-4471-4908-8. URL: https://books.google.de/books?id=%7B%5C_%7D1wZXxz1TIQC.
- [Lik79] Richard S Likes. *Moving gradient zeugmatography*. 1979.
- [Lju83] Stig Ljunggren. “A Simple Graphical Representation of Fourier-Based Imaging Methods”. In: *Journal of Magnetic Resonance* 54.2 (1983), pp. 338–343. DOI: [https://doi.org/10.1016/0022-2364\(83\)90060-4](https://doi.org/10.1016/0022-2364(83)90060-4).
- [Loh+16] Jessica Lohrke et al. “25 Years of Contrast-Enhanced MRI: Developments, Current Challenges and Future Perspectives”. In: *Advances in Therapy* 33.1 (2016), pp. 1–28. ISSN: 18658652. DOI: 10.1007/s12325-015-0275-4.
- [Lüd+09a] Lutz Lüdemann et al. “Absolute quantification of regional renal blood flow in swine by dynamic contrast-enhanced magnetic resonance imaging using a blood pool contrast agent.” In: *Investigative radiology* 44.3 (Mar. 2009), pp. 125–34. ISSN: 1536-0210. DOI: 10.1097/RLI.0b013e318193598c. URL: <http://www.ncbi.nlm.nih.gov/pubmed/19151609>.
- [Lüd+09b] Lutz Lüdemann et al. “Simultaneous quantification of perfusion and permeability in the prostate using dynamic contrast-enhanced magnetic resonance imaging with an inversion-prepared dual-contrast sequence”. In: *Annals of Biomedical Engineering* 37.4 (Apr. 2009), pp. 749–762. ISSN: 00906964. DOI: 10.1007/s10439-009-9645-x. URL: <http://www.ncbi.nlm.nih.gov/pubmed/19169821>.
- [Lus+08] M Lustig et al. *Compressed Sensing MRI*. 2008. DOI: 10.1109/MSP.2007.914728.
- [Mag17a] International Society for Magnetic Resonance in Medicine. *Proceedings of the ISMRM 24th Annual Meeting & Exhibition 2017*. 2017. URL: <http://indexsmart.mirasmart.com/ISMRM2016/searchresults.php?q=Deep+Learning> (visited on 06/11/2017).

- [Mag17b] International Society for Magnetic Resonance in Medicine. *Proceedings of the ISMRM 25th Annual Meeting & Exhibition 2017*. 2017. URL: <http://indexsmart.mirasmart.com/ISMRM2017/SearchResults.php?q=Deep+Learning> (visited on 06/11/2017).
- [Mag18] International Society for Magnetic Resonance in Medicine. *Proceedings of the Joint Annual Meeting ISMRM - ESMRMB 2018*. 2018. URL: <http://indexsmart.mirasmart.com/ISMRM2018/SearchResults.php?q=Deep+Learning> (visited on 06/25/2018).
- [Mar09] C B Markwardt. “Non-linear Least-squares Fitting in IDL with MP-FIT”. In: *Astronomical Data Analysis Software and Systems XVIII ASP Conference Series* 411 (Feb. 2009), p. 251. ISSN: 1050-3390. DOI: [citeulike-article-id:4067445](https://doi.org/10.1006/proc.2009.1145). arXiv: 0902.2850.
- [Mat] MatWorks. *MATLAB (R2016a)*. URL: <https://mathworks.com/> (visited on 03/02/2018).
- [McR+86] D W McRobbie et al. “Investigation of slice characteristics in nuclear magnetic resonance imaging”. In: *Physics in Medicine & Biology* 31.6 (1986), p. 613. URL: <http://stacks.iop.org/0031-9155/31/i=6/a=003>.
- [McR+06] D W McRobbie et al. *MRI from Picture to Proton*. 2nd ed. Cambridge University Press, 2006. ISBN: 9780521865272. URL: <https://books.google.de/books?id=SONWngEACAAJ>.
- [Met+13] P. Metcalfe et al. “The Potential for an Enhanced Role for MRI in Radiation-Therapy Treatment Planning”. In: *Technology in Cancer Research & Treatment* 12.5 (2013), pp. 429–446. ISSN: 1533-0346. DOI: [10.7785/tcrt.2012.500342](https://doi.org/10.7785/tcrt.2012.500342). URL: <http://journals.sagepub.com/doi/10.7785/tcrt.2012.500342>.
- [Miy+97] T Miyati et al. “Dual dynamic contrast-enhanced MR imaging.” In: *Journal of magnetic resonance imaging : JMRI* 7.1 (1997), pp. 230–235. ISSN: 1053-1807. URL: <http://www.ncbi.nlm.nih.gov/pubmed/9039621>.
- [Moe+10] Steen Moeller et al. “Multiband multislice GE-EPI at 7 tesla, with 16-fold acceleration using partial parallel imaging with application to high spatial and temporal whole-brain fMRI”. In: *Magnetic Resonance in Medicine* 63.5 (May 2010), pp. 1144–1153. ISSN: 07403194. DOI: [10.1002/mrm.22361](https://doi.org/10.1002/mrm.22361). URL: <http://www.ncbi.nlm.nih.gov/pubmed/20432285>
<http://www.pubmedcentral.nih.gov/articlerender.fcgi?artid=PMC2906244>.

- [Moe+18] Steen Moeller et al. “Application of a Scan-Specific Deep Learning Reconstruction to Multiband/SMS Imaging”. In: *Proc Intl Soc Mag Reson Med*. 2018, p. 0577.
- [MSM18] Grégoire Montavon, Wojciech Samek, and Klaus-Robert Müller. “Methods for interpreting and understanding deep neural networks”. In: *Digital Signal Processing* 73 (Feb. 2018), pp. 1–15. ISSN: 10512004. DOI: 10.1016/j.dsp.2017.10.011. arXiv: 1706.07979. URL: <http://arxiv.org/abs/1706.07979><https://linkinghub.elsevier.com/retrieve/pii/S1051200417302385>.
- [MB96] J P Mugler and J R Brookeman. “Off-resonance image artifacts in interleaved-EPI and GRASE pulse sequences.” In: *Magnetic resonance in medicine : official journal of the Society of Magnetic Resonance in Medicine / Society of Magnetic Resonance in Medicine* 36.2 (Aug. 1996), pp. 306–313. ISSN: 0740-3194. URL: <http://www.ncbi.nlm.nih.gov/pubmed/8843385>.
- [Mül88] S Müller. “Multifrequency selective rf pulses for multislice MR imaging.” In: *Magnetic resonance in medicine : official journal of the Society of Magnetic Resonance in Medicine / Society of Magnetic Resonance in Medicine* 6.1 988 (1988), pp. 364–371. ISSN: 0740-3194. DOI: 10.1002/mrm.1910060315.
- [New+07] Rexford D. Newbould et al. “Perfusion mapping with multiecho multi-shot parallel imaging EPI”. In: *Magnetic Resonance in Medicine* 58.1 (2007), pp. 70–81. ISSN: 07403194. DOI: 10.1002/mrm.21255.
- [New+16] A. T. Newton et al. “Improving perfusion measurement in DSC-MR imaging with multiecho information for arterial input function determination”. In: *American Journal of Neuroradiology* 37.7 (2016), pp. 1237–1243. ISSN: 1936959X. DOI: 10.3174/ajnr.A4700.
- [Nie15] Micheal A. Nielsen. *Neural Networks and Deep Learning*. Determination Press, 2015. URL: <http://neuralnetworksanddeeplearning.com/>.
- [Nun+06] Rita G Nunes et al. “Simultaneous slice excitation and reconstruction for single shot EPI .” In: *Proc Intl Soc Mag Reson Med* 14.2 (2006), p. 293.
- [Ope17] OpenStax. *Anatomy & Physiology*. Ed. by OpenStax. OpenStax CNX, 2017. ISBN: 9781938168130. URL: <http://cnx.org/contents/14fb4ad7-39a1-4eee-ab6e-3ef2482e3e22@8.108>.

- [Pol12] Jonathan R. Polimeni. “Rapid multi-shot segmented EPI using the Simultaneous Multi-Slice acquisition method”. In: *Proceedings of the 20th Annual Meeting of the ISMRM* 20 (2012), p. 2222.
- [Pol+15] Jonathan R Polimeni et al. “Reducing sensitivity losses due to respiration and motion in accelerated echo planar imaging by reordering the autocalibration data acquisition.” In: *Magnetic Resonance in Medicine* 00.January (2015), pp. 1–15. ISSN: 1522-2594. DOI: 10.1002/mrm.25628. URL: <http://www.ncbi.nlm.nih.gov/pubmed/25809559>.
- [PH09] David A. Porter and Robin M. Heidemann. “High resolution diffusion-weighted imaging using readout-segmented echo-planar imaging, parallel imaging and a two-dimensional navigator-based reacquisition”. In: *Magnetic Resonance in Medicine* 62.2 (2009), pp. 468–475. ISSN: 07403194. DOI: 10.1002/mrm.22024.
- [PN09] Benedikt A. Poser and David G. Norris. “Investigating the benefits of multi-echo EPI for fMRI at 7 T”. In: *NeuroImage* 45.4 (May 2009), pp. 1162–1172. ISSN: 10538119. DOI: 10.1016/j.neuroimage.2009.01.007. URL: <http://linkinghub.elsevier.com/retrieve/pii/S105381190900055X>.
- [Pru+99] Klaas P. Pruessmann et al. “SENSE: Sensitivity encoding for fast MRI”. In: *Magnetic Resonance in Medicine* 42.5 (1999), pp. 952–962. ISSN: 07403194. DOI: 10.1002/(SICI)1522-2594(199911)42:5<952::AID-MRM16>3.0.CO;2-S.
- [Pru+01] Klaas P. Pruessmann et al. “Advances in Sensitivity Encoding With Arbitrary k-Space Trajectories”. In: *Magnetic Resonance in Medicine* 46.4 (Oct. 2001), pp. 638–651. ISSN: 07403194. DOI: 10.1002/mrm.1241. URL: <http://www.mr-tip.com/serv1.php?type=co%20http://doi.wiley.com/10.1002/mrm.1241>.
- [RR93] J B Ra and C Y Rim. “Fast imaging using subencoding data sets from multiple detectors.” In: *Magnetic resonance in medicine : official journal of the Society of Magnetic Resonance in Medicine / Society of Magnetic Resonance in Medicine* 30.1 (1993), pp. 142–145. ISSN: 0740-3194. DOI: 10.1002/mrm.1910300123.
- [Rob+08] Philip M. Robson et al. “Comprehensive quantification of signal-to-noise ratio and g-factor for image-based and k-space-based parallel imaging reconstructions”. In: *Magnetic Resonance in Medicine* 60.4 (2008), pp. 895–907. ISSN: 07403194. DOI: 10.1002/mrm.21728. URL: <http://doi.wiley.com/10.1002/mrm.21728>.

- [REH90] P B Roemer, W A Edelstein, and C E Hayes. “The NMR Phased Array”. In: 225 (1990), pp. 192–225. ISSN: 07403194. DOI: 10.1002/mrm.1910160203.
- [Ros+90] B R Rosen et al. “Perfusion imaging with contrast agents”. In: *Magnetic Resonance in Medicine* 14 (1990), pp. 249–265.
- [Ros+17] Sebastian Rosenzweig et al. “Simultaneous multi-slice MRI using cartesian and radial FLASH and regularized nonlinear inversion: SMS-NLINV”. In: *Magnetic Resonance in Medicine* 00 (Aug. 2017), pp. 1–10. ISSN: 07403194. DOI: 10.1002/mrm.26878. URL: <http://doi.wiley.com/10.1002/mrm.26878><http://www.ncbi.nlm.nih.gov/pubmed/28840612><http://doi.wiley.com/10.1002/mrm.26878>.
- [Rud16] Sebastian Ruder. “An overview of gradient descent optimization algorithms”. In: (Sept. 2016), pp. 1–12. arXiv: 1609.04747. URL: <http://arxiv.org/abs/1609.04747>.
- [ROF92] L I Rudin, Stanley Osher, and Emad Fatemi. “Nonlinear total variation based noise removal algorithms”. In: *Physica D: Nonlinear Phenomena* 60 (1992), pp. 259–268.
- [RHW86] David E. Rumelhart, Geoffrey E. Hinton, and Ronald J. Williams. “Learning representations by back-propagating errors”. In: *Nature* 323.6088 (1986), pp. 533–536. ISSN: 0028-0836. DOI: 10.1038/323533a0. arXiv: arXiv:1011.1669v3. URL: <http://www.nature.com/doi/10.1038/323533a0>.
- [Sam16] Federico von Samson-Himmelstjerna. “Robust and time-efficient determination of perfusion parameters using time-encoded Arterial Spin Labeling MRI”. PhD thesis. 2016. URL: <http://oatd.org/oatd/record?record=oai%7B%5C%7D5C:elib.suub.uni-bremen.de%7B%5C%7D5C:DISS%7B%5C%7D5C%7B%5C%7D2F00105573%7B%5C%7Dq=federico%20von%20samson-himmelstjerna>.
- [Sau+14] Anika Sauerbrey et al. “Establishment of a swine model for validation of perfusion measurement by dynamic contrast-enhanced magnetic resonance imaging”. In: *BioMed Research International* 2014 (2014), p. 390506. ISSN: 23146141. DOI: 10.1155/2014/390506.
- [SM14] J. H. Scatliff and P. J. Morris. “From roentgen to magnetic resonance imaging: the history of medical imaging”. In: *North Carolina Medical Journal* 75.2 (2014), pp. 111–113. ISSN: 0029-2559. DOI: 10.18043/ncm.75.2.111. URL: <http://www.ncbi.nlm.nih.gov/pubmed/24663131>.

- [Sch15] Jürgen Schmidhuber. *Deep Learning in neural networks: An overview*. 2015. DOI: 10.1016/j.neunet.2014.09.003. arXiv: 1404.7828. URL: <http://dx.doi.org/10.1016/j.neunet.2014.09.003>.
- [SST98] Franz Schmitt, Michael K. Stehling, and Robert Turner. *Echo-Planar Imaging: Theory, Technique and Application*. Softcover reprint of the hardcover 1st edition. Springer-Verlag Berlin Heidelberg, 1998, p. 662. ISBN: 978-3-642-80445-8.
- [Sco12] Greig C Scott. “MRI Transmitter Amplifier Systems”. In: *Proc Intl Soc Mag Reson Med* (2012).
- [Set+12a] K. Setsompop et al. “Improving diffusion MRI using simultaneous multislice echo planar imaging”. In: *NeuroImage* 63.1 (2012), pp. 569–580. ISSN: 10538119. DOI: 10.1016/j.neuroimage.2012.06.033. eprint: NIHMS150003. URL: <http://dx.doi.org/10.1016/j.neuroimage.2012.06.033>.
- [Set+12b] Kawin Setsompop et al. “Blipped-controlled aliasing in parallel imaging for simultaneous multislice echo planar imaging with reduced g-factor penalty”. In: *Magnetic Resonance in Medicine* 67.5 (May 2012), pp. 1210–1224. ISSN: 07403194. DOI: 10.1002/mrm.23097. arXiv: NIHMS150003. URL: <http://www.pubmedcentral.nih.gov/articlerender.fcgi?artid=3323676%7B%5C%7Dtool=pmcentrez%7B%5C%7Drendertype=abstract>.
- [SM97] Daniel K. Sodickson and Warren J. Manning. “Simultaneous acquisition of spatial harmonics (SMASH): Fast imaging with radiofrequency coil arrays”. In: *Magnetic Resonance in Medicine* 38.4 (1997), pp. 591–603. ISSN: 07403194. DOI: 10.1002/mrm.1910380414.
- [Sou+09] S. Sourbron et al. “Bolus-tracking MRI with a simultaneous T1- and T2*-measurement”. In: *Magnetic Resonance in Medicine* 62.3 (Sept. 2009), pp. 672–681. ISSN: 07403194. DOI: 10.1002/mrm.22042. URL: <http://www.ncbi.nlm.nih.gov/pubmed/19585599>.
- [SB13] Steven P Sourbron and David L Buckley. “Classic models for dynamic contrast-enhanced MRI.” In: *NMR in biomedicine* 26.8 (Aug. 2013), pp. 1004–1027. ISSN: 1099-1492. DOI: 10.1002/nbm.2940. URL: <http://www.ncbi.nlm.nih.gov/pubmed/23674304>.
- [Sou+88] SP Souza et al. “SIMA: simultaneous multislice acquisition of MR images by Hadamard-encoded excitation.” In: *Journal of computer assisted tomography* 12.6 (1988), pp. 1026–30. ISSN: 0363-8715. URL: <http://www.ncbi.nlm.nih.gov/pubmed/3183105>.

- [Sri+14] Nitish Srivastava et al. “Dropout: A Simple Way to Prevent Neural Networks from Overfitting”. In: *Journal of Machine Learning Research* 15 (2014), pp. 1929–1958. ISSN: 15337928. DOI: 10.1214/12-AOS1000. arXiv: 1102.4807.
- [18] *Statistical Parameter Mapping*. Nov. 16, 2018. URL: <https://www.fil.ion.ucl.ac.uk/spm/>.
- [Sze15] Christian Szegedy. “Batch Normalization: Accelerating Deep Network Training by Reducing Internal Covariate Shift”. In: (2015). arXiv: arXiv:1502.03167v3.
- [TH12] T. Tielmann and Geoffrey Hinton. *RMSProp in COURSERA: Neural Networks for Machine Learning*. Tech. rep. 2012.
- [Tof09] Paul S Tofts. “Methods for quantitative relaxation parameter mapping : measuring T1 and T2”. In: *ISMRM 17th Scientific Meeting and Exhibition* (2009).
- [Twi83] Donald B Twieg. “The k-trajectory formulation of the NMR imaging process with applications in analysis and synthesis of imaging methods”. In: *Medical Physics* 10.5 (Sept. 1983), pp. 610–621. ISSN: 0094-2405. DOI: 10.1118/1.595331. URL: <https://doi.org/10.1118/1.595331>.
- [Uec+08] Martin Uecker et al. “Image reconstruction by regularized nonlinear inversion - Joint estimation of coil sensitivities and image content”. In: *Magnetic Resonance in Medicine* 60.3 (2008), pp. 674–682. ISSN: 07403194. DOI: 10.1002/mrm.21691.
- [Uec+14] Martin Uecker et al. “ESPIRiT - An eigenvalue approach to autocalibrating parallel MRI: Where SENSE meets GRAPPA”. In: *Magnetic Resonance in Medicine* 71.3 (2014), pp. 990–1001. ISSN: 07403194. DOI: 10.1002/mrm.24751. eprint: 15334406.
- [Vap99] V.N. Vapnik. “An Overview of Statistical Learning Theory”. In: *IEEE Transactions on Neural Networks* 10.5 (1999), pp. 988–999. ISSN: 10459227. DOI: 10.1109/72.788640. URL: <http://ieeexplore.ieee.org/document/788640/>.
- [Von+00] Evert-jan Ph.A. Vonken et al. “Simultaneous quantitative cerebral perfusion and Gd-DTPA extravasation measurement with dual-echo dynamic susceptibility contrast MRI”. In: *Magnetic Resonance in Medicine* 43.6 (June 2000), pp. 820–827. ISSN: 0740-3194. DOI: 10.1002/1522-2594(200006)43:6<820::AID-MRM7>3.0.CO;2-F. URL: <http://doi.wiley.com/10.1002/1522-2594%7B%5C%%7D28200006%7B%>

- 5C%7D2943%7B%5C%7D3A6%7B%5C%7D3C820%7B%5C%7D3A%7B%5C%7D3AAID-MRM7%7B%5C%7D3E3.O.CO%7B%5C%7D3B2-F.
- [Wal+14] Stéfan van der Walt et al. “scikit-image: image processing in Python”. In: *PeerJ* 2 (June 2014), e453. ISSN: 2167-8359. DOI: 10.7717/peerj.453. URL: <http://dx.doi.org/10.7717/peerj.453>.
- [Wan16] Ge Wang. “A Perspective on Deep Imaging”. In: *IEEE Access* 4.2 (Sept. 2016), pp. 8914–8924. ISSN: 2169-3536. DOI: 10.1109/ACCESS.2016.2624938. URL: <http://arxiv.org/abs/1609.04375><http://ieeexplore.ieee.org/document/7733110/>.
- [Wan+04] Zhou Wang et al. “Image Quality Assessment: From Error Visibility to Structural Similarity”. In: 13.4 (2004), pp. 600–612. DOI: 10.1109/TIP.2003.819861.
- [Wea88] J B Weaver. “Simultaneous multislice acquisition of MR images.” In: *Magnetic resonance in medicine : official journal of the Society of Magnetic Resonance in Medicine / Society of Magnetic Resonance in Medicine* 8.3 (1988), pp. 275–284. ISSN: 0740-3194. DOI: 10.1002/mrm.1910080305.
- [Wei+09] Florian Weiler et al. “NeuroQLab - A Software Assistant for Neurosurgical Planung and Quantitative Image Analysis”. In: *Lecture Notes in Informatics (LNI) - Proceedings*. GI, 2009, pp. 1352–58. URL: <http://subs.emis.de/LNI/Proceedings/Proceedings154/P-154.pdf>.
- [WE16] Markus Wenzel and Klaus Eickel. “”System, insbesondere Magnetresonanzenzsystem, zum Erzeugen von Bildern”,” DE102016113138. Fraunhofer Gesellschaft zur Forderung der Angewandten Forschung. July 15, 2016.
- [Wu+18] Junjie Wu et al. “Simultaneous perfusion and permeability assessments using multiband multi-echo EPI (M2-EPI) in brain tumors”. In: *Magnetic Resonance in Medicine* August (Oct. 2018), p. 0648. ISSN: 07403194. DOI: 10.1002/mrm.27532. URL: <http://doi.wiley.com/10.1002/mrm.27532>.
- [Yan+15] Nathan Yanasak et al. *Parallel Imaging in MRI : Technology , Applications , and Quality Control*. Tech. rep. 118. American Association of Physicists in Medicine, 2015.
- [Yos+14] Jason Yosinski et al. “How transferable are features in deep neural networks?” In: *Advances in Neural Information Processing Systems 27 (Proceedings of NIPS)* 27 (2014), pp. 1–9. ISSN: 10495258. arXiv: 1411.1792. URL: <http://arxiv.org/abs/1411.1792>.

- [You84] Ian R. Young. “Considerations affecting signal and contrast in NMR imaging.” In: *British Medical Bullentin* 40.2 (1984), pp. 139–147.
- [ZWZ10] Huiyu Zhou, Jiahua Wu, and Jianguo Zhang. *Digital Image Processing : Part 1*. Ventus Publishing Aps, 2010. ISBN: 9788776815417.
- [Zhu+18] Bo Zhu et al. “Image reconstruction by domain-transform manifold learning”. In: *Nature* 555.7697 (Mar. 2018), pp. 487–492. ISSN: 0028-0836. DOI: 10.1038/nature25988. eprint: 1704.08841. URL: <http://arxiv.org/abs/1704.08841><http://dx.doi.org/10.1038/nature25988><http://www.nature.com/doifinder/10.1038/nature25988>.

Acknowledgments

The time it took me to write this thesis was one of the most exhausting and energizing, boring and interesting, stupefying and creative, rational and emotional periods of my life. In the end, it was rather a marathon than a short distance run - with all its facets. I am happy to finally say thank you.

For the mentoring and support on many different levels, I would like to thank my supervisor Matthias Günther. You gave me the chance to do and finish this work despite the 'evil of contrast agent'. In particular, you were always open for discussion. This allowed me to think freely, to talk about 'what so ever', to intensify off- and on-topic ideas and to get an experience and valuable second opinion for many decisions.

I would like to thank Tony Stöcker for reading my thesis and joining me from our first meeting in February 2013 until this point. Your advises back then helped me a lot to find my way into MR physics.

An important part of the recent years, I spent at Fraunhofer MEVIS and could enjoy the helpful company of many colleagues.

Sincerely, I would like to thank Anja for being my co-mentor. Thank goes also to Markus, who inspired me to think about Deep Learning. I thank you, Felix, for the hours we shared 'our office', hopefully there are some more to come.

To the colleagues in the MR physics group: with many of you, I have been traveling to conferences, spent hours of meeting time, had interesting MR LALs and enjoyed MR BBQs and Herbstküchen. Therefore, I would like to say thank you to Amnah, Cristoffer, Daniel, Dennis, Jochen, Jörn, Marco, Nora, Saulius and Volker, and also the former group members David and Ina. Thanks also to Robin, Simon and Sven for proof-reading and comments to this work.

Thank you, 12:30-Mensamost group! The break after some hours of work has often maximized the off-topic creativity.

An extra portion of thanks goes to you, Rico. Thank you for your friendship, support and advice.

A special and big thank you goes to Heidelberg. Thank you mediri! The support I received was essential to me and allowed me to continue my PhD.

I would like to thank the University Hospital Essen and Lutz Lüdemann for the first

time I spent on research in the field of MRI.

For support, code snippets and proof-reading, I would like to thank Martin Blaimer.

I am grateful to many people outside work. I would like to thank Tobias for a care-parcel which helped me through some night-shifts. Thank you, friends and family in Bern, Bochum, Bremen, Dortmund, Dresden, Mettmann, Rheinberg, Rüthen and Utrecht.

A special thank 'runs' to Ingo, Philipp and Yannick. You often managed to get some fresh air into my brain and made me suffering from something different than problems with physics or informatics.

I would also like to thank my second family: thank you, Günter, Irene, Jacob, Sinja and Yannick.

A very big thank goes to my family. I am very grateful to my parents and my brother. Thanks for everything!

The greatest thanks, however, goes to you, Anica! You have been at my side during this (long) journey. We have discussed so many meaningless and important things of life. You pushed me when I was down, you were happy with me when some problem was finally solved, you gave me a break when I needed a break, you were patient with me and understood late night and weekend shifts. Thank you for all that!